

Modelling the surface mass balance of the
Greenland ice sheet and neighbouring ice
caps: a dynamical and statistical
downscaling approach

Brice Noël

Copyright © 2018, B. Noël, Utrecht, The Netherlands

Author: Brice Noël

ISBN: 978-90-393-6936-4

Printing: Imprimerie Andrien Optima, Rue Saint-Hadelin 14, Visé (Belgium)

Institute for Marine and Atmospheric research Utrecht (IMAU)

Department of Physics and Astronomy

Faculty of Science

Utrecht University

Financial support was provided by the Netherlands Polar Programme (NPP) of the Netherlands Organisation for Scientific Research (NWO), grant number 823.01.002, and the Netherlands Earth System Science Center (NESSC).

Modelling the surface mass balance of the Greenland ice sheet and neighbouring ice caps: a dynamical and statistical downscaling approach

Modélisation du bilan de masse en surface de la calotte glaciaire du Groenland et des calottes voisines: une approche de downscaling dynamique et statistique
(avec un résumé en français)

Modelleren van de oppervlakttemassabalans van de Groenlandse ijskap en aangrenzende ijskappen: een dynamische en statistische downscaling benadering
(met een samenvatting in het Nederlands)

PROEFSCHRIFT

ter verkrijging van de graad van doctor aan de Universiteit Utrecht
op gezag van de rector magnificus, prof. dr. G. J. van der Zwaan,
ingevolge het besluit van het college voor promoties
in het openbaar te verdedigen op
maandag 22 januari 2018 des middags te 2.30 uur

door

Brice Paul Y Noël

geboren op 22 mei 1991 te Oupeye, België

Promotor: Prof. dr. M. R. van den Broeke
Copromotor: Dr. W. J. van de Berg

Contents

| | |
|--|------------|
| Summary | vii |
| 1 Introduction | 1 |
| 1.1 The Greenland ice sheet | 2 |
| 1.2 Greenland and its climate | 4 |
| 1.2.1 Precipitation and meltwater runoff | 5 |
| 1.2.2 Meltwater retention in firn | 6 |
| 1.2.3 Recent changes | 7 |
| 1.3 Quantifying mass changes in Greenland | 8 |
| 1.3.1 Gravimetry | 8 |
| 1.3.2 Altimetry | 9 |
| 1.3.3 Mass budget method | 9 |
| 1.4 Reconstructing the GrIS surface mass balance | 11 |
| 1.4.1 Interpolation of in situ measurements | 12 |
| 1.4.2 PDD and SEB models | 12 |
| 1.4.3 Climate re-analyses | 12 |
| 1.4.4 Climate models and dynamical downscaling | 13 |
| 1.4.5 Statistical downscaling | 13 |
| 1.5 Regional Atmospheric Climate Model: RACMO2 | 14 |
| 1.5.1 Surface melt | 16 |
| 1.5.2 Refreezing and runoff | 17 |
| 1.5.3 Evaluation using in situ measurements | 18 |
| 1.6 Contemporary GrIS mass balance | 19 |
| 1.6.1 Mass loss acceleration | 19 |
| 1.6.2 Potential tipping point | 20 |
| 1.7 Objectives and outline | 21 |

| | | |
|----------|--|-----------|
| 2 | Evaluation of RACMO2.3: summer snowfall impact on the Greenland ice sheet | 25 |
| 2.1 | Introduction | 26 |
| 2.2 | Model and data | 27 |
| 2.2.1 | The regional climate model RACMO2 | 27 |
| 2.2.2 | RACMO2.3 update | 27 |
| 2.2.3 | RACMO2 simulations set-up | 28 |
| 2.2.4 | Observational data | 28 |
| 2.3 | Changes in SMB components | 30 |
| 2.3.1 | SMB change pattern | 30 |
| 2.3.2 | Large-scale precipitation changes | 31 |
| 2.3.3 | Summer snowfall events: the snow-albedo-melt feedback | 32 |
| 2.4 | Evaluation using observational data | 32 |
| 2.4.1 | SEB evaluation along the K-transect | 32 |
| 2.4.2 | SMB evaluation | 38 |
| 2.5 | Conclusions | 41 |
| 3 | A daily, 1 km data set of downscaled Greenland ice sheet surface mass balance | 43 |
| 3.1 | Introduction | 44 |
| 3.2 | Model and data | 45 |
| 3.2.1 | The regional climate model RACMO2 | 45 |
| 3.2.2 | GIMP DEM | 46 |
| 3.2.3 | Ablation and accumulation measurements | 47 |
| 3.2.4 | MODIS bare ice albedo | 47 |
| 3.3 | Methods | 47 |
| 3.3.1 | Elevation dependent downscaling | 49 |
| 3.3.2 | Sensitivity experiment | 50 |
| 3.3.3 | Melt and runoff adjustments | 51 |
| 3.4 | Evaluation of daily downscaled SMB | 53 |
| 3.5 | High-resolution SMB patterns: case studies | 58 |
| 3.5.1 | Central east Greenland | 58 |
| 3.5.2 | Central west Greenland | 60 |
| 3.5.3 | South Greenland | 60 |
| 3.5.4 | North Greenland | 62 |
| 3.5.5 | Greenland ice sheet | 64 |
| 3.6 | Added value, limitations and uncertainties | 64 |
| 3.7 | Conclusions | 66 |

| | | |
|----------|--|-----------|
| 4 | A tipping point in refreezing accelerates mass loss of Greenland's ice caps | 67 |
| 4.1 | Introduction | 68 |
| 4.2 | Evaluation against observations | 68 |
| 4.3 | A tipping point in GICs mass balance | 71 |
| 4.4 | Discussion | 71 |
| 4.5 | Methods | 78 |
| 4.5.1 | Regional climate model | 78 |
| 4.5.2 | Topography and ice mask | 78 |
| 4.5.3 | Bare ice albedo | 78 |
| 4.5.4 | In situ measurements | 79 |
| 4.5.5 | Remote sensing | 80 |
| 4.5.6 | Downscaling procedure | 80 |
| 4.5.7 | Elevation dependence | 80 |
| 4.5.8 | Runoff and melt adjustments | 81 |
| 4.5.9 | Precipitation correction | 83 |
| 4.5.10 | Product uncertainty | 83 |
| 4.5.11 | Breakpoint analysis | 83 |
| 4.6 | Supplementary Discussion | 84 |
| 5 | Six decades of glacial mass loss in the Canadian Arctic Archipelago | 85 |
| 5.1 | Introduction | 86 |
| 5.2 | Model and data | 88 |
| 5.2.1 | The regional climate model RACMO2.3 | 88 |
| 5.2.2 | DEM, glacier outlines and ice albedo | 88 |
| 5.2.3 | In situ SMB measurements | 88 |
| 5.3 | Methods | 90 |
| 5.3.1 | Downscaling procedure | 90 |
| 5.3.2 | Evaluation and uncertainties | 94 |
| 5.4 | Contemporary climate and recent changes | 97 |
| 5.4.1 | Drivers of the recent warming | 100 |
| 5.4.2 | Before the warming (1958-1995) | 100 |
| 5.4.3 | Mass loss acceleration (1996-2015) | 103 |
| 5.5 | Changes in the firn structure | 103 |
| 5.6 | Six decades of mass loss in the Canadian Arctic Archipelago | 106 |
| 5.6.1 | Agassiz ice cap | 106 |

| | | |
|----------|---|------------|
| 5.6.2 | Bylot Island | 108 |
| 5.6.3 | Penny ice cap | 110 |
| 5.6.4 | Barnes ice cap | 112 |
| 5.6.5 | CAA climate sensitivity | 114 |
| 5.7 | Procedure limitations | 116 |
| 5.8 | Conclusions | 117 |
| 6 | Modelling the Greenland ice sheet surface mass balance with RACMO2.3p2 | 119 |
| 6.1 | Introduction | 120 |
| 6.2 | Model and observational data | 121 |
| 6.2.1 | The Regional Atmospheric Climate Model RACMO2 | 121 |
| 6.2.2 | Surface energy budget and surface mass balance | 121 |
| 6.2.3 | Model updates | 122 |
| 6.2.4 | Initialisation and set up | 123 |
| 6.2.5 | Observational data | 126 |
| 6.3 | Results: near-surface climate and SEB | 127 |
| 6.3.1 | Near-surface meteorology | 127 |
| 6.3.2 | Radiative fluxes | 127 |
| 6.3.3 | Seasonal SEB cycle along the K-transect | 130 |
| 6.3.4 | Model comparison along the K-transect | 132 |
| 6.4 | Results: regional SMB | 135 |
| 6.4.1 | Changes in SMB patterns | 135 |
| 6.4.2 | Northeast Greenland | 138 |
| 6.4.3 | K-transect | 140 |
| 6.4.4 | Southeast Greenland | 142 |
| 6.5 | Results: SMB of the contiguous ice sheet | 143 |
| 6.5.1 | Modelled SMB at 11 km | 143 |
| 6.5.2 | Downscaled SMB to 1 km | 143 |
| 6.6 | Remaining limitations and challenges | 145 |
| 6.6.1 | Model resolution | 145 |
| 6.6.2 | Turbulent fluxes | 145 |
| 6.6.3 | Surface albedo | 145 |
| 6.7 | Summary and conclusions | 146 |

| | |
|---|------------|
| 7 Discussion and outlook | 147 |
| 7.1 General conclusions | 147 |
| 7.2 Modelling challenges | 149 |
| 7.2.1 Clouds and turbulent fluxes | 149 |
| 7.2.2 Surface albedo | 150 |
| 7.2.3 Firn processes | 150 |
| 7.2.4 Spatial resolution and non-hydrostatic models | 151 |
| 7.3 Outlook | 152 |
| Bibliography | 155 |
| Abbreviations | 167 |
| Acknowledgements | 169 |
| Publications | 171 |
| Curriculum vitae | 175 |

Summary

The Greenland ice sheet (GrIS) is the world's second largest ice mass, storing about one tenth of the Earth's freshwater in the form of snow and ice. If totally melted, global sea level would rise by 7.4 m, affecting low-lying regions worldwide. Since the mid-1990s, increased atmospheric and oceanic temperatures have accelerated GrIS mass loss through increased meltwater runoff and ice discharge across the grounding line of marine-terminating outlet glaciers.

To understand the causes of recent GrIS surface-driven mass loss, we use the Regional Atmospheric Climate Model (RACMO2) to dynamically downscale climate. This meteorological model, coupled to a multi-layer snow model, simulates the evolution of the surface mass balance (SMB), i.e. the difference between snowfall accumulation and ablation from sublimation, drifting snow erosion and meltwater runoff. In this thesis, we show that RACMO2 realistically simulates the extent of the elevated inland accumulation zone, where the GrIS gains mass at the surface as snowfall exceeds sublimation and runoff, as well as the narrow ablation zone along the low-lying margins where mass is lost through runoff of meltwater exceeding snowfall. Separating these two areas is the equilibrium line, where accumulation and ablation cancel ($SMB = 0$).

In order to cover a large domain at reasonable computational cost, RACMO2 is run at a relatively coarse horizontal resolution of 11 km (1958-2016). At this spatial resolution, the model does not well resolve small glaciated bodies, such as narrow marginal glaciers, typically only a few km wide, and small peripheral ice caps (GICs), detached from the main ice sheet. To address this issue, we developed a statistical downscaling algorithm that reprojects the original RACMO2 output on a 1 km ice mask and topography derived from the high-resolution Greenland Ice Mapping Project (GIMP) Digital Elevation Model (DEM). Correcting for surface elevation and ice albedo biases over the topographically complex GrIS margins, the downscaling procedure accurately reproduces the large ablation rates over narrow ablation zones, marginal outlet glaciers, and GICs, all important contributors to ongoing sea level rise. This downscaled 1 km product proves to be very useful for studies quantifying mass changes of these spatially restricted ice masses.

For instance, using the new 1 km data set, we identify 1997 as a tipping point for the mass balance of Greenland's GICs. Before 1997, ablation and accumulation were in approximate balance, and these peripheral ice masses remained stable. After 1997, following significant warming, the accumulation zone retreated to the highest sectors of these ice caps and their mass loss accelerated. Although previously reported by satellite altimetry measurements, no clear explanation has been provided for this acceleration so far; with the 1 km SMB product, we can identify the acting surface processes. Greenland's GICs are located in relatively dry regions where summer melt nominally exceeds winter snowfall. To sustain these ice caps, the refreezing of meltwater in the snow is a key process. The snow acts as a "sponge" that buffers a large fraction of meltwater, which subsequently refreezes in winter. The remaining meltwater that can't be buffered runs off to the ocean and directly contributes to mass loss. Until 1997, the snow layer in the interior of these ice caps could compensate for increased melt by refreezing

more meltwater. Around 1997, following decades of increased melt, the snow became saturated with refrozen meltwater, so that any additional summer melt was forced to run off to the ocean, tripling the mass loss. We call this a tipping point, as it would take decades to regrow a new, healthy snow layer that could buffer enough summer meltwater. In a warmer climate, this is highly unlikely to happen: rainfall will increase at the expense of snowfall, further preventing the formation of a new snow buffer.

Similar mechanisms are at play in the Canadian Arctic. Here, the downscaled SMB product reveals that while the northern ice caps, that are larger and more elevated, can still efficiently buffer meltwater in their extensive snow covered accumulation zones, the southern smaller and lower-lying ice fields have already lost most of their meltwater retention capacity, causing uninterrupted mass loss during the last six decades. These results suggest that the ice caps of Greenland and Canada will likely undergo irreversible mass loss. In the southern Canadian Arctic, the remaining ice fields may disappear within the next 400 years.

For now, the main Greenland ice sheet is still safe, as porous snow in the extensive accumulation zone, covering about 90% of the GrIS, still buffers most of the summer melt. At the current rate of mass loss, it would still take 10,000 years to melt the GrIS completely. However, the tipping point reached for the peripheral GICs must be regarded as an alarm-signal for the GrIS in the near future, if temperatures continue to increase.

To better resolve surface processes in RACMO2, we regularly update the model physics and evaluate the resulting simulated climate and SMB using a combination of in situ and remote sensing measurements. The latest model version, RACMO2.3p2, generally improves on previous versions. This model version will be used to conduct future climate scenario projections in forthcoming studies, essential to identify processes causing longterm GrIS mass loss and estimate Greenland's contribution to the projected sea level rise.

Résumé

Après le continent Antarctique, le Groenland possède la plus importante calotte glaciaire terrestre. A elle seule, celle-ci contient le dixième des réserves d'eau douce disponibles sur terre, conservées sous forme de neige et de glace. Si la calotte venait à fondre entièrement, elle élèverait le niveau global des océans d'environ 7,4 m, submergeant les régions côtières du monde entier. Depuis le milieu des années 90, l'augmentation croissante des températures atmosphériques et océaniques a renforcé la fonte des glaces, accélérant ainsi la perte de masse du Groenland. Cette accélération s'explique par la récente intensification de l'écoulement de fonte, dont les eaux se déversent directement dans l'océan, ainsi qu'au vèlage continu d'icebergs le long de la ligne de flottaison des glaciers à terminaison marine.

Pour mieux comprendre cette récente accélération, nous utilisons le modèle atmosphérique régional RACMO2. Ce modèle climatique permet de reconstruire l'évolution du bilan de masse en surface (BMS) de la calotte glaciaire du Groenland. Le BMS exprime la différence entre l'accumulation neigeuse déposée en surface de la calotte et la perte de glace résultant des processus de sublimation, d'érosion éolienne du manteau neigeux, ainsi que de l'écoulement de l'eau de fonte vers l'océan. Le BMS permet d'identifier deux régions distinctes: la zone d'accumulation au centre de la calotte où le dépôt neigeux surpasse la perte de glace par écoulement de fonte et la zone d'ablation située en marge de la calotte où l'écoulement de fonte l'emporte sur l'accumulation neigeuse. Ces deux zones sont séparées par la ligne d'équilibre où accumulation et ablation s'égalisent ($BMS = 0$).

RACMO2 modélise le climat du Groenland à une résolution horizontale de 11 km au cours de la période 1958-2016. L'utilisation d'une résolution spatiale relativement grossière permet de couvrir de larges régions polaires tout en limitant la puissance de calcul nécessaire. Cependant, cette grille à 11 km ne représente correctement ni les glaciers de quelques kilomètres de large, s'écoulant en bordure de la calotte, ni les masses de glace périphériques du Groenland détachées de la calotte principale. Afin de remédier à ce problème, nous avons développé un algorithme de downscaling statistique, projetant les sorties du modèle RACMO2 à 11 km vers une topographie et un masque de glace définis sur une grille à 1 km de résolution. Cette topographie et ce masque de glace à très haute résolution sont dérivés du modèle numérique de terrain Greenland Ice Mapping Project (GIMP). Cet algorithme corrige les biais d'élévation de surface et d'albédo de la glace au bord de la calotte, région présentant généralement une topographie complexe et irrégulière. De ce fait, l'algorithme de downscaling reproduit précisément les taux de fonte élevés caractérisant les étroites zones d'ablation, glaciers et calottes secondaires périphériques du Groenland qui contribuent de manière significative à l'élévation globale du niveau des mers. Cette estimation du BMS à 1 km de résolution se montre très utile pour quantifier la perte de masse des calottes glaciaires de petite taille.

L'utilisation de ces données à 1 km a permis d'identifier 1997 comme point de non retour pour le bilan de masse des calottes périphériques du Groenland. Avant 1997, ces calottes secondaires maintenaient un équilibre quasiment stable où ablation et accumulation se compensaient approximativement. Après 1997, suite à une augmentation significative des températures, les zones d'accumulation se sont retirées vers les secteurs les plus élevés de ces calottes, accélérant leur perte de masse. Bien que de précéden-

tes mesures satellitaires (altimètres) confirment cette récente accélération de fonte, aucune explication claire de ce phénomène n'a été avancée. L'intérêt majeur de notre estimation du BMS à 1 km consiste en l'identification des processus de surface impliqués dans cette accélération. Les calottes périphériques secondaires du Groenland sont situées dans des régions relativement sèches où la fonte estivale surpasse les précipitations neigeuses hivernales. Par conséquent, le gel de l'eau de fonte dans le manteau neigeux est essentiel afin de préserver ces calottes glaciaires. La neige agit comme une éponge, absorbant une part importante de l'eau de fonte. En hiver, cette réserve d'eau peut geler à nouveau au sein des pores de la couche neigeuse. La quantité d'eau de fonte non absorbée par la neige s'écoule en surface avant de se déverser dans l'océan, ce qui contribue directement à la perte de masse. Jusqu'en 1997, la couche neigeuse couvrant l'intérieur de ces calottes périphériques compensait l'augmentation de la fonte en absorbant, puis en regelant une quantité toujours croissante d'eau de fonte. Vers 1997, suite à l'intensification de cette fonte, l'absorption suivie du regel de l'eau de fonte a fini par saturer la neige. Cette saturation force toute eau de surface additionnelle à s'écouler vers l'océan, triplant ainsi la perte de masse après 1997. Ces calottes périphériques ont donc atteint un point de non retour, car une couche neigeuse saine, capable d'absorber suffisamment d'eau de fonte en été, nécessiterait plusieurs décennies afin de se reformer. La formation d'une nouvelle couche de neige absorbante est plus qu'improbable: un réchauffement climatique futur augmenterait les précipitations pluvieuses au détriment des chutes de neige.

Des mécanismes similaires agissent dans l'Arctique Canadien. Là-bas, le BMS à 1 km révèle un contraste prononcé entre les calottes de glace situées au Nord et au Sud de l'archipel. Alors que les calottes du Nord, étendues et relativement élevées, absorbent encore activement l'eau de fonte dans la neige couvrant d'importantes zones d'accumulation, les calottes du Sud, plus étroites et moins élevées, ont déjà perdu leur capacité de rétention. Par conséquent, celles-ci ont perdu de la masse de manière ininterrompue depuis ces six dernières décennies. Ces résultats suggèrent que les calottes périphériques du Groenland et du Canada connaîtront une perte de masse irréversible dans le futur. Pire encore, les calottes situées au Sud de l'archipel Arctique Canadien pourraient même disparaître définitivement au cours des 400 prochaines années.

Pour l'instant, la calotte principale du Groenland reste sauve, car son importante zone d'accumulation centrale, dont plus de 90% de la surface est couverte de neige poreuse, continue d'absorber efficacement une grande partie de l'eau de fonte estivale. Au rythme de fonte actuel, la calotte disparaîtrait entièrement au bout de 10.000 ans. Néanmoins, le point de non retour atteint par les glaciers périphériques du Groenland en 1997 doit être considéré comme un signal d'alarme inquiétant. Si le réchauffement continue, la calotte principale du Groenland pourrait bientôt être menacée.

Afin d'améliorer la représentation de ces processus de surface, la physique du modèle RACMO2 est régulièrement mise à jour. Les sorties climatiques et le BMS obtenus sont évalués à l'aide de mesures in situ et satellitaires. La dernière version, RACMO2.3p2, dépasse les performances de ses prédécesseurs. Cette nouvelle version sera utilisée afin de réaliser des scénarios de projections futures du climat. Ces simulations permettront d'identifier les mécanismes gouvernant la perte de masse du Groenland à long terme, mais également d'estimer la contribution du Groenland à l'élévation future du niveau des océans.

Samenvatting

De Groenlandse ijskap is de op één na grootste ijskap ter wereld, na die van Antarctica. Ongeveer één-tiende van al het zoetwater op aarde ligt in de Groenlandse ijskap opgeslagen in de vorm van sneeuw en ijs. Als de gehele ijskap van Groenland zou smelten zou dit de mondiale zeespiegel doen stijgen met circa 7,4 m en zodoende veel kustgebieden onder water zetten. Vanaf het midden van de jaren '90 versnelt het massaverlies van de Groenlandse ijskap door het opwarmen van de omringende oceaan en atmosfeer. Deze versnelling komt door toenemende smelt van sneeuw en ijs - dit smeltwater komt uiteindelijk terecht in de oceaan - en een versnelling van de ijsstroming aan de randen van de ijskap, waar het ijs de oceaan in stroomt en afbreekt als ijsbergen.

Om deze processen beter te begrijpen gebruiken we het regionale atmosferische klimaatmodel RACMO2. Dit model berekent de oppervlaktemassabalans (OMB) van de Groenlandse ijskap. De OMB drukt het verschil uit tussen enerzijds de accumulatie van massa bovenop de ijskap door sneeuwval en anderzijds ablatie, het verlies van massa door sublimatie, winderosie en afsmelten. RACMO2 laat zien dat de OMB van Groenland zich laat opdelen in twee duidelijke gebieden: een accumulatiezone in het binnenland waar de sneeuwval groter is dan het massaverlies door smelt en een ablatiezone aan de randen van de ijskap waar het smeltverlies groter is dan de sneeuwaccumulatie. De evenwichtslijn scheidt deze twee zones, hier zijn accumulatie en ablatie gelijk ($OMB = 0$).

Met RACMO2 hebben we het klimaat en de OMB van Groenland berekend voor de periode 1958-2016 op een relatief fijne horizontale resolutie van 11 km. Desalniettemin is deze resolutie te grofmazig om een OMB schatting te krijgen voor de kleinere gletsjers van slechts enkele km breed aan de rand van de ijskap en voor de kleinere perifere ijskappen op Groenland. Om dit probleem te verhelpen hebben we een algoritme ontwikkeld dat de modeluitvoer van RACMO2 verfijnt naar een rooster op 1 km resolutie. Dankzij dit algoritme kunnen we met hogere precisie de smeltintensiteit en het massaverlies reproduceren die kenmerkend zijn voor de ablatiezones van de gletsjers en de perifere ijskappen van Groenland. Dit is zeer relevant omdat beide momenteel significant bijdragen aan de mondiale zeespiegelstijging.

Onze resultaten laten bijvoorbeeld zien dat 1997 een kantelpunt was voor het massaverlies van de perifere Groenlandse ijskappen. Voor 1997 waren deze ijskappen nagenoeg stabiel. Door een significante temperatuurstijging hebben de accumulatiezones zich na 1997 teruggetrokken naar de hoger gelegen gebieden van deze ijskappen en verliezen deze ijskappen in toenemende mate massa. Hoewel met behulp van satellietwaarnemingen al geconstateerd was dat de ijskappen dunner werden en massa verloren, werden de oorzaken van dit massaverlies nog niet volledig begrepen. Dankzij onze modelresultaten weten we nu beter welke processen verantwoordelijk zijn: de perifere ijskappen bevinden zich in relatief droge gebieden, waardoor de zomersmelt groter is dan de sneeuwval in de winter. De ijskappen behielden desondanks hun massa omdat dit smeltwater in de onderliggende sneeuwlaag werd vastgehouden en 's winters weer bevroor. Dit proces is te vergelijken met een spons die een belangrijk deel van het smeltwater vasthoudt. Tot 1997 kon de sneeuwlaag het smeltwater nog grotendeels opvangen, maar sinds 1997 is de sneeuwlaag verzadigd geraakt en dunner geworden door steeds meer smelt. Hierdoor stroomt het extra smeltwater nu vrijwel direct weg en is het massaverlies van deze ijskappen sinds

1997 verdrievoudigd. We noemen dit een kantelpunt, omdat het meerdere decennia met kouder weer zou vergen om weer een sneeuwlaag op te bouwen die al het smeltwater kan opvangen. Bovendien zal in een toekomstig warmer klimaat, waarin de neerslag steeds meer als regen en niet als sneeuw zal vallen, de sneeuwlaag nog verder worden aangetast.

Eenzelfde soort proces is actief op de gletsjers en ijskappen in de Canadese Arctische archipel. Daar laat de OMB, wederom verfijnd naar 1 km resolutie, een duidelijk contrast zien tussen de noordelijke en de zuidelijke ijskappen van deze archipel. Waar in het noorden de uitgestrekte en relatief hooggelegen ijskappen nog uitgebreide accumulatiezones hebben, zijn de ijskappen in het zuiden hun bufferfunctie al verloren. De ijskappen in het zuidelijke gedeelte van de archipel verliezen daarom al zes decennia lang ononderbroken massa. Het is de verwachting dat deze ijskappen in de komende 400 jaar helemaal zullen verdwijnen. De resultaten in dit proefschrift tonen dus aan dat de Groenlandse en de Canadese ijskappen in de toekomst onherroepelijk massa zullen gaan verliezen.

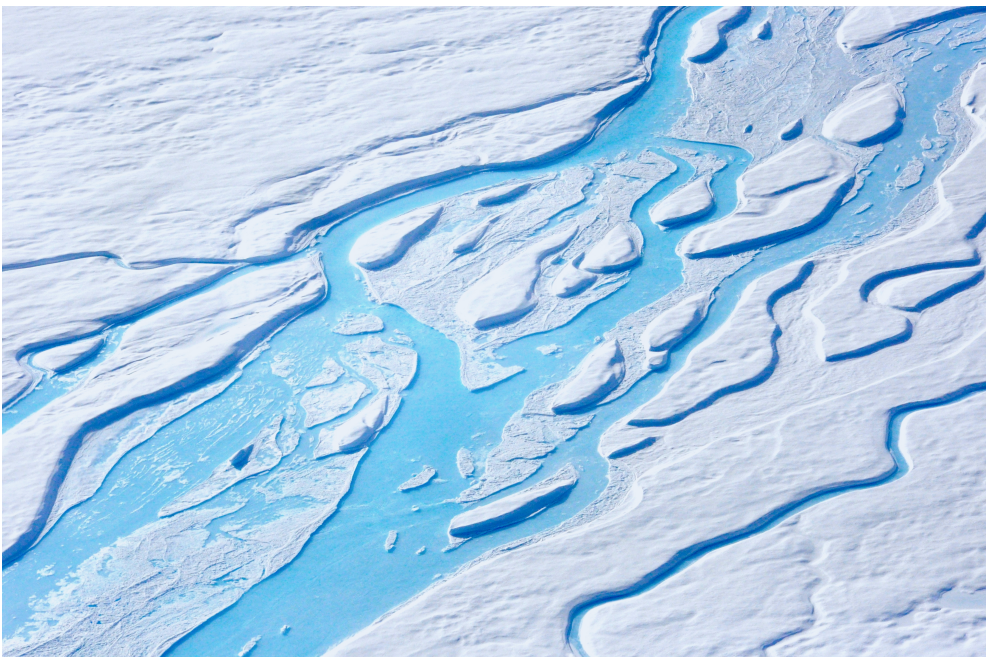
Voorlopig heeft de grote Groenlandse ijskap dit kantelpunt nog niet bereikt. De poreuze sneeuw in de accumulatiezone, die 90% van het totale oppervlak bestrijkt, is nog steeds in staat om veruit het grootste gedeelte van het smeltwater op te vangen. Met het huidige tempo van massaverlies duurt het nog 10.000 jaar voordat de hele ijskap is weggesmolten. Echter, het kantelpunt van de perifere ijskappen is een waarschuwing. Als de opwarming blijft voortduren zal ook de Groenlandse hoofdijskap op zeker moment dit kantelpunt bereiken.

Om de nauwkeurigheid van dit soort verwachtingen te verhogen wordt de numerieke beschrijving van de relevante processen in de atmosfeer en sneeuwlaag in het klimaatmodel RACMO2 regelmatig verbeterd. Dit proefschrift laat naast de al besproken resultaten zien dat de meest recente versie, RACMO2.3p2, nog beter het klimaat en de OMB representeert. Daarom zal vanaf nu deze nieuwste versie worden gebruikt om het toekomstige klimaat van Groenland te simuleren. Met deze versie kan dan uiteindelijk beter worden gekwantificeerd hoe in de toekomst de bijdrage van de Groenlandse ijskap aan zeespiegelstijging zal veranderen.

CHAPTER 1

Introduction

In this introductory chapter, we first introduce the Greenland ice sheet (Section 1.1), its climate and recent changes (Section 1.2). Then, we discuss different techniques commonly used to quantify mass changes (Section 1.3) and to reconstruct the present-day surface mass balance of the ice sheet (Section 1.4), with a special reference to the Regional Atmospheric Climate Model RACMO2 (Section 1.5). Section 1.6 briefly summarises the contemporary mass changes over the ice sheet, followed by objectives and outline of the thesis in Section 1.7.



"Climate change is no longer some far-off problem; it is happening here, it is happening now."

Barack Obama (2015).

Meltwater rivers draining the accumulation zone of the Greenland ice sheet after the extreme melt event of summer 2012, photo courtesy of Paul Smeets.

1.1 The Greenland ice sheet

The Arctic is home to numerous glaciated regions of different sizes (Fig. 1.1) including:

- the extensive Greenland ice sheet (GrIS) and its peripheral glaciers and ice caps (GICs).
- the ice caps of the Canadian Arctic Archipelago (CAA) to the west of Greenland.
- the ice caps of Svalbard and Iceland to the east and southeast of Greenland, respectively.

Greenland is the largest island on Earth, extending over 20° of latitude, stretching from Cape Farewell in the south (63°N) to Cape Morris Jesup in the north (83°N). As a result, coastal Greenland experiences a large latitudinal temperature gradient, from an annual mean of approximately 0°C in the warmer and wetter south to about -15°C in the colder and drier northern regions, and values as low as -30°C at the top of its elevated ice sheet. From west to east, the island extends at most about 1000 km. Every year in March, the sea ice cover around Greenland reaches its maximum extent, covering the whole of Baffin Bay to the west of Greenland. Sea ice also fringes the eastern coast from Fram Strait in the north down to Denmark Strait in the south, separating Greenland from Svalbard and Iceland, respectively. Until mid-September, sea ice gradually retreats northward, where it persists through summer in the Arctic Ocean to the north of Greenland.

With an area of 1.7 million km^2 , covering more than 80% of Greenland, the GrIS is the world's second largest ice mass. The GrIS consists of an up to 3 km thick ice layer that stores ~ 2.9 million km^3 or gigaton (Gt) of water, representing roughly one tenth of the Earth's total freshwater volume. The elevated GrIS interior is covered by a permanent snow layer, whereas the marginal winter snow cover eventually melts in summer, exposing bare ice at the surface.

The GrIS and the smaller peripheral GICs, detached from the main ice sheet, are highly sensitive to climate warming and have recently become the major contributor to global sea level rise [Rignot et al., 2011], with a peak contribution of 43% in 2012, i.e. 1.2 mm sea level rise equivalent (SLR) [Van den Broeke et al., 2016]. Since the early 1990s, Greenland has lost more than 3.000 Gt of ice, equivalent to approximately 8 mm SLR [Van den Broeke et al., 2017]. If completely melted, the GrIS and GICs would rise global sea level by 7.4 m, affecting low-lying regions worldwide [Vaughan et al., 2013].

Freshwater discharge into the North Atlantic Ocean not only raises global sea level, but also has the potential to weaken the large-scale thermohaline circulation [Rahmstorf et al., 2015]. This might mitigate projected European climate warming by weakening the northwards branch of the Gulf Stream, well known for transporting large amounts of heat to the western coasts of Europe [Dickson et al., 2002].

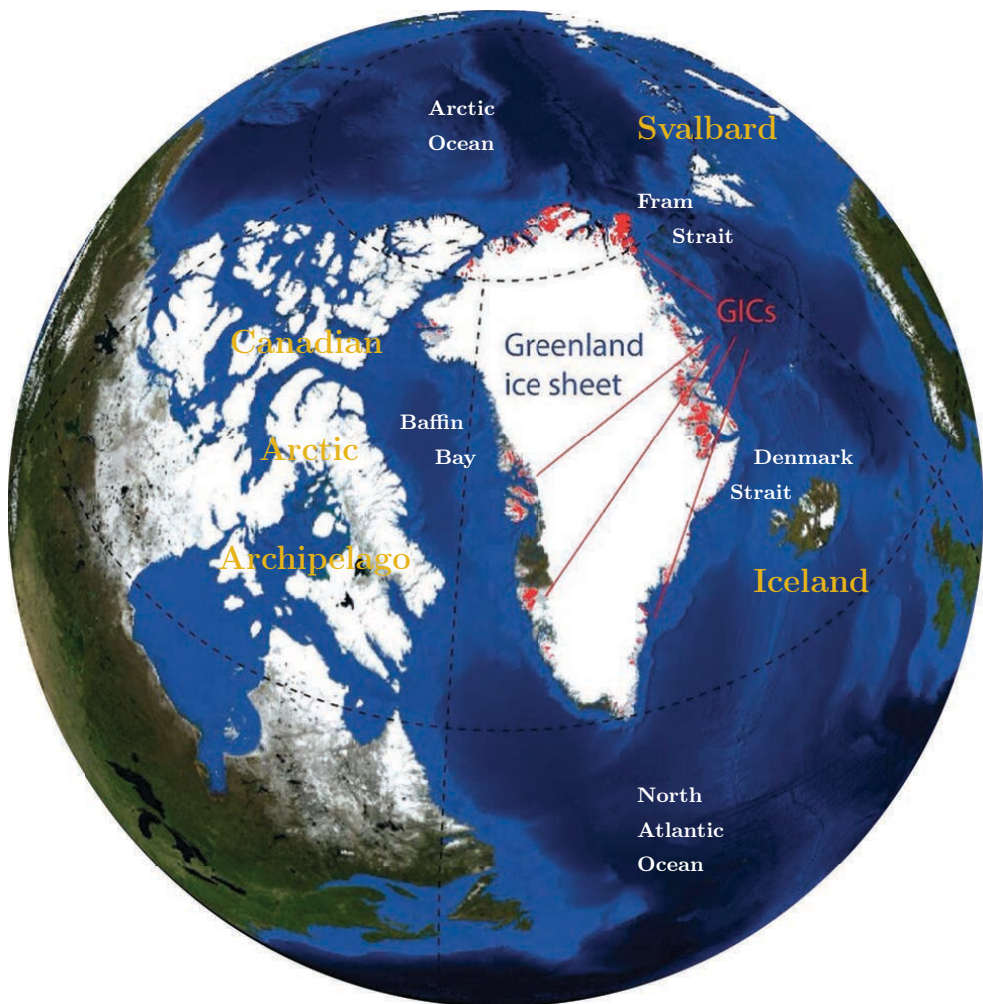
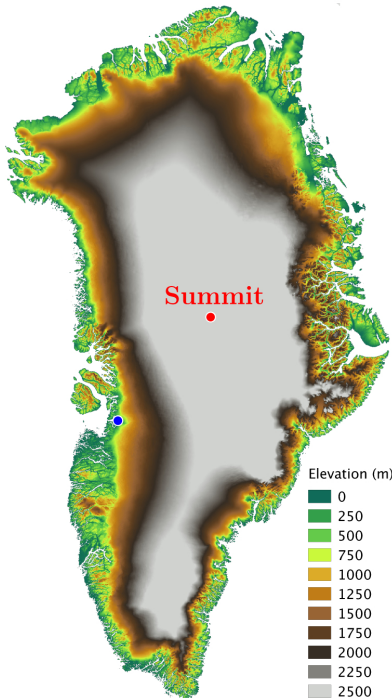


Figure 1.1: Mosaic of satellite images representing the Arctic and its numerous glaciated regions. Greenland's peripheral GICs are represented in red. Picture courtesy of Stef Lhermitte [Blue Marble, <https://earthobservatory.nasa.gov/Features/BlueMarble>].

1.2 Greenland and its climate

The surface elevation of the GrIS (Fig. 1.2a) increases inland and peaks at Summit (72.5°N, 37.6°W; red dot in Fig. 1.2a), the highest location on the ice sheet at 3216 m above sea level (m a.s.l.). The GrIS interior is a relatively flat plateau gradually becoming steeper towards the margins. Most of the ice sheet is terminating in the low-lying ice-free tundra regions that can be ~ 150 km wide, e.g. in southwest and north Greenland (Fig. 1.2b). The rugged GrIS margins include narrow fjords and deeply incised valleys, shaped over multiple glacial cycles by the erosion of fast flowing outlet glaciers, draining the ice sheet. Greenland is home to over 200 outlet glaciers [Moon et al., 2012], from which at least 178 are marine-terminating [Enderlin et al., 2014]. The largest marine-terminating glacier in the Northern Hemisphere is Jakobshavn Isbræ in western Greenland (blue dot in Fig. 1.2a). It drains about 6.5% of the GrIS area, and has recently accelerated, reaching flow velocities of ~ 17 km yr⁻¹ in 2012 [Joughin et al., 2004, 2014].

a) Topography



b) Ice mask

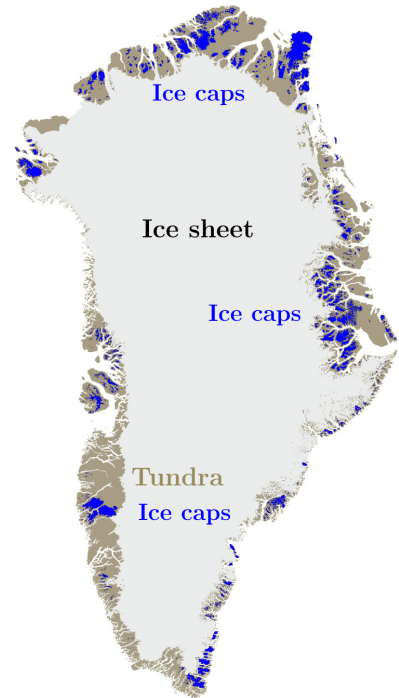


Figure 1.2: a) Surface topography and b) ice mask derived from the Greenland Ice Mapping Project (GIMP) Digital Elevation Model (DEM) down-sampled to 1 km resolution [Howat et al., 2014].

1.2.1 Precipitation and meltwater runoff

The interaction of the GrIS topography with the large-scale atmospheric circulation governs the precipitation distribution over the ice sheet [Petersen et al., 2004]. Figure 1.3a shows modelled total annual precipitation, combining snowfall and rainfall, averaged for the period 1958-2015 [Noël et al., 2016]. The GrIS experiences prevailing southwesterly large-scale winds (in the middle troposphere), following the polar front which is on average located at about 60°N . As a result, relatively warm and humid air masses propagate from southwest to northeast over Greenland, creating a large-scale negative precipitation gradient in that direction. The west coast of Greenland receives 400 to 1000 mm water equivalent precipitation per year (w.e. yr^{-1}), while the northeastern coast, located at the lee side of the central topographical divide, remains relatively dry, i.e. ~ 100 mm w.e. yr^{-1} . In southeast Greenland, humid air masses are deflected onshore by the Icelandic Low, a climatological low pressure system over Iceland. This leads to pronounced topographically forced precipitation maxima that can locally exceed 3.000 mm w.e. yr^{-1} [Box, 2013], corresponding to a ~ 10 m layer of fresh snow. The elevated ice sheet interior receives only 50 to 100 mm w.e. yr^{-1} [Hawley et al., 2014]. Interpolating between in situ measurements retrieved from 289 firn cores and snow pits scattered all over the ice sheet interior, Bales et al. [2009] estimated a spatially averaged mass gain of 300 ± 24 mm w.e. yr^{-1} over the GrIS.

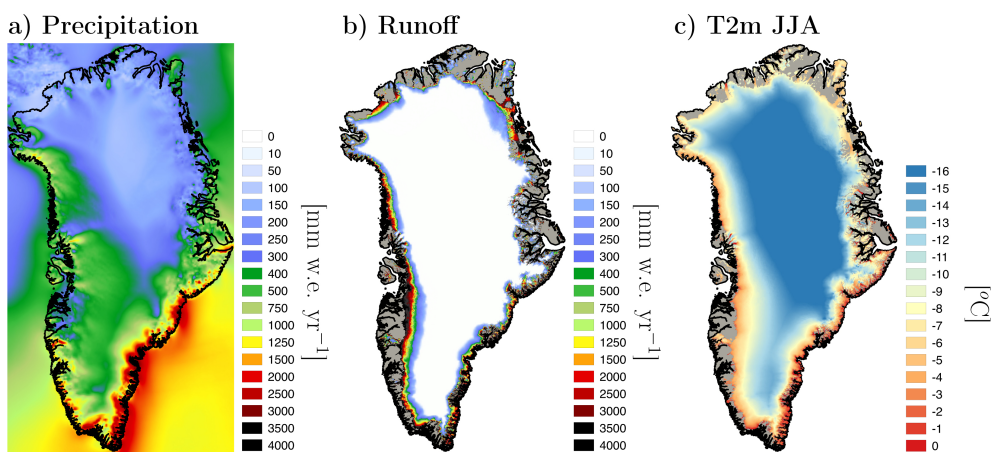


Figure 1.3: Annual modelled a) total precipitation, i.e. snow and rain, b) runoff. c) Annual mean summer (June-July-August) 2-m temperature. All fields are downscaled from RACMO2.3 to 1 km for 1958-2015 [Noël et al., 2016].

In summer (June-July-August), the ice sheet loses mass through runoff of meltwater (Fig. 1.3b). In marginal regions below 1500 m a.s.l., summer temperatures persistently exceed the melting point (Fig. 1.3c), especially over low-lying, narrow outlet glaciers. As a result, surface melt rapidly erodes the winter snow cover before bare ice is exposed. Over $\sim 10\%$ of the GrIS surface, summer meltwater runoff exceeds winter snowfall: these regions are referred to as ablation zones. Runoff progressively decreases with elevation and lower inland temperatures until it ceases in the extensive ice sheet interior. This high elevated region is called the accumulation zone, where a perennial firn layer has formed.

1.2.2 Meltwater retention in firn

The firn consists of an up to 100 m thick layer of compressed snow persisting through summer and covering over 90% of the GrIS area (Fig. 1.4a) [Machguth et al., 2016b]. It plays a critical role in the response of the GrIS to atmospheric warming, since it acts as an efficient meltwater buffer (Fig. 1.4b). In the lower accumulation area, we find the percolation zone or wet snow zone, where meltwater infiltrates in the firn and is retained either by refreezing or by capillary forces in the available pore space (Fig. 1.4c) [Harper et al., 2012]. Once the firn column is saturated with meltwater, the remainder runs off downslope to the ocean (Fig. 1.3b). In most of the percolation zone, experiencing relatively low melt and accumulation rates, runoff is exacerbated by impermeable ice lenses that form in the upper parts of the firn layer (see the introduction picture on page 1). Ice lenses significantly reduce the firn buffering capacity by preventing vertical percolation [De la Peña et al., 2015; Machguth et al., 2016b]. The GrIS currently retains $\sim 45\%$ of the total meltwater production in the firn layer [Steger et al., 2017]. In south-east Greenland, a unique combination of high summer melt rates and pronounced winter accumulation allows for the formation of perennial firn aquifers, covering $\sim 4\%$ of the GrIS and storing 140 ± 20 Gt of meltwater [Koenig et al., 2014; Kuipers Munneke et al., 2014; Miège et al., 2016]. Figure 1.4c highlights these firn aquifers as regions with high retention rates, i.e. 500 to 600 mm w.e. yr^{-1} . Meltwater in these aquifers remains liquid as the thick winter snow layer insulates the water from the cold winter atmosphere, maintaining deep snowpack temperatures close to the melting point [Forster et al., 2014].

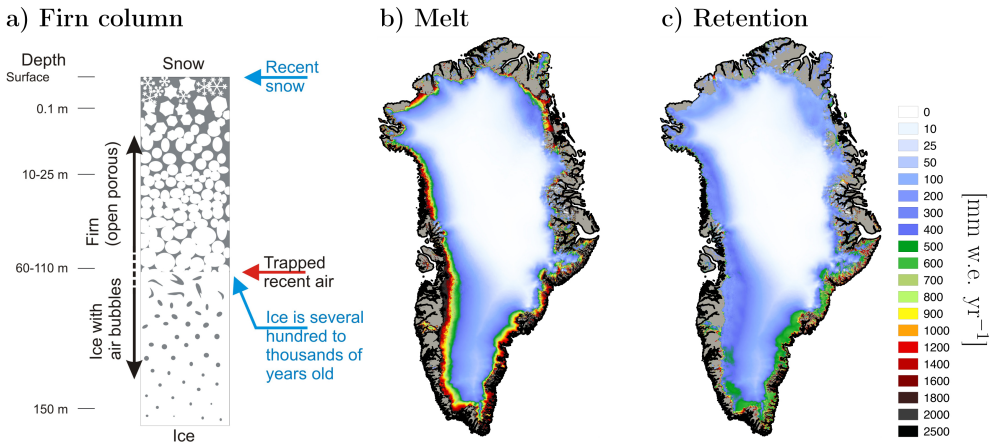


Figure 1.4: a) Schematic representation of a vertical profile in the firn column. Annual cumulative b) melt, i.e. snow and ice, c) retention, the sum of refreezing and capillary forces, modelled by RACMO2.3 and downscaled to 1 km for 1958-2015 [Noël et al., 2016].

The dry snow zone is restricted to the highest sectors of the GrIS accumulation zone, where extremely cold surface conditions, with temperatures down to -70°C in winter and -20°C in summer, on average prevent any wetting of the firn by the occurrence of surface melt (Fig. 1.4b). This region will act as a meltwater buffer that will mitigate surface runoff in a future warmer climate. In contrast, peripheral GICs experience melt at all elevations. Peripheral GICs are situated mostly below 1500 m a.s.l., and as a result experience relatively high near-surface temperatures in summer. The large summer melt rates often exceed the relatively low winter accumulation. Therefore, efficient refreezing of meltwater in firn

is crucial to sustain these smaller ice caps. The same also applies to the ice caps located in the Canadian Arctic to the west of Greenland.

1.2.3 Recent changes

Recently, the GrIS has experienced record warm summers leading to extreme melt episodes [Hanna et al., 2014], notably in 2007, 2010, 2012 and 2016 [Tedesco et al., 2011, 2013, 2016a]. Fettweis et al. [2013b] attribute $\sim 70\%$ of the recent warming to more frequent anticyclonic conditions over Greenland, favouring large-scale southwesterly advection of warm air towards the GrIS (Fig. 1.5) [Hanna et al., 2016; Tedesco et al., 2016c]. The warmer atmosphere leads to pronounced changes over the GrIS:

- extension of the melt season [Tedesco et al., 2011].
- inland propagation of the ablation zone [Fettweis et al., 2011].
- darkening of the snow/ice surface [Box et al., 2012; Tedesco et al., 2016b].

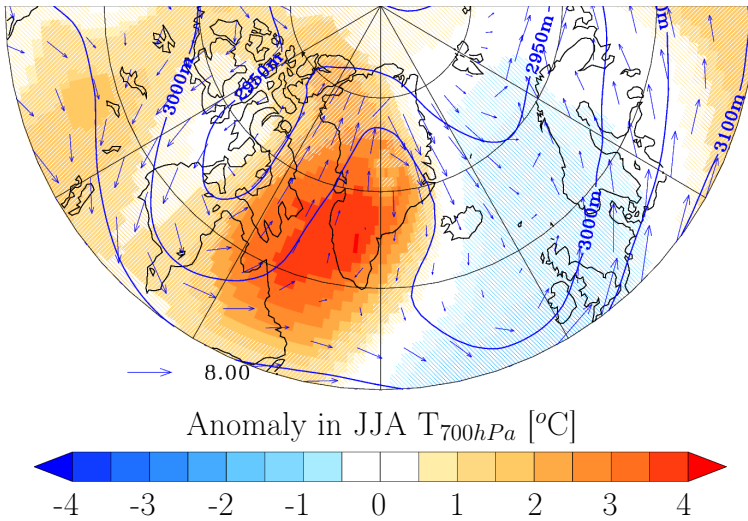


Figure 1.5: Anomalies in temperature ($^{\circ}\text{C}$) at 700 hPa height (blue contours) in summer 2012 (June-July-August) retrieved from ERA-Interim. Wind speed (m s^{-1}) and direction can be estimated from the blue arrows [Van den Broeke et al., 2017].

In warm summers, surface albedo decreases through i) a faster snow metamorphism in the percolation zone, i.e. fine fresh snow flakes grow into larger old and wet snow grains that are less reflective [Tedesco et al., 2016b], ii) the premature disappearance of the winter snow cover exposing darker bare ice at the surface [Tedesco et al., 2013], iii) the formation of meltwater ponds at increasingly higher elevations [Tedesco et al., 2012], and iv) growth and accumulation of algae and cryoconites, i.e. windblown particles including dust, soot and microbes, darkening bare ice surfaces [Musilova et al., 2016; Stibal et al., 2017]. These processes act in concert to intensify surface melt.

In July 2012, over 98% of the ice sheet area experienced melt [Nghiem et al., 2012], an unprecedented event in the satellite era (post-1979). Even Summit, situated in the dry snow zone, experienced significant melt. Evidence of such strong melt episodes can be found in the firn layer of the GrIS percolation zone as impermeable ice lenses [McGrath et al., 2013; De la Peña et al., 2015], reminiscent of active meltwater refreezing. These ice lenses have the potential to enhance GrIS mass loss, as they prevent the underlying firn to buffer meltwater to its full capacity, increasing runoff [Machguth et al., 2016b].

Fettweis et al. [2013a] and Rae et al. [2012] suggested that the projected increase in surface melt will saturate the remaining snow pore space, reducing the firn buffering capacity of the GrIS to about 30% of its current value by 2100 [Van Angelen et al., 2013]. This chain of events might tip the ice sheet into a state of sustained mass loss, with significant runoff contribution from all elevations [McGrath et al., 2013].

1.3 Quantifying mass changes in Greenland

The Mass Balance (MB) of an ice sheet quantifies the change in ice mass (M) with time (dM/dt), and can be expressed as:

$$MB = \frac{dM}{dt} = SMB - D \quad [Gt \text{ yr}^{-1}] \quad (1.1)$$

SMB represents surface processes, i.e. accumulation (snowfall) and ablation (runoff) of mass at the snow/ice surface, and D represents the ice flow dynamics, i.e. icebergs calving at the snout of marine-terminating glaciers and basal melt of floating ice tongues. Three methods are commonly used to quantify the mass balance of the GrIS: satellite gravimetry, satellite altimetry and the mass budget method (MBM). In this section, we briefly describe these different approaches and list their respective advantages and drawbacks.

1.3.1 Gravimetry

In March 2002, the twin satellites of the Gravity Recovery and Climate Experiment (GRACE) were launched. GRACE has the advantage that it provides a direct measure of GrIS MB by monitoring gravity anomalies, resulting from mass gains or losses [Velicogna, 2009; Wouters et al., 2013]. This method provided the first irrefutable proof that the GrIS was losing mass in 2005 [Velicogna and Wahr, 2006].

GRACE has several limitations. It does not discriminate between SMB and D , and its time series are relatively short (2003-2017). The footprint of the measurements is large (~ 200 km) limiting the applicability to large ice bodies. This also causes signal leakage between neighbouring glacier catchments [Velicogna, 2009]. In addition, the data set requires multiple corrections to eliminate external signals from mass transport in the atmosphere, ocean and solid earth, e.g. glacial isostatic adjustment (GIA) [King et al., 2010]. The GRACE mission ended in September 2017 and a follow-on mission GRACE-FO is planned for 2018.

1.3.2 Altimetry

Unlike GRACE, laser and radar altimeters do not directly measure mass changes, but a change in ice sheet volume [Sørensen et al., 2011; Helm et al., 2014; McMillan et al., 2016]. Recording the time-of-flight of a laser or radar pulse reflected by the GrIS surface, and resorting to the propagation velocity of the emitted signal in the atmosphere, these altimeters estimate changes in GrIS surface elevation h in time (dh/dt). Interpolating between satellite ground tracks, the obtained dh/dt field is integrated over the GrIS area to estimate a volume change (dV/dt). The latter is converted into mass balance (MB) after correcting for firn compaction processes, usually using modelled snow density profiles [Sørensen et al., 2011]. Exploiting model data inherently introduces additional uncertainties to the final product [Kuipers Munneke et al., 2015]. The method also suffers from measurement errors due to variable penetration depth in firn affecting radar altimeter data, while laser altimeters are highly sensitive to the presence of clouds, scattering back the emitted pulse.

Modern satellite altimetry provides dh/dt at kilometre resolution, allowing to quantify the MB of small ice bodies such as Greenland's peripheral GICs [Noël et al., 2017a], the ice caps of the Canadian Arctic [Noël et al., 2017b], Svalbard [McMillan et al., 2014] or Iceland [Foresta et al., 2016]. Furthermore, time series are longer than that of gravimetry, starting in the mid-1990s for satellite altimetry and extending back to the mid-1980s for aerial photography. Ice, Cloud and Land Elevation Satellite (ICESat, 2003-2010) and CryoSat-2 (2010 onwards) are the two most recent radar and laser altimeters operating in space. To ensure continuous time series in the future, ICESat-2 will be launched in 2018.

1.3.3 Mass budget method

The mass budget method (MBM) estimates MB from the difference between surface mass balance (SMB) and solid ice discharge (D) across the grounding line of calving glaciers:

$$MB = SMB - D \quad (1.2)$$

Solid ice discharge

D is calculated by summing the estimated ice discharge of 178 GrIS marine-terminating glaciers from combined measurements of ice thickness and surface velocity close to the glaciers' grounding lines [Enderlin et al., 2014]. In general, ice thickness is calculated as the elevation difference between the GrIS surface and the underlying bedrock. Coverage and quality of ice thickness data have much improved recently as a result of the repeated airborne ice-penetrating radar surveys compiled by NASA Operation IceBridge. Ice flow velocity is estimated using satellite radar interferometers (SAR) and applying tracking algorithms to derive the motion of surface features from successive satellite images [Moon et al., 2012].

Surface mass balance

Figure 1.6 shows the different processes that add mass to or remove mass from the ice sheet surface. Total precipitation (P_{tot}), consisting for $\sim 96\%$ of snowfall (SF) with rainfall (RA) as a remainder, is the major ice sheet mass source, with an average of 695 Gt yr^{-1} for 1961-1990 [Van den Broeke et al., 2016]. Meltwater runoff (RU), i.e. the amount of surface melt (ME) that is not refrozen (RF) or retained (RT) in the snow, is the primary surface mass sink with 256 Gt yr^{-1} . Total sublimation (SU) from surface and drifting snow processes removes 41 Gt yr^{-1} . SU can act both as a source (deposition or riming) or a sink depending on the season and location on the ice sheet. Although not negligible locally, when integrated over the GrIS snow erosion by drifting snow transport (ER) removes less than 1 Gt yr^{-1} , representing the flux of drifting snow that is transported away from the GrIS towards the ocean or tundra. SMB is the sum of these four mass fluxes:

$$SMB = P_{\text{tot}} - RU - SU - ER \quad [\text{Gt yr}^{-1}] \quad (1.3)$$

Using SMB data, we can now define three different regions on the ice sheet as illustrated in Fig. 1.7: i) the inland accumulation zone where the GrIS gains mass at the surface ($SMB > 0$), ii) the marginal ablation zone where $SMB < 0$, and iii) the equilibrium line separating these two areas ($SMB = 0$).

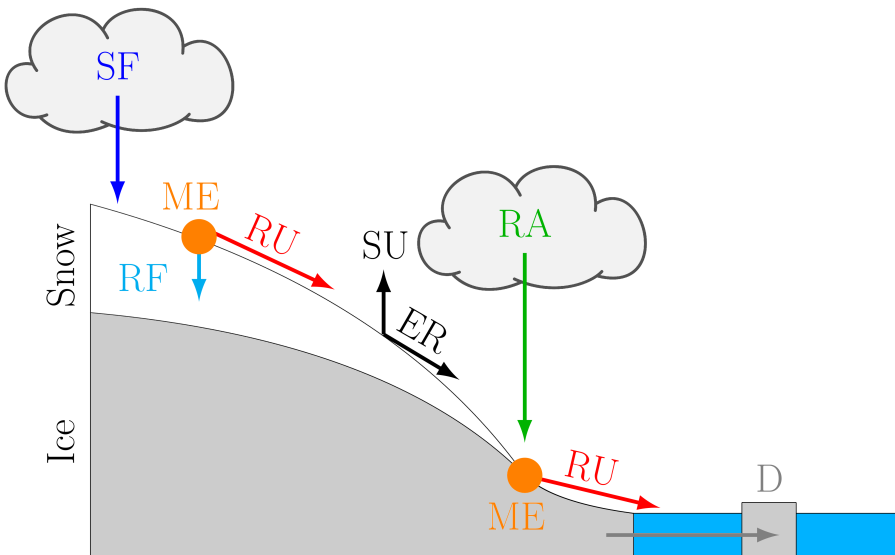


Figure 1.6: Cartoon showing the different components of SMB and D required to estimate the mass balance of an ice sheet using the mass budget method.

1.4 Reconstructing the GrIS surface mass balance

In this section, we introduce and discuss different techniques commonly used to reconstruct the contemporary GrIS SMB. Previously, SMB has been estimated by:

- spatially and temporally interpolating in situ measurements. [Bales et al., 2009; Box, 2013].
- using Positive Degree Day (PDD) or surface energy budget (SEB) models forced by climate model data or statistically downscaled climate re-analyses, i.e. assimilation of measured climate data including precipitation. [Wilton et al., 2016; Krapp et al., 2017; Zekollari et al., 2017].
- forcing mass balance models by re-analyses or climate model data. [Mernild et al., 2010, 2011].
- modelling the climate and surface processes of the GrIS with Earth System Models (ESMs; Fig. 1.7a). [Vizcaíno et al., 2013; Fyke et al., 2014].
- dynamically downscaling climate re-analyses or ESM output with regional climate models (RCMs; Fig. 1.7b). [Noël et al., 2015; Fettweis et al., 2017; Langen et al., 2017].
- statistically downscaling RCMs output to higher horizontal resolution (Fig. 1.7c). [Franco et al., 2012; Machguth et al., 2013; Noël et al., 2016].

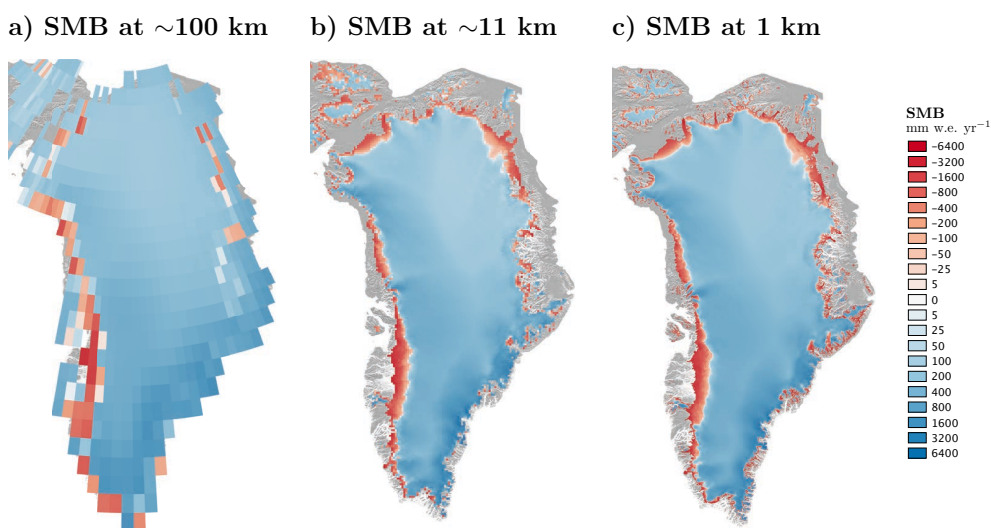


Figure 1.7: SMB as modelled by a) the Community Earth System Model (CESM) at ~ 100 km resolution, b) RACMO2.3 at ~ 11 km resolution, and c) RACMO2.3 downscaled to 1 km resolution for the period 1958-2015. Ablation zones are displayed in red, the accumulation zone in blue, and the equilibrium line in white.

1.4.1 Interpolation of in situ measurements

Bales et al. [2001, 2009] compiled an accumulation data set including in situ measurements from 289 inland ice cores and snow pits. By interpolating (kriging) data between these measurement sites, Bales et al. [2009] created a spatially continuous field of accumulation covering the whole ice sheet. Combining interpolated in situ measurements and climate model data of accumulation and surface temperature, Box [2013] estimated the contemporary GrIS SMB using a PDD model (see section 1.4.2).

The greatest advantage of this technique stems from the utilisation of observations to obtain realistic GrIS SMB. However, these measurements are sparse, scattered over the GrIS and only cover short time periods, including numerous data gaps. Furthermore, local measurements are not necessarily representative of the larger surrounding areas, inherently causing large uncertainties in the resulting SMB product.

1.4.2 PDD and SEB models

PDD and SEB models calculate ice and snow melt as a function of daily near-surface temperature (T_{2m}). PDD models use observed or modelled daily mean surface temperature to derive melt as the excess surface energy resulting from near-surface temperatures being above the melting point [Janssens and Huybrechts, 2000]. SEB models explicitly resolve the radiative and turbulent fluxes at the ice sheet surface, and estimate the available energy for melting ice or snow by closing the surface energy balance (see section 1.5.1) [Krapp et al., 2017]. To account for meltwater retention in snow and estimate surface runoff, PDD and SEB models usually incorporate a snow module.

While these two models resolve melt, retention and runoff, they do not simulate the atmosphere physics and its interactions with the GrIS surface. Therefore, they rely on modelled (climate models) or observed (climate re-analyses, see section 1.4.3) precipitation fields to estimate SMB, making the resulting product highly sensitive to the quality of the selected forcing.

1.4.3 Climate re-analyses

Climate re-analyses assimilate, on a global grid, local surface and atmospheric measurements of e.g. temperature, pressure, humidity, wind speed and direction, and sea ice extent. These data, retrieved from satellite, aircraft, weather station, ship and buoy measurements, are dynamically extrapolated in time and space using a global forecast model to obtain spatially and temporally continuous re-analyses fields. The forecast model explicitly resolves the dynamics and physics of the atmosphere and its interactions with the surface. As an example, ERA-40 and ERA-Interim are state-of-the-art global re-analyses [Uppala et al., 2005; Dee et al., 2011], covering the period 1958-2016 on a three hourly basis and at a spatial resolution of 0.75° (~ 80 km). The latest product ERA5 has recently been released and currently provides climate data for 2010-2016 at ~ 31 km resolution (<https://www.ecmwf.int/>).

1.4.4 Climate models and dynamical downscaling

Climate models simulate gridded fields of individual SMB components at high temporal resolution (sub-daily) over extensive time periods (~ 60 years), and do not rely on scarce in situ measurements. In contrast to PDD, SEB or mass balance models, they explicitly resolve the atmospheric physics, large-scale circulation, and the physical processes at the snow/ice surface, i.e. melt, refreezing and runoff. While ESMs simulate Earth's climate on a global grid with variable regional performance, polar RCMs zoom in on smaller integration domains and are specifically adapted to model ice-covered regions. In addition, ESMs are usually not constrained by observations and generally provide a much better representation of polar climates than do re-analyses, as they include a dedicated snow module. In contrast, RCMs are forced by climate re-analyses at the domain lateral boundaries every six hours, preventing simulations to diverge too far from observed conditions. In the domain interior, RCMs dynamically downscale the re-analyses to the model grid. As a result, polar RCMs model SMB components at high spatial resolutions, typically 5 to 20 km, whereas ESMs currently run at ~ 100 km. This higher resolution is essential to resolve the narrow ablation zone of the GrIS (Figs. 1.7a and b).

1.4.5 Statistical downscaling

RCM output can be further statistically downscaled to (sub) kilometre resolution (Fig. 1.7c). Statistical downscaling procedures correct individual SMB components for surface elevation biases using the topography and glacier outlines of a high-resolution Digital Elevation Model (DEM). To achieve this, Machguth et al. [2013] used precipitation and temperature lapse rates spatially interpolated from sparse in situ observations, while Franco et al. [2012] and Noël et al. [2016] used modelled SMB gradients derived from RCMs. Statistical downscaling further improves the representation of SMB patterns especially in narrow ablation zones, small outlet glaciers and neighbouring ice caps that are not accurately resolved in RCMs (Fig. 1.8).

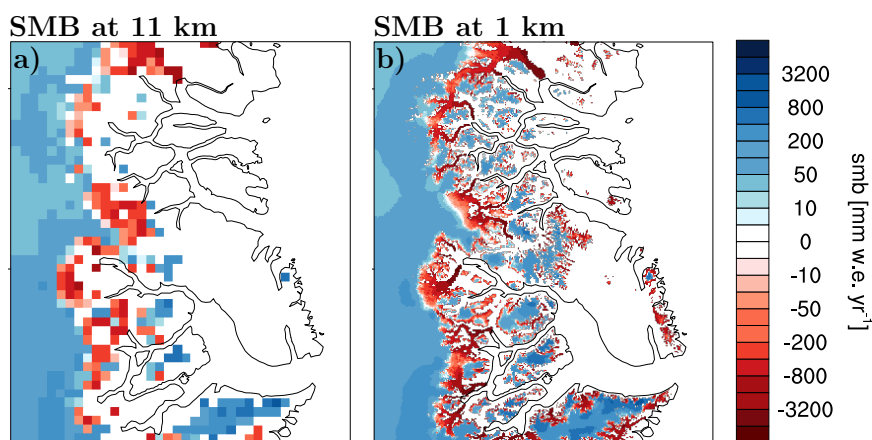


Figure 1.8: SMB of central east Greenland a) dynamically downscaled by RACMO2.3 at 11 km, b) statistically downscaled to 1 km averaged for 1958-2015. Note how the high resolution product resolves the large mass loss rates over marginal outlet glaciers and peripheral ice caps.

The major advantage of the mass balance method (MBM) combining D measurements with (down-scaled) RCM data is that it resolves individual SMB components on a spatially continuous grid, allowing for partitioning their relative contribution to the total mass balance. However, it is important to note that this method also suffers from potentially large uncertainties as individual SMB components cannot be directly evaluated using in situ or remote sensing measurements [Van den Broeke et al., 2016].

1.5 Regional Atmospheric Climate Model: RACMO2

As discussed in the previous section, a polar-adapted RCM is very suitable to estimate the climate and SMB of the GrIS and neighbouring ice masses (Fig. 1.9). In this thesis, we use the polar version of the Regional Atmospheric Climate Model (RACMO2) [Van Meijgaard et al., 2008].

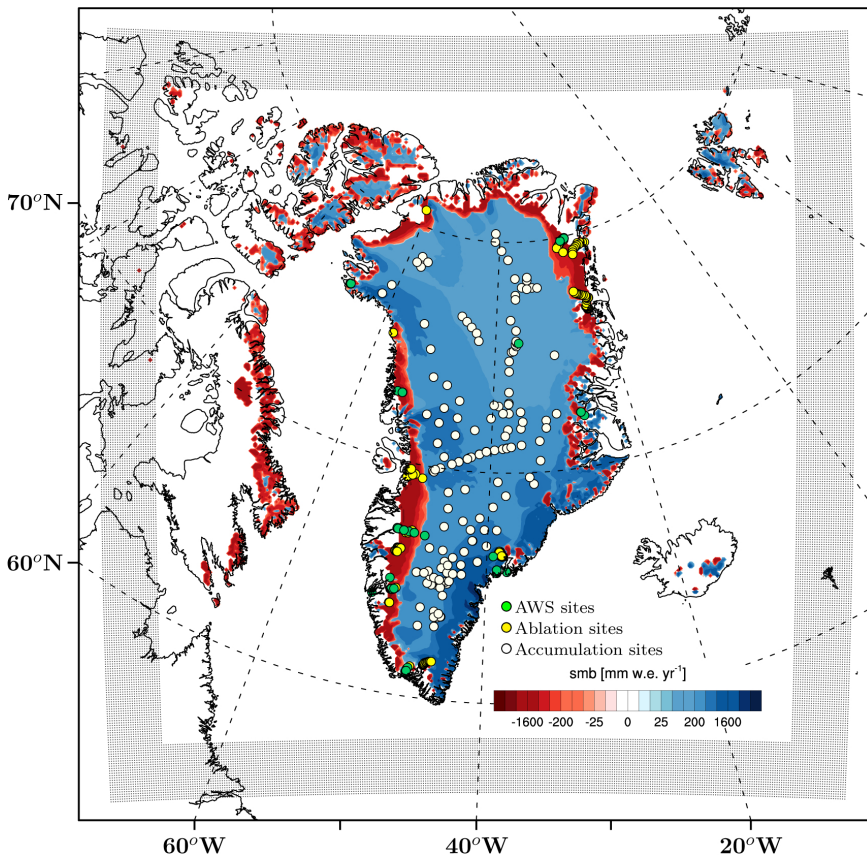


Figure 1.9: SMB (mm w.e. yr⁻¹) modelled by RACMO2 at 11 km resolution for 2016. Black dots delineate the relaxation zone where the model is forced by ERA re-analyses. SMB measurement sites in the ablation zone are displayed as yellow dots, and as white dots in the accumulation zone. Automatic Weather Stations (AWS) are represented in green [Noël et al., 2017c].

Figure 1.10 shows the different modules of RACMO2, their interactions and forcing. The model is developed and maintained at the Royal Netherlands Meteorological Institute (KNMI) and adopts the atmosphere physics from the European Centre for Medium-Range Weather Forecasts Integrated Forecast System [ECMWF-IFS, 2008] and the atmosphere dynamics of the High Resolution Limited Area Model (HIRLAM) [Undèn et al., 2002]. The polar version of RACMO2 implements a dedicated snow module developed at IMAU to specifically simulate the SMB of land ice in polar regions [Ettema et al., 2010b], including the ice sheets of Greenland and Antarctica. In addition, RACMO2 includes a snow albedo scheme [Kuipers Munneke et al., 2011] and a drifting snow routine accounting for wind-driven snow erosion and sublimation [Lenaerts et al., 2012a].

Greenland climate simulations are currently conducted at 11 km horizontal resolution with 40 vertical atmospheric levels, and cover a large integration domain, including Greenland, the Canadian Arctic, Svalbard and Iceland (Fig. 1.9). RACMO2 is forced at its lateral boundaries by ERA-40 (1958-1978) [Uppala et al., 2005] and ERA-Interim (1979-2016) [Dee et al., 2011] re-analyses within the domain relaxation zone (black dots in Fig. 1.9). The forcing consists of temperature, humidity, pressure, wind speed and direction being prescribed every six hours at each of the 40 vertical atmosphere model levels. As RACMO2 does not include an ocean module, sea surface temperature and sea ice cover are prescribed from the same re-analyses [Stark et al., 2007]. To represent accurate surface elevation and glacier outlines of the GrIS, RACMO2 uses a high-resolution DEM [Bamber et al., 2001; Howat et al., 2014].

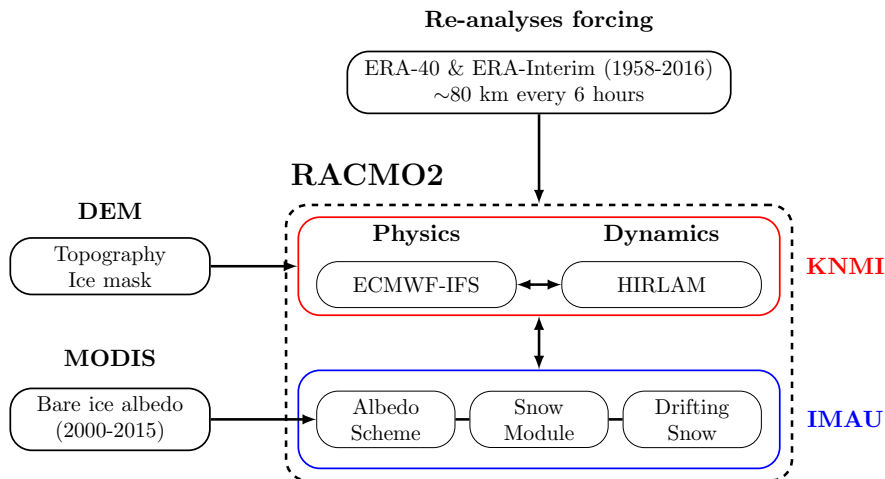


Figure 1.10: Schematic representation of the forcings and modules implemented in RACMO2.

1.5.1 Surface melt

RACMO2 calculates snow and ice melt (ME) as the excess energy in W m^{-2} (M) at the ice sheet surface after closing the surface energy budget (SEB, Fig. 1.11):

$$\begin{aligned} M &= SW_d + SW_u + LW_d + LW_u + SHF + LHF + G_s \\ &= SW_d (1 - \alpha) + LW_d + LW_u + SHF + LHF + G_s \end{aligned} \quad (1.4)$$

where SW_d and SW_u are the downward and upward shortwave (solar) radiation fluxes, respectively, LW_d and LW_u the longwave (terrestrial) downward and upward radiation fluxes, SHF and LHF the turbulent sensible and latent heat fluxes, G_s the subsurface heat flux, and α the broadband surface albedo of snow or ice. All fluxes are defined positive when directed towards the surface.

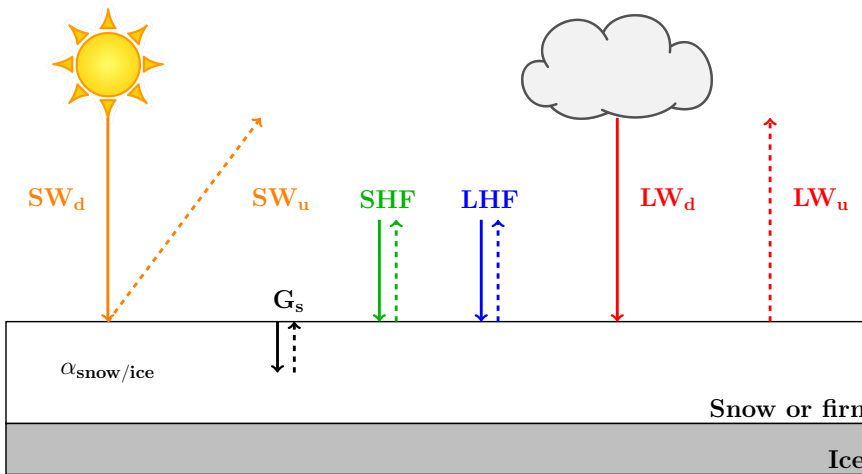


Figure 1.11: Scheme showing the different components required to close the surface energy balance.

The incoming solar radiation, SW_d , usually represents the largest source of melt energy [Box, 2013], modulated by the albedo, α , of the snow or ice surface. To provide realistic melt, the albedo scheme explicitly models the annual snow albedo cycle, ranging from 0.85 for bright fresh snow in winter to 0.60 for old wet snow in summer. Among other factors, snow albedo is modelled based on snow grain size and impurity concentration in snow, i.e. including soot and dust [Kuipers Munneke et al., 2011]. In contrast, physical processes controlling ice albedo variations in space and time remain poorly known. Therefore, ice albedo is directly prescribed from the MODerate-resolution Imaging Spectroradiometer (MODIS) satellite measurements and is currently assumed constant in time (Fig. 1.10). Bare ice albedo is minimised at 0.30 for dark ice in the low-lying ablation zone, and maximised at 0.55 for clean, bright ice.

1.5.2 Refreezing and runoff

In RACMO2, firn is represented as a multi-layer column, including 40 active snow layers, through which liquid water from melt (ME) and rain (RA) can percolate. Liquid water is either retained in firn by capillary forces as irreducible water (RT) or refreezes (RF) [Ettema et al., 2010b] (Fig. 1.12). The snow module also accounts for dry snow densification, i.e. compaction caused by the overburden pressure of fresh snow deposition [Ligtenberg et al., 2011], which acts together with refreezing to progressively deplete firn pore space until the entire column turns into ice with a density of $\sim 900 \text{ kg m}^{-3}$. The fraction of meltwater not retained is assumed to runoff immediately. RACMO2 estimates runoff of excess water (RU) calculating the liquid water balance:

$$RU = ME + RA - RT - RF. \quad (1.5)$$

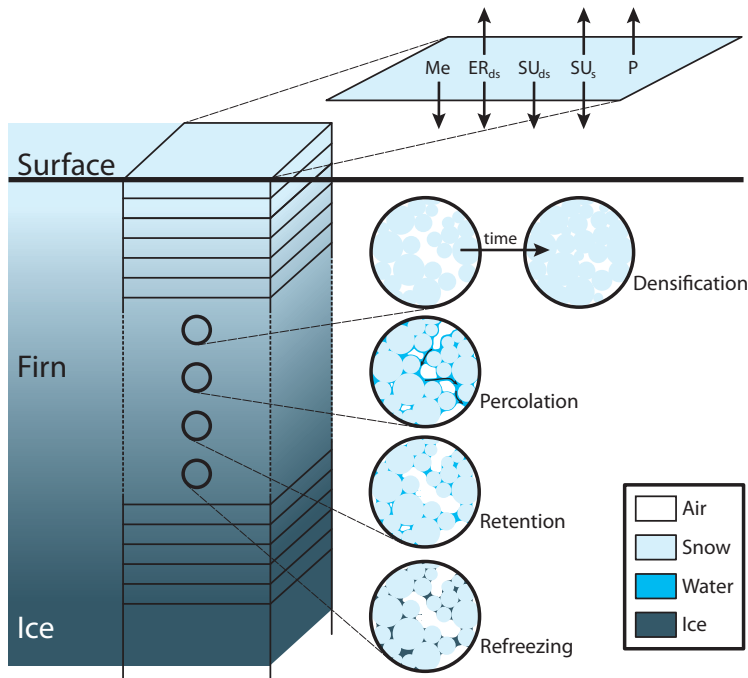


Figure 1.12: Water percolation and retention in the firn column [Ligtenberg et al., 2014].

1.5.3 Evaluation using in situ measurements

In situ measurements of SMB and SEB components are essential for model evaluation, and helped to significantly reduce uncertainties in polar RCMs [Noël et al., 2015; Fettweis et al., 2017; Langen et al., 2017]. Recently, Machguth et al. [2016a] compiled an archive of historical GrIS ablation records collected since the early 1890s (yellow dots in Fig. 1.9). Accumulation is estimated from snow pits and firn cores [Bales et al., 2001, 2009], and airborne radar measurements in the GrIS interior [Koenig et al., 2016; Overly et al., 2016; Lewis et al., 2017] (white dots in Fig. 1.9). Furthermore, longterm measurements of radiative fluxes, i.e. SW_u , SW_d , LW_u and LW_d , and meteorological variables, including near-surface temperature, specific humidity, wind speed and surface pressure, are collected using automatic weather stations (AWS) as part of the Kangerlussuaq transect (K-transect) operated by the Institute for Marine and Atmospheric research at Utrecht University (IMAU) in western Greenland at $\sim 67^\circ N$ and spanning $47\text{--}50^\circ W$ (Fig. 1.13) [Smeets et al., 2017], and of the Programme for Monitoring of the Greenland Ice Sheet (PROMICE, green dots in Fig. 1.9) [Van As et al., 2011]. RACMO2 generally shows good agreement when compared to these measurements [Noël et al., 2017c], although this might result from compensating errors between poorly parameterised processes, e.g. cloud physics [Van Tricht et al., 2016] and turbulent fluxes [Fausto et al., 2016]. Therefore, continuous monitoring of the GrIS SMB/SEB and meteorological conditions is essential to further improve the model physics and evaluate the simulated contemporary climate and SMB.

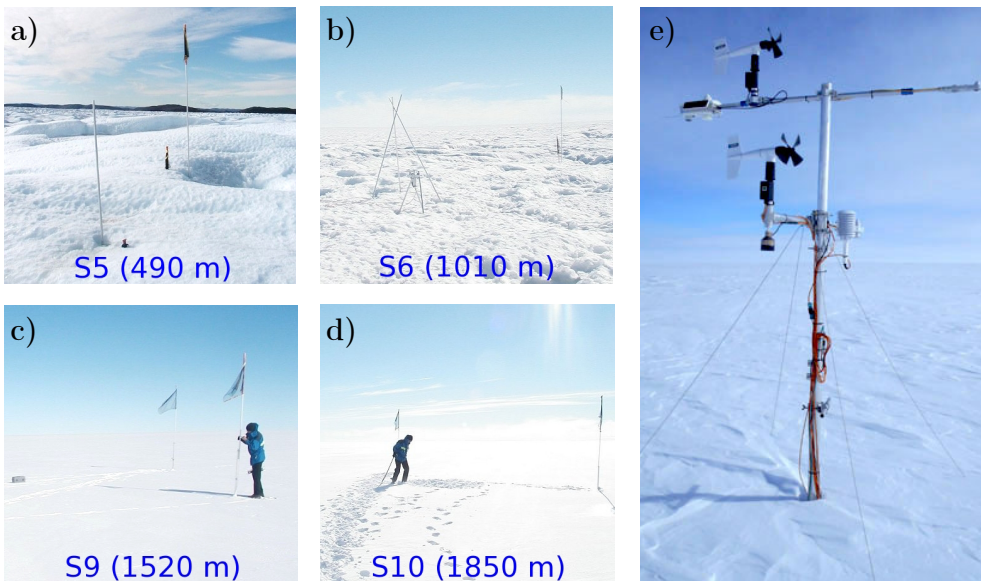


Figure 1.13: Stakes measuring SMB along the K-transect in west Greenland ($67^\circ N$) at station a) S5 and b) S6 located in the lower and upper ablation zone, respectively, c) S9 close to the equilibrium line and d) S10 in the accumulation zone [Van de Wal et al., 2012]. e) AWS site measuring meteorological data at S10 (<http://www.projects.science.uu.nl/iceclimate/>).

1.6 Contemporary GrIS mass balance

Figure 1.14 shows time series of GrIS D (blue), SMB (orange) modelled by RACMO2 and MB (red) expressed in Gt yr^{-1} for the period 1958-2015, reconstructed using the MBM method [Van den Broeke et al., 2016]. Negative MB is also expressed in terms of mm yr^{-1} sea level rise equivalent (SLR). Before the mid-1990s, average SMB of 418 Gt yr^{-1} (1958-1995) was equivalent to the mass lost through glacial discharge at the grounding line (411 Gt yr^{-1} for 1995), reminiscent of an ice sheet in approximate balance, i.e. $\text{MB} \approx 0$. In other words, over this early period, the GrIS was not significantly contributing to sea level rise.

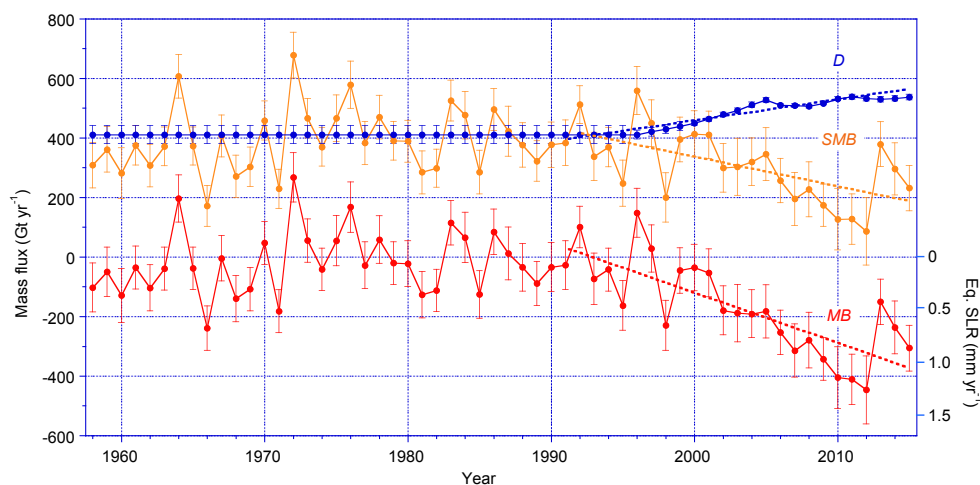


Figure 1.14: Time series of total mass balance (MB in red) and its components: surface mass balance (SMB in orange) as modelled by RACMO2.3 and solid ice discharge (D in blue) in Gt yr^{-1} for 1958-2015. Mass loss (negative MB) is also expressed in sea level rise equivalent (SLR; mm yr^{-1}) [Van den Broeke et al., 2016].

1.6.1 Mass loss acceleration

Following the recent atmospheric and oceanic warming in the Arctic [Fettweis et al., 2013b; Hanna et al., 2009, 2014], the GrIS has experienced sustained mass loss from enhanced meltwater runoff and solid ice discharge [Rignot et al., 2011; Shepherd et al., 2012; Wouters et al., 2013]. Enhanced runoff is responsible for 61% of the recent mass loss acceleration ($-16.8 \pm 2.8 \text{ Gt yr}^{-2}$ after 1991), while the remainder is ascribed to sustained elevated solid ice discharge from fast flowing marine-terminating outlet glaciers [Van den Broeke et al., 2016].

Since the 1990s, Hanna et al. [2013] and Box [2013] have reported a summer warming of 2°C over the GrIS, increasing runoff by 40% (363 Gt yr^{-1} for 1991-2015) with no significant change in precipitation, hence decreasing the GrIS SMB to 306 Gt yr^{-1} [Van den Broeke et al., 2016]. At the same time, most marginal outlet glaciers have accelerated [Joughin et al., 2004, 2014; Howat and Eddy, 2011; Moon

et al., 2012; Enderlin et al., 2014], gradually increasing D until it stabilised around 560 Gt yr^{-1} in 2010 [Van den Broeke et al., 2016]. As a result, the total mass loss increased six-fold compared to preceding decades (1958-1995), attaining an average of $\sim 300 \text{ Gt yr}^{-1}$ and peaking at $\sim 450 \text{ Gt yr}^{-1}$ in 2012, i.e. representing 1.2 mm SLR for that year (Fig. 1.14).

Mass loss acceleration has also dramatically affected glaciers and ice caps along the GrIS periphery, especially in north Greenland where accumulation zones significantly retreated to the highest sectors of the GICs [Noël et al., 2017a]. Consequently, Greenland is now the largest single contributor to ongoing global sea level rise.

1.6.2 Potential tipping point

In the future, glacial discharge will eventually cease when the ice sheet retreats further inland and loses contact with the ocean [Goelzer et al., 2012], making runoff the sole contributor to sea level rise. This will not happen overnight, given the deeply incised glacial valleys in which many marine terminating outlet glaciers are situated [Morlighem et al., 2017]. As D is definite positive, increasingly larger runoff fluxes in a warmer climate will lead to permanently negative SMB and hence negative MB. This is often referred to as a tipping point, for which Greenland ice loss becomes irreversible [Van den Broeke et al., 2016]. According to Rae et al. [2012], a 2°C increase in mean annual temperature is sufficient to tip the GrIS into irreversible mass loss. Such a tipping point could be crossed by 2070 [Van Angelen et al., 2013]. Nevertheless, at the current mass loss rate of $\sim 300 \text{ Gt yr}^{-1}$ and without additional positive feedbacks, the GrIS will still require about 10,000 years to melt completely [Van den Broeke et al., 2016].

1.7 Objectives and outline

In this thesis, we use the state-of-the-art regional climate model RACMO2 to simulate the contemporary climate and SMB of the GrIS and its surroundings. Model updates are detailed in relevant chapters. Using in situ measurements, remote sensing and regional climate modelling, we aim to:

1. demonstrate that dynamical downscaling using RACMO2.3 realistically simulates present-day GrIS SMB, SEB and climate,
2. better resolve SMB over narrow ablation zones and small outlet glaciers at the GrIS margins by further statistical downscaling,
3. identify the surface processes that caused recent GrIS, GICs and CAA mass loss acceleration,
4. improve the performance of RACMO2.3 through further physics developments.

To achieve these goals, we first conduct a present-day climate simulation using RACMO2.3 at 11 km forced by ERA re-analyses (1958-2015). The model is successfully evaluated using in situ measurements and improves on the previous model version RACMO2.1.

However, a spatial resolution of 11 km proves insufficient to resolve the large SMB gradients on the steep slopes of the GrIS margins, including narrow ablation zones, small outlet glaciers and peripheral GICs that significantly contribute to Greenland ice loss. To address this issue, we developed a novel technique that statistically downscales, on a daily basis, individual SMB components to a 1 km grid. The downscaled product provides SMB patterns over the large network of narrow outlet glaciers fringing the GrIS margins in unprecedented detail (Fig. 1.15).

Complementing remote sensing data, the downscaled product stands out as a key tool to estimate the mass balance of small glaciated features not accurately resolved in the original RACMO2.3 grid. Providing individual SMB components at 1 km resolution on a daily time scale, this new data set also opens the way to identify the surface processes responsible for the recent mass loss acceleration affecting not only the GrIS, but also its peripheral GICs and the neighbouring ice masses of the Canadian Arctic (Fig. 1.15).

Finally, to address most remaining biases in the 11 km product, we updated the cloud scheme and snow module of RACMO2.3 to version RACMO2.3p2. This data set, extending to 2016, is also statistically downscaled to 1 km, and the new model settings will soon be used for future climate scenario projections.

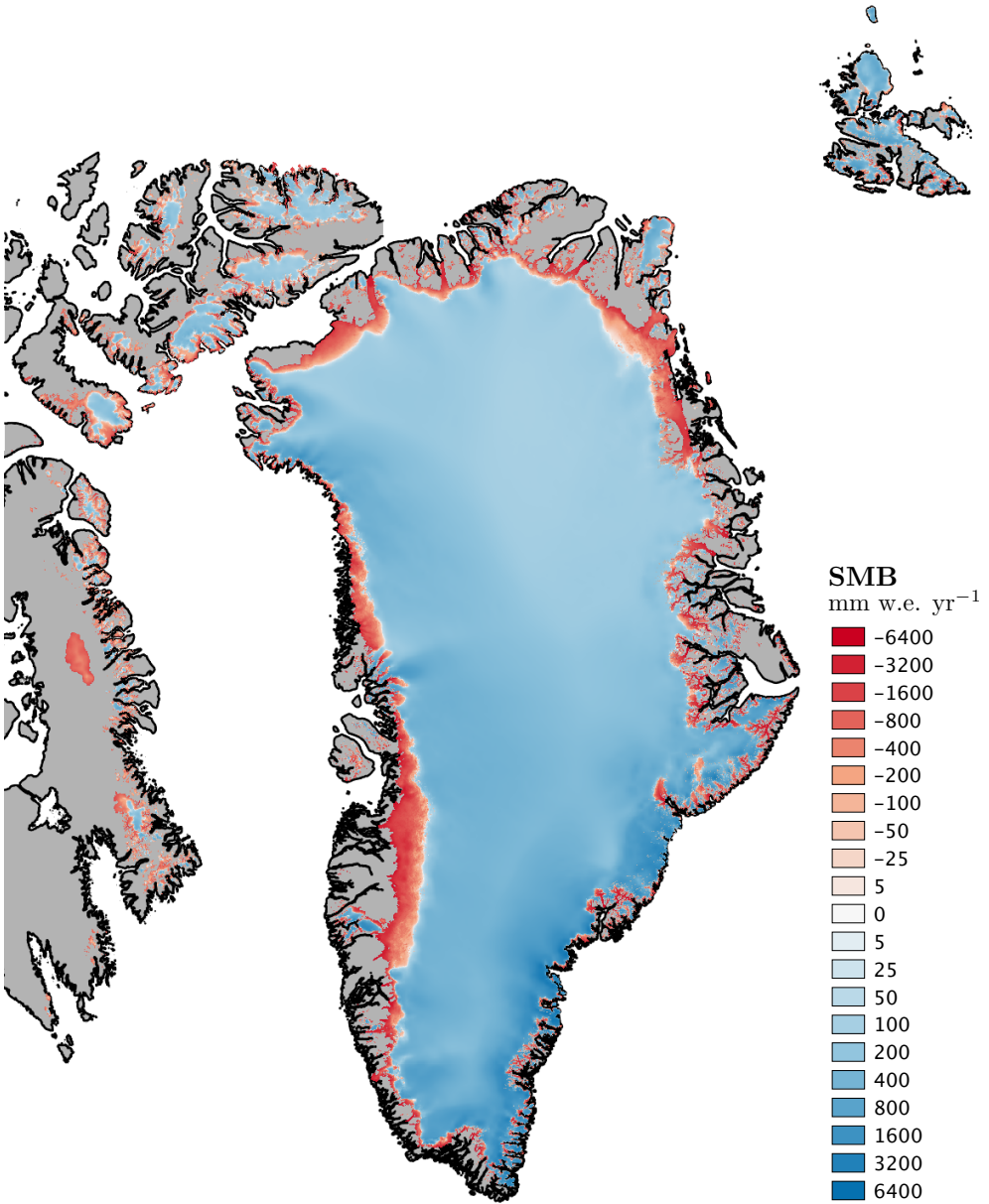


Figure 1.15: *SMB as modelled by RACMO2.3 and downscaled to 1 km resolution over the GrIS, the peripheral GICs and the neighbouring ice masses of the CAA and to 0.5 km over Svalbard for 1958-2015.*

Thesis outline

Figure 1.16 summarises the different goals achieved in this thesis work (continuous lines) and suggested future work (dashed lines).

In chapter 2, we present the climate data simulated by RACMO2.3 at 11 km (1958-2015), evaluated using in situ SMB and SEB measurements collected along the K-transect (67°N) in southwest Greenland. Using model output, we investigate the impact of summer snowfalls on the GrIS surface albedo and SMB. The daily 1 km GrIS SMB data set (1958-2015), statistically downscaled from the output of RACMO2.3, is presented in chapter 3. We also discuss the downscaling procedure, added value and limitations. Then, the downscaled product is used to identify the surface processes that accelerated the mass loss over Greenland's peripheral GICs (chapter 4) and the small ice masses of the CAA (chapter 5). In chapter 6, we update the cloud scheme and snow module of RACMO2.3 and carry out a new simulation covering 1958-2016. The updated model, RACMO2.3p2, is thoroughly evaluated using in situ SMB/SEB and point meteorological records, and shows important improvements. Finally, chapter 7 summarises the major results compiled in this thesis and discusses remaining modelling challenges and future research avenues.

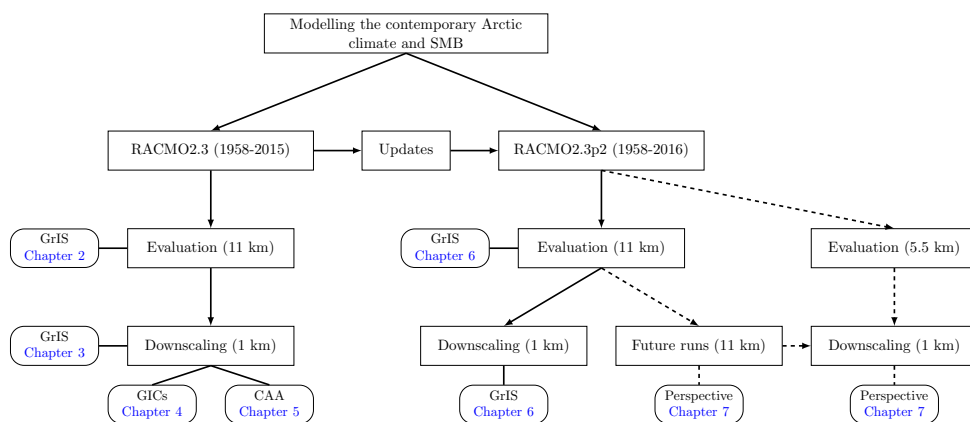


Figure 1.16: Flow chart of the thesis.

Evaluation of RACMO2.3: summer snowfall impact on the Greenland ice sheet

Summary

We discuss Greenland ice sheet (GrIS) surface mass balance (SMB) differences between the updated polar version of the RACMO climate model (RACMO2.3) and the previous version (RACMO2.1). Among other revisions, the updated model includes an adjusted rainfall-to-snowfall conversion, that produces exclusively snowfall under freezing conditions; this especially favours snowfall in summer. Summer snowfall in the ablation zone of the GrIS has a pronounced effect on melt rates, affecting modelled GrIS SMB in two ways. By covering relatively dark ice with highly reflective fresh snow, these summer snowfalls have the potential to locally reduce melt rates in the ablation zone of the GrIS through the snow-albedo-melt feedback. At larger scales, SMB changes are driven by differences in orographic precipitation following a shift in large-scale circulation, in combination with enhanced moisture to precipitation conversion for warm to moderately cold conditions. A detailed comparison of model output with observations from automatic weather stations, ice cores and ablation stakes shows that the model update generally improves the simulated SMB-elevation gradient as well as the representation of the surface energy balance, although significant biases remain.

This chapter is based on: B. Noël et al. (2015), Evaluation of the updated regional climate model RACMO2.3: summer snowfall impact on the Greenland Ice Sheet, *The Cryosphere*, 2015

2.1 Introduction

Since the mid-1990s, atmospheric and oceanic warming in the Arctic has led to accelerated Greenland ice sheet (GrIS) mass loss [Enderlin and Howat, 2013; Fettweis et al., 2013b; Wouters et al., 2013]. Combined observational and model studies show that increased meltwater runoff, and solid ice discharge through the acceleration of marine-terminating outlet glaciers [Hanna et al., 2009; Nick et al., 2009; Fettweis et al., 2011; Rignot et al., 2011], account for $\sim 60\%$ and $\sim 40\%$ respectively of the recent GrIS mass loss [Rignot et al., 2008; Van den Broeke et al., 2009; Enderlin and Howat, 2013].

Since surface melt over the GrIS is mainly driven by the absorption of shortwave radiation [Van den Broeke et al., 2008], surface albedo is a primary factor governing ice sheet surface mass balance (SMB) [Bougamont et al., 2005; Tedesco et al., 2011; Fitzgerald et al., 2012] and surface energy balance (SEB) [Tedesco et al., 2008; Van Angelen et al., 2012]. Ice albedo is mainly a function of impurity content, while snow albedo is sensitive to several snow physical properties, e.g. grain size, liquid water content, soot concentration and the presence of cryoconite. Satellite and in situ observations have revealed a general decay of GrIS surface albedo in recent years [Box et al., 2012; Stroeve et al., 2013]. In the ablation zone, this decrease is mainly caused by the prolonged exposure of dark, bare ice [Fettweis et al., 2011; Tedesco et al., 2011]. In the accumulation zone, it is proposed that higher temperatures lead to enhanced snow metamorphism and surface darkening [Box et al., 2012], resulting in enhanced melt through the positive melt-albedo feedback [Stroeve, 2001].

Summer snowfall events can interrupt this feedback, by covering dark ice and/or metamorphosed snow with a highly reflective fresh snow layer. Greuell and Oerlemans [1986] showed that significant summer snowfall events (> 5 mm w.e.) on an Alpine glacier caused a major reduction in ablation during the following days, subsequently leading to a long-term positive SMB anomaly. They estimated this positive SMB response to be two to three times larger than the mass of deposited solid precipitation. Fettweis et al. [2005] analysed two heavy snowfall events in southeast Greenland at the end of July 1991, using MAR (Modèle Atmosphérique Régional) and AVHRR satellite imagery. These events temporarily raised surface albedo, delaying the appearance of darker bare ice. Based on data from automatic weather stations (AWS), Van den Broeke et al. [2011] showed that even minor summer snowfall events (< 5 mm w.e.) can considerably reduce surface melting.

Therefore, an accurate representation of (summer) snowfall events is essential to model the SMB of the GrIS [Fettweis et al., 2005; Van Angelen et al., 2012]. This requires a high-resolution model, to resolve the narrow ablation zone, and an explicit model of atmospheric and surface snow/ice physics. Here, we use the polar version of the regional atmospheric climate model RACMO2.3, at 11 km horizontal resolution, which is coupled to a multi-layer snow model with prognostic albedo formulation. We compare the simulated GrIS SMB and SEB with the previous model version (RACMO2.1, Van Angelen et al. [2012]) and with ice cores, stake and AWS measurements along the K-transect in west Greenland, with special reference to the representation of summer snowfalls. In Section 2.2, the physics upgrades in RACMO2.3 and the measurements along the K-transect are briefly described. The impact of upgraded physics on GrIS SMB through the snow-albedo feedback is discussed in Section 2.3. Section 2.4 evaluates model output using K-transect and accumulation zone data, after which conclusions are drawn in Section 2.5.

2.2 Model and data

2.2.1 The regional climate model RACMO2

The Regional Atmospheric Climate Model (RACMO2) is developed and maintained at the Royal Netherlands Meteorological Institute (KNMI) [Van Meijgaard et al., 2008]. RACMO2 adopts the atmospheric physics module from the European Centre for Medium-range Weather Forecasts Integrated Forecast System (ECMWF-IFS) [ECMWF-IFS, 2008] and the dynamical core of the High Resolution Limited Area Model (HIRLAM) [Undèn et al., 2002]. The polar version of RACMO2 was developed by the Institute for Marine and Atmospheric Research (IMAU), Utrecht University to specifically represent the SMB evolution over the ice sheets of Greenland, Antarctica and other glaciated regions. To that end, the atmosphere model has been interactively coupled to a multi-layer snow model that simulates meltwater percolation, refreezing and runoff [Ettema et al., 2010b]. It includes an albedo scheme with prognostic snow grain size [Kuipers Munneke et al., 2011] and a drifting snow routine that simulates interactions between drifting snow, the ice sheet surface and the lower atmosphere [Lenaerts et al., 2012a].

2.2.2 RACMO2.3 update

The RACMO2 physics package has recently been updated from cycle CY23r4 used in RACMO2.1 [White, 2001] to cycle CY33r1 in the current RACMO2.3 version [ECMWF-IFS, 2008]. These updates include major changes in the description of cloud microphysics, surface and boundary layer turbulence, and radiation transport [Van Wessem et al., 2014a]. The updated physics package includes an eddy-diffusivity mass flux scheme [Siebesma et al., 2007], representing turbulence and shallow convection in the atmospheric boundary layer. The surface flux computation is based on Monin-Obukhov similarity theory [Beljaars et al., 2004]. The new radiation scheme McRad [Morcrette et al., 2008], based on the Monte Carlo independent column approximation [Barker et al., 2008], computes the shortwave and longwave radiation transmission through clouds. In addition, the interaction of shortwave or longwave radiation with multi-layered clouds has been improved by revising the cloud optical properties [ECMWF-IFS, 2008].

The new cloud scheme includes an ice supersaturation parameterisation, which prolongs the vapour phase at low temperatures [Tompkins et al., 2007]. The auto-conversion coefficient, controlling the conversion rate of water-vapour into precipitation in convective clouds, has been defined individually for liquid and ice water clouds, following Sundqvist [1978]. Moreover, under marginally freezing conditions, i.e. between -7°C and -1°C , precipitation occurs exclusively as snowfall even though the precipitating clouds are mixed phase. In the previous model version, similar atmospheric conditions could also have resulted in a mix of liquid and solid precipitation for temperatures above -7°C . The update results in improved relative contributions of rainfall and snowfall to the total precipitation flux [Lin et al., 1983]. Furthermore, the cloud water-to-snowfall conversion coefficient now remains constant for liquid ($> 0^{\circ}\text{C}$) and mixed phase clouds (-23°C to 0°C) whereas it decreases with temperature for ice clouds ($< -23^{\circ}\text{C}$), resulting in slower snowfall production. The cloud content to ice and liquid water conversion coefficients have been increased in CY33r1 to reduce the overestimated updraft condensation simulated in previous cycles, leading to enhanced convective precipitations [ECMWF-IFS, 2008];

Van Wessem et al., 2014a]. Other minor adjustments have been applied to the physics package and the dynamical core but these are not relevant for this study. A complete overview of all updates is provided by ECMWF-IFS [2008] and Van Meijgaard et al. [2012].

2.2.3 RACMO2 simulations set-up

In the polar version of RACMO2.3, identical domain and resolutions (~ 11 km, 40 vertical layers) were used as in the previous RACMO2.1 simulation [Van Angelen et al., 2013a]. The integration domain includes the GrIS, the Canadian Arctic Archipelago, Iceland and Svalbard (Fig. 2.1). At the lateral atmospheric boundaries, RACMO2.3 is forced at 6-hourly time interval by re-analysis data of ERA-40 [Uppala et al., 2005] for the period 1958-1978 and ERA-Interim [Stark et al., 2007; Dee et al., 2011] for the period 1979-2014. Sea surface temperature and sea ice cover are prescribed from the same re-analysis data. Since RACMO2.1 has been forced by ERA-Interim data only for the period 1990-2012 and by ERA-40 prior to that, we compare model results for the overlapping period (1990-2012). This period coincides with long-term SMB and AWS measurements performed along the K-transect in west Greenland, which are therefore also used for model evaluation (see Section 2.4) together with accumulation data from ice cores covering the same period.

In both RACMO2 versions, Moderate Resolution Imaging Spectroradiometer (MODIS) albedo products [Stroeve et al., 2005] are used to prescribe a background ice albedo, which is assumed to vary in space but to be constant in time. The background ice albedo field (Fig. 2.1) consists of the lowest 5% albedo values retrieved from 16-day integrated MODIS data (MOD43) at 0.05 degree of spatial resolution for the period 2001-2010 and are clipped between 0.30 and 0.55 [Van Angelen et al., 2012].

2.2.4 Observational data

For model evaluation, we use long-term measurements from the K-transect, operated by the Institute for Marine and Atmospheric Research of Utrecht University (IMAU) in the Netherlands. The K-transect runs for a distance of approximately 140 km from the ice margin through the ablation zone and into the lower accumulation zone of the west Greenland ice sheet along $\sim 67^\circ\text{N}$, covering the elevation interval between 400 m a.s.l. and 1850 m a.s.l. (Fig. 2.1, white dots). Since 1990, annual stake measurements have been performed at eight sites along the transect: S4, S5, SHR, S6, S7, S8, S9 and S10 [Van de Wal et al., 2005, 2012]. Since August 2003, three AWS with capability to close the SEB have been operated at sites S5 (~ 500 m a.s.l.), S6 (~ 1000 m a.s.l.) and S9 (~ 1500 m a.s.l.) [Van den Broeke et al., 2008, 2009, 2011]. Stations S5 and S6 are located in the ablation zone at about 5 km and 40 km from the ice sheet margin, while station S9 is located close to the equilibrium line at approximately 90 km from the ice sheet margin. Since 2011, an AWS is also operated in the accumulation zone at S10 (~ 1850 m a.s.l.), about 140 km from the ice sheet margin. At this location, data consist of a merged time series collected at KAN_U (~ 1850 m a.s.l.) in 2010 and S10 for 2011-2012. Both stations are located ~ 30 m apart, carry the same instrumentation with similar setup and present measurements overlap for the period 2011-2012. During the overlapping period, only differences smaller than the measurements uncertainty were observed. Therefore, a combined time series was obtained by substituting KAN_U records to fill the gaps in the S10 data set without applying any homogenisation. At the AWS sites, SEB components are computed using a SEB model that uses as input hourly mean observations of wind, temperature,

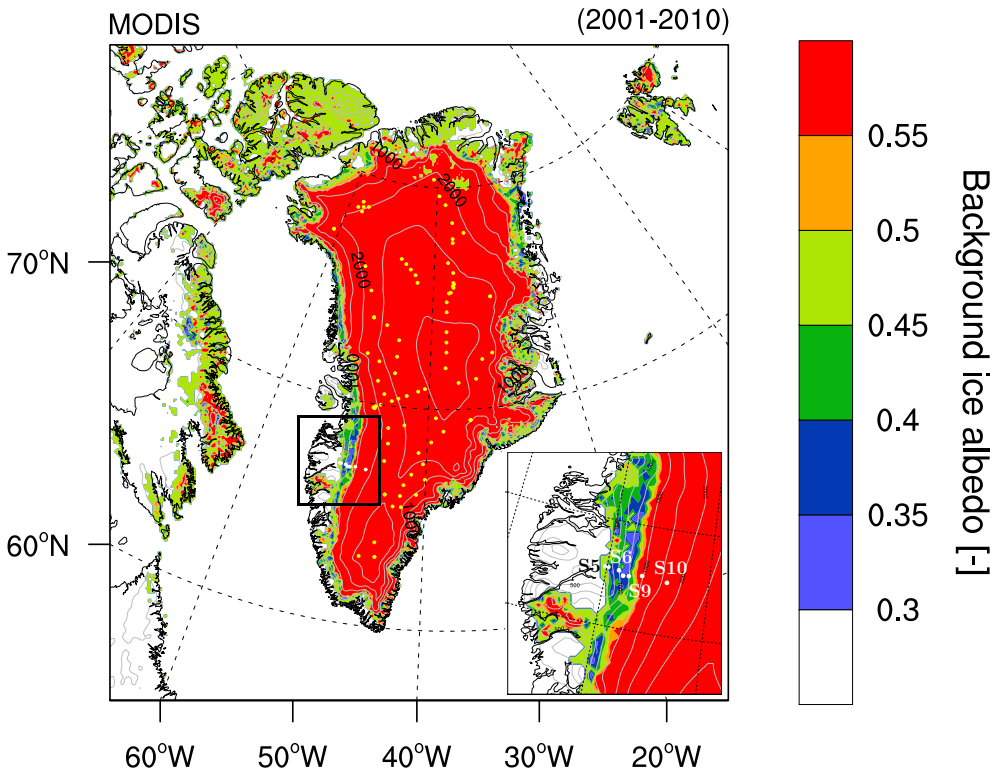


Figure 2.1: MODIS background ice albedo prescribed in RACMO2.3. The RACMO2 integration domain is displayed as well as the location of the K-transect (white dots, see also inset) and accumulation zone sites (yellow dots).

humidity and radiation components [Van den Broeke et al., 2011]. The model evaluation also includes a comparison with accumulation measurements collected at 87 sites (Fig. 2.1, yellow dots). This data set is based on a compilation of deep snow pit and firn core measurements presented in Bales et al. [2001, 2009], selected for the period 1979-2012, when temporal overlap occurs between model and observations.

To compare model results to observations, we apply different selection methods in the ablation and accumulation zones of the GrIS. In the accumulation zone, modelled SMB is obtained by selecting the closest RACMO2 grid cell. Due to significant dependence of ablation terms on elevation, modelled SMB and SEB components were retrieved by successively selecting the nearest grid cell and then applying an altitude correction. To do so, we select a grid cell, among the closest pixel and its 8 adjacent neighbours, which minimises the elevation bias between the model and the stations.

2.3 Changes in SMB components

2.3.1 SMB change pattern

Figure 2.2 shows a) RACMO2.3 average SMB (1990-2012) and b) the difference in SMB between RACMO2.3 and RACMO2.1. Both model versions simulate a qualitatively realistic SMB field, with a narrow ablation zone fringing the ice sheet (Fig. 2.2). The ablation zone is widest (~ 100 - 150 km) in the southwest and northeast, but too narrow in the southeast to be resolved at a resolution of 11 km; in this part of the ice sheet, the steep topography and high precipitation rates induce a large SMB gradient, resulting in an ablation zone only a few km wide.

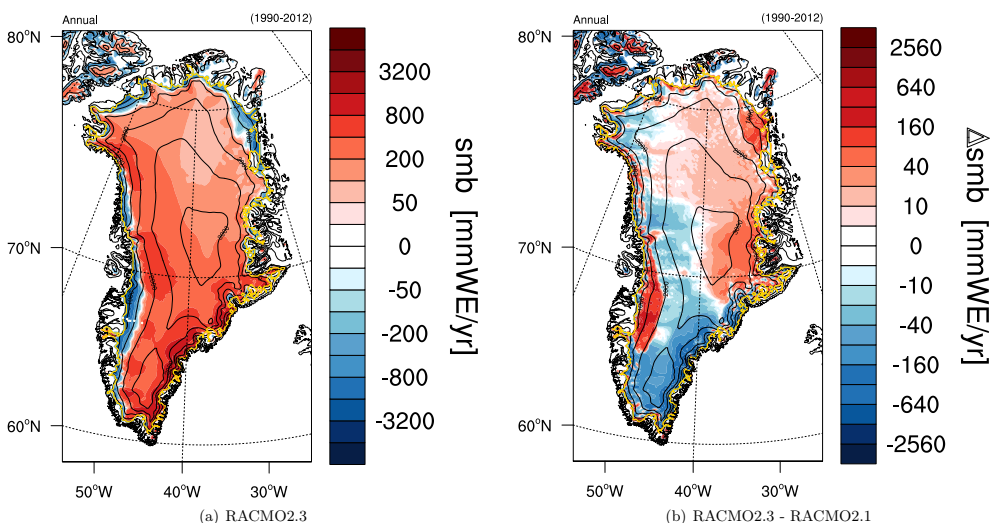


Figure 2.2: (a) Mean annual SMB (mm w.e. yr^{-1}) in RACMO2.3; (b) change in mean annual SMB (mm w.e. yr^{-1}) between RACMO2.3 and RACMO2.1 (1990-2012). The ice sheet margin is displayed in yellow.

The SMB fields from RACMO2.1 and RACMO2.3 are qualitatively similar, but two patterns of difference can be discerned (Fig. 2.2b). First, a large-scale pattern with lower SMB in the west and higher SMB in the east results in enhanced longitudinal SMB gradients across the main topographical divide. The negative SMB change becomes gradually more pronounced towards the southern and southeastern ice sheet, while the positive anomalies peak in the east. This large-scale pattern can be attributed to changes in the general circulation over the GrIS, as developed in Section 2.3.2.

Secondly, superimposed on this large-scale pattern, Fig. 2.2b shows pronounced positive SMB changes that are spatially restricted to the ablation and lower accumulation zones of the southwestern and northeastern ice sheet. These regional changes can be ascribed to enhanced summer snowfall in RACMO2.3, following the revised rainfall-to-snowfall partitioning. These changes are discussed in detail in Section 2.3.3.

2.3.2 Large-scale precipitation changes

The average mid-tropospheric circulation at 500 hPa is directed from southwest to northeast over Greenland (Fig. 2.3a), resulting in a large-scale negative precipitation gradient in the same direction. In addition, the proximity of the polar front, which predominantly produces easterly flow to its north, causes depressions to propagate eastward towards southern Greenland. This leads to a pronounced topographically forced precipitation maximum along the southeastern coast.

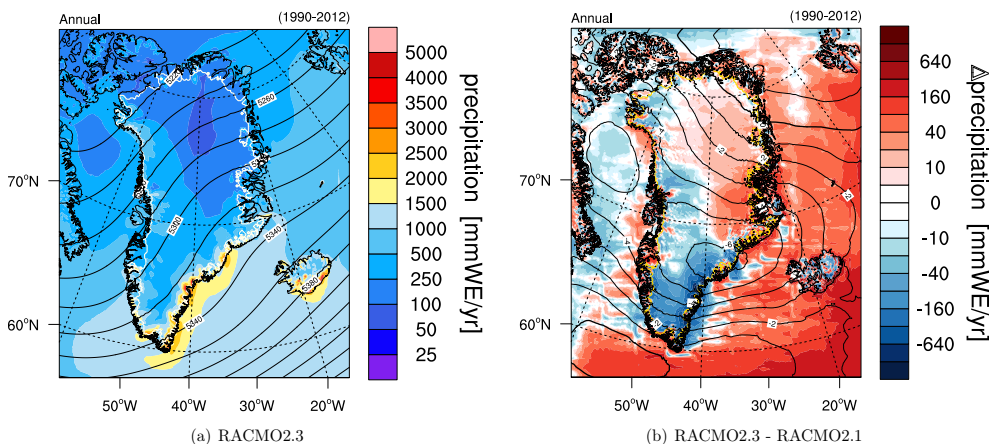


Figure 2.3: (a) Mean annual total (rain and snow) precipitation (mm w.e. yr^{-1}) and 500 hPa geopotential height (m) in RACMO2.3; (b) change in mean annual total precipitation (mm w.e. yr^{-1}) and 500 hPa geopotential height (m) between RACMO2.3 and RACMO2.1 (1990-2012).

Relative to RACMO2.1, RACMO2.3 is 0.1 to 0.3°C colder in the upper troposphere (above 500 hPa, not shown). Among other processes, reduced upper-air condensation, attributed to the introduction of ice supersaturation in the updated physics, contributes to this cooling. Moreover, a lowering of the 500 hPa geopotential height is modelled over the ice sheet with a minimum situated over coastal southeast Greenland (Fig. 2.3b). The resulting cyclonic circulation anomaly results in stronger onshore flow and increased precipitation in the northeastern GrIS and a decrease in the northwestern ice sheet, on the lee side of the main divide. In south Greenland, RACMO2.3 simulates decreased precipitation with respect to the previous model version; this is related to enhanced northwesterly advection of colder and drier air masses on the western side of the divide, more frequent offshore katabatic circulation and consequently weakened onshore flow to the east [Noël et al., 2014].

The large-scale circulation anomaly also reduces evaporation over the north Atlantic Ocean, by up to 200 mm w.e. yr^{-1} (not shown). Moreover, because condensation in the updated scheme is enhanced for moderately cold conditions ($< 10^\circ\text{C}$), precipitation over the ocean is enhanced, further limiting precipitation in coastal southeast Greenland. Precipitation differences locally reach 25%, and integrated over the GrIS the average 1990-2012 precipitation is reduced by 6%, from 741 Gt yr^{-1} in RACMO2.1 to 698 Gt yr^{-1} in RACMO2.3. Note that the erratic box-like pattern in Fig. 2.3b results from an error in the meridional momentum advection scheme in RACMO2.1, which is solved in the current formulation.

2.3.3 Summer snowfall events: the snow-albedo-melt feedback

Owing to an increase of the cloud water-to-snowfall conversion coefficient, the revised physics in RACMO2.3 favours solid precipitation at the expense of liquid precipitation, especially for cloud temperatures between -7°C and -1°C . In winter this has no major impact on the rainfall/snowfall ratio because the air temperature remains mostly below the solid precipitation threshold. In summer (JJA), however, RACMO2.3 predicts locally enhanced snowfall (10-40 mm w.e.), notably in southwest, northeast and northwest Greenland (Fig. 2.4a). These regional changes are accompanied by an equivalent decrease in rainfall (Fig. 2.4b), so we conclude that they result from the updated precipitation scheme. The reduced summer snowfall in the centre and southeast and the increase in east Greenland are not compensated by opposite and equivalent rainfall changes; here, precipitation changes are caused by the circulation change discussed in Subsection 2.3.2.

The regions experiencing increased summer snowfall coincide with positive changes in JJA surface albedo (Fig. 2.4c). The impact of summer snowfall on albedo is largest in the ablation zone, where the amount of absorbed shortwave radiation is reduced by a factor of ~ 3 when dark bare ice (albedo $\sim 0.30 - 0.55$) is covered by fresh snow (albedo ~ 0.85). As a consequence, meltwater runoff, which in RACMO2 is assumed to occur instantaneously over bare ice, is also substantially reduced (Fig. 2.4d). Note that this reduction in runoff (40-160 mm w.e.) significantly exceeds in magnitude the snowfall anomaly in Fig. 2.4a (5-30 mm w.e.), stressing the importance of the snow-albedo-melt feedback mechanism, in line with previously published results for valley glaciers [Greuell and Oerlemans, 1986]. The pronounced runoff reductions are mirrored in the map of SMB change (Fig. 2.2b).

2.4 Evaluation using observational data

2.4.1 SEB evaluation along the K-transect

In this section, we compare modelled and observed monthly mean SEB components (2004-2012) along the K-transect, conveniently situated in a region of west Greenland where there are significant differences in SMB between the two model versions (Fig. 2.2b). We adopted the convention of positive energy fluxes when directed towards the surface. The melt flux (M , W m^{-2}) is given by:

$$\begin{aligned} M &= SW_d + SW_u + LW_d + LW_u + SHF + LHF + G_s \\ &= SW_n + LW_n + SHF + LHF + G_s \end{aligned} \quad (2.1)$$

where SW_d and SW_u are the downward and upward shortwave radiation fluxes (W m^{-2}), LW_d and LW_u are the downward and upward longwave radiation fluxes (W m^{-2}), SHF and LHF are the sensible and latent turbulent heat fluxes (W m^{-2}), and SW_n and LW_n are the net short/longwave radiation fluxes (W m^{-2}), and G_s is the subsurface heat flux (W m^{-2}) which remains small, i.e. not exceeding $-1.43 \text{ W m}^{-2} \text{ yr}^{-1}$, and is not further discussed in this paper.

SEB data from the AWS at S6 are not used because of gaps in the time series. Figure 2.5 and Tables 2.1 to 2.3 show observed and modelled monthly mean SEB components, surface albedo, melt energy and

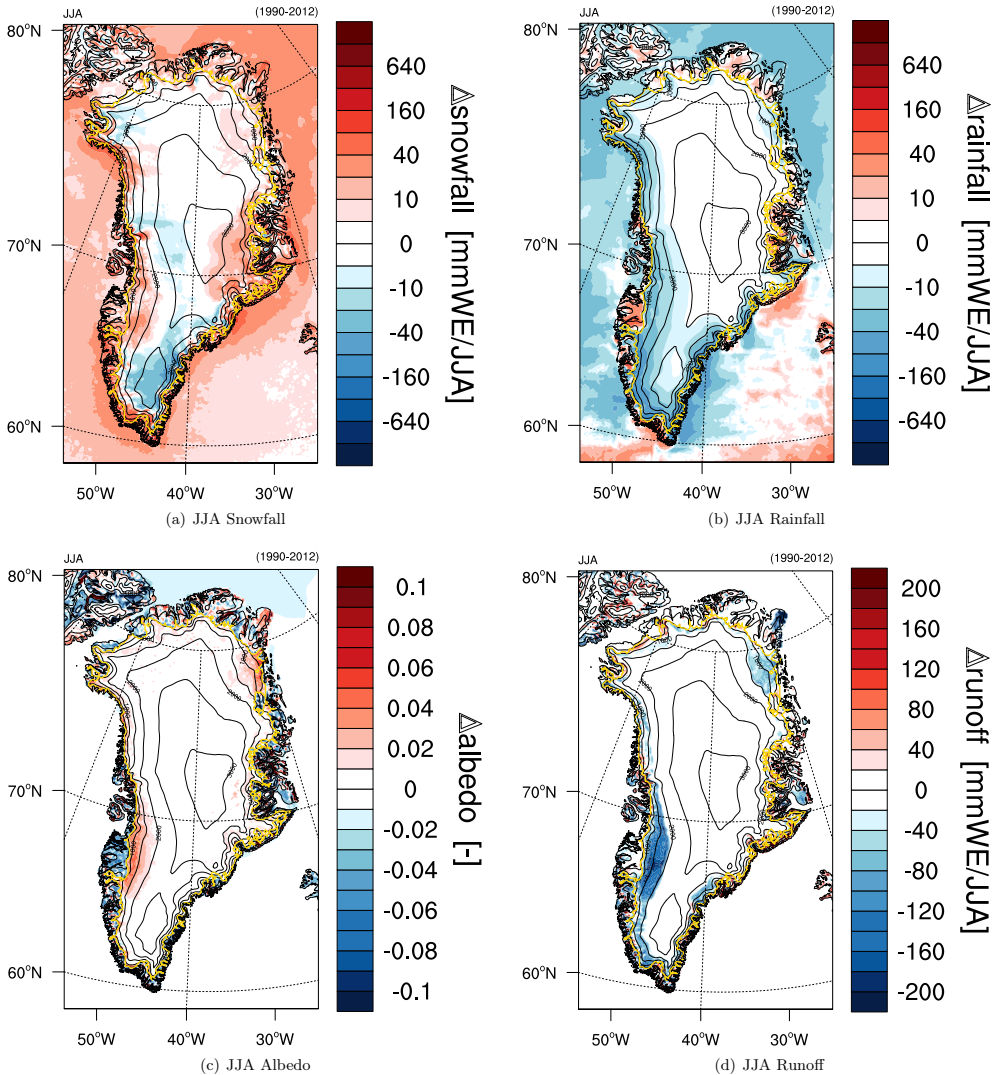


Figure 2.4: Change in JJA mean (a) snowfall (mm w.e./JJA), (b) rainfall (mm w.e./JJA), (c) surface albedo and (d) runoff (mm w.e./JJA) between RACMO2.3 and RACMO2.1 (1990-2012).

the differences for the period 2004-2012 (S5 and S9) and 2010-2012 (S10). For station S9, a distinction is made between the sub-periods 2004-2008 and 2009-2012; this is deemed relevant because of the significantly warmer summer conditions near the surface and in the upper atmosphere during the latter period. Figures 2.5a, c, e and g show that there is qualitative agreement between the modelled and observed seasonal cycle of the SEB in the ablation, equilibrium and accumulation zones. However, important biases remain, as discussed below.

Ablation zone (S5)

At station S5, Table 2.1 shows that both RACMO2 versions significantly overestimate SW_d and underestimate LW_d , even more so in RACMO2.3, which is indicative of underestimated cloud optical thickness. In combination with underestimated ice albedo (Fig. 2.5b) this leads to significantly overestimated net shortwave radiation (SW_n) in summer (Fig. 2.5a). On the other hand, RACMO2 underestimates the large summertime SHF values at S5, although this is improved in RACMO2.3 (Table 2.1). The reason is that station S5 has a complex topography: neither the summertime advection of warm tundra air over the glacier tongue that protrudes onto the tundra, leading to underestimated air temperature (Table 2.1), nor the high surface roughness at the marginal glaciers [Smeets and Van den Broeke, 2008] are well described at 11 km resolution. This leads to underestimated surface to air gradients of temperature and wind, and hence to too small SHF. This does not strongly affect LHF, which remains close to zero at S5. The net effect on melt energy is a negative bias (Fig. 2.5b) that has become smaller in RACMO2.3 (from 18 to 13%), albeit owing to significant error compensation.

| AWS Variable | S5 unit | OBS mean | RACMO2.1 | | | | RACMO2.3 | | | |
|-----------------|-------------|-------------|----------|------------------------|------|-------|----------|------------------------|------|-------|
| | | | bias | σ_{bias} | RMSD | R^2 | bias | σ_{bias} | RMSD | R^2 |
| SW_d | $W m^{-2}$ | 108.7 | 16.3 | 18.7 | 24.8 | 0.98 | 26.2 | 20.8 | 33.4 | 0.99 |
| SW_u | $W m^{-2}$ | -69.8 | -8.5 | 16.2 | 18.3 | 0.95 | -15.4 | 18.4 | 24.0 | 0.93 |
| LW_d | $W m^{-2}$ | 244.8 | -17.2 | 8.6 | 19.2 | 0.97 | -18.4 | 6.9 | 19.7 | 0.97 |
| LW_u | $W m^{-2}$ | -280.6 | 15.4 | 9.6 | 18.1 | 0.98 | 13.9 | 8.3 | 16.2 | 0.98 |
| SHF | $W m^{-2}$ | 37.4 | -11.8 | 19.7 | 23.0 | 0.21 | -8.9 | 17.3 | 19.4 | 0.46 |
| LHF | $W m^{-2}$ | 4.1 | -2.6 | 5.3 | 5.9 | 0.60 | -1.6 | 5.0 | 5.3 | 0.66 |
| MELT | $W m^{-2}$ | 42.8 | -7.8 | 17.7 | 19.4 | 0.96 | -5.4 | 14.2 | 15.2 | 0.97 |
| ALB | (-) | 0.73 | 0.03 | 0.09 | 0.09 | 0.73 | 0.03 | 0.08 | 0.09 | 0.74 |
| T_{2m} | $^{\circ}C$ | -6.0 | -2.7 | 1.7 | 3.2 | 0.99 | -2.3 | 1.1 | 2.6 | 0.99 |

Table 2.1: Modelled and observed annual mean SEB components and statistics of the differences (2004-2012) at station S5 (67°06' N, 50°05' W, 490 m a.s.l) in the ablation zone. Statistics include means of measurements collected at S5, model bias (RACMO2 - observations), standard deviation of the bias, Root Mean Square Difference (RMSD) of the bias as well as determination coefficient between RACMO2 and S5 observations. Fluxes are set positive for downward radiation.

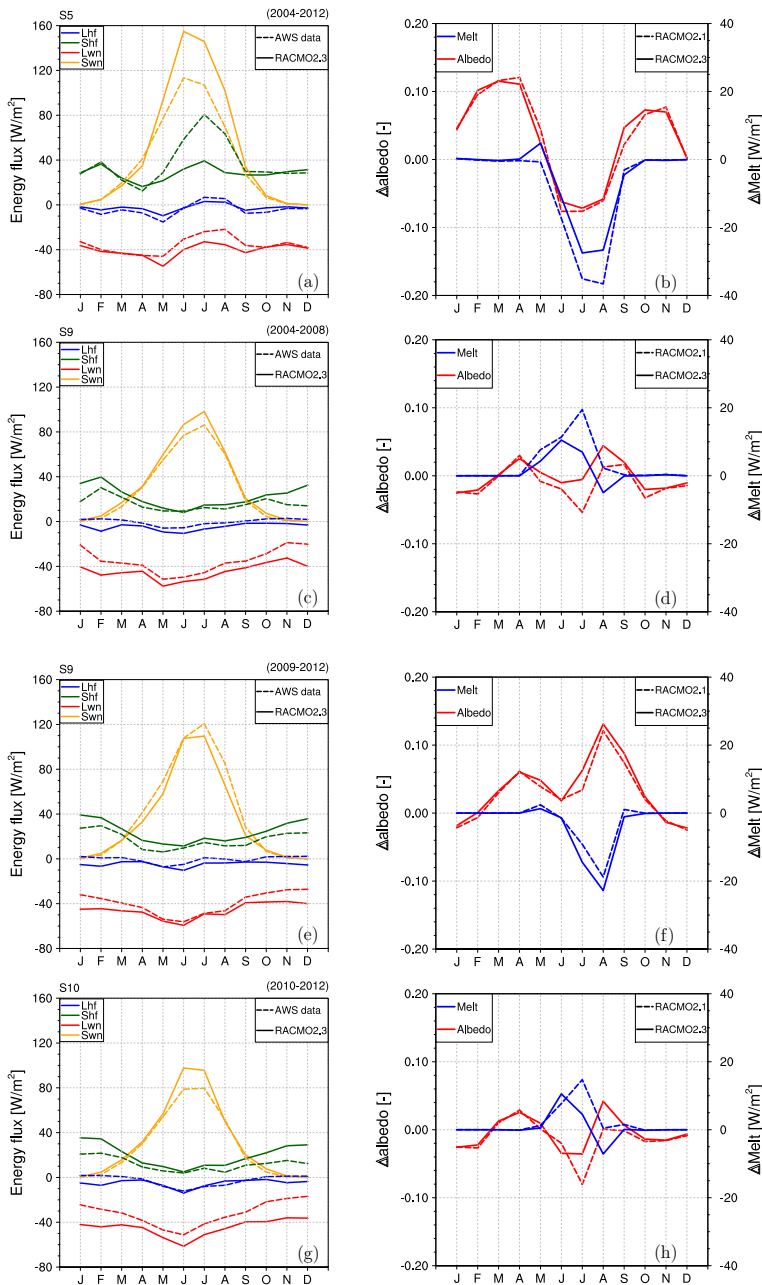


Figure 2.5: Observed and modelled turbulent and net shortwave/longwave fluxes ($W m^{-2}$) at station (a) S5 for 2004-2012, (c) S9 for 2004-2008, (e) S9 for 2009-2012 and (g) S10 for 2010-2012; difference in modelled and observed surface albedo and surface melt energy ($W m^{-2}$) at stations (b) S5, (d) S9, (f) S9 and (h) S10 for the same periods.

Around the equilibrium line (S9)

At S9, RACMO2.3 reduces the bias in most SEB components (Table 2.2). The 2 meter temperature bias has almost vanished, which has improved the representation of SHF. Despite a notable improvement of winter LW_n (not shown), LW_d remains underestimated (Table 2.2). Average biases in SW_d , SW_u and SW_n are greatly reduced in RACMO2.3. In RACMO2.1, the average melt bias was small at S9 (Table 2.2), but this was the result of overestimated melt in the period 2004–2008, and underestimated melt in 2009–2012 (Fig. 2.5d and f). For the period 2004–2008, enhanced summer snowfall has increased surface albedo in RACMO2.3 (Fig. 2.6a), which leads to an overall improved representation and a clearly reduced melt bias (Fig. 2.5d). In contrast, simulated summer snowfall has not considerably changed at station S9 for the period 2009–2012 (Fig. 2.6b) and biases in albedo and melt energy have persisted (Fig. 2.5d and f). The explanation is that summer atmospheric temperatures in 2009–2012 were too high for the new precipitation scheme to enhance snowfall.

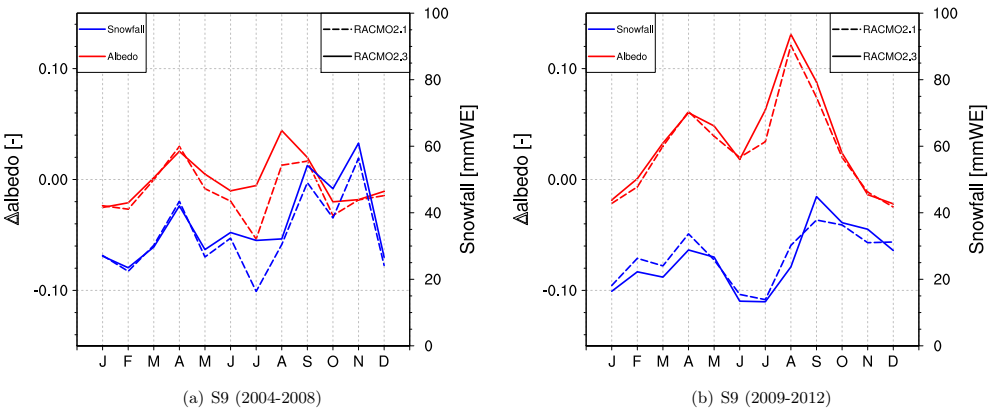


Figure 2.6: Differences in monthly mean surface albedo between models and S9 measurements, and monthly mean modelled snowfall for the periods (a) 2004–2008 and (b) 2009–2012.

The bias in surface albedo between model and observations (Fig. 2.5f) can be explained by the too high prescribed bare ice albedo (Fig. 2.1). No ice albedo could be derived from MODIS imagery for this location, in which case we prescribe a constant ice albedo of 0.55. However, in recent warm summers, the surface at S9 showed lower albedo values of ~ 0.43 and ~ 0.45 in 2010 and 2012, respectively. As a consequence, both RACMO2 versions fail to capture this ongoing decline of summer ice albedo.

Accumulation zone (S10)

At S10, biases in shortwave fluxes are greatly reduced but again the negative LW_d bias persists (Table 2.3). In winter this is mainly compensated by an overestimated SHF, but not so in summer (Fig. 2.5g). In June and July, the representation of albedo has improved, but in August albedo is now overestimated. SW_n remains somewhat too large. However, since LW_n is underestimated, the errors in melt energy are less than 10 W m^{-2} (Fig. 2.5h). The lower accumulation zone responds similarly to station S9

during 2004-2008 but with a reduced surface albedo sensitivity to summer snowfall, because snow metamorphism is slower in this colder area and snow wetting occurs less frequently.

The generally improved representation of surface snow albedo is attributed to enhanced summer snowfall in RACMO2.3 (see Section 2.3.3), thickening the melting snow cover and allowing the snow layer to persist longer over bare ice areas in summer. As a result, snowmelt decreases, further delaying snow cover disappearance and maintaining the surface albedo high until summer snowfall events cease (Fig. 2.6a). The summer surface albedo increase is further reinforced by a drop in cloud cover. This process reduces LW_d , also decreasing snowmelt at station S9 (Fig. 2.5d).

| AWS Variable | S9 unit | OBS mean | RACMO2.1 | | | | RACMO2.3 | | | |
|-----------------|-------------|-------------|----------|------------------------|------|-------|----------|------------------------|------|-------|
| | | | bias | σ_{bias} | RMSD | R^2 | bias | σ_{bias} | RMSD | R^2 |
| SW_d | $W m^{-2}$ | 139.8 | -9.5 | 11.4 | 14.8 | 0.994 | 3.2 | 6.6 | 7.3 | 0.997 |
| SW_u | $W m^{-2}$ | -105.9 | 9.0 | 12.8 | 15.7 | 0.99 | -3.3 | 9.1 | 9.7 | 0.99 |
| LW_d | $W m^{-2}$ | 219.1 | -9.1 | 12.4 | 15.4 | 0.92 | -9.4 | 9.1 | 13.1 | 0.94 |
| LW_u | $W m^{-2}$ | -256.1 | -0.2 | 4.5 | 4.5 | 0.99 | 1.1 | 3.9 | 4.1 | 0.99 |
| SHF | $W m^{-2}$ | 16.5 | 9.8 | 7.5 | 12.4 | 0.61 | 6.6 | 5.8 | 8.8 | 0.69 |
| LHF | $W m^{-2}$ | 0.3 | 4.3 | 3.1 | 5.3 | 0.34 | 4.4 | 3.4 | 5.6 | 0.28 |
| MELT | $W m^{-2}$ | 12.6 | 1.0 | 9.2 | 9.2 | 0.86 | -0.6 | 8.3 | 8.3 | 0.89 |
| ALB | (-) | 0.83 | 0.01 | 0.05 | 0.05 | 0.79 | 0.01 | 0.04 | 0.05 | 0.82 |
| T_{2m} | $^{\circ}C$ | -13.0 | 0.6 | 0.9 | 1.1 | 0.99 | 0.1 | 0.7 | 0.7 | 0.99 |

Table 2.2: Same as Table 2.1 but for station S9 ($67^{\circ}03' N$, $48^{\circ}15' W$, 1520 m a.s.l.) close to the equilibrium line. SEB components include annual mean data for period 2004-2012.

| AWS Variable | S10 unit | OBS mean | RACMO2.1 | | | | RACMO2.3 | | | |
|-----------------|-------------|-------------|----------|------------------------|------|-------|----------|------------------------|------|-------|
| | | | bias | σ_{bias} | RMSD | R^2 | bias | σ_{bias} | RMSD | R^2 |
| SW_d | $W m^{-2}$ | 141.5 | -11.8 | 12.9 | 17.5 | 0.994 | 1.8 | 7.7 | 7.9 | 0.997 |
| SW_u | $W m^{-2}$ | -113.8 | 15.3 | 18.0 | 23.7 | 0.98 | 2.3 | 12.1 | 12.4 | 0.99 |
| LW_d | $W m^{-2}$ | 220.4 | -14.1 | 12.3 | 18.7 | 0.92 | -14.1 | 8.9 | 16.7 | 0.93 |
| LW_u | $W m^{-2}$ | -252.5 | 0.6 | 5.2 | 5.2 | 0.98 | 1.6 | 4.2 | 4.5 | 0.99 |
| SHF | $W m^{-2}$ | 11.9 | 11.6 | 7.7 | 13.9 | 0.64 | 7.9 | 5.7 | 9.8 | 0.74 |
| LHF | $W m^{-2}$ | 2.7 | 1.5 | 3.8 | 4.1 | 0.41 | 2.5 | 4.0 | 4.7 | 0.39 |
| MELT | $W m^{-2}$ | 8.9 | 2.1 | 5.9 | 6.2 | 0.94 | 0.7 | 4.3 | 4.3 | 0.94 |
| ALB | (-) | 0.86 | -0.01 | 0.04 | 0.04 | 0.69 | -0.001 | 0.04 | 0.04 | 0.71 |
| T_{2m} | $^{\circ}C$ | -14.6 | 1.0 | 1.4 | 1.7 | 0.98 | 0.5 | 1.0 | 1.1 | 0.99 |

Table 2.3: Same as Table 2.1 but for station S10 ($67^{\circ}00' N$, $47^{\circ}01' W$, 1850 m a.s.l.) in the accumulation zone. SEB components include annual mean data for the period 2010-2012.

2.4.2 SMB evaluation

Temporal SMB variability

Table 2.4 compares time series of modelled and measured annual SMB values (1990-2012) collected at 7 stake sites, ranging from station S5 in the lower ablation zone to station S10 in the accumulation zone (Fig. 2.1, white dots). Figure 2.7 shows these time series for RACMO2.3 at four sites. The lowermost stake S4 (~400 m a.s.l.) is excluded from the analysis because it is not well resolved by the model ice sheet mask. At all sites except S10, the agreement improves in RACMO2.3, expressed as lower biases and a higher percentage of variance explained (R^2 , Table 2.4). At S10, SMB interannual variability is not well captured, but it must be stated that stake SMB measurements have limited accuracy in the percolation zone due to uncertainties in the snow density and subsurface refreezing.

| Stakes SMB | OBS mean | RACMO2.1 | | | | RACMO2.3 | | | |
|---------------|-------------|----------|------------------------|------|-------|----------|------------------------|------|-------|
| | | bias | σ_{bias} | RMSD | R^2 | bias | σ_{bias} | RMSD | R^2 |
| S5 | -3.7 | 1.0 | 0.5 | 1.1 | 0.36 | 0.7 | 0.4 | 0.8 | 0.49 |
| SHR | -3.1 | 0.4 | 0.5 | 0.6 | 0.41 | 0.3 | 0.4 | 0.5 | 0.53 |
| S6 | -1.7 | -0.8 | 0.6 | 1.0 | 0.25 | -0.7 | 0.6 | 0.9 | 0.28 |
| S7 | -1.5 | -0.7 | 0.4 | 0.9 | 0.59 | -0.6 | 0.4 | 0.7 | 0.66 |
| S8 | -0.8 | -0.7 | 0.4 | 0.8 | 0.55 | -0.4 | 0.4 | 0.5 | 0.64 |
| S9 | -0.1 | -0.4 | 0.2 | 0.5 | 0.73 | -0.2 | 0.2 | 0.3 | 0.80 |
| S10 | 0.3 | -0.03 | 0.2 | 0.2 | 0.34 | 0.2 | 0.1 | 0.3 | 0.25 |

Table 2.4: Modelled and observed mean annual SMB ($m \text{ w.e. yr}^{-1}$) and statistics of the differences at S5 ($67^{\circ}06' \text{ N}$, $50^{\circ}05' \text{ W}$, 490 m a.s.l.), SHR ($67^{\circ}06' \text{ N}$, $49^{\circ}56' \text{ W}$, 710 m a.s.l.), S6 ($67^{\circ}05' \text{ N}$, $49^{\circ}24' \text{ W}$, 1010 m a.s.l.), S7 ($66^{\circ}59' \text{ N}$, $49^{\circ}09' \text{ W}$, 1110 m a.s.l.), S8 ($67^{\circ}00' \text{ N}$, $48^{\circ}53' \text{ W}$, 1260 m a.s.l.) and S9 ($67^{\circ}03' \text{ N}$, $48^{\circ}15' \text{ W}$, 1520 m a.s.l.) over 1990-2012; S10 ($67^{\circ}00' \text{ N}$, $47^{\circ}01' \text{ W}$, 1850 m a.s.l.) covers the period 1994-2010.

Spatial SMB variability

Figure 2.8 compares modelled and observed SMB in the GrIS accumulation zone retrieved from snow pits and firn cores (Fig. 2.1, yellow dots). In the accumulation zone, the difference in modelled SMB between both RACMO2 versions (Fig. 2.2b) is mostly driven by changes in precipitation (Fig. 2.3b). Relative to the previous model version, RACMO2.3 simulates wetter conditions in central and north-east Greenland whereas the southern region shows reduced precipitation. These changes improve the agreement with accumulation measurements at most locations in the accumulation zone (Fig. 2.8).

Table 2.4 and Fig. 2.9 compare modelled and observed K-transect average SMB (1991-2012) as deduced from annual stake measurements. Figure 2.9 also shows the prescribed MODIS background albedo (green dots, scale on right axis). The covariance of ice albedo with modelled SMB once more underlines the importance of ice albedo for the ablation zone SMB [Van Angelen et al., 2012]. Again it must be noted that the stake sites are not necessarily representative for a larger region, e.g. for the area of a model grid cell ($\sim 120 \text{ km}^2$).

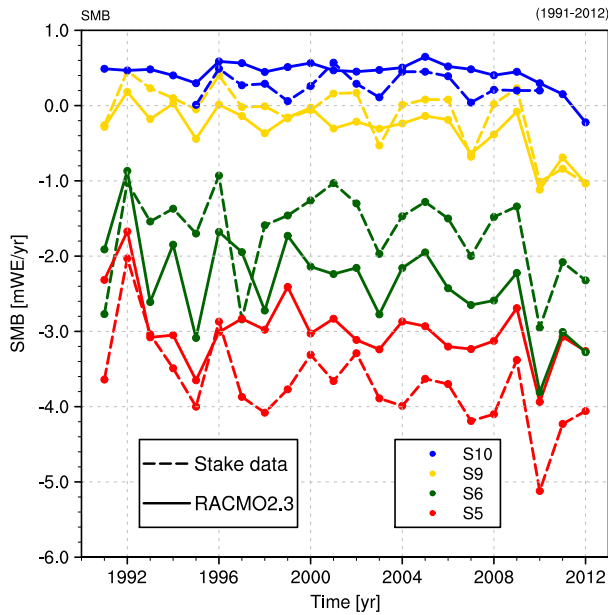


Figure 2.7: Time series of observed (AWS) and modelled (RACMO2.3 and 2.1) annual mean SMB along the K-transect ($m\ w.e.\ yr^{-1}$) for the period 1991-2012.

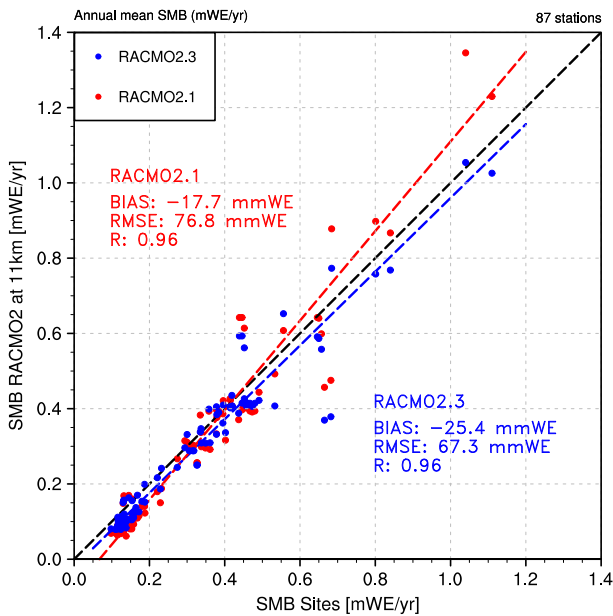


Figure 2.8: Observed and simulated SMB ($m\ w.e.\ yr^{-1}$) across the accumulation zone of the GrIS averaged for the period 1979-2012. The regression lines are displayed as dashed lines for RACMO2.3 (blue) and 2.1 (red). For observation locations, see yellow dots in Fig. 2.1.

In the lower ablation zone, between 500 to 800 m a.s.l., RACMO2.3 simulates lower (more negative) SMB values than RACMO2.1, which better matches observations. This improvement can be ascribed to a smaller bias in melt energy (Table 2.1) and hence a more realistic runoff. Correcting the persistent overestimation of SMB between 500 m a.s.l. and 800 m a.s.l. will require a better representation of SHF which, in combination with SW_d and LW_d , is a primary factor governing melt rate in the lower ablation zone. For elevations between 800 m and the equilibrium line at about 1500 m a.s.l., RACMO2.3 simulates higher SMB values compared to RACMO2.1, resulting mainly from reduced runoff following enhanced summer snowfall through the snow-albedo-melt feedback. The absence of rapid SMB fluctuations in the model between 1400 m a.s.l. and the equilibrium line is clearly related to the fixed upper threshold (0.55) of bare ice albedo prescribed in RACMO2 [Van Angelen et al., 2012]. In the accumulation zone (above 1500 m), enhanced snowfall and less runoff have significantly improved the agreement with the K-transect stake observations.

An alternative way to assess model performance is to quantify SMB gradients, here determined by simple least-squares fitting of a linear function. This yields $3.15 \pm 0.22 \text{ mm w.e. yr}^{-1} \text{ m}^{-1}$ for the observations and 2.73 ± 0.09 and $2.91 \pm 0.07 \text{ mm w.e. yr}^{-1} \text{ m}^{-1}$ for RACMO2.1 and RACMO2.3, respectively; in the updated model, the deviation from the observed gradient has thus decreased from 0.42 to 0.24 $\text{mm w.e. yr}^{-1} \text{ m}^{-1}$, a 43% improvement of the SMB gradient representation.

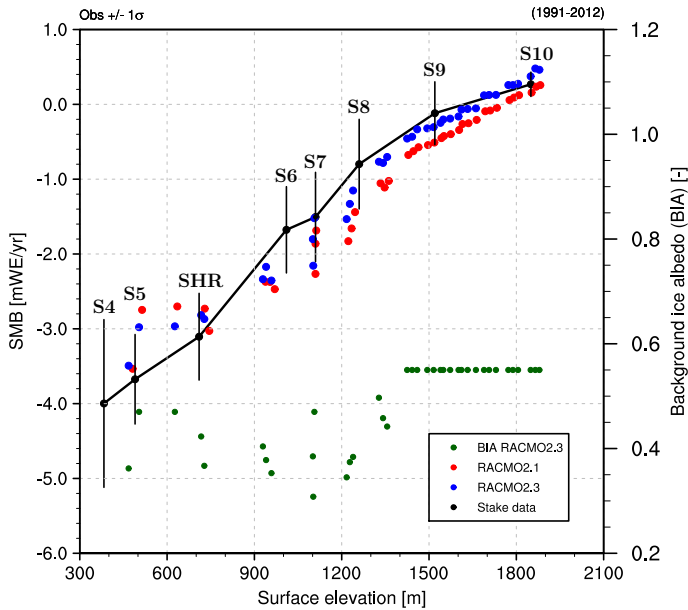


Figure 2.9: Observed and simulated SMB (m w.e. yr^{-1}) along the K-transect in western Greenland ($\sim 67^\circ\text{N}$), averaged for the period 1991-2012. The observed SMB (black dots) at S4, S5, SHR, S6, S7, S8, S9 and S10 are based on annual stake measurements. S10 observations cover 1994-2010. The black bars represent the standard deviation ($\pm 1\sigma$) around the 1991-2012 mean value. Modelled SMB at stake sites and intermediate locations are displayed for RACMO2.3 (blue dots) and RACMO2.1 (red dots). MODIS background ice albedo as prescribed in RACMO2.3, is depicted in green (axis on right).

2.5 Conclusions

An updated physics package has been implemented in the regional climate model RACMO2.3. Among other changes, the rainfall-to-snowfall conversion has been revised and an ice supersaturation parameterisation included, to favour solid over liquid precipitation in summer and reduce the overestimated coastal cloud cover and precipitation simulated in previous versions, respectively [Van de Berg et al., 2006]. The subsequent increase in modelled summer snowfall has generally improved the representation of surface energy balance (SEB) and surface mass balance (SMB) along the K-transect in west Greenland. For SEB, these improvements are more pronounced in the lower accumulation zone, where summer temperatures are generally below zero. Close to the equilibrium line, SMB is especially sensitive to snowfall-induced fluctuations in surface albedo. The increase in summer snowfall enhances surface reflectivity, improving the modelled surface albedo in summer as well as SMB representation. However, in recent warm years (e.g. 2010 and 2012) rainfall prevailed even in the new formulation, and no improvement was obtained. At station S5 in the lower ablation zone, summer albedo in RACMO2 is mainly determined by the prescribed MODIS ice albedo, due to near-continuous bare ice exposure. The updated physics in RACMO2.3 have considerably improved the modelled SMB gradient along the K-transect when compared to ablation stake measurements, reducing the bias by 43%.

Two remaining problems require particular attention in future model updates. Current RCMs still struggle to model the correct cloud cover and cloud type (ice/water) over the GrIS [Box et al., 2012]. For instance, both RACMO2 and MAR models underestimate summer LW_d and overestimate SW_d due to an underestimated cloud optical thickness [Ettema et al., 2010a; Fettweis et al., 2011]. In fact, the inclusion of ice supersaturation in RACMO2.3 might aggravate this problem over the ablation zone, because, for inland-propagating air masses, this process delays cloud condensation to higher ice sheet elevations, as was also seen in simulations of Antarctic climate [Van Wessem et al., 2014a]. Evaluation of the modelled cloud properties and surface properties using CloudSAT/Calypto data will be addressed in a forthcoming paper.

Another revision that is simpler to implement is improvement of the background ice albedo, that is currently too low at the ice sheet margin. However, at this point, it is also important to realise that point AWS (SEB) and stake (SMB) measurements may not be representative for a wider area, especially for a spatially heterogeneous variable such as surface albedo. Sub-grid albedo variability should therefore become an important future topic of study. To assess the quality of the simulated SMB in the ablation zone elsewhere in Greenland, an evaluation of downscaled RACMO2.3 data against a much larger data set of ablation measurements, covering all sectors of the Greenland ice sheet, is currently being conducted.

A daily, 1 km data set of downscaled Greenland ice sheet surface mass balance

Summary

This study presents a data set of daily, 1 km resolution Greenland ice sheet (GrIS) surface mass balance (SMB) covering the period 1958-2015. Applying corrections for elevation, bare ice albedo and accumulation bias, the high-resolution product is statistically downscaled from the native daily output of the polar regional climate model RACMO2.3 at 11 km. The data set includes all individual SMB components projected to a down-sampled version of the Greenland Ice Mapping Project (GIMP) digital elevation model and ice mask. The 1 km mask better resolves narrow ablation zones, valley glaciers, fjords and disconnected ice caps. Relative to the 11 km product, the more detailed representation of isolated glaciated areas leads to increased precipitation over the southeastern GrIS. In addition, the downscaled product shows a significant increase in runoff owing to better resolved low-lying marginal glaciated regions. The combined corrections for elevation and bare ice albedo markedly improve model agreement with a newly compiled data set of ablation measurements.

This chapter is based on: B. Noël et al. (2016), A daily, 1 km resolution data set of downscaled Greenland ice sheet surface mass balance (1958-2015), *The Cryosphere*, 2016

3.1 Introduction

During the last two decades, the Greenland ice sheet (GrIS) experienced significant mass loss as a result of increased meltwater runoff and sustained high solid ice discharge from marine-terminating outlet glaciers [Van den Broeke et al., 2009; Rignot et al., 2008, 2011; Sasgen et al., 2012; Shepherd et al., 2012; Enderlin et al., 2014]. To fill spatial and temporal gaps in the scarce in situ observations, regional climate models (RCMs) are often used to produce maps of the GrIS surface mass balance (SMB; Van Angelen et al. [2013a]; Burgess et al. [2010]; Ettema et al. [2010b,a]; Fettweis [2007]; Fettweis et al. [2005, 2011]; Noël et al. [2015]; Lucas-Picher et al. [2012]). RCMs explicitly calculate the individual SMB components [Lenaerts et al., 2012a], i.e. precipitation, runoff and sublimation, over the entire ice sheet (Fig. 3.1) at high spatial and temporal resolution and over extended periods. However, the current spatial resolution of RCMs, typically 5 to 20 km, remains too coarse to accurately resolve glaciated areas in topographically complex regions such as small isolated ice caps and marginal outlet glaciers flowing into narrow fjords. In these regions, the relatively coarse elevation and land ice masks used in RCMs might result in runoff underestimation [Franco et al., 2012; Noël et al., 2015], hampering realistic regional SMB estimates. Performing higher-resolution simulations to address these issues would require a substantial computational effort and is thus restricted to case studies of small regions and relatively short time periods.

As an alternative, statistical downscaling can be applied to RCM output. Previously, this method has been applied to the GrIS using global re-analysis and climate data [Hanna et al., 2005, 2008, 2011]. Machguth et al. [2013] downscaled near-surface temperature and precipitation from 3 different RCMs (11-25 km spatial resolution) to force a glacier mass balance model on a 250 m grid derived from the Greenland Ice Mapping Project (GIMP) digital elevation model (DEM) [Howat et al., 2014], accurately resolving local glaciers and ice caps of Greenland. Vertical gradients of climate parameters were iteratively calibrated to enable the mass balance model to generate a realistic melt distribution for the period 1980-2010, but the very high resolution restricted the analysis to a few regions. Franco et al. [2012] statistically downscaled GrIS SMB by interpolating each component of the *Modèle Atmosphérique Régional* (MAR) from the original 25 km grid to a 15 km resolution. This method used local daily vertical gradients, except for precipitation, to correct for elevation differences between MAR and a down-sampled version of the 5 km DEM from Bamber et al. [2001]. The elevation correction significantly reduced SMB biases. However, a resolution of 15 km remains insufficient to resolve the rugged topography at the ice sheet margins; to address this issue, near-km resolution is necessary.

Here, we present a new data set of daily, 1 km resolution GrIS SMB components (precipitation, melt, runoff, refreezing, sublimation and snowdrift erosion) covering the period 1958-2015. The SMB product is statistically downscaled from data of the polar regional climate model RACMO2.3 at 11 km (Fig. 3.1), using an elevation dependent technique based on the elevation and ice mask from the GIMP DEM [Howat et al., 2014], down-sampled to 1 km. The following section briefly describes RACMO2.3, the GIMP DEM, observational data sets and MODIS bare ice albedo product used to evaluate and correct the downscaled data set. The downscaling algorithm is explained in Section 3.3. Downscaled SMB is evaluated using ablation and accumulation measurements in Section 3.4. Section 3.5 discusses the downscaling results for four different regions and for the entire ice sheet. The added value, limitations and uncertainties of the downscaling method are argued in Section 3.6, followed by conclusions in Section 3.7.

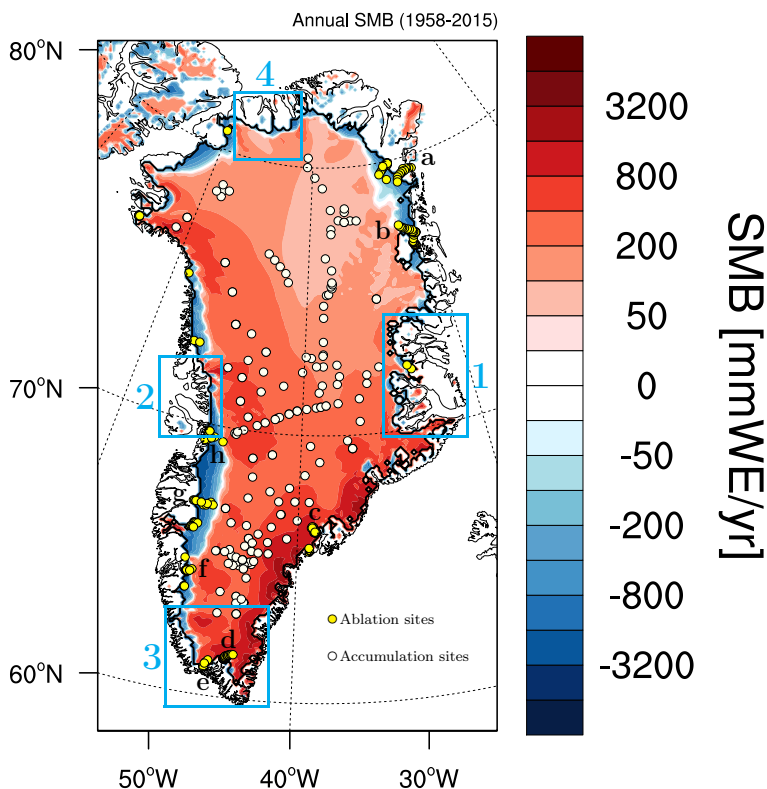


Figure 3.1: Annual mean SMB modelled by RACMO2.3 at 11 km over the GrIS and surrounding ice caps for the period 1958-2015. This figure also depicts the location of 213 ablation measuring sites (yellow dots) and 182 accumulation sites (white dots) used for downscaled SMB evaluation as well as the four GrIS marginal regions (blue boxes), discussed in Section 3.5. Letters refer to the different transects shown in Fig. 3.8.

3.2 Model and data

3.2.1 The regional climate model RACMO2

A detailed description of the Regional Atmospheric Climate Model (RACMO2) is presented in Van Meijgaard et al. [2008]. RACMO2 incorporates the atmospheric dynamics and physics modules from the High Resolution Limited Area Model (HIRLAM, Undèn et al. [2002]) and the European Centre for Medium-range Weather Forecasts Integrated Forecast System (ECMWF-IFS, ECMWF-IFS [2008]). The polar version of RACMO2 is developed by the Institute for Marine and Atmospheric Research (IMAU), Utrecht University, and is especially adapted for use over ice sheets and other glaciated regions. Polar RACMO2 is interactively coupled to a multi-layer snow module, accounting for firm densification, meltwater percolation, refreezing and runoff [Ettema et al., 2010b]; an albedo scheme with prognostic snow grain size [Kuipers Munneke et al., 2011] and a drifting snow module, simulat-

ing snow erosion and the drifting snow contribution to sublimation [Lenaerts et al., 2012a]. Recently, RACMO2.1 has been updated to RACMO2.3 as discussed in Van Wessem et al. [2014a] and Noël et al. [2015]. Model evaluation against SMB measurements, collected in the accumulation and ablation zones of the GrIS, showed generally improved agreement [Noël et al., 2015]. The native 11 km climate run is forced at the lateral boundaries by ERA-40 (1958-1978, Uppala et al. [2005]) and ERA-Interim (1979-2015, Stark et al. [2007]; Dee et al. [2011]) re-analyses and uses the 5 km DEM and ice mask from Bamber et al. [2001].

3.2.2 GIMP DEM

To downscale RACMO2.3 output, we use the ice mask and topography from the GIMP DEM, described in Howat et al. [2014], and currently considered to be one of the most complete ice masks for Greenland [Rastner et al., 2012]. A 1 km ice mask and DEM are obtained by averaging the original 90 m GIMP grid cells in each 1 km pixel covering Greenland. A 1 km resolution is deemed an acceptable trade-off between improved resolution, i.e. a 121 fold improvement compared to the 11 km grid, and manageable data handling given the daily time resolution, time span (1958-2015) and the number of SMB components. As an example, Fig. 3.2a shows the topography and ice mask from RACMO2.3 at 11 km in central east Greenland (blue box 1 in Fig. 3.1) and Fig. 3.2b the GIMP DEM at 1 km. The latter better resolves small scale landforms such as narrow fjords and calving glacier tongues. Integrated over the contiguous GrIS, the ice-covered area of $1.69 \cdot 10^6 \text{ km}^2$ for the 1 km grid represents a 0.5% decrease relative to the 11 km mask. For our SMB calculations, we only consider grounded ice, i.e. we discarded floating ice pixels using a 1 km version of the 90 m grounded ice mask used in Enderlin and Howat [2013].

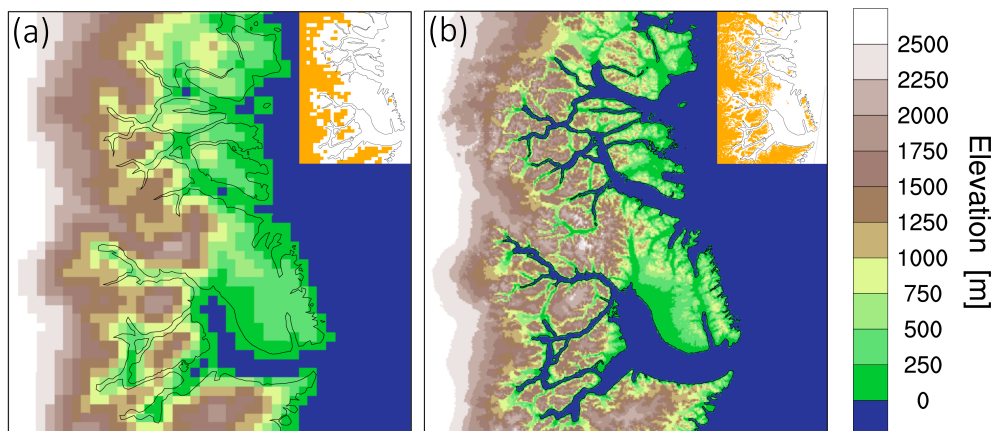


Figure 3.2: Elevation and ice mask (orange, shown in inset) as prescribed in RACMO2.3 at 11 km (a) and derived from the GIMP DEM down-sampled to 1 km (b) over central east Greenland (blue box 1 in Fig. 3.1).

3.2.3 Ablation and accumulation measurements

To evaluate the daily downscaled SMB product, we use 1155 SMB measurements collected in the GrIS ablation (1073) and accumulation (182) zones. The ablation data set [Machguth et al., 2016b] was compiled as part of the Programme for Monitoring of the Greenland Ice Sheet (PROMICE) [Van As et al., 2011] and includes stake and AWS measurements retrieved from 213 sites (yellow dots in Fig. 3.1). Accumulation observations were derived from 182 sites including snow pits and firn cores [Bales et al., 2001, 2009] as well as airborne radar measurements [Overly et al., 2015] (white dots in Fig. 3.1). We exclusively selected data that temporally overlaps with RACMO2.3 simulations (1958-2015; 205 sites discarded). We rejected observations from sites with a > 100 m height bias relative to the representative elevation of the 1 km GIMP topography (1 site discarded).

To compare modelled and downscaled SMB with observations, different selection approaches were applied in the ablation and accumulation zones, as described in Noël et al. [2015]. In the accumulation zone, we select the closest grid cell on the 11 km and 1 km grids to represent modelled and downscaled SMB, respectively. In the ablation zone, an altitude correction is applied by selecting the grid cell with the smallest elevation bias among the closest pixel and its eight adjacent neighbours.

3.2.4 MODIS bare ice albedo

A 1 km version of the 500 m MODerate-resolution Imaging Spectroradiometer (MODIS) 16-day Albedo product (MCD43A3) is used to retrieve estimates of bare ice albedo in the GrIS ablation zone. Bare ice albedo is estimated as the average of the 5% lowest surface albedo measurements for the period 2000-2015. A similar ice albedo product is used in RACMO2.3 based on MODIS observations between 2001 and 2010 [Noël et al., 2015]. In RACMO2.3, bare ice albedo ranges from 0.30, i.e. dark bare ice exposed in the low ablation zone, to 0.55 under persistent snow cover in the GrIS accumulation zone. Bare ice albedo of glaciated pixels with no valid MODIS estimate are set to 0.47.

3.3 Methods

The daily, 1 km SMB product consists of statistically downscaled output from a previously conducted RACMO2.3 simulation at 11 km, covering the period 1958-2015. RACMO2.3 settings and lateral forcing are described in Noël et al. [2015]. The downscaling algorithm corrects the interpolated SMB components using their local regression to elevation. Figure 3.3 shows the spatial correlation of individual SMB components with elevation on the 11 km RACMO2.3 grid. The spatial correlation is calculated for each grid-box using 8 adjacent ice-covered pixels.

The elevation correction is exclusively applied to the SMB components which show a significant and spatially homogeneous correlation with elevation, i.e. melt, runoff and sublimation (Fig. 3.3). These SMB components decrease with decreasing air temperature, represented by a negative correlation with elevation (Fig. 3.3b, d and e). Although precipitation negatively correlates with elevation over most of the ice sheet, the correlation remains small and highly heterogeneous at the margins (Fig. 3.3a). Snowdrift erosion exhibits a noisy correlation pattern. Therefore, daily precipitation and snowdrift erosion are bi-linearly interpolated to the 1 km ice mask without elevation corrections. Refreezing

exhibits a marked bimodal correlation pattern (not shown), gradually increasing with height in the ablation zone, where pore space is more abundant, and decreasing towards the ice sheet interior due to limited meltwater supply.

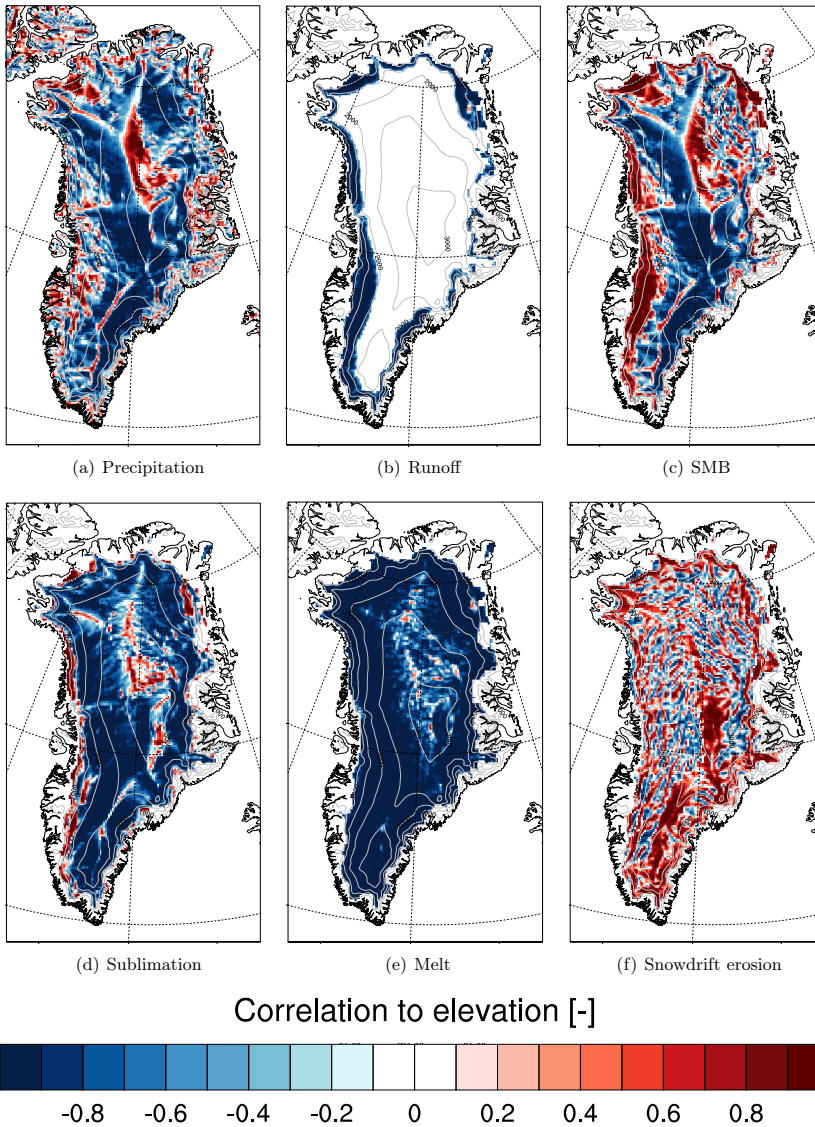


Figure 3.3: Correlation to elevation of annual mean a) total precipitation (solid and liquid), b) runoff, c) SMB, d) sublimation, e) melt and f) drifting snow erosion modelled by RACMO2.3 and calculated on the 11 km grid for the period 1958-2015.

For this reason, and in order to have a consistent liquid water balance, daily refreezing is calculated as a residual:

$$RF = RA + ME - RU \quad (3.1)$$

where RF is the residual refreezing, RA is rainfall, ME is surface melt, and RU is meltwater runoff.

Daily SMB values are obtained by summing the individually downscaled components:

$$SMB = P_{\text{tot}} - RU - SU - ER \quad (3.2)$$

where P_{tot} is total precipitation (liquid and solid), RU is meltwater runoff, SU is total sublimation (from surface and drifting snow) and ER is drifting snow erosion.

3.3.1 Elevation dependent downscaling

The downscaling algorithm interpolates daily SMB components to the 1 km topography and ice mask in three successive steps (Fig. 3.4).

First, the local dependence on elevation is calculated on the original RACMO2.3 11 km grid. Regression parameters are computed on a daily basis and are, therefore, only valid for that specific day. A local regression slope, $b_{11\text{km}}$ (mm w.e. per m, Fig. 3.4), is calculated for each ice-covered RACMO2.3 grid point using the maximum amount of points available, i.e. we use a total of six to nine ice-covered grid cells, the current one and the minimum five to maximum eight adjacent pixels. This minimum number is chosen after testing the downscaling sensitivity to the number of regression cells used, as discussed in Section 3.3.2. An approximation of the SMB components at mean sea level, $a_{11\text{km}}$ (mm w.e., Fig. 3.4), is then obtained using $b_{11\text{km}}$ and the current pixel. The regression is applied to the current grid cell to prevent local estimates of $a_{11\text{km}}$ to significantly differ from the original RACMO2.3 value. Local regression parameters for melt and runoff are only computed for pixels experiencing ablation. Moreover, erroneous positive regression slopes, i.e. increasing melt rates with altitude, are discarded until the following stage.

Next, valid estimates of $b_{11\text{km}}$ and $a_{11\text{km}}$ are extrapolated iteratively on the 11 km grid to fully cover the more extensive 1 km ice mask. To that end, daily regression parameters are extrapolated outwards of the 11 km ice mask by averaging $b_{11\text{km}}$ from at least 3 ice-covered pixels from the eight cells surrounding the current one.

Finally, the extrapolated fields of $b_{11\text{km}}$ and $a_{11\text{km}}$ are bi-linearly interpolated to the 1 km ice mask, providing estimates of $b_{1\text{km}}$ and $a_{1\text{km}}$. The downscaled SMB components ($X_{v0.2}$), i.e. runoff, melt and sublimation, are then computed as a linear function of the high-resolution topography ($h_{1\text{km}}$) as:

$$X_{v0.2} = a_{1\text{km}} + b_{1\text{km}} \times h_{1\text{km}} \quad (3.3)$$

The downscaled data set that is based on the above elevation dependent technique is hereafter referred to as version v0.2.

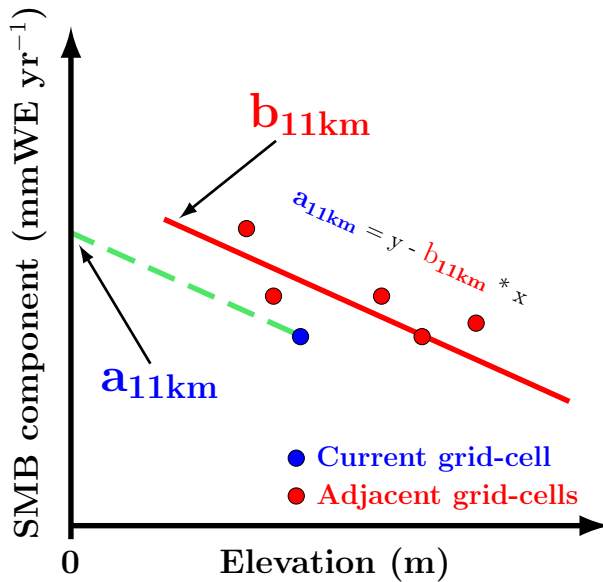


Figure 3.4: Elevation dependent downscaling procedure: b_{11km} and a_{11km} are respectively the daily local estimates of the SMB components regression to elevation and the SMB components value at mean sea level obtained on the RACMO2.3 grid at 11 km. The red line corresponds to the regression (b_{11km}) calculated using the current grid cell (blue dot) and the adjacent ones (red dots). The dashed green line applies the regression slope to the current grid cell to estimate a_{11km} .

3.3.2 Sensitivity experiment

Figure 3.5 shows the difference between 11 km and downscaled GrIS integrated daily runoff in summer 2011. Each line represents a different minimum number of grid cells, ranging from 3 to 9, used to estimate the local regression of runoff with elevation (b_{11km} ; Fig. 3.4). The results are moderately sensitive to the number of regression points used except for the 9 cells setting which systematically underestimates runoff at the beginning and the end of the melt season as it discards all low-lying glaciated pixels at the edge of the GrIS, which experience early melt and the largest values of runoff. The standard deviation between the different settings (~ 0.2 Gt/day) is smaller than the difference between 11 km and 1 km runoff (~ 0.6 Gt/day). The more regression points used, the smoother the runoff to elevation gradient field becomes, lowering the downscaled runoff and bringing it closer to the 11 km model output. Conversely, a small number of regression points can lead to spuriously large local gradients. To prevent the downscaling algorithm from substantially converging to, or diverging away from, 11 km RACMO2.3 output, we adopted a setting of minimum 6 regression points, which is closest to the average value of the different experiments (± 0.1 Gt/day).

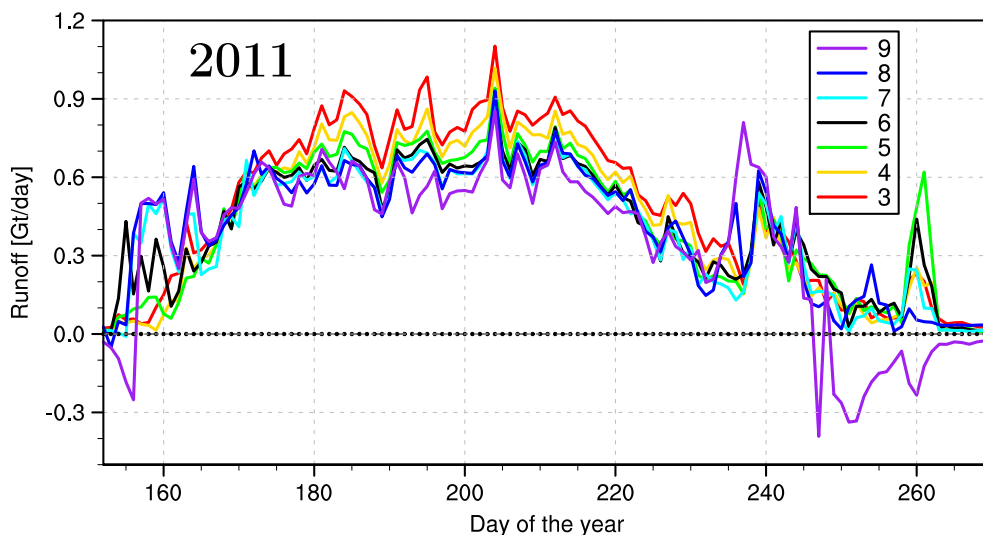


Figure 3.5: Summer 2011 time series of daily, ice sheet integrated runoff difference (Gt/day) between the downscaled product at 1 km, using a minimum threshold of 3 to 9 regression points (legend), and the RACMO2.3 model at 11 km.

3.3.3 Melt and runoff adjustments

RACMO2.3 uses a prescribed bare ice albedo field, typically ranging from 0.30 in the low ablation zone to 0.55 under persistent snow cover. It is based on the lowest 5% of MODIS surface albedo values averaged for the period 2001-2010 [Noël et al., 2015]. A comparison with a similar 1 km MODIS product averaged for 2000-2015, ranging from 0.15 to 0.55, shows a systematic overestimation of ice albedo at 11 km, especially for low-lying marginal glacier tongues (Fig. 3.13i). This causes melt energy to be underestimated during the melt season. To correct for this, downscaled melt and runoff are adjusted by estimating the missing amount of ice melt (ME_{add}) resulting from underestimated absorption of downward shortwave radiation (SW_{d}). In addition, as RACMO2.3 calculates radiative fluxes on a horizontal plane, the direct fraction of SW_{d} is corrected for the slope and orientation of each 1 km glaciated grid cell, as described in Weiser et al. [2016]. For simplicity, we assume SW_{d} to be equally partitioned between diffuse and direct radiation, and that the sun is exactly in the South at noon. This assumption is purely pragmatic; on the basis of data availability, it could be further refined in future versions of the downscaling procedure. Figures 3.7b and 3.9 show that ablation underestimation in v0.2 is restricted to the low ablation zone ($SMB < -4$ m w.e.), where bare ice is exposed for long episodes in summer. Therefore, the following corrections are only applied to the ablation zone on days of melting bare ice when both surface runoff and melt are non-zero in the downscaled product v0.2:

$$ME_{\text{add}} = \Delta\alpha \times 0.5 \left(\frac{SW_{\text{d } 1\text{km}}}{L_f} + \xi \frac{SW_{\text{d } 1\text{km}}}{L_f} \right) \quad (3.4)$$

where ME_{add} (mm w.e. per day) is the additional amount of ice melt calculated at 1 km; $\Delta\alpha$ (-) is the difference between the averaged bare ice albedo retrieved from the set of regression cells used to

downscale runoff at 11 km and the MODIS albedo product at 1 km; $SW_{d\ 1km}$ is the modelled daily cumulated downward shortwave radiation bi-linearly interpolated to 1 km; L_f is the latent heat of fusion ($3.337 \cdot 10^5$ J/kg) and ξ (-) is the correction factor for a tilted plane (Fig. 3.6), applied to the direct component of downward shortwave radiation:

$$\xi = \frac{\cos(\zeta^*)}{\cos(\zeta)} \quad (3.5)$$

$$\zeta^* = \sin(\zeta)\cos(a)\cos(\sigma)\cos(\Theta) + \sin(\zeta)\sin(\sigma)\sin(\Theta) + \cos(\zeta)\cos(\sigma) \quad (3.6)$$

$$\zeta = \arccos\left(\sin(\phi)\sin(\delta) + \cos(H)\cos(\phi)\cos(\delta)\right) \quad (3.7)$$

where ζ^* is the solar angle of incidence for a tilted plane, ζ is the solar zenith angle, a is the azimuth of the tilted plane, σ is the local surface slope, Θ is the orientation, ϕ is the latitude, δ is the solar declination and H is the hour angle set to 0 at noon (Fig. 3.6). All angles are expressed in radians.

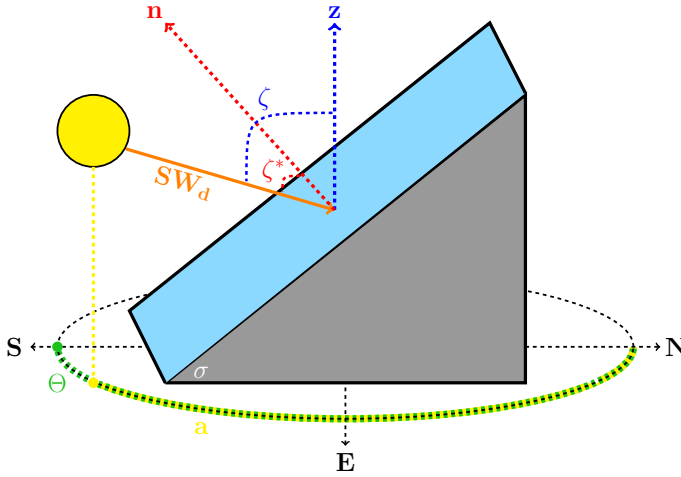


Figure 3.6: Scheme of a tilted plane as described in the GIMP DEM at 1 km. SW_d is the downward shortwave radiation, ζ^* is the solar angle of incidence for a tilted plane, ζ is the solar zenith angle, a is the azimuth of the tilted plane, σ is the local surface slope, Θ is the orientation. \mathbf{n} and \mathbf{z} are respectively the vector normal to the tilted plane and the local vertical axis.

The bare ice albedo bias correction aims at minimising the misfit between downscaled SMB v0.2 and in situ measurements (Fig. 3.7b) by estimating the missing runoff in the low ablation zone. Additional runoff RU_{add} is calculated by applying a daily specific fraction Γ (-) to ME_{add} , estimating the melt contribution to surface runoff. Γ is defined as the ratio between daily downscaled runoff and melt in v0.2 estimated using elevation dependence only:

$$RU_{add} = \Gamma \times ME_{add} \quad (3.8)$$

Assuming that the residual misfit between reconstructed and observed SMB (ΔSMB , Fig. 3.7b) for the different ablation sites can be ascribed to underestimated runoff in the low ablation zone of the GrIS, RU_{add} is then scaled by a factor f_{scale} (-), obtained by computing a least-square fit minimising the difference between ΔSMB and RU_{add} using all ablation measurements:

$$\Delta\text{SMB} = f_{\text{scale}} \times \text{RU}_{\text{add}} \quad (3.9)$$

$$f_{\text{scale}} = \frac{\sum \Delta\text{SMB} \times \text{RU}_{\text{add}}}{\sum (\text{RU}_{\text{add}})^2} \quad (3.10)$$

The least square fit yields a value of $f_{\text{scale}} = 1.176$ for the GrIS. This means that RU_{add} , i.e. accounting for elevation and bare ice albedo corrections, has yet to be increased by $\sim 18\%$ to optimise the agreement between downscaled and in situ SMB (Fig. 3.7c). The fact that $f_{\text{scale}} > 1$ strongly suggests that additional processes might play a role in enhancing surface ablation, e.g. underestimation of modelled sensible heat flux from warm air advection along the GrIS periphery [Noël et al., 2015; Fausto et al., 2016] and uncertainties in cloud representation [Van Tricht et al., 2016]. However, as the statistical downscaling approach is not designed to correct for these physical processes, we adopted the empirical approach presented above. The adjusted amount of runoff ($\text{RU}_{\text{v1.0}}$) is obtained by adding the missing runoff to the downscaled runoff ($\text{RU}_{\text{v0.2}}$).

$$\text{RU}_{\text{v1.0}} = \text{RU}_{\text{v0.2}} + f_{\text{scale}} \times \text{RU}_{\text{add}} \quad (3.11)$$

The corrected melt ($\text{ME}_{\text{v1.0}}$) is obtained in a similar fashion and refreezing ($\text{RF}_{\text{v1.0}}$) is estimated as a residual between adjusted melt, runoff and rainfall:

$$\text{ME}_{\text{v1.0}} = \text{ME}_{\text{v0.2}} + \text{ME}_{\text{add}} \quad (3.12)$$

$$\text{RF}_{\text{v1.0}} = \text{RA} + \text{ME}_{\text{v1.0}} - \text{RU}_{\text{v1.0}} \quad (3.13)$$

The downscaled SMB data set resulting from the combined elevation correction and runoff adjustment is referred to as version v1.0 in the following sections.

3.4 Evaluation of daily downscaled SMB

Figure 3.7 evaluates the original RACMO2.3 SMB at 11 km (a), the 1 km raw downscaled SMB version v0.2 (b) and the 1 km corrected downscaled SMB version v1.0 (c) (m w.e. per year) with 1073 observations from 213 ablation sites (yellow dots in Fig. 3.1). The observational period was matched with the modelled and downscaled SMB using the exact number of days. Each blue star corresponds to the cumulative SMB for a duration ranging from 10 days to a full hydrological year. The downscaled SMB v0.2 agrees better with observations compared to the RACMO2.3 output at 11 km (Figs. 3.7a and b): we find a significant decrease of the RMSE (190 mm w.e. or -16%) and a smaller bias (100 mm w.e. or -21%). The deviation from unity of the regression slope decreases from 0.28 to 0.21 (-25%), and the

variance explained increases from 47% to 61%. When applying the bare ice albedo and local orientation corrections, we find further significant improvements relative to version v0.2 (Fig. 3.7c), with now 78% of the variance explained and a significant decrease in RMSE (270 mm w.e. or -27%) and bias (310 mm w.e. or -84%). Red stars represent data from PROMICE station QAS_L (61.03°N, 46.85°W, 310 m.a.s.l.; yellow dot in Fig. 3.12a) situated in an extremely narrow ablation zone (~ 10 km) at the southwestern tip of Greenland. Here, modelled ablation gradients at 11 km are strongly underestimated in RACMO2.3 and are only marginally better resolved at 1 km. At this site, the additional corrections are especially important to obtain agreement with observations.

Figure 3.8 compares annual mean observed and downscaled SMB (v1.0) along 8 different SMB transects. There is good agreement for most transects, except for Helheim glacier (66.41N, -38.34W). The downscaled product fails at reproducing the quasi-constant ablation rate (~ -1 m w.e.) characterising the Helheim transect. The reason for this low SMB gradient is not clear at present; it may be due to uncertainties in individual observation covering relatively short periods, i.e. 1 or 2 months, which are only limited to the melt season (July-August). Another possible explanation is that Helheim glacier experiences large and variable winter accumulation at low elevations, potentially caused by drifting snow transport, limiting summer ablation. In addition, Nioghalvjerds-fjorden and Storstrømmen transects (Figs. 3.8a-b) also show significant remaining biases between in situ and downscaled SMB at elevations lower than 200 m. We hypothesise that these SMB measurements are located on floating glacier tongues with melt ponds, resulting in very low satellite albedo, while stake measurements are performed between ponds on brighter surfaces. As a result, the bare ice albedo correction could be overestimated.

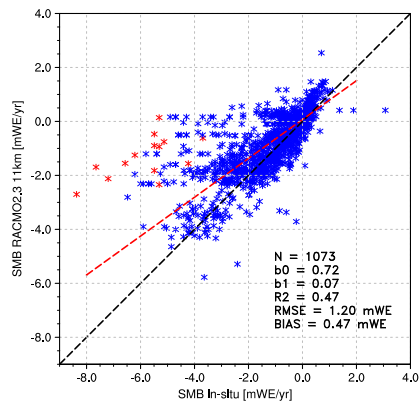
In the accumulation zone, a small improvement is also found in v0.2 compared to RACMO2.3 (Fig. 3.9), but accumulation remains underestimated. The SMB bias and RMSE are reduced by 0.7 (-2%) and 1.8 mm w.e. (-3%) whereas the regression slope and variance explained remain unchanged. In the accumulation zone, SMB is mostly driven by precipitation which is bi-linearly interpolated to 1 km without elevation correction. In addition, changes in sublimation are small due to the relatively homogeneous topography of the ice sheet interior, limiting SMB changes through downscaling. Despite significant improvements in the cloud scheme of RACMO2.3 [Noël et al., 2015], clouds become saturated and start to produce precipitation at too low elevations, resulting in overestimated precipitation at the margins, e.g. southeast Greenland, while the ice sheet interior experiences too dry conditions. This precipitation bias is currently being investigated, and we aim to resolve it in the upcoming version RACMO2.3p2. To overcome the systematic negative SMB bias of RACMO2.3 in the GrIS accumulation zone (-37.5 mm w.e. yr^{-1} , Fig. 3.9), the daily total precipitation v0.2 is adjusted to correct for underestimation in the ice sheet accumulation zone ($\text{SMB} > 0$ mm w.e. yr^{-1}):

$$PR_{v1.0} = PR_{v0.2} + \frac{PR_{v0.2}}{PR_{v0.2}^a} \times \sigma_{SMB} \quad (3.14)$$

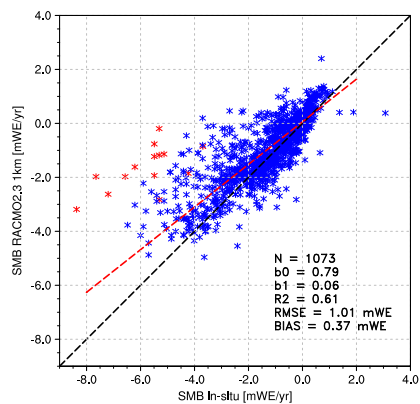
where $PR_{v1.0}$ is the daily adjusted total precipitation v1.0, $PR_{v0.2}$ is the daily bi-linearly interpolated total precipitation v0.2, $PR_{v0.2}^a$ is the annual cumulative bi-linearly interpolated total precipitation v0.2 and σ_{SMB} is the accumulation zone SMB bias in the downscaled product v1.0.

The final $\text{SMB}_{v1.0}$ product is reconstructed as:

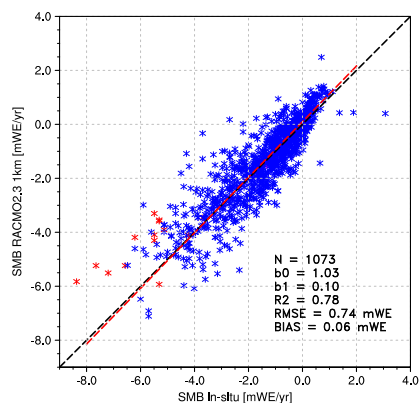
$$\text{SMB}_{v1.0} = PR_{v1.0} - RU_{v1.0} - SU - ER \quad (3.15)$$



(a) Modelled SMB at 11 km



(b) Downscaled SMB at 1 km version v0.2



(c) Corrected SMB at 1 km version v1.0

Figure 3.7: Comparison of SMB measurements collected at 213 sites with (a) modelled SMB from RACMO2.3 at 11 km; (b) downscaled SMB at 1 km (v0.2) and (c) corrected downscaled SMB at 1 km (v1.0). The red stars correspond to PROMICE station *QAS_L* located in southern Greenland (61.03°N, 46.85°W, 310 m.a.s.l.). The red dashed line represents the regression including all measurements using a perpendicular fit.

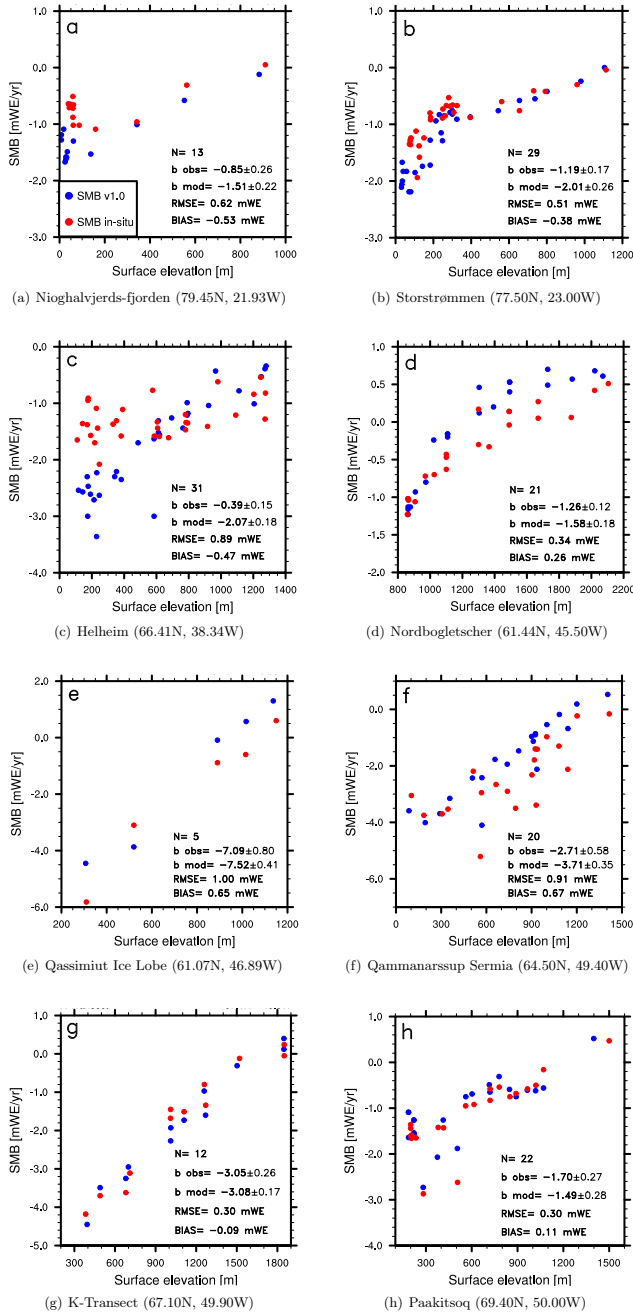


Figure 3.8: Annual mean observed (red dots) and downscaled (blue dots, v1.0) SMB for 8 selected transects in the GrIS ablation zone ($m \text{ w.e. yr}^{-1}$). Name and locations of these transects (Fig. 3.1) are listed at the bottom of each graph. Graphs also list the number of sites used for each transect, linear SMB-to-elevation regression retrieved from observations and downscaled (v1.0) data in $mm \text{ w.e. yr}^{-1}$ per m, RMSE and mean bias.

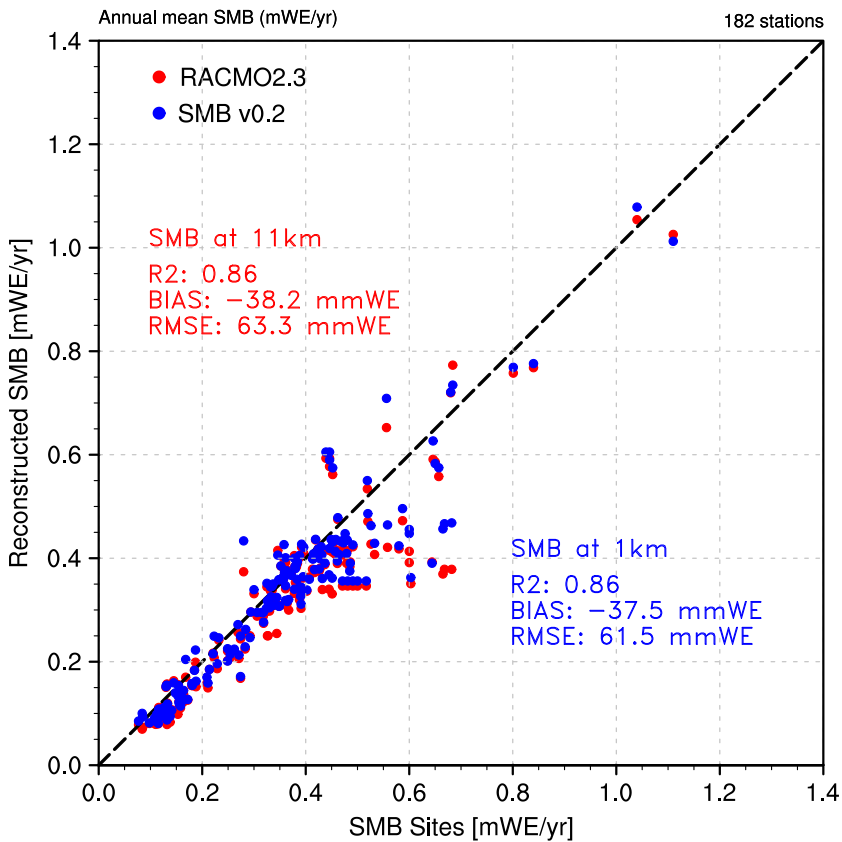


Figure 3.9: Comparison of accumulation observations collected at 182 sites with modelled SMB from RACMO2.3 at 11 km (red) and downscaled SMB v0.2 at 1 km (blue) in $m\ w.e.\ yr^{-1}$. Note that bias correction has not yet been applied.

3.5 High-resolution SMB patterns: case studies

Table 3.1 lists annual mean modelled and downscaled SMB components (Gt per year) integrated over four different regions (blue boxes in Fig. 3.1) as well as over the entire GrIS. These regions were selected for their specific climates, rough topography and narrow glaciated features which were not well resolved at 11 km. Figures 3.10, 3.11, 3.12 and 3.13 show the ice sheet mask for the selected regions at 11 km (red cells) and 1 km (orange cells) as well as peripheral glaciers and ice caps at 1 km (blue cells), the elevation bias between the 1 km and 11 km DEMs, and the bare ice albedo bias between the 1 km MODIS product and RACMO2.3 at 11 km; the latter figures moreover show the main SMB components at both resolutions for the two downscaled products (v0.2 and v1.0). In the following sections, we discuss the impact of downscaling on regional SMB. Here, SMB components are exclusively integrated over the contiguous GrIS; the SMB of detached ice caps will be discussed in a forthcoming paper.

3.5.1 Central east Greenland

Central east Greenland (blue box 1 in Fig. 3.1) is characterised by a large body of interconnected valley glaciers, mostly terminating in narrow glacial fjords. Figures 3.10a, e and i underline the inability of the 11 km mask to properly represent many glaciated areas, local topography or bare ice albedo. In the 1 km mask, the ice-covered area increases ($\sim 2\%$) while the elevation bias can locally exceed 500 m over glacial valleys and small scale promontories (Table 3.1 and Fig. 3.10e); the average elevation bias is 80 m. These differences affect SMB in two ways. First, precipitation increases by 2.6 Gt yr^{-1} (12%) in v0.2 (Table 3.1 and Figs. 3.10b and f), exclusively caused by the expansion of glaciated area (no elevation correction is applied). Another 1.6 Gt yr^{-1} (6%) of precipitation is added in v1.0 (Fig. 3.10j) to compensate for the systematic negative SMB bias in the GrIS accumulation zone, as discussed in Section 3.4. For both downscaling versions, changes in runoff mirror the elevation change between the two resolutions (Fig. 3.10e), highlighting the high sensitivity of runoff to elevation. In version v0.2, integrated runoff increases by 7.7 Gt yr^{-1} (48%) (Figs. 3.10c and g). Furthermore, Fig. 3.10i reveals a systematic overestimation of bare ice albedo at 11 km. Correcting for this further increases runoff over the glaciers tongues (Fig. 3.10k), accounting for $\sim 13 \text{ Gt yr}^{-1}$ (55%) of additional runoff with respect to v0.2 (Table 3.1). Negligible changes in sublimation and drifting snow are found (Table 3.1). As a consequence, integrated SMB on the 1 km mask decreases by 5.3 Gt yr^{-1} in version v0.2 (Figs. 3.10d and h) and by 16.6 Gt yr^{-1} in version v1.0 (Fig. 3.10l). This analysis for central east Greenland demonstrates the importance of accurately reproducing small scale topography and ice albedo to realistically capture local SMB variations.

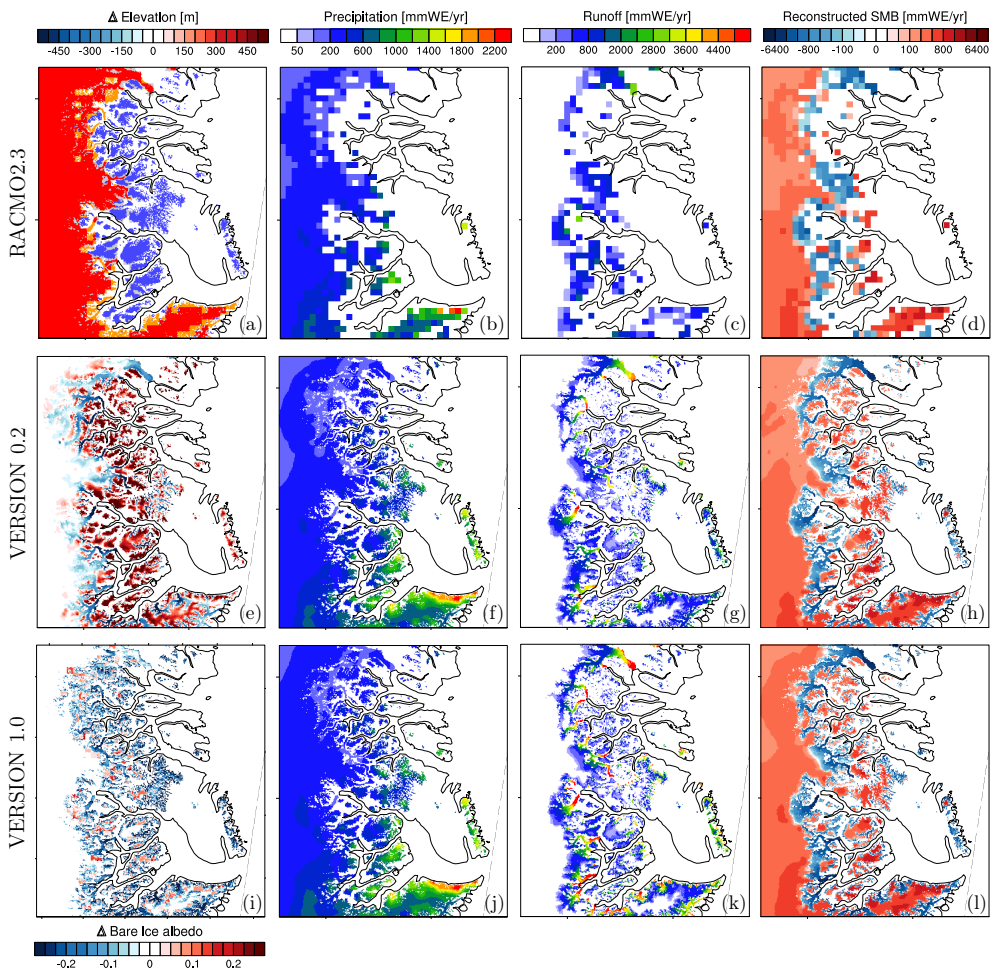


Figure 3.10: Centre east: a) Ice sheet mask in RACMO2.3 at 11 km (red) and in the down-sampled GIMP DEM at 1 km (orange) (blue box 1 in Fig. 3.1), and the mask of disconnected glaciers and ice caps at 1 km (blue); average (1958-2015) annual mean b) total precipitation, c) runoff and d) SMB (mm w.e. yr^{-1}) modelled by RACMO2.3 at 11km; e) elevation bias (m) between 1 km and 11 km resolutions. Figures f, g, h) represent annual mean total precipitation, runoff and SMB downscaled to 1 km using elevation dependence only (v0.2). Figure i) shows the bare ice albedo bias between MODIS measurements at 1 km (2000-2015) and RACMO2.3 at 11 km (2001-2010). Figures j, k) and l) are similar to f, g) and h) but incorporate the bare ice albedo and precipitation corrections (v1.0).

3.5.2 Central west Greenland

The 11 km resolution DEM provides a reasonable representation of the wide, gently sloping western ablation zone of the GrIS, where most glaciers are land-terminating. The northern part of the selected area includes several marine-terminating glaciers which are better represented at 1 km (Figs. 3.11d and h). Owing to negligible difference in glaciated area, precipitation remains almost unchanged for the two resolutions and versions ($\sim 15 \text{ Gt yr}^{-1}$). In both downscaled versions, enhanced runoff is mostly obtained over narrow, low-lying glaciers tongues and detached ice caps (Figs. 3.11c, g and k) where most of the elevation and ice albedo biases are found (Figs. 3.11e, i). On the ice sheet, the elevation correction increased runoff by about 1 Gt yr^{-1} (5%) (Fig. 3.11g) while an additional $\sim 2 \text{ Gt yr}^{-1}$ (10%) (Fig. 3.11k) can be ascribed to the ice albedo correction (Table 3.1).

3.5.3 South Greenland

Southeast Greenland (blue box 3 in Fig. 3.1) is a rugged region (Fig. 3.12e), characterised by multiple topographically-forced precipitation maxima (Figs. 3.12b and f) and narrow marginal ablation zones (Figs. 3.12c, g and k). Similar to central east Greenland, the larger glaciated area (+6.5%, Fig. 3.12a) at 1 km enhances integrated precipitation by $\sim 6 \text{ Gt yr}^{-1}$ (+7%) in v0.2 and 8.4 Gt yr^{-1} (+9%) in v1.0. Increased runoff (2.2 Gt yr^{-1} or 5% in version v0.2) at the southern margins can be ascribed to additional melt production over the better resolved narrow ablation zones (Figs. 3.12g and k) combined with a moderate mean elevation difference ($\sim 17 \text{ m}$) between both resolutions. In v0.2, the ice mask expansion explains most of the integrated SMB changes, leading to an overall mass gain of 3.3 Gt yr^{-1} .

Figure 3.7b reveals considerable ablation underestimation in southern Greenland, expressed as a systematic SMB bias of 2 to 4 m w.e. relative to measurements collected at PROMICE station QAS_L (red stars in Fig. 3.7a). The main reason for this underestimation is that SMB at this location is characterised by a rare combination of high snowfall and strong summer melt.

The remaining ablation underestimation in v0.2 can be partly ascribed to an overestimated bare ice albedo (0.47) prescribed in RACMO2.3 [Noël et al., 2015]; observed albedo at QAS_L frequently falls to 0.2 during the melt season [Fausto et al., 2016]. As a result, the additional bare ice albedo correction significantly improves runoff at station QAS_L (Fig. 3.7c). Integrated over region 3, runoff increases by another $\sim 13 \text{ Gt yr}^{-1}$ (29%) relative to v0.2 (Fig. 3.12k). The increased marginal mass loss leads to the expansion of the southern ablation zone towards higher elevations (Figs. 3.12k and l), in line with local observations (Fig. 3.7c).

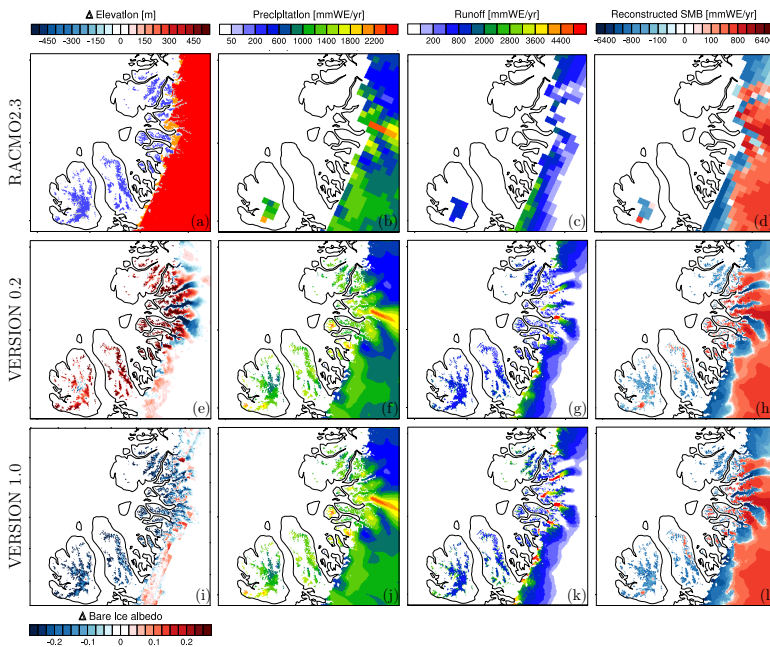


Figure 3.11: Centre west: same as Fig. 3.10 but for central west Greenland (blue box 2 in Fig. 3.1).

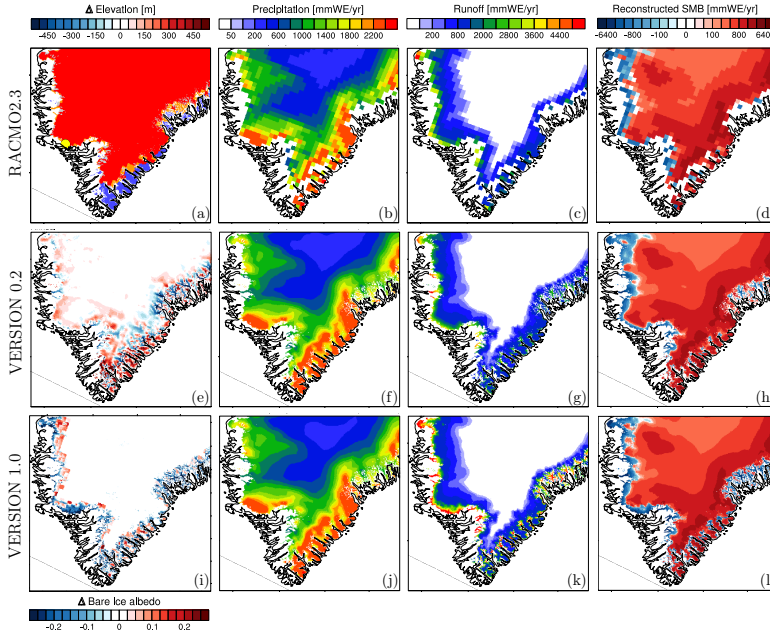


Figure 3.12: South: same as Fig. 3.10 but for south Greenland (blue box 3 in Fig. 3.1). The yellow dot in a) locates station QAS_L.

3.5.4 North Greenland

In north Greenland (blue box 4 in Fig. 3.1), the climate is dry, and most glaciers are marine-terminating. The ice sheet surface is relatively smooth and homogeneous. The wide ablation zone is reasonably well captured at 11 km, leading to a modest deviation in elevation (~ 43 m) (Fig. 3.13e). However, the ice-covered area decreases by $\sim 11\%$ between both resolutions as the 11 km grid contained erroneous floating glacier tongues (Fig. 3.13a). The ice area reduction at 1 km affects precipitation (-0.8 Gt yr^{-1} or -12%) (Figs. 3.13b and f) and runoff (-3.1 Gt yr^{-1} or -35%) (Figs. 3.13c and g), resulting in a small SMB increase (2.3 Gt yr^{-1}) in version v0.2 (Figs. 3.13d and h). Large bare ice albedo discrepancies can be found on five major glaciers (Fig. 3.13i) where runoff increases substantially (~ 2 Gt yr^{-1} or 34%) in version v1.0, further decreasing the integrated SMB by 1.0 Gt yr^{-1} compared to v0.2 (Figs. 3.13h and l).

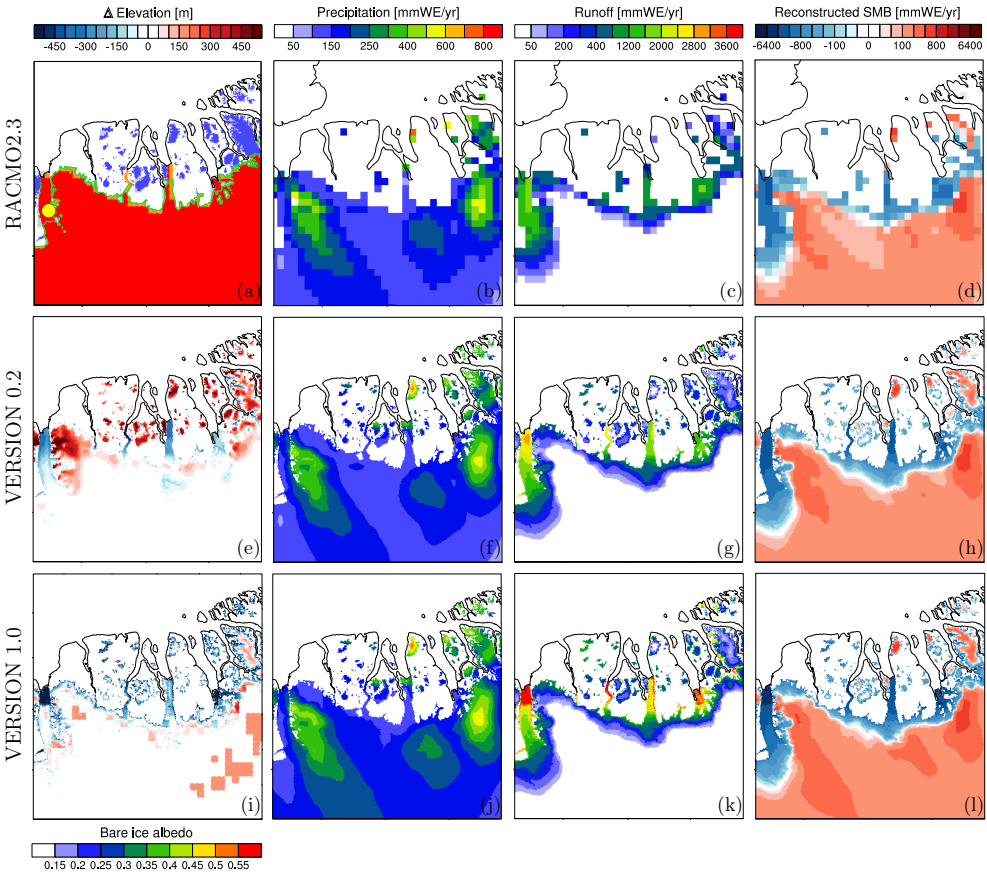


Figure 3.13: North: same as Fig. 3.10 but for north Greenland (blue box 4 in Fig. 3.1). The green line in a) shows the grounded ice mask at 1 km. The yellow dot in a) locates the Petermann glacier site settled on a floating ice tongue.

| 1958-2015 Resolution | Regions Unit | Centre east | | Centre west | | South | | North | | GrIS | | | | | | |
|-------------------------|---------------------------------|-------------|-------|-------------|------|-------|-------|-------|------|------|------|------|------|-------|-------|-------|
| | | 11km | 1km | Δ | 11km | 1km | Δ | 11km | 1km | Δ | 11km | 1km | Δ | | | |
| SMB v0.2 | Gt _{yr} ⁻¹ | 5.0 | -0.3 | -5.3 | -4.6 | -5.4 | -0.8 | 44.3 | 47.6 | 3.3 | -2.6 | -0.3 | 2.3 | 349.3 | 351.3 | 2.0 |
| Runoff v0.2 | Gt _{yr} ⁻¹ | 16.1 | 23.8 | 7.7 | 18.3 | 19.2 | 0.9 | 42.4 | 44.6 | 2.2 | 8.9 | 5.8 | -3.1 | 284.1 | 297.7 | 13.6 |
| Precip v0.2 | Gt _{yr} ⁻¹ | 22.6 | 25.2 | 2.6 | 15.0 | 15.2 | 0.2 | 91.4 | 97.2 | 5.8 | 6.9 | 6.1 | -0.8 | 675.4 | 692.0 | 16.6 |
| SMB v1.0 | Gt _{yr} ⁻¹ | 5.0 | -11.6 | -16.6 | -4.6 | -6.7 | -2.1 | 44.3 | 37.3 | -7.0 | -2.6 | -1.3 | 1.3 | 349.3 | 338.2 | -11.1 |
| Runoff v1.0 | Gt _{yr} ⁻¹ | 16.1 | 36.7 | 20.6 | 18.3 | 21.1 | 2.8 | 42.4 | 57.5 | 15.1 | 8.9 | 7.7 | -1.2 | 284.1 | 367.0 | 82.9 |
| Precip v1.0 | Gt _{yr} ⁻¹ | 22.6 | 26.8 | 4.2 | 15.0 | 15.8 | 0.8 | 91.4 | 99.8 | 8.4 | 6.9 | 7.0 | 0.1 | 675.4 | 748.2 | 72.8 |
| Sublimation | Gt _{yr} ⁻¹ | 2.1 | 2.1 | 0.0 | 1.6 | 1.6 | 0.0 | 4.4 | 4.7 | 0.3 | 0.8 | 0.7 | -0.1 | 41.3 | 41.9 | 0.6 |
| Snow drift | Gt _{yr} ⁻¹ | -0.5 | -0.4 | 0.1 | -0.3 | -0.2 | 0.1 | 0.2 | 0.3 | 0.1 | -0.1 | -0.1 | 0.0 | 0.7 | 1.1 | 0.4 |
| Ice area | 10 ⁴ km ² | 5.9 | 6.0 | 0.1 | 2.7 | 2.7 | -0.02 | 7.7 | 8.2 | 0.5 | 3.5 | 3.1 | -0.4 | 170.3 | 169.4 | -0.9 |

Table 3.1: Table listing (top) the annual mean integrated SMB components (Gt per year) covering the period 1958-2015 over four different regions, centre east (69.6° N – 74.3° N; 21° W – 31° W; blue box 1 in Fig. 3.1), centre west (69.3° N – 72.5° N; 49° W – 57° W; blue box 2), south (59.5° N – 63.3° N; 41° W – 51° W; blue box 3) and north (80.5° N – 83° N; 42° W – 62° W; blue box 4), and for the entire GrIS at both resolutions as well as the difference between 1 km and 11 km; (bottom) same for the ice-covered area (km²).

3.5.5 Greenland ice sheet

Although similar in area, the 1 km ice sheet mask better resolves peripheral glaciers at the GrIS margins than RACMO2.3 at 11 km. GrIS integrated precipitation increases by 16.6 Gt yr^{-1} (+2%) in v0.2, most of which can be ascribed to ice area expansion in the east (2.6 Gt yr^{-1}) and south of Greenland (5.8 Gt yr^{-1}), where precipitation is large. An additional 56.2 Gt yr^{-1} (+8%) is obtained in v1.0 when correcting for the accumulation zone SMB bias. The smooth topography of the ice sheet interior results in a small elevation difference of 4 m between both resolutions. Significant elevation biases are mostly restricted to peripheral glaciers and narrow ablation zones at the GrIS margins. As a result, runoff increases by 13.6 Gt yr^{-1} (+5%) in version v0.2. Accounting for the bare ice albedo bias in RACMO2.3 further increases runoff by 69.3 Gt yr^{-1} in version v1.0, leading to a much improved agreement with ablation measurements. Of our selected areas, central east and south Greenland contribute 25% and 18% to the total runoff increase in the downscaled product v1.0 owing to the many low-lying glaciers tongues that can only be resolved at 1 km. Due to their smoother topography, north and centre west Greenland contribute much less to the runoff change ($\sim 3\%$ and 1% , respectively). Integrated over the contiguous ice sheet, SMB is not significantly affected by the elevation dependence for which enhanced precipitation (16.6 Gt yr^{-1}) yearly balances the moderate increase in runoff (13.6 Gt yr^{-1}). In contrast, the bare ice albedo and precipitation corrections substantially increase marginal runoff (82.9 Gt yr^{-1}) and accumulation (72.8 Gt yr^{-1}), resulting in a decrease of SMB of -11.1 Gt yr^{-1} (-3%) relative to the 11 km product.

3.6 Added value, limitations and uncertainties

The downscaled SMB v1.0 is the first data set to provide daily SMB estimates for all outlet glaciers of the GrIS at a 1 km resolution for 58 years (1958-2015). Relative to the original RACMO2.3 output, this data set improves local SMB values (Fig. 3.8) and produces more realistic SMB patterns over rugged glaciated areas along the GrIS margins (Figs. 3.10-3.13). Figures 3.7 and 3.9 show that SMB v1.0 is an overall improvement on the original RACMO2.3. To further investigate this, Fig. 3.14 shows the annual mean SMB RMSE (model vs. observations) of the 11 km SMB field in RACMO2.3 (red), the downscaled product v0.2 (green) and v1.0 (blue) as a function of observed SMB, binned in 0.5 m w.e. intervals. In the ablation zone ($\text{SMB} < 0$), the SMB RMSE is reduced by 29-65% in v1.0 relative to the 11 km product, owing to the elevation correction in v0.2 (9-23%) and the additional albedo correction (20-42%). In the accumulation zone, the elevation dependence (9%) and the precipitation adjustment (19%) also contribute to reduce the SMB RMSE by 28% in v1.0. The largest RMSE reduction occurs in the lower GrIS ablation zone, where improvements in topography and bare ice albedo in v1.0 are greatest.

Although significantly improved, the downscaled SMB v1.0 is likely to be locally underestimated for four reasons: a) the bare ice albedo correction is evenly applied to both snow covered and bare ice regions experiencing surface melt and runoff, as no relevant proxy, reflecting day-to-day snow coverage, could be derived from RACMO2.3. However, this issue should have a limited effect on the magnitude of downscaled melt and runoff since the albedo correction is most efficient in summer, when the snow cover of low-lying glaciers has likely melted; b) the MODIS ice albedo product at 1 km becomes less accurate at high latitudes, likely suffering from bare soil contamination resulting from mixed reflectance

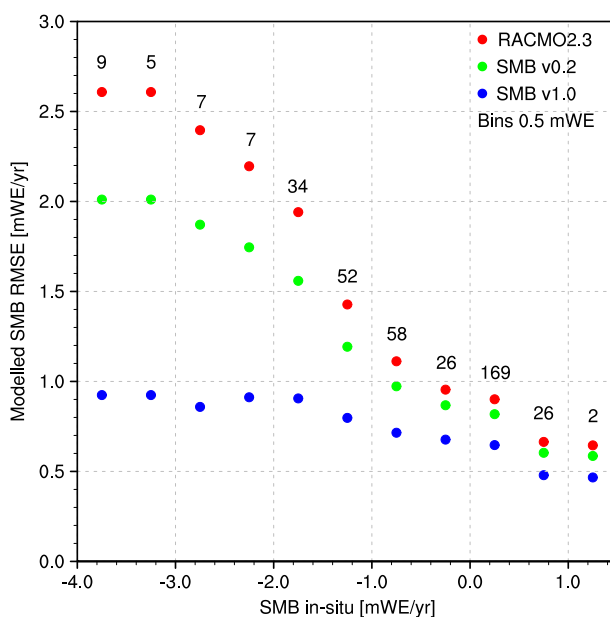


Figure 3.14: Annual mean modelled SMB RMSE (model vs. observations) of the 11 km SMB field in RACMO2.3 (red dots), the downscaled SMB data set v0.2 (green dots) and v1.0 (blue dots) as a function of observed SMB (395 observations). Modelled SMB is grouped in 0.5 m w.e. yr^{-1} bins except for the first bin, which ranges from -6.00 to -3.75 m w.e. yr^{-1} . Numbers indicate the amount of observations used in each bin.

signals recorded in both the tundra and ice covered regions. Note that floating glacier tongues also show too low surface albedo, e.g. Petermann glacier (yellow dot in Fig. 3.13a), resulting from mixed signals from adjacent dark melt pond and brighter dry ice. The resulting albedo underestimation over low-lying floating tongues below 200 m leads to overestimated ablation (~ 0.2 m w.e. yr^{-1} ; Figs. 3.8a and b); c) the average 1 km MODIS ice albedo product for 2000-2015 used in the melt correction remains constant in time and might underestimate the bare ice albedo prior to 2000 as the period 2000-2015 encompasses multiple record high melt years; d) the degradation of MODIS Terra sensors [Polashenski et al., 2015]. These limitations underline the high sensitivity of the downscaled product to the input fields used to initialise the downscaling procedure, i.e. RCM version used, the resulting modelled SMB components, bare ice albedo records, ablation measurements, topography and ice mask. The downscaled SMB v1.0 presents an estimated uncertainty of ~ 12 Gt yr^{-1} in the GrIS ablation zone, which was estimated by integrating the SMB bias in v1.0 (60 mm w.e., Fig. 3.7c) over the ablation zone of the contiguous ice sheet ($\sim 202,000$ km 2).

We anticipate that the new, 1 km Greenland SMB product is especially useful for studies that address the mass balance of Greenland outlet glaciers that are too steep and/or narrow to be properly resolved at the typical horizontal resolution of regional climate models (~ 5 -20 km). Future downscaled products can have even higher resolution (100 m) and will be based on further improved RCM output fields of precipitation and melt.

3.7 Conclusions

The relatively coarse spatial resolution currently used in RCMs remains insufficient to properly resolve small scale variations in elevation and ice cover at the ice sheet margins, significantly affecting the calculation of melt and runoff. In the present study, we statistically downscale individual SMB components from RACMO2.3 at 11 km to a 1 km ice mask and topography derived from the GIMP DEM, using a daily specific elevation dependence. Moreover, runoff and melt are corrected for biases in bare ice albedo in RACMO2.3. Precipitation and snowdrift erosion are bi-linearly interpolated without applying an elevation correction. Total precipitation is also adjusted to compensate for the dry accumulation bias of RACMO2.3 in the ice sheet interior. Downscaled daily SMB is then retrieved for the period 1958-2015 by summing daily downscaled precipitation, runoff, sublimation and drifting snow erosion. An evaluation of the downscaled SMB product against observations, collected both in the ablation and accumulation zones of the GrIS, shows improved agreement. In the ablation zone, the variance explained by the downscaled product v1.0 increased by 31% relative to the original RACMO2.3 11 km output, mainly through better resolved narrow outlet glaciers at the GrIS margins.

Integrated over the GrIS, precipitation increased by 16.6 Gt yr^{-1} due to the larger glaciated area in south and east Greenland at 1 km; an additional correction of 56.2 Gt yr^{-1} must account for the accumulation bias in the ice sheet interior in RACMO2.3. Likewise, a 13.6 Gt yr^{-1} increase in runoff is attributed to elevation corrections on the 1 km topography and another 69.3 Gt yr^{-1} extra runoff can be ascribed to underestimated bare ice albedo over narrow outlet glaciers at the GrIS margins. A small area in central east Greenland alone, characterised by multiple narrow glacier tongues poorly resolved at 11 km, accounts for $\sim 25\%$ of the total additional runoff.

A tipping point in refreezing accelerates mass loss of Greenland's ice caps

Summary

Melting of the Greenland ice sheet (GrIS) and its peripheral glaciers and ice caps (GICs) contributes about 43% to contemporary sea level rise. While patterns of GrIS mass loss are well studied, the spatial and temporal evolution of GICs mass loss and the acting processes have remained unclear. Here we use a novel, 1 km surface mass balance product, evaluated against in situ and remote sensing data, to identify 1997 (± 5 years) as a tipping point for GICs mass balance. That year marks the onset of a rapid deterioration in the capacity of the GICs firm to refreeze meltwater. Consequently, GICs runoff increases 65% faster than meltwater production, tripling the post-1997 mass loss to $36 \pm 16 \text{ Gt yr}^{-1}$, or $\sim 14\%$ of the Greenland total. In sharp contrast, the extensive inland firm of the GrIS retains most of its refreezing capacity for now, buffering 22% of the increased meltwater production. This underlines the very different response of the GICs and GrIS to atmospheric warming.

This chapter is based on: B. Noël et al. (2017a), A tipping point in refreezing accelerates mass loss of Greenland's glaciers and ice caps, *Nature Communications*, 2017a

4.1 Introduction

Covering a total area of $\sim 90,000 \text{ km}^2$, Greenland's peripheral glaciers and ice caps (GICs) represent $\sim 12\%$ of the world's glacierized area outside of the Antarctic and Greenland ice sheets [Vaughan et al., 2013]. Greenland's GICs account for 14 to 20% of total current Greenland glacial mass loss [Bolch et al., 2013], although they only represent $\sim 5\%$ of the area and $\sim 0.5\%$ ($\sim 39 \text{ mm SLR}$) of the volume of the Greenland ice sheet (GrIS). In a scenario of continued global warming, Greenland's GICs may lose 19-28% (7.5-11 mm) of their volume by 2100 [Machguth et al., 2013]. Despite multiple in situ observational campaigns since the early 1950s [Machguth et al., 2016b], glacier modelling [Marzeion et al., 2012] and satellite-based [Bolch et al., 2013; Gardner et al., 2013] estimates, large uncertainties remain in the spatial and temporal distribution of Greenland's GICs mass loss. To fill these gaps, regional climate models (RCMs) are often used [Van Angelen et al., 2013a; Burgess et al., 2010; Ettema et al., 2010b,a; Fettweis, 2007; Fettweis et al., 2005, 2011; Noël et al., 2015; Lucas-Picher et al., 2012], but their horizontal resolution (typically 5 to 20 km) fails to resolve the steep surface mass balance (SMB) gradients in the topographically complex regions in which GICs are often situated [Noël et al., 2016]. To address this issue, we created a 1 km data set, statistically downscaled from output of the regional atmospheric climate model RACMO2.3 using regressions of SMB components against elevation estimated at the model resolution of 11 km. These regressions are then applied to a down-sampled 1 km version of the topography and ice mask of the Greenland Ice Mapping Project (GIMP) Digital Elevation Model (DEM) [Howat et al., 2014]. The downscaling procedure also includes a bare ice albedo correction based on a 1 km MODIS albedo product to avoid underestimation of melt and runoff, especially on dark, low-lying glacier tongues. Earlier, the downscaling method was successfully applied to the GrIS [Noël et al., 2016].

Here we use the novel SMB product at 1 km resolution to quantify Greenland's GICs mass loss, assuming changes in solid ice discharge to be negligible [Price et al., 2011; Goelzer et al., 2013; Nick et al., 2013]. The data set includes individual SMB components (precipitation, sublimation, melt, refreezing and runoff) for all GICs on a daily time scale (1958-2015), which is crucial for evaluation using irregular (in time and space) observations and to understand the drivers of mass loss. Using this product, we identify 1997 (± 5 years) as a tipping point for the mass balance of Greenland's GICs, which marks the onset of a rapid deterioration of inland firn capacity to refreeze meltwater, causing long-term mass loss.

4.2 Evaluation against observations

Figure 4.1a shows average (1958-2015) downscaled SMB for the whole of Greenland, and Fig. 4.1b compares the downscaled SMB to 965 SMB measurements from 101 GICs sites [Machguth et al., 2016b] (yellow dots in Fig. 4.1a). With 77% of the variance explained, the downscaled SMB agrees well with observations, although significant deviations and a negative bias of $240 \text{ mm w.e. yr}^{-1}$ (water equivalent) remain. We selected five GICs regions (black boxes) to highlight the agreement and differences of the downscaled SMB product with observations (Fig. 4.1a). Figure 4.10 shows and briefly discusses the intricate patterns of SMB and its components over GICs in four of these regions (Section 4.6); sector five is discussed below.

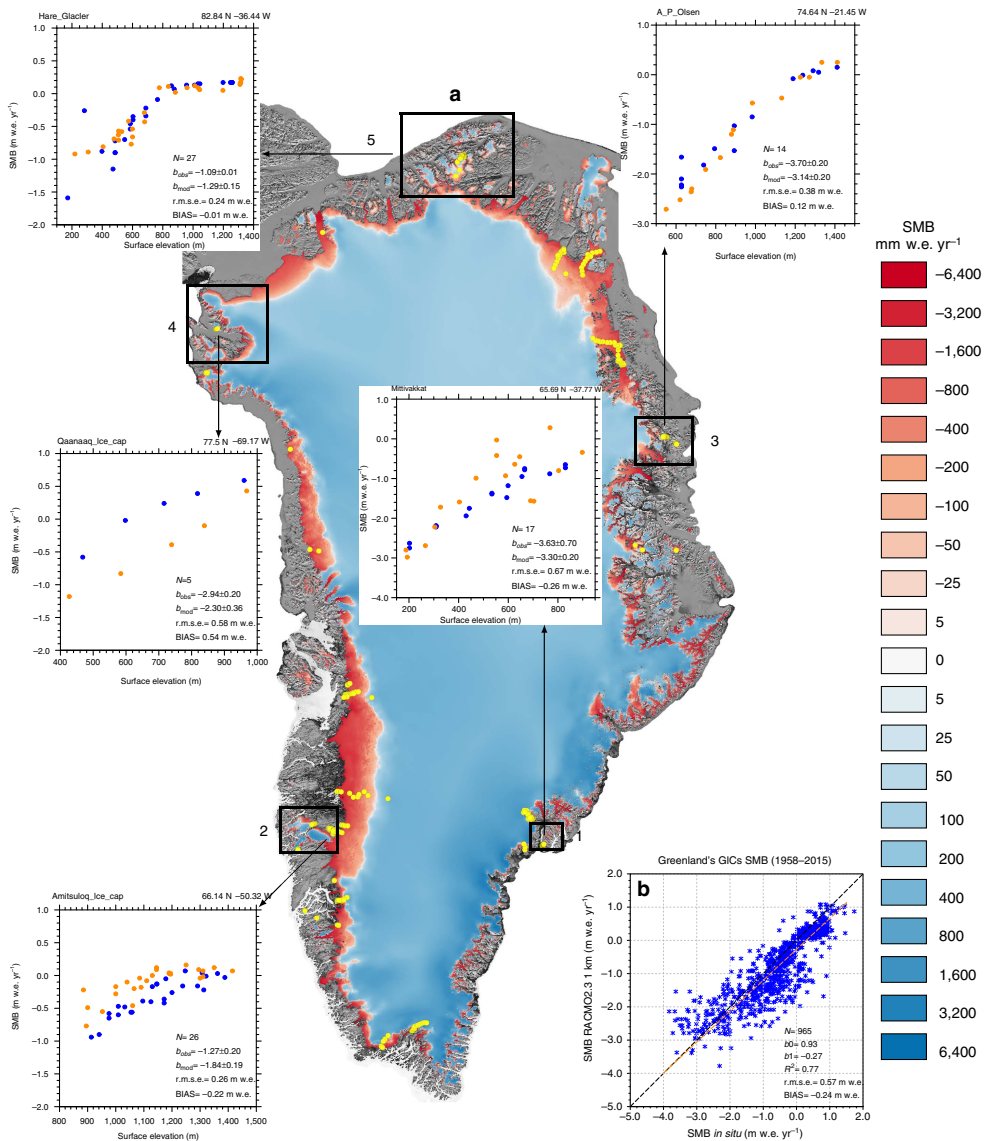


Figure 4.1: Greenland SMB patterns and evaluation. a) Annual mean downscaled SMB (v1.0, see Section 4.5) at 1 km resolution over the GrIS and neighbouring GICs for 1958-2015. Yellow dots correspond to 331 SMB observation sites used for GrIS (230) and GICs (101) evaluation. Numbered black boxes depict 5 regions including stake transects collected over GICs. For each transect, annual mean SMB is plotted from downscaled simulation v1.0 (b mod; dark blue dots) and in situ data (b obs; orange dots). The number of observations, observed and downscaled SMB gradients, RMSE and mean bias are also listed for each transect. b) Comparison of ablation measurements collected at 101 GICs sites with downscaled SMB at 1 km (v1.0). The orange dashed line represents the regression including all measurements ($y = b_1 + b_0 \times x$).

A direct comparison with mass loss estimates from independent ICESat/CryoSat-2 measurements over the period 2004–2015 demonstrates that the downscaled SMB product with albedo correction successfully reproduces GICs mass changes (Fig. 4.2), including seasonal and interannual variability, e.g. the large difference in mass loss between the summers of 2012 and 2013. The uncertainty in downscaled SMB was estimated at 15.7 Gt yr^{-1} ($\sim 40\%$, see Section 4.5.10). Note that the Greenland's GICs area of $\sim 81,400 \text{ km}^2$ used in this study is smaller by $\sim 8\%$ than previous estimates [Rastner et al., 2012; Citterio and Ahlström, 2013] due to the omission of unresolved small ice bodies ($< 1 \text{ km}^2$) in the original GIMP DEM.

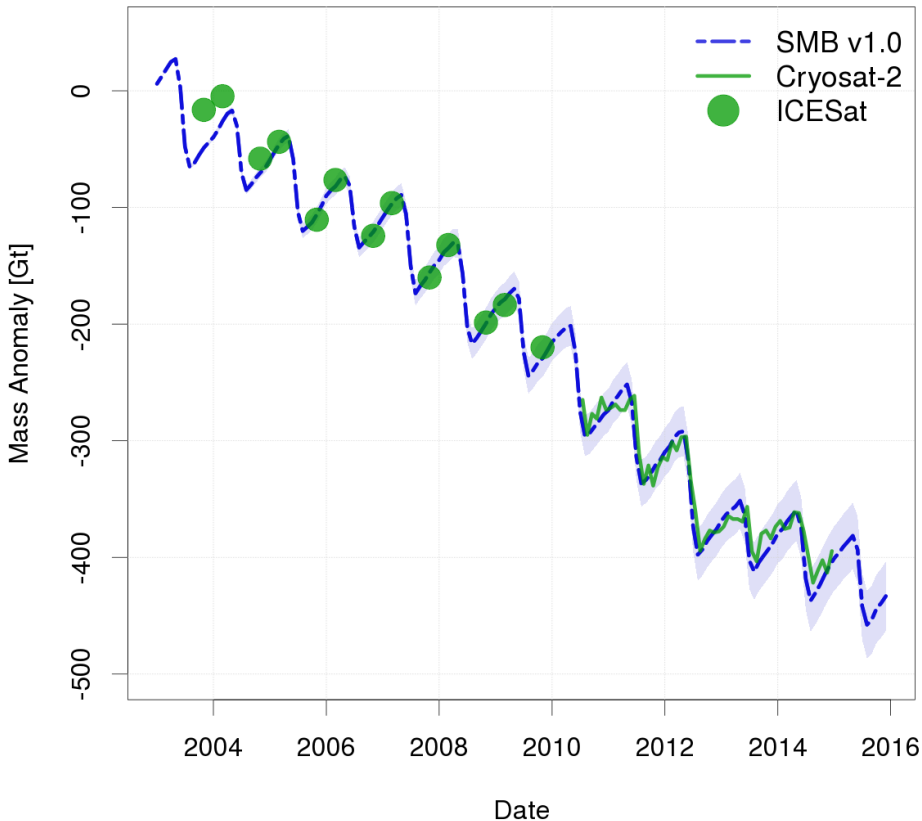


Figure 4.2: Contemporary Greenland's GICs mass anomaly. Comparison of Greenland's GICs-integrated mass anomaly (2004–2015) derived from ICESat (green dots)/CryoSat-2 (green line) altimetry with the downscaled SMB v1.0 (dashed blue line). The light blue belt represents the estimated uncertainty of the downscaled SMB product.

4.3 A tipping point in GICs mass balance

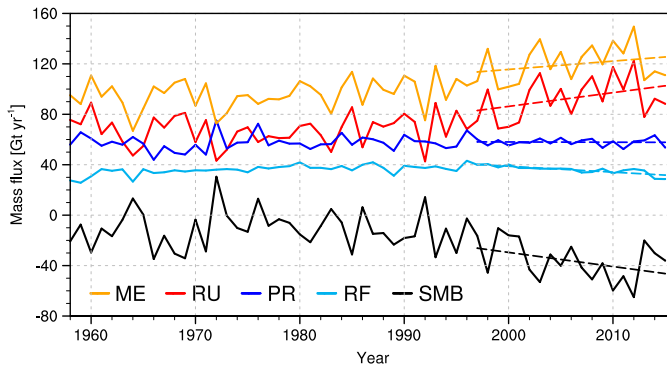
Figure 4.3 shows time series (1958–2015) of annual mean SMB components precipitation (PR), melt (ME), refreezing (RF) and runoff (RU), all in Gt yr^{-1} and spatially integrated over a) Greenland's GICs and b) the GrIS. Figure 4.3c zooms in on the refreezing time series. Using a breakpoint analysis (see Section 4.5.11), we identify 1997 (± 5 years) as the year after which the GICs refreezing regime starts to decrease and diverges significantly from the GrIS refreezing regime (black point in Fig. 4.3c). This marked reduction in refreezing capacity is representative of a deteriorating firn layer, the porous, multiyear snow layer between surface fresh snow ($\sim 350 \text{ kg m}^{-3}$) and the underlying ice ($\sim 900 \text{ kg m}^{-3}$). Decades of increased melt have reduced pore space to such a degree that enhanced refreezing can no longer compensate for increased meltwater production. Because it would take decades to regrow a healthy firn layer, we interpret 1997 as a tipping point in the mass balance of Greenland's GICs.

4.4 Discussion

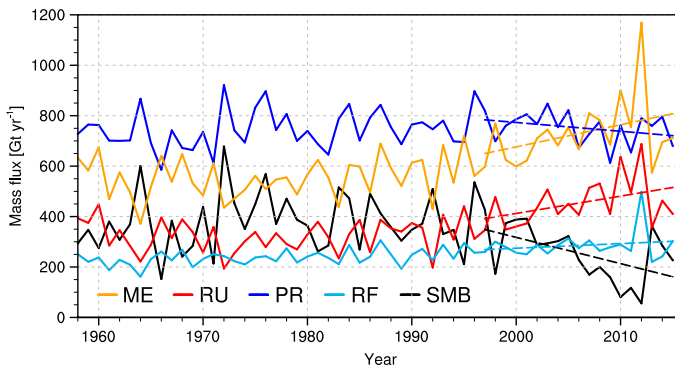
Prior to 1997, Greenland's GICs average SMB was marginally negative ($-11.3 \pm 15.7 \text{ Gt yr}^{-1}$; see Tables 4.1 and 4.2 for numbers in mm w.e. yr^{-1}), with an insignificant trend of $-0.01 \pm 0.22 \text{ Gt yr}^{-2}$. Note how, even in this earlier period, melt (95 Gt yr^{-1}) persistently and significantly exceeded precipitation (58 Gt yr^{-1}), stressing the importance of the refreezing process for maintaining the mass balance of these Arctic GICs close to zero (Table 4.1). The situation is very different for the GrIS, where pre-1997 precipitation (746 Gt yr^{-1}) exceeded melt (556 Gt yr^{-1}) by a wide margin (Table 4.2). Coincidentally, before 1997 the GICs and the GrIS had a similar refreezing fraction (RF/ME) of 38% and 43%, respectively.

Between 1997 and 2015, the integrated GICs SMB decreased at a rate of $1.1 \pm 0.6 \text{ Gt yr}^{-2}$, signifying mass loss acceleration, resulting in an average SMB over this period of $-36.2 \pm 15.7 \text{ Gt yr}^{-1}$. Previous estimates for different periods [Marzeion et al., 2012; Bolch et al., 2013; Gardner et al., 2013] (Table 4.3) confirm this recent increase of GICs mass loss. However, with the new SMB product we are now able to identify the physical processes responsible for the post-1997 mass loss acceleration. Figure 4.3a unambiguously shows that the trend in SMB is almost exclusively driven by increased runoff ($1.1 \pm 0.6 \text{ Gt yr}^{-2}$), while precipitation remains constant. A similar pattern emerges for the GrIS; here, a negative trend in precipitation ($-3.5 \pm 2.6 \text{ Gt yr}^{-2}$) somewhat reinforces the decrease in SMB ($-10.4 \pm 4.0 \text{ Gt yr}^{-2}$), but again the latter is dominated by the increase in runoff ($6.9 \pm 3.7 \text{ Gt yr}^{-2}$). But Fig. 4.3 and Tables 4.1 and 4.2 also reveal a striking difference in the responses of the GrIS and Greenland's GICs to atmospheric warming. On the GrIS (Fig. 4.3b and Table 4.2), an important fraction (22%) of the excess meltwater produced since 1997 has been retained in the extensive interior firn layer, driven by an increase in refreezing (RF). In contrast, refreezing decreased on Greenland's GICs (Fig. 4.3c). As a result, runoff outpaces excess meltwater production by 65% since 1997. It thus appears that the mass balance of Greenland's GICs crossed a tipping point in 1997 (Fig. 4.3c), implying eventual long-term loss of the firn layer's refreezing capacity.

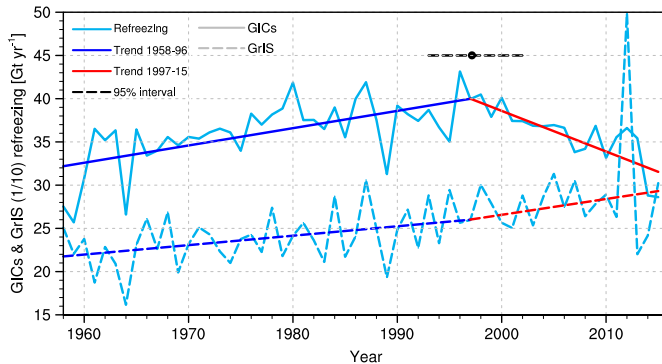
Figure 4.4 confirms these findings by comparing vertical profiles of surface mass fluxes integrated over GICs and GrIS elevation bins, scaled by the maximum height per region (h_{max}), prior to and after 1997. Figures 4a and b show that the equilibrium line (SMB = 0) of the GICs moved significantly upward, i.e.



(a) Greenland's glaciers and ice caps (GICs)



(b) Greenland ice sheet (GrIS)



(c) Refreezing tipping point

Figure 4.3: Mass flux evolution and refreezing tipping point. *a)* Time series of GICs annual cumulative SMB components for the period 1958-2015. *b)* Same as *a)* but for the contiguous GrIS. Dashed lines show 1997-2015 trends. Total sublimation (SU) and snow drift erosion (ER) are not included in the above time series as they contribute relatively little to SMB and trends are very small compared to the other components. *c)* Time series of GICs (continuous lines) and GrIS (1/10, dashed lines) integrated annual mean refreezing and trends for 1958-1996 (blue) and 1997-2015 (red). The GICs refreezing tipping point (1997) is represented in black with a 95% confidence interval (dashed black line).

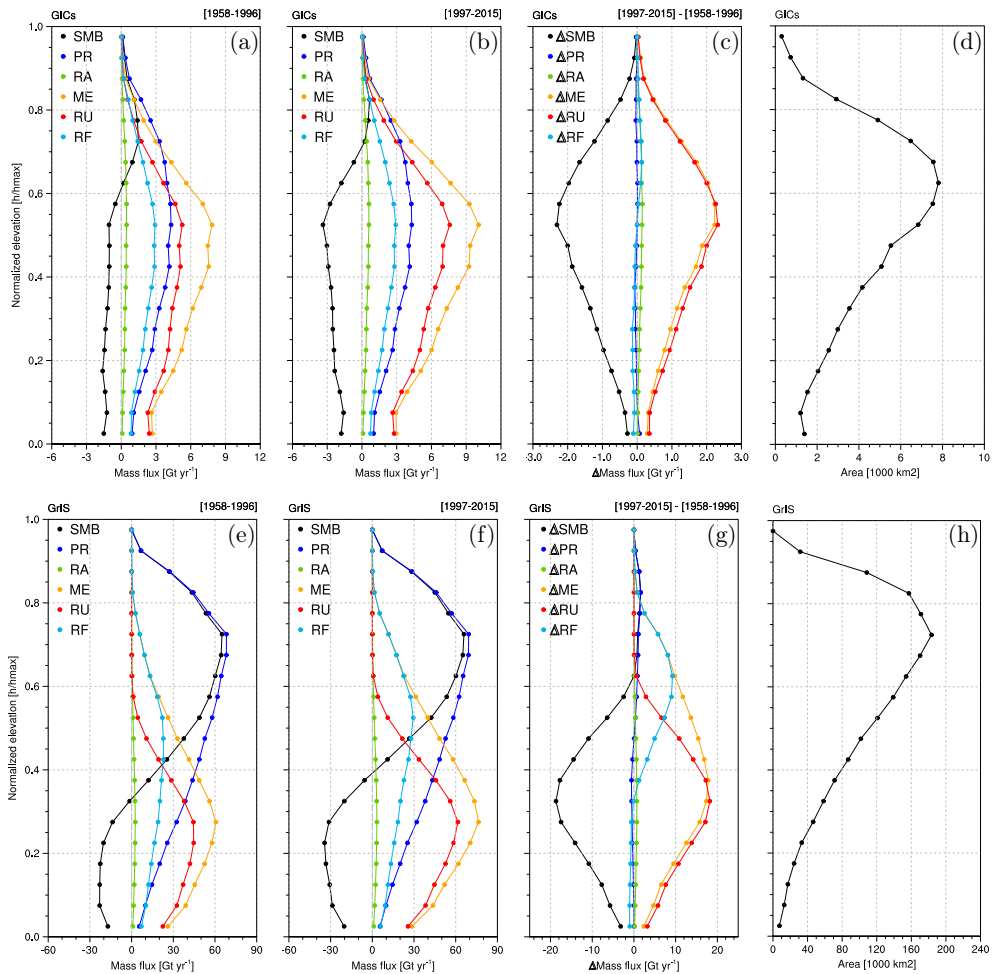


Figure 4.4: Shrinking of the accumulation zones. Vertical profiles of surface mass fluxes integrated over GICs (upper row) and GrIS (lower row) elevation bins, scaled by the maximum height per region (h_{max}), for the period 1958-1996 (a and e), 1997-2015 (b and f) and the difference between the two periods (1997-2015 minus 1958-1996, c and g). SMB components are spatially integrated within normalised elevation bins (h/h_{max}) of magnitude 0.05. For the GICs, SMB components are first integrated in elevation bins over twelve individual regions, each with different h_{max} (boxes in Fig. 4.5); the GICs-integrated SMB components are obtained by summing the contribution of the twelve regions to each scaled elevation bin. Figures 4 d) and h) show the scaled hypsometries, i.e. total area occupied by each elevation bin, for the GICs and the GrIS, respectively.

from 0.61 to 0.71 of h_{\max} , and is now situated well above the peak in the hypsometry (0.62, Fig. 4.4d). In combination with decades of increased melt, which depleted firn pore space, the GICs firn layer is no longer capable of buffering the excess meltwater production. As a result, runoff increases at the same rate as melt and fully governs the GICs mass loss (Fig. 4.4c). Figures 4a and b also show that rainfall (RA) is a small (6%) fraction of the liquid water flux available at the firn layer top, which is dominated by melt. For the GrIS the equilibrium line has moved upwards from 0.33 to 0.40 of h_{\max} (Figs. 4.4e and f), but remains well below the maximum in the GrIS hypsometry (0.73, Fig. 4.4h). Therefore, a significant part of the excess melt is buffered by refreezing (Fig. 4.4g) and runoff remains constant above 0.61 of h_{\max} . Although formation of ice lenses may reduce the retention efficiency in the lower accumulation zone [Polashenski et al., 2015; Machguth et al., 2016b], we conclude that the extensive and elevated inland firn area of the GrIS (Fig. 4.4h) maintains its refreezing capacity for now. As a result, the acceleration of GrIS surface mass loss is less than half that of the GICs ($-6.1 \pm 2.4 \text{ mm w.e. yr}^{-2}$ vs. $-13.5 \pm 7.4 \text{ mm w.e. yr}^{-2}$).

To analyse spatial differences, we examined the changes in runoff, refreezing fraction (RF/ME) and 2-m air temperature in twelve marginal regions of Greenland (1997-2015 minus 1958-1996), covering 85% of all Greenland's GICs (Fig. 4.5). All regions experienced warming and an increase in runoff, but a marked contrast is found between GICs in north and south Greenland. Northern GICs experienced a significantly greater warming than southern GICs ($+1.0$ – $1.5 \text{ }^\circ\text{C}$, orange boxes vs. $+0.6$ – $0.8 \text{ }^\circ\text{C}$, black boxes) [Khan et al., 2014; Tedesco et al., 2016c] and a larger relative increase in runoff ($+50$ – 74% vs. $+17$ – 34%). The reduction in refreezing fraction is also twice as large for northern than for southern GICs (-9 – 14% vs. -5 – 7%) (Fig. 4.5). To further investigate the mechanisms involved, Fig. 4.6a zooms in on the region of Hans Tausen ice cap in north Greenland (region 5 in Fig. 4.1a). The Hans Tausen region shows a small steady mass loss ($-2.6 \pm 1.4 \text{ Gt yr}^{-1}$) before 1997 and a tripling in mass loss ($-7.6 \pm 1.4 \text{ Gt yr}^{-1}$) afterwards (Fig. 4.7). Figure 4.6b shows that the change in runoff (1997-2015 minus 1958-1996) is largest in the narrow ablation zone along the margins (300 – $500 \text{ mm w.e. yr}^{-1}$), but with a significant contribution from the interior ($\sim 100 \text{ mm w.e. yr}^{-1}$). This implies that all but the very highest parts of the GICs accumulation zones now regularly experience runoff, i.e. the firn layer is no longer capable of refreezing all meltwater that is produced in summer. Figure 4.6c confirms that the upper firn area of northern Greenland GICs has experienced the largest negative changes, up to 50%, in the refrozen meltwater fraction (RF/ME). Figure 4.6d relates these changes, as well as changes in rainfall, to annual mean (downscaled) 2-m air temperature anomalies. The strong correlation proves that the recent warming has reduced the refreezing capacity of the firn layer in these high northern GICs: in warm years, enhanced dry snow densification and surface melt quickly saturate the pore space of the firn layer. In addition, the fraction of rainfall doubles from $\sim 5\%$ to $\sim 10\%$ in warm compared to cold years, further limiting the formation of firn. The resulting reduced refreezing capacity means that continuous warming in the future is likely to further accelerate Greenland's GICs mass loss and rapidly erode these highly sensitive northern ice masses.

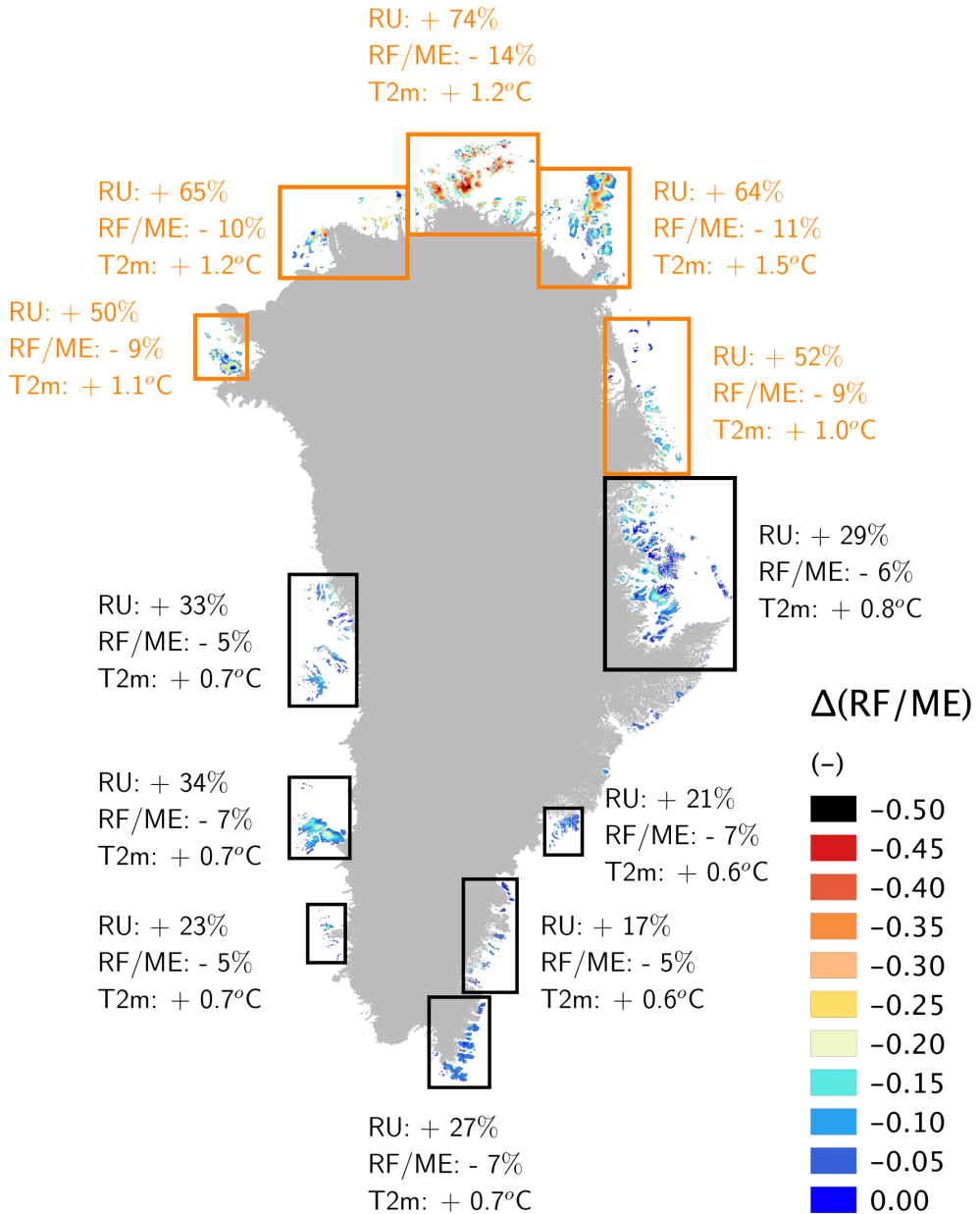


Figure 4.5: Drivers of the latitudinal contrast in runoff intensification. Regional differences in annual mean refreezing-to-melt ratio between 1997-2015 and 1958-1996. The change in runoff, refreezing-to-melt ratio and near-surface temperature is estimated for twelve different regions in north (orange boxes) and south Greenland (black boxes). The contiguous GrIS is displayed in grey.

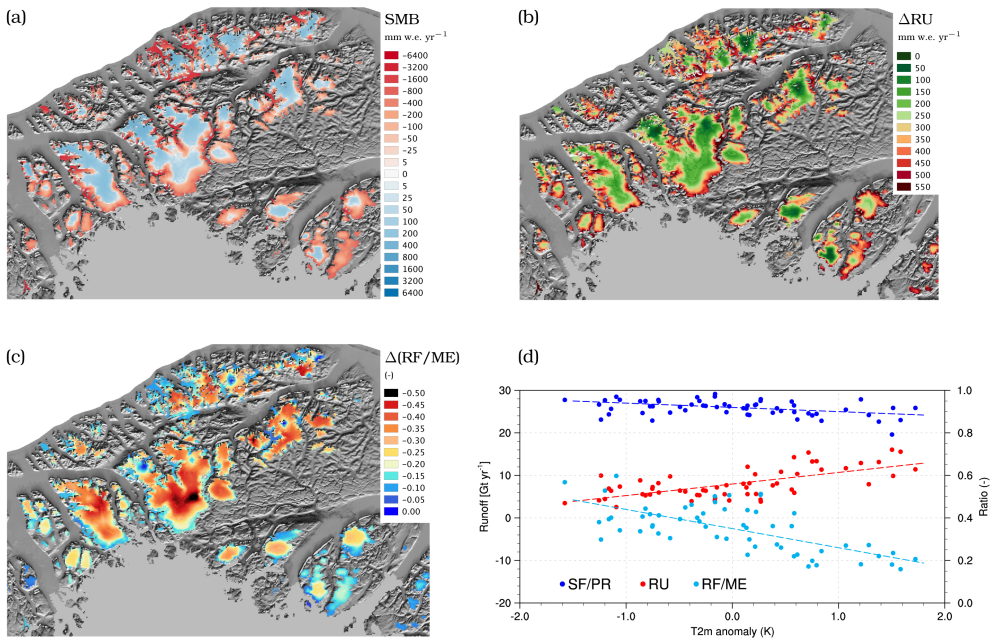


Figure 4.6: Mass loss amplification in the Hans Tausen region. *a)* Annual mean SMB patterns over the Hans Tausen region for 1958-2015 (black box 5 in Fig. 4.1), *b)* difference in annual runoff between 1997-2015 and 1958-1996, *c)* difference in the annual mean refreezing-to-melt ratio between 1997-2015 and 1958-1996 and *d)* annual runoff (red), snowfall-to-precipitation ratio (dark blue) and refreezing-to-melt ratio (light blue) as a function of the anomaly in annual mean 2-m temperature.

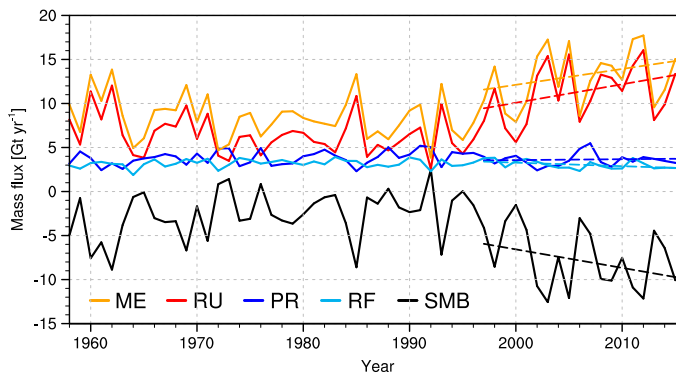


Figure 4.7: Mass flux evolution in the Hans Tausen region. *Time series of annual cumulative SMB components over the Hans Tausen ice cap and surroundings (black box 5 in Fig. 4.1) for the period 1958-2015. Trends in SMB components are represented as coloured dashed lines (1997-2015).*

| Mean | Units | SMB | RU | PR | ME | RF |
|-----------|--------------------------|--------------|-------------|--------------|-------------|--------------|
| 1958-1996 | Gt yr ⁻¹ | -11.3 ± 15.7 | 67.5 | 57.5 | 95.1 | 36.0 |
| 1997-2015 | Gt yr ⁻¹ | -36.2 ± 15.7 | 92.8 | 57.9 | 119.5 | 36.0 |
| 1958-1996 | mm w.e. yr ⁻¹ | -139 ± 193 | 829 | 706 | 1168 | 442 |
| 1997-2015 | mm w.e. yr ⁻¹ | -445 ± 193 | 1140 | 711 | 1468 | 442 |
| Trend | Units | SMB | RU | PR | ME | RF |
| 1958-1996 | Gt yr ⁻² | -0.01 ± 0.22 | 0.06 ± 0.17 | 0.06 ± 0.09 | 0.26 ± 0.16 | 0.20 ± 0.04 |
| 1997-2015 | Gt yr ⁻² | -1.12 ± 0.63 | 1.09 ± 0.64 | -0.02 ± 0.13 | 0.66 ± 0.61 | -0.47 ± 0.08 |

Table 4.1: GICs SMB average and trends. Greenland's GICs-integrated annual mean cumulative SMB components (top) and trends (bottom) for the periods 1958-1996 and 1997-2015. SMB components include runoff (RU), total precipitation (PR), total melt (ME) and refreezing (RF).

| Mean | Units | SMB | RU | PR | ME | RF |
|-----------|--------------------------|---------------|-------------|--------------|-------------|-------------|
| 1958-1996 | Gt yr ⁻¹ | 378.6 ± 52.5 | 324.9 | 746.3 | 556.4 | 238.3 |
| 1997-2015 | Gt yr ⁻¹ | 255.0 ± 52.5 | 453.6 | 752.1 | 728.9 | 285.5 |
| 1958-1996 | mm w.e. yr ⁻¹ | 193 ± 27 | 165 | 380 | 283 | 121 |
| 1997-2015 | mm w.e. yr ⁻¹ | 130 ± 27 | 231 | 383 | 371 | 145 |
| Trend | Units | SMB | RU | PR | ME | RF |
| 1958-1996 | Gt yr ⁻² | 1.11 ± 1.62 | 0.19 ± 0.90 | 1.36 ± 1.08 | 1.26 ± 1.12 | 1.09 ± 0.39 |
| 1997-2015 | Gt yr ⁻² | -10.41 ± 4.02 | 6.86 ± 3.69 | -3.49 ± 2.57 | 8.77 ± 5.40 | 1.83 ± 2.41 |

Table 4.2: GrIS SMB average and trends. GrIS-integrated annual mean cumulative SMB components (top) and trends (bottom) for the periods 1958-1996 and 1997-2015. SMB components include runoff (RU), total precipitation (PR), total melt (ME) and refreezing (RF).

| Gt yr ⁻¹ | 1971-09 ^{1*} | 1993-09 ^{1*} | 2003-08 ^{2*} | 2003-09 ^{2*} | 2005-09 ^{3*} |
|---------------------|-----------------------|-----------------------|-----------------------|-----------------------|-----------------------|
| Recent studies | -21 ± 10 | -37 ± 10 | -41 ± 17 | -38 ± 7 | -56 ± 10 |
| Current study | -17 ± 16 | -30 ± 16 | -40 ± 16 | -40 ± 16 | -39 ± 16 |

Table 4.3: GICs mass loss estimates. Annual mean mass loss estimated for different periods and derived from previous studies (top, 1* Marzeion et al., 2012; 2* Bolch et al., 2013; 3* Gardner et al. 2013) and the downscaled data set v1.0 (bottom). Uncertainties in the downscaled data set are obtained by integrating the SMB mean bias (see Section 4.5.10) over the GICs area.

4.5 Methods

4.5.1 Regional climate model

Output of the Regional Atmospheric Climate Model (RACMO2.3) is used as input for the downscaling procedure [Noël et al., 2015, 2016]. RACMO2.3 combines the atmospheric dynamics from the High Resolution Limited Area Model (HIRLAM, Undèn et al. [2002]) and the physics from the European Centre for Medium-range Weather Forecasts Integrated Forecast System [ECMWF-IFS, 2008]. The polar version of RACMO2.3 is developed by the Institute for Marine and Atmospheric Research Utrecht University (IMAU), to simulate the evolution of surface mass balance (SMB) over ice sheets and surrounding smaller glacierized regions. Polar RACMO2.3 incorporates a multi-layer snow module to simulate firn compaction, meltwater retention and percolation, refreezing and runoff [Ettema et al., 2010b]. In RACMO2.3, the excess energy available at the surface, resulting from closure of the surface energy budget, is used to melt snow and ice. Liquid water from melt and rain percolates through the firn column, and is either held as irreducible water or refreezes, progressively reducing pore space from bottom to top layers until the entire firn column turns into ice (900 kg m^{-3}) and no additional water can be stored. At this point, any additional water is assumed to run off. The model also includes a snow albedo scheme using prognostic snow grain size [Kuipers Munneke et al., 2011]; a drifting snow routine accounting for sublimation and snow erosion [Lenaerts et al., 2012a]. For the contemporary Arctic simulation, RACMO2.3 was run at 11 km and forced on a 6-hourly basis by ERA-40 [Uppala et al., 2005] (1958-1978) and ERA-Interim [Dee et al., 2011] (1979-2015) re-analyses. The ice mask and topography at 11 km are based on a 5 km Greenland DEM [Bamber et al., 2001]. For more information about RACMO2.3, recent updates and evaluation, the reader is referred to Van Meijgaard et al. [2008]; Van Wessem et al. [2014a]; Noël et al. [2015].

4.5.2 Topography and ice mask

We used a down-sampled version of the Greenland Ice Mapping Project (GIMP) Digital Elevation Model (DEM) [Howat et al., 2014] to downscale the output of RACMO2.3 to a 1 km topography and ice mask (Figs. 4.8a and b), obtained by averaging the original GIMP DEM at 90 m resolution. To distinguish between the ice sheet, including glaciers strongly connected to the ice sheet (corresponding to connectivity level CL2 in Rastner et al. [2012]), and GICs that are physically or dynamically separated from the ice sheet (respectively CL0 and CL1 in Rastner et al. [2012]), we used the Programme for Monitoring of the Greenland Ice Sheet (PROMICE) ice classes projected on the 1 km GIMP ice mask (Fig. 4.8b). In addition, floating glacier tongues were eliminated using a 1 km ice grounding line [Enderlin et al., 2014]. This results in a GICs area of $\sim 81,400 \text{ km}^2$, $\sim 8\%$ less than previous estimates [Citterio and Ahlstrøm, 2013], owing to unresolved small glaciers in the original GIMP DEM at 90 m [Howat et al., 2014].

4.5.3 Bare ice albedo

To correct for the systematic bare ice albedo overestimation of RACMO2.3 in low-lying glaciated regions at 11 km, we used a 1 km version of the 500 m MODerate-resolution Imaging Spectroradiometer

(MODIS) 16-day Albedo product (MCD43A3). Bare ice albedo is defined as the average of the 5% lowest surface albedos recorded for 2000-2015. At 1 km, bare ice albedo values range from 0.15 for dark ice surfaces at the ablation zone edges and local glacier tongues, to 0.55 under persistent snow cover in the accumulation zone [Noël et al., 2016] (Fig. 4.8c). In RACMO2.3, bare ice albedo is prescribed from a similar 11 km product (2001-2010) with a lower threshold of 0.30 [Noël et al., 2015]. A value of 0.47 is assigned to glaciated pixels showing no valid MODIS estimate.

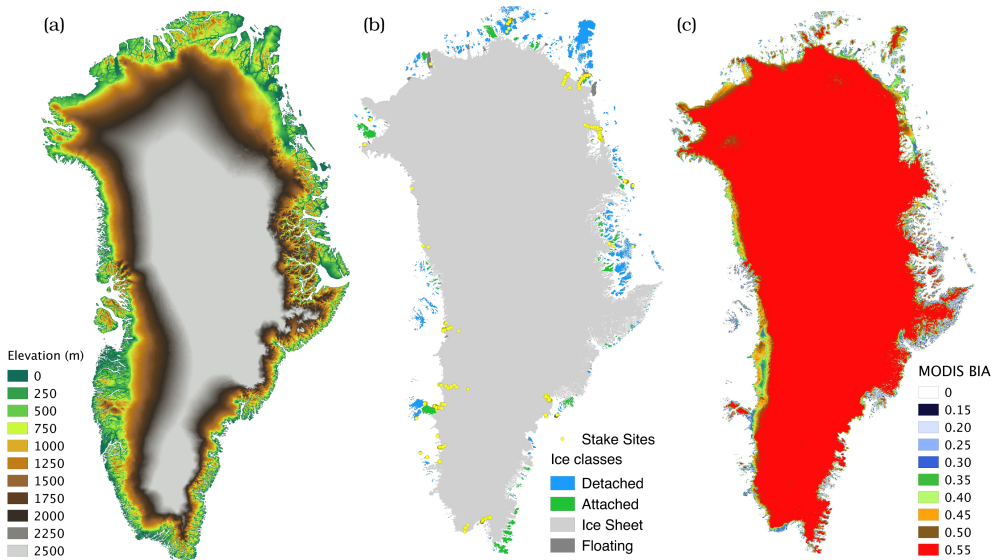


Figure 4.8: High-resolution Greenland surface properties. *a) Elevation (m) derived from the GIMP DEM at 1 km; b) PROMICE ice mask showing the contiguous ice sheet (light grey), GICs attached to the ice sheet but not dynamically connected (green), physically detached GICs (blue) and floating glacier tongues (dark grey); c) MODIS bare ice albedo at 1 km (2000-2015). Stake sites used for SMB evaluation are displayed in yellow in b).*

4.5.4 In situ measurements

A total of 965 SMB measurements collected at 101 stake sites [Machguth et al., 2016b] was used to evaluate the downscaled GICs SMB product at 1 km. These records were combined with another 1073 observations from 230 sites on the GrIS (yellow dots in Fig. 4.1a) to adjust runoff and melt in the downscaling procedure. The ablation data set [Machguth et al., 2016b] was compiled as part of the Programme for Monitoring of the Greenland Ice Sheet [Van As et al., 2011] (PROMICE). For consistency, we only selected data with a temporal overlap with RACMO2.3 (1958-2015), and rejected sites with a > 100 m height difference relative to the GIMP DEM at 1 km. To compare downscaled and observed SMB (Fig. 4.1b), we selected the grid cell with the smallest elevation bias among the closest pixel and its eight neighbours.

4.5.5 Remote sensing

Elevation changes for 2003-2009 and 2010-2014 were derived from ICESat and CryoSat-2 measurements, following the methods of Gardner et al. [2013]; Wouters et al. [2015]. For ICESat, observations were grouped every 700 m along repeated ground tracks, whereas for CryoSat-2, neighbouring observations are collected within 1 km of each individual echo location. To these clusters of elevation observations, a model is fitted to estimate the local surface topography and elevation rate at the central point, where outliers are removed in an iterative procedure. For full details, we refer the reader to Wouters et al. [2015]. After estimating the local topography and elevation rate for the ICESat and CryoSat-2 periods, local elevation anomalies at the echo locations can be estimated by adding back the constant elevation rate of the fitted model to the residuals. These anomalies are subsequently used to compute monthly volume anomalies for selected regions. We do so by parameterising the elevation anomalies as a function of absolute elevation using a third-order polynomial. The resulting fit is then used to derive regional volume anomalies within 100 m elevation intervals, by multiplying the polynomial value at each interval's midpoint with the total glaciated area within this elevation bin [Moholdt et al., 2010]. We perform the polynomial fit for nine regions individually [Gardner et al., 2013] and sum the results to obtain the GICs volume anomaly. Finally, volume anomalies are converted to mass anomalies by assuming a constant density profile, using the density of ice below the equilibrium line altitude (ELA), and a density of $600 \pm 250 \text{ kg m}^{-3}$ above the ELA. Figure 4.2 shows the cumulative GICs mass change; using cumulative values suppresses noise in the ICESat and CryoSat-2 time series.

4.5.6 Downscaling procedure

The daily, 1 km SMB product is statistically downscaled from the output of RACMO2.3 at 11 km resolution (1958-2015) to the 1 km GIMP topography and ice mask (Figs. 4.8a and b), using elevation dependence. Elevation correction is only applied to SMB components showing a significant correlation with height: runoff (RU), melt (ME) and sublimation (SU) [Noël et al., 2016]; total precipitation (P_{tot}), i.e. rainfall (RA) and snowfall (SF), and snowdrift erosion (ER) are bi-linearly interpolated to the 1 km ice mask, without elevation correction. Daily SMB is then reconstructed as:

$$SMB = P_{\text{tot}} - RU - SU - ER \quad (4.1)$$

4.5.7 Elevation dependence

Daily regression parameters are calculated for the dependence of modelled SMB components on the 11 km RACMO2.3 topography. A local regression slope, $b_{11\text{km}}$ (mm w.e. per m, Fig. 4.9), is estimated for each glaciated 11 km pixel using at least five adjacent ice-covered pixels. By applying the obtained $b_{11\text{km}}$ to the current pixel, the SMB component is approximated at mean sea level, $a_{11\text{km}}$ (mm w.e., Fig. 4.9). To fully cover the GrIS and detached GICs, the latter regression parameters are extrapolated outwards by averaging $b_{11\text{km}}$ from at least three glaciated pixels. An estimate of $a_{1\text{km}}$ and $b_{1\text{km}}$ is then obtained by interpolating bi-linearly the 11 km regression parameters to the 1 km ice mask.

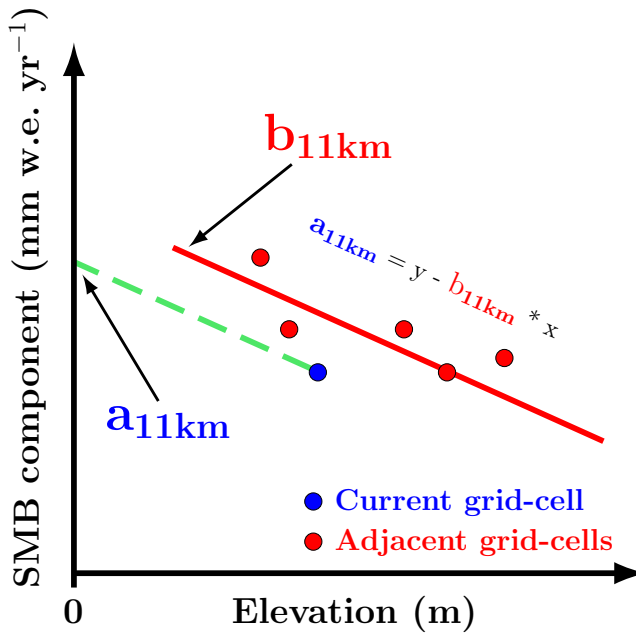


Figure 4.9: Elevation-dependent downscaling procedure. b_{11km} and a_{11km} are respectively the daily local estimates of the SMB components regression to elevation and the SMB components value at mean sea level obtained on the RACMO2.3 grid at 11 km. The red line corresponds to the regression (b_{11km}) calculated using the current grid cell (blue dot) and the adjacent ones (red dots). The dashed green line applies the regression slope to the current grid cell to estimate a_{11km} (from Noël et al., 2016).

Runoff, melt and sublimation ($X_{v0.2}$) are calculated using a linear function of the high-resolution topography (h_{1km}) as:

$$X_{v0.2} = a_{1km} + b_{1km} \times h_{1km} \quad (4.2)$$

The downscaled product based on elevation dependence only is hereafter referred to as version v0.2.

4.5.8 Runoff and melt adjustments

To correct for bare ice albedo overestimation in RACMO2.3 at 11 km, melt and runoff (v0.2) are adjusted to account for additional ice melt (ME_{add}) observed in low-lying regions compared to the downscaled product v0.2.

$$ME_{add} = \Delta\alpha \times 0.5 \times \frac{SW_{direct\ 1km}}{L_f} \times (1 + \xi) \quad (4.3)$$

where ME_{add} (mm w.e. per day) is the additional amount of ice melt calculated at 1 km (Fig. 4.8c); $\Delta\alpha$ (dimensionless) is the difference between the averaged bare ice albedo retrieved from the set of

regression cells used to downscale runoff at 11 km and the MODIS albedo product at 1 km; $SW_{\text{direct } 1\text{km}}$ is the modelled daily cumulated downward shortwave radiation bi-linearly interpolated to 1 km; L_f is the latent heat of fusion ($3.337 \times 10^5 \text{ J kg}^{-1}$). To account for the slope of the glacier surface, the dimensionless correction factor for a tilted plane ξ is applied to the direct component of modelled downward shortwave radiation. This correction is required as RACMO2.3 models radiation assuming a horizontal surface. This factor ranges from 0 for north sloping glaciers to values larger than 1 for south oriented slopes.

A daily ratio Γ , between downscaled runoff and melt in v0.2, is applied to ME_{add} to calculate the additional runoff (RU_{add}).

$$RU_{\text{add}} = \Gamma \times ME_{\text{add}} \quad (4.4)$$

Assuming that the residual misfit between reconstructed and observed SMB (ΔSMB) for the different GICs ablation sites is ascribable to underestimated runoff in narrow ablation zones, RU_{add} is then scaled by a factor f_{scale} (0.682), obtained by computing a least-squares fit minimising ΔSMB using both GICs and GrIS ablation measurements. The justification for including GrIS observations is that GICs SMB is not independent of the GrIS as the regression parameters were extrapolated from the ice sheet margins onto the GICs. The fact that $f_{\text{scale}} < 1$ indicates a slight overestimation of the melt adjustment calculated in Eq. (3), which could be due to uncertainties in clouds [Van Tricht et al., 2016] and/or ice albedo underestimation at the ice caps margins.

$$f_{\text{scale}} = \frac{\sum \Delta\text{SMB} \times RU_{\text{add}}}{\sum (RU_{\text{add}})^2} \quad (4.5)$$

The adjusted amount of runoff ($RU_{v1.0}$) is obtained by adding RU_{add} to the downscaled runoff ($RU_{v0.2}$):

$$RU_{v1.0} = RU_{v0.2} + f_{\text{scale}} \times RU_{\text{add}} \quad (4.6)$$

The corrected melt ($ME_{v1.0}$) is obtained in a similar fashion:

$$ME_{v1.0} = ME_{v0.2} + ME_{\text{add}} \quad (4.7)$$

Refreezing ($RF_{v1.0}$) is estimated as a residual between adjusted melt, runoff and rainfall:

$$RF_{v1.0} = RA + ME_{v1.0} - RU_{v1.0} \quad (4.8)$$

The downscaled SMB data set resulting from the combined elevation correction and runoff adjustment is referred to as version v1.0.

4.5.9 Precipitation correction

To eliminate the systematic negative SMB bias of RACMO2.3 in Greenland's accumulation zones [Noël et al., 2016] (-37.5 mm w.e. yr^{-1}), daily precipitation totals from v0.2 were adjusted in regions presenting a positive annual cumulative SMB in v1.0:

$$PR_{v1.0} = PR_{v0.2} \times \left(1 + \frac{\sigma_{SMB}}{PR_{v0.2}^a} \right) \quad (4.9)$$

where $PR_{v1.0}$ is the daily adjusted total precipitation v1.0, $PR_{v0.2}$ is the daily bi-linearly interpolated total precipitation v0.2, $PR_{v0.2}^a$ is the annual cumulative bi-linearly interpolated total precipitation v0.2 and σ_{SMB} is the accumulation zone SMB bias in the downscaled product v1.0.

4.5.10 Product uncertainty

Assuming that the remaining discrepancies in Fig. 4.1b consist of a systematic bias due to model uncertainty, combined with additional random scatter, attributed to observations, a product uncertainty can be obtained by integrating the average accumulation and ablation zone biases and adding them as if they were independent. To that end, SMB measurements (Fig. 4.1b) were binned in 500 mm w.e. bins for which the mean bias was estimated, i.e. modelled minus measured SMB. The average uncertainty that results is 247 mm w.e. for the ablation zones (8 bins) and 135 mm w.e. for the accumulation zones (6 bins). The product SMB uncertainty of 15.7 Gt yr^{-1} ($\sim 40\%$) is obtained by summing the mean ablation bias integrated over the GICs ablation zones ($45,600$ km²) and the mean accumulation bias over the whole GICs area ($81,400$ km²), to account for a potential precipitation bias in the ablation zones.

$$Uncertainty = \sqrt{(bias_{ablation} \times area_{ablation})^2 + (bias_{accumulation} \times area_{GICs})^2} \quad (4.10)$$

Average biases for the GrIS accumulation (22 mm w.e.) and ablation zones (170 mm w.e.) have been calculated in a similar fashion and provided a product SMB uncertainty of 52.5 Gt yr^{-1} ($\sim 20\%$). These calculations were repeated for 250 mm w.e. SMB bins, which yielded similar results.

4.5.11 Breakpoint analysis

We applied the segmented regression method of Muggeo [2003] to retrieve breakpoints, i.e. structural changes, in the GICs-integrated refreezing time series. To detect a break-point, the technique fits a regression function, consisting of segments with different slopes, to the studied data set. The algorithm calculates multiple continuous regressions before and after the break-points and determines an optimised solution. A confidence interval can be estimated for the resulting break-point by using the 95% Wald-based statistics. In this study, we used the segmented regression method to identify a tipping point in the GICs refreezing capacity at 1997 ± 5 years.

4.6 Supplementary Discussion

We select five GICs regions (black boxes in Fig. 4.1) to highlight the downscaled SMB data set and demonstrate its ability to resolve realistic patterns over small glaciers. Figure 4.10 shows Landsat satellite imagery for four of these regions, with superimposed downscaled 1958-2015 average total precipitation (solid and liquid), runoff and SMB (v1.0).

Mittivakkat (region 1; 65.69°N, 37.77°W; Fig. 4.1 and Fig. 4.10a) is a small glacier in southeast Greenland. This region experiences relatively large precipitation (~ 1600 mm w.e. yr^{-1}) combined with pronounced summer runoff (~ 2000 mm w.e. yr^{-1}). The downscaled SMB shows realistic gradients (Fig. 4.1). Figures 4.1 and 4.10b show two ice caps in southwest Greenland, Sukkertoppen and Amitsuloq (region 2; 66.20°N, 52.10°W). These ice caps have well-defined accumulation zones owing to pronounced precipitation maxima in their interior and runoff being restricted to the margins. Interestingly, the area with large ablation in the southeastern corner of the downscaled product mirrors the region of dark bare ice exposed at the surface in the satellite image. Figures 4.10c and d show the Zackenberg (74.64°N, 21.45°W) and Qaanaaq regions (77.50°N, 69.17°W) in northeast and northwest Greenland, respectively (regions 3 and 4 in Fig. 4.1). Compared to southern Greenland, these regions are characterised by a relatively cold and dry climate resulting in less marginal runoff, narrowing the ablation zone. The modelled SMB profile for the southern slope of Qaanaaq ice cap shows a systematic positive bias of ~ 0.5 m w.e. (Fig. 4.1), potentially as a result of inaccurate representation of the narrow ablation zone.

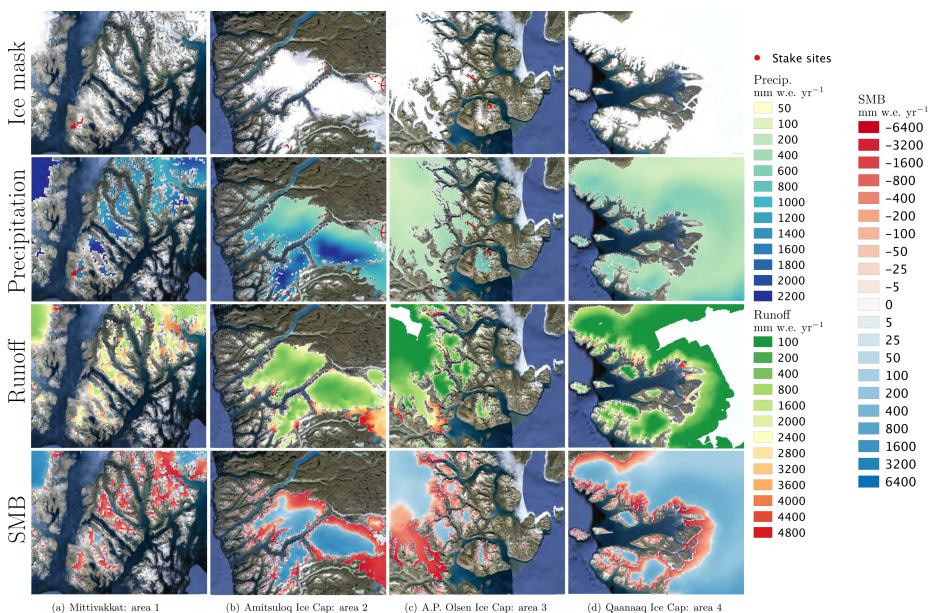


Figure 4.10: High-resolution GICs SMB patterns. Example maps of ice mask, downscaled total precipitation (solid and liquid), runoff and reconstructed SMB v1.0 in a) Mittivakkat region (black box 1 in Fig. 4.1), b) Amitsuloq and Sukkertoppen ice caps (black box 2), c) Zackenberg region (black box 3) and d) Qaanaaq ice caps (black box 4). Red dots locate the selected stake transects shown in Fig. 4.1.

Six decades of glacial mass loss in the Canadian Arctic Archipelago

Summary

The Canadian Arctic Archipelago (CAA) comprises multiple small glaciers and ice caps mostly concentrated on Ellesmere and Baffin Islands in the northern (NCAA) and southern parts (SCAA) of the archipelago, respectively. Because these glaciers are small and show complex geometries, current regional climate models, using 5 to 20 km horizontal resolution, do not properly resolve surface mass balance (SMB) patterns. Here, we present a 58-year (1958-2015) reconstruction of daily SMB of the CAA, statistically downscaled to 1 km from the output of the regional climate model RACMO2.3 at 11 km. By correcting for biases in elevation and ice albedo, the downscaling method significantly improves runoff estimates over narrow outlet glaciers and isolated ice fields. Since the last two decades, NCAA and SCAA glaciers have experienced warmer conditions (+1.1°C) resulting in continued mass loss of $28.2 \pm 11.5 \text{ Gt yr}^{-1}$ and $22.0 \pm 4.5 \text{ Gt yr}^{-1}$ respectively, almost tripling (11.9 Gt yr^{-1}) and doubling (11.9 Gt yr^{-1}) the pre-1996 average. While the interior of NCAA ice caps can still buffer most of the additional melt, the lack of a perennial firn area over low-lying SCAA glaciers caused uninterrupted mass loss since the 1980s. In the absence of significant refreezing capacity, this indicates inevitable disappearance of these highly sensitive glaciers.

This chapter is based on: B. Noël et al. (2017b), Six decades of glacial mass loss in the Canadian Arctic Archipelago, *Journal of Geophysical Research Earth Surface*, in review, 2017b

5.1 Introduction

The Canadian Arctic Archipelago (CAA) is home to one of the world's largest glaciated areas ($\sim 148,000 \text{ km}^2$) comprising $\sim 14\%$ of earth's total ice-covered area outside the ice sheets of Greenland and Antarctica [Sharp et al., 2011b]. Most glaciers and ice caps can be found on Ellesmere, Devon, Axel Heiberg and Meighen Islands forming the northern archipelago (NCAA; $\sim 106,000 \text{ km}^2$) and on Baffin-Bylot Islands located further south (SCAA; $\sim 42,000 \text{ km}^2$) (see inset in Fig. 5.1). The NCAA encompasses small ice caps feeding marine-terminating glaciers and flowing into narrow fjords. Van Wychen [2012, 2016] estimated the NCAA glacial discharge at $2.2 \pm 0.7 \text{ Gt yr}^{-1}$, with small temporal variability. In a recent study, Millan et al. [2017] showed that NCAA ice discharge decreased from $4.5 \pm 0.5 \text{ Gt yr}^{-1}$ in 1991 to $3.5 \pm 0.5 \text{ Gt yr}^{-1}$ in 2000, with no significant change afterwards. In contrast, the SCAA includes Bylot, Barnes and Penny ice caps, that are flanked by a network of small ice fields and disconnected grounded glaciers, contributing little to glacial discharge ($\sim 0.06 \text{ Gt yr}^{-1}$, Van Wychen et al. [2015]).

Recent satellite gravimetry (GRACE) and altimetry (ICESat) measurements [Gardner et al., 2013] revealed that over the period 2003-2009 NCAA and SCAA lost mass at a rate of $33 \pm 4 \text{ Gt yr}^{-1}$ and $27 \pm 4 \text{ Gt yr}^{-1}$, respectively. Under a moderate warming scenario (RCP 4.5), CAA glaciers could lose $\sim 18\%$ of their volume by the end of the 21st Century, yielding $0.35 \pm 0.24 \text{ mm yr}^{-1}$ of sea level rise [Lenaerts et al., 2013].

To date, the horizontal resolution used in regional climate models, typically 5 to 20 km, remains insufficient to accurately resolve the complex topography of the CAA's small ice bodies. As a consequence, modelled surface mass balance (SMB) components, notably surface melt and runoff, are affected by significant biases in elevation, hypsometry and ice albedo [Noël et al., 2016, 2017a]. Lenaerts et al. [2013] evaluated the output of the regional climate model RACMO2.1 at 11 km (1960-2011) against point SMB and near-surface temperature measurements collected in the NCAA [Gardner et al., 2011]. SMB components were corrected for a hypsometry bias, i.e. an overestimation of glacierized area below 1000 m in the RACMO2.1 ice mask. The remaining discrepancies were attributed to model elevation bias and local meteorological processes unresolved in RACMO2.1 [Lenaerts et al., 2013]. Gardner et al. [2011] used a Positive Degree-Days (PDD) SMB model presented in Gardner and Sharp [2009] to reconstruct daily NCAA SMB for the period 1949-2009 at a resolution of 500 m. The PDD model was forced by National Center for Environmental Prediction / National Center for Atmospheric Research (NCEP/NCAR) Reanalysis 1. The PDD model was bias-corrected using lapse rate estimates derived from local precipitation and temperature measurements. The PDD model successfully reproduced the recent mass loss in NCAA, but the paucity of in situ observations precluded estimation of contemporary SMB changes in SCAA [Gardner et al., 2011].

Here, we present a daily, 1 km data set of SMB components covering both NCAA and SCAA for the period 1958-2015 (Fig. 5.1). RACMO2.3 SMB components are statistically downscaled from the original model resolution of 11 km to 1 km. The downscaling procedure corrects for biases in elevation and ice albedo using a digital elevation model (DEM), glacier outlines and ice albedo product at 1 km resolution. The method resolves all SMB components, i.e. total precipitation (PR), total melt (ME), runoff (RU), refreezing (RF), sublimation (SU) and drifting snow erosion (ER), at high spatial (1 km) and temporal (daily) resolution. Previously, it has been successfully applied to the Greenland ice sheet and surrounding glaciers and ice caps [Noël et al., 2016, 2017a].

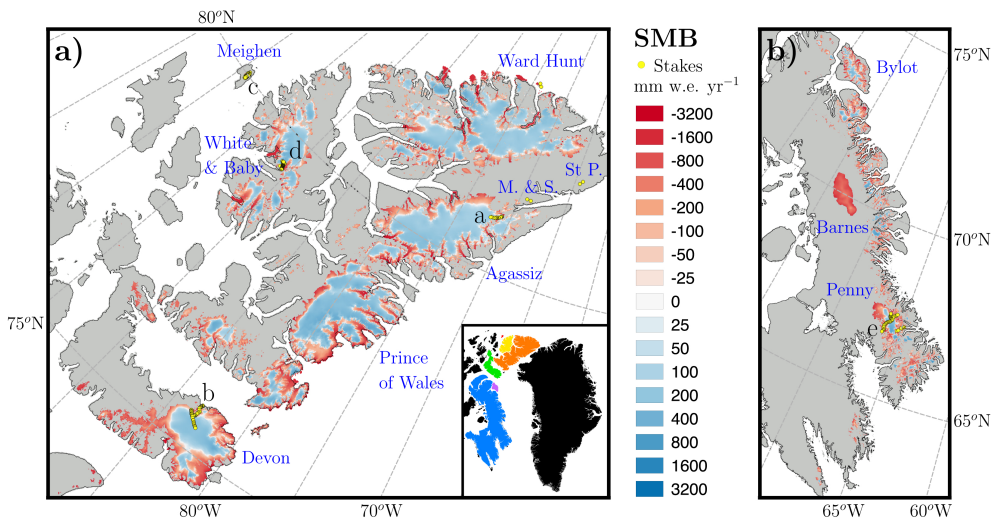


Figure 5.1: Average SMB of a) NCAA and b) SCAA for the period 1958-2015. SMB observations used for evaluation and calibration are displayed as yellow dots. Letters refer to the five transects showed in Figs. 5.6a-e. The maps show the location and name of NCAA and SCAA ice caps. The inset locates the ice-covered CAA islands relative to Greenland: Ellesmere (orange), Axel Heiberg (yellow), Meighen (red), Devon (green), Baffin (blue) and Bylot (purple).

Section 5.2 briefly describes the regional climate model RACMO2.3, the 1 km DEM, glacier outlines and ice albedo products used to downscale the SMB components, and in situ SMB measurements used for evaluation. The downscaling procedure, product evaluation and resulting uncertainties are discussed in Section 5.3. Sections 5.4 and 5.5 describe the contemporary climate of CAA glaciers and the recent changes. A more detailed analysis of mass loss acceleration over one NCAA and the three major SCAA ice caps is provided in Section 5.6. Section 5.7 discusses the remaining limitations of the downscaling procedure, followed by conclusions in Section 5.8.

5.2 Model and data

Methods closely follow Noël et al. [2016, 2017a], who applied the downscaling technique to the Greenland ice sheet and peripheral glaciers and ice caps.

5.2.1 The regional climate model RACMO2.3

The Regional Atmospheric Climate Model (RACMO2.3; Van Meijgaard et al. [2008], Noël et al. [2015]) combines the physics and dynamics from the European Center for Medium-Range Weather Forecasts-Integrated Forecast System (ECMWF-IFS; White [2001]) and the High Resolution Limited Area Model (HIRLAM; Undén et al. [2002]). To simulate the climate of polar regions, RACMO2.3 incorporates a multi-level snow module, accounting for melt, runoff, percolation and refreezing [Ettema et al., 2010b]. The model also includes a prognostic snow grain size albedo scheme [Kuipers Munneke et al., 2011] and a routine calculating drifting snow sublimation and erosion [Lenaerts et al., 2012a]. In this study, RACMO2.3 is forced by 6-hourly data from ERA-40 (1958-1978; Uppala et al. [2005]) and ERA-Interim re-analyses (1979-2015; Dee et al. [2011]). The integration domain includes Greenland, Svalbard, Iceland and the Canadian Arctic at a horizontal resolution of 11 km. Topography and ice mask of the Canadian Arctic are derived from the GTOPO30 data set at 30" [Gesch and Larson, 1998] and the Global Land Cover Characteristics (GLCC; ECMWF-IFS [2008]) at 1 km resolution, respectively. Bare ice albedo is prescribed from MODIS surface albedo, averaged for the period 2001-2010 [Van Angelen et al., 2012; Noël et al., 2015].

5.2.2 DEM, glacier outlines and ice albedo

The downscaling method uses high-resolution fields of elevation, ice mask and ice albedo to correct for RACMO2.3 biases. CAA topography and glacier outlines are down-sampled to 1 km using the Canadian Digital Elevation Model (CDEM; Government of Canada Natural Resources Canada Map Information Branch [2016]) at 0.75" (~20 m; Fig. 5.2a) and the Randolph Glacier Inventory 5.0 (RGI; Pfeffer et al. [2014]). Bare ice albedo is obtained by averaging the 5% lowest surface albedo measurements from the 500 m MODerate-resolution Imaging Spectroradiometer (MODIS) 16-day albedo product (MCD43A3) for the period 2000-2015. Ice albedo ranges from 0.15 over dark low-lying glaciers to 0.55 for bright ice located under the perennial firn layer in the CAA accumulation zones (Fig. 5.2b).

5.2.3 In situ SMB measurements

For evaluation and calibration, we use 4356 SMB measurements (yellow dots in Fig. 5.1) collected in NCAA (198 sites; Gardner et al. [2011]) and in SCAA (39 sites; N. Schaffer, personal communication). In NCAA, observations are retrieved from transects on four ice caps, namely Agassiz, Devon, Meighen and White glacier (a-d in Fig. 5.1a) and four smaller ice fields, i.e. Baby, Murray & Simmons and St Patrick. All measurements in SCAA are concentrated on Penny ice cap (e in Fig. 5.1b). Measurements span the period 1959-2010 and 2006-2014 in NCAA and SCAA, respectively. Observations from eight sites with a >100 m height difference relative to the 1 km CDEM elevation were rejected.

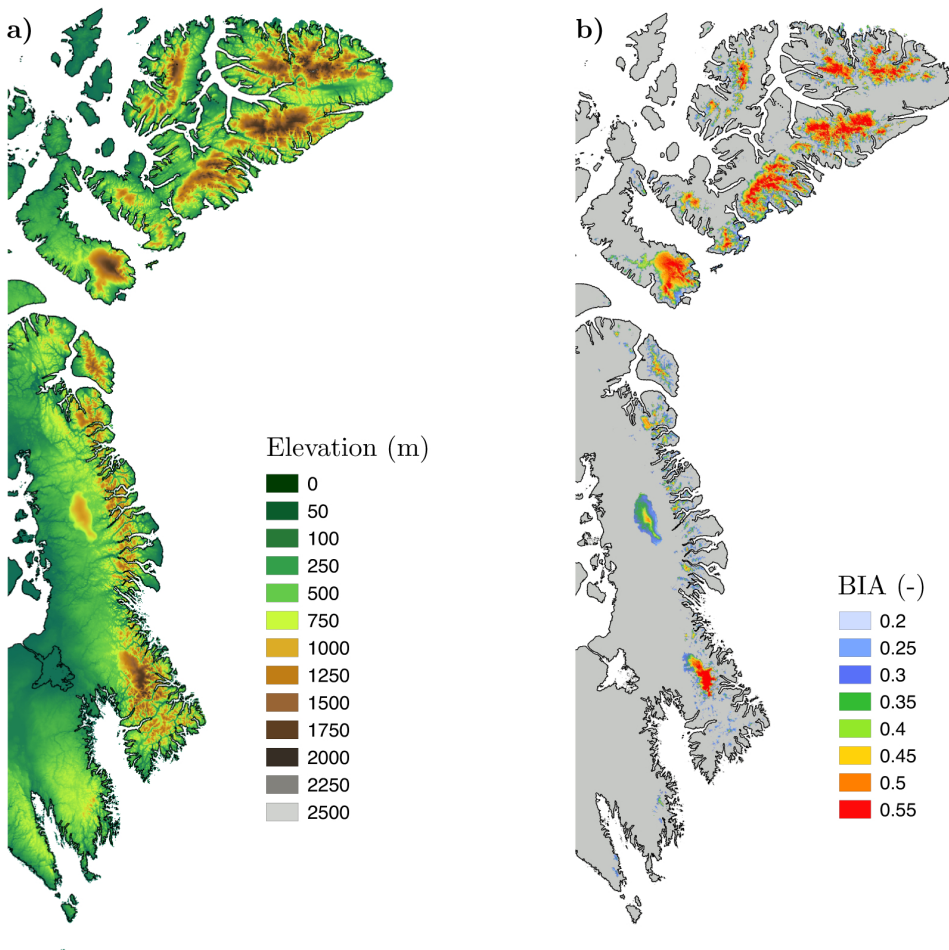


Figure 5.2: a) CAA topography at 1 km derived from CDEM and b) MODIS bare ice albedo at 1 km averaged over 2000-2015. In Fig. 2b, the tundra region is displayed in grey.

5.3 Methods

5.3.1 Downscaling procedure

The downscaling method, described in Noël et al. [2016], is applied to CAA glaciers with adjusted settings. Combining elevation and ice albedo corrections, the output of RACMO2.3 is statistically downscaled to 1 km using the topography and glacier outlines from CDEM (Fig. 5.2a) and RGI (yellow in Fig. 5.4c), and the 1 km bare ice albedo product from MODIS (Fig. 5.2b). A significant correlation to altitude is essential to correct SMB components for elevation bias, for which runoff (RU), melt (ME), and sublimation (SU) qualify (Figs. 5.3a-c). Snow drift erosion (ER, not shown) and total precipitation (PR), including solid and liquid precipitation, and snowfall (SF) show no systematic correlation with elevation (Figs. 5.3d and e), and are simply bi-linearly interpolated to the 1 km glacier outlines, without correcting for elevation. The daily 1 km climatic mass balance [Cogley et al., 2011], hereafter referred to as SMB, is reconstructed as:

$$SMB = PR - RU - SU - ER \quad (5.1)$$

Contrary to Noël et al. [2016], no additional correction is applied to total precipitation as no systematic SMB bias relative to in situ measurements could be identified in the accumulation zones, where SMB is primarily governed by precipitation (see Section 5.3.2). However, to better partition total precipitation into snowfall and rainfall, we use the fraction of snowfall on total precipitation (SF_{frac}) which shows a strong positive correlation with altitude on ice-covered regions (yellow line in Fig. 5.3f), indicating that solid precipitation prevails in the ice caps' interior. Statistically downscaling SF_{frac} on a daily basis over land ice allows to estimate corrected snowfall and calculate rainfall (RA) as a residual:

$$SF = PR \times SF_{\text{frac}} \quad (5.2)$$

$$RA = PR \times (1 - SF_{\text{frac}}) \quad (5.3)$$

Elevation correction

To correct for elevation bias in RACMO2.3 (Fig. 5.4a), daily regression parameters between SMB components and the model elevation are estimated for each glacierized grid cell at 11 km resolution. Using at least 5 adjacent pixels, a local regression slope ($b_{11 \text{ km}}$; mm w.e. per m) is calculated and applied to the current grid cell in order to estimate the SMB component at mean sea-level ($a_{11 \text{ km}}$; mm w.e.). Because CAA glaciers cover a relatively small area and show complex geometries, many ice bodies are not or not well resolved in RACMO2.3 (Fig. 5.4c). To address this issue, regression parameters are extrapolated outwards of the 11 km ice mask by averaging $b_{11 \text{ km}}$ from at least three adjacent glaciated pixels. These regression parameters are then bi-linearly interpolated to the 1 km glacier outlines to derive an estimate of $b_{1 \text{ km}}$ and $a_{1 \text{ km}}$.

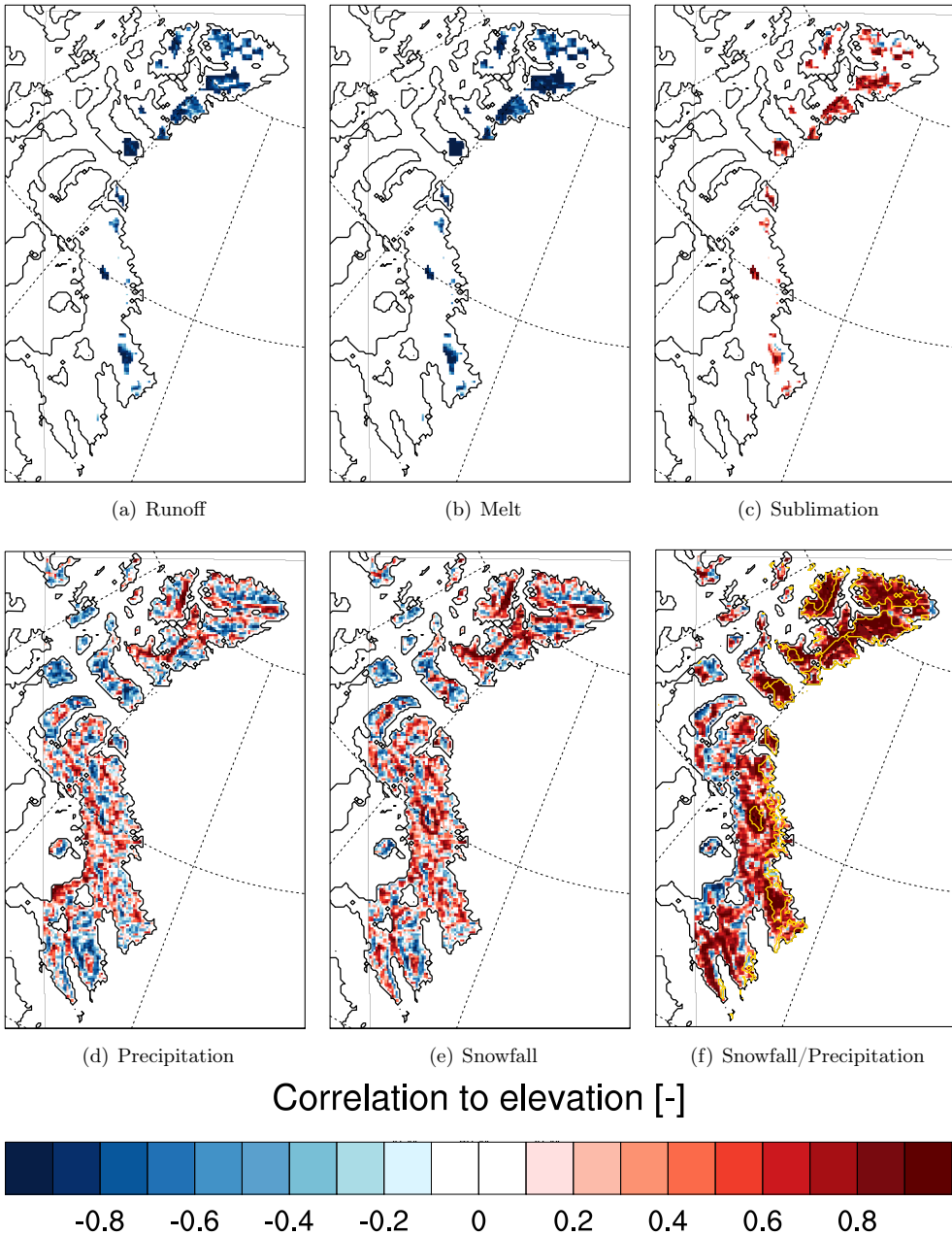


Figure 5.3: Correlation to elevation of annual mean a) runoff, b) melt and c) sublimation, d) total precipitation (solid and liquid), e) snowfall, f) snowfall on total precipitation fraction (SF_{frac}) modelled by RACMO2.3 and calculated on the 11 km grid for the period 1958-2015. The yellow line in Fig. 5.3f outlines the ice-covered areas.

Using the CDEM topography ($h_{1 \text{ km}}$), runoff, melt and sublimation ($X_{v0.2}$) are calculated at 1 km:

$$X_{v0.2} = a_{1 \text{ km}} + b_{1 \text{ km}} \times h_{1 \text{ km}} \quad (5.4)$$

The downscaled data set that only uses elevation correction is referred to as version v0.2.

Ice albedo correction

The albedo of exposed bare ice is generally overestimated in RACMO2.3 (Fig. 5.4b). Here, melt and runoff in v0.2 are adjusted to account for the resulting lack of ice melt (ME_{add}) in dark, low-lying regions.

$$ME_{\text{add}} = \Delta\alpha \times 0.5 \times \frac{SW_{\text{dir } 1 \text{ km}}}{L_f} \times (1 + \xi) \quad (5.5)$$

where ME_{add} (mm w.e. per day) is the additional amount of ice melt calculated at 1 km; $\Delta\alpha$ (-) is the difference between the averaged bare ice albedo retrieved from the set of regression cells used to downscale runoff at 11 km and the MODIS albedo product at 1 km; $SW_{\text{dir } 1 \text{ km}}$ is the modelled daily cumulated downward shortwave radiation bi-linearly interpolated to 1 km; L_f is the latent heat of fusion ($3.337 \times 10^5 \text{ J kg}^{-1}$). To account for the slope of the glacier surface, the dimensionless correction factor for a tilted plane ξ is applied to the direct component of modelled downward shortwave radiation. This correction is required as RACMO2.3 models radiation assuming a horizontal surface. This factor ranges from 0 for north sloping glaciers to values larger than 1 for south oriented slopes.

The ratio Γ between daily downscaled runoff and melt in v0.2 is applied to ME_{add} to calculate the additional runoff (RU_{add}).

$$RU_{\text{add}} = \Gamma \times ME_{\text{add}} \quad (5.6)$$

Assuming that the residual misfit between reconstructed and observed SMB (ΔSMB) for the different CAA ablation sites is attributable to underestimated runoff in narrow ablation zones, RU_{add} is then scaled by a factor f_{scale} (0.200), obtained by computing a least-squares fit minimising ΔSMB using both NCAA and SCAA ablation measurements. The fact that f_{scale} is much smaller than 1 suggests that the elevation bias in RACMO2.3 is the dominant factor contributing to ΔSMB , and that the ice albedo correction only slightly further improves the performance of the downscaled product (see Section 5.3.2). The low value is also attributed to limitations in the input data as well as in the downscaling procedure (see Section 5.7).

$$f_{\text{scale}} = \frac{\sum \Delta\text{SMB} \times RU_{\text{add}}}{\sum (RU_{\text{add}})^2} \quad (5.7)$$

The adjusted amount of runoff ($RU_{v1.0}$) is obtained by adding RU_{add} to the downscaled runoff ($RU_{v0.2}$):

$$RU_{v1.0} = RU_{v0.2} + f_{scale} \times RU_{add} \quad (5.8)$$

The corrected melt ($ME_{v1.0}$) is obtained in a similar fashion:

$$ME_{v1.0} = ME_{v0.2} + ME_{add} \quad (5.9)$$

Refreezing ($RF_{v1.0}$) is estimated as a residual between adjusted melt, runoff and rainfall:

$$RF_{v1.0} = RA + ME_{v1.0} - RU_{v1.0} \quad (5.10)$$

The downscaled product combining both elevation and ice albedo corrections is referred to as version v1.0.

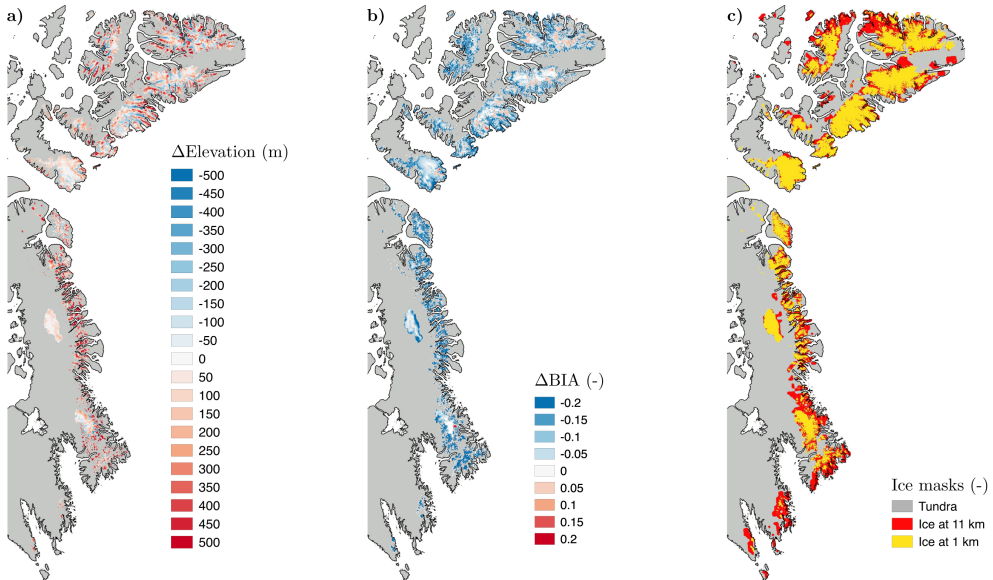


Figure 5.4: Difference in a) elevation, b) bare ice albedo and c) ice mask between the 1 km product and RACMO2.3 at 11 km. Negative values represent an overestimation in RACMO2.3.

5.3.2 Evaluation and uncertainties

In situ measurements

Figure 5.5 compares SMB derived from a) the original output of RACMO2.3 at 11 km, b) the down-scaled product version v0.2 and c) the corrected downscaled version v1.0 against 4356 stake measurements collected in NCAA (blue symbols) and SCAA (orange symbols). While RACMO2.3 performs reasonably well in capturing SMB in the high ablation and accumulation zones (SMB > -2 m w.e. in Fig. 5.5a), SMB is overestimated in low-lying regions by 200 mm w.e. on average and up to 4 m w.e. locally. Figure 5.5b shows that correcting for elevation bias in RACMO2.3 (Fig. 5.4a) significantly improves the agreement with observations: the mean SMB bias is reduced by almost a factor 2 and R^2 increases by 0.55. Applying the bare ice albedo bias correction (Fig. 5.4b) further improves the performance as indicated by smaller mean SMB bias (40 mm w.e.) and RMSE (380 mm w.e.) and a larger R^2 (0.74).

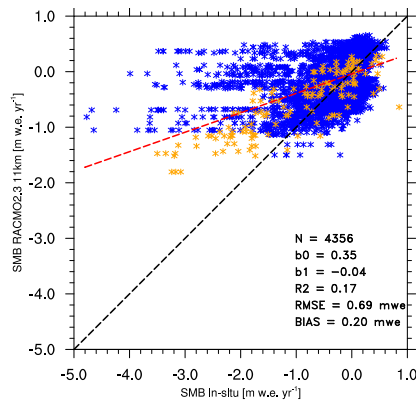
Figures 5.6a-e show observed (red) and downscaled (blue) SMB along five transects (a-e in Fig. 5.1). Agreement is generally good except for low-lying floating glacier tongues of Agassiz, Devon and Penny ice caps (< 300 m; Figs. 5.6a, b and e). The reason is that MODIS measures too low surface albedo over floating glacier tongues, as a result of mixing values of adjacent dark melt ponds with brighter dry ice [Noël et al., 2016]. Figure 5.6f shows the progressive performance improvements binned in 0.5 m w.e. SMB intervals. Clearly, the elevation correction in v0.2 dominates the improvements, reducing the RMSE by 53-68% in the ablation zones and by 47% in the accumulation zones, respectively. Relative to v0.2, the ice albedo correction in v1.0 reduces the RMSE by an additional 16% in the low ablation zone (SMB < -2 m w.e) and by 2-9% at higher elevations.

Product uncertainty

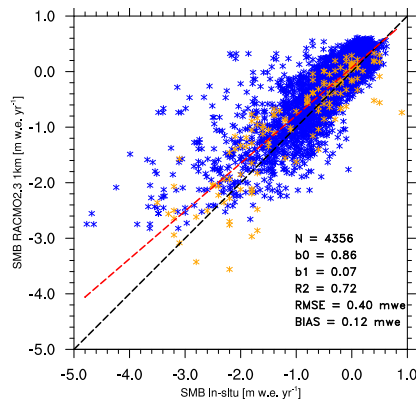
Following the method outlined in Noël et al. [2017a], a product uncertainty of 11.0 Gt yr^{-1} and 4.5 Gt yr^{-1} is obtained for SMB estimates of NCAA and SCAA, respectively. To obtain these, SMB measurements (yellow dots in Fig. 5.1) were binned in 250 mm w.e. intervals for which the mean bias was estimated, i.e. modelled minus measured SMB, resulting in 129 mm w.e. for the ablation zones (12 bins) and 162 mm w.e. for the accumulation zones (4 bins). SMB uncertainty is estimated for NCAA and SCAA individually (σ_{XCAA}) by summing the mean ablation bias integrated over their respective ablation zones area ($\sim 48,000 \text{ km}^2$ and $\sim 32,800 \text{ km}^2$) and the mean accumulation bias over the accumulation area of NCAA and SCAA ($\sim 56,400 \text{ km}^2$ and $\sim 10,400 \text{ km}^2$).

$$\sigma_{XCAA} = \sqrt{(\beta^{\text{abl.}} \times A_{XCAA}^{\text{abl.}})^2 + (\beta^{\text{acc.}} \times A_{XCAA}^{\text{acc.}})^2} \quad (5.11)$$

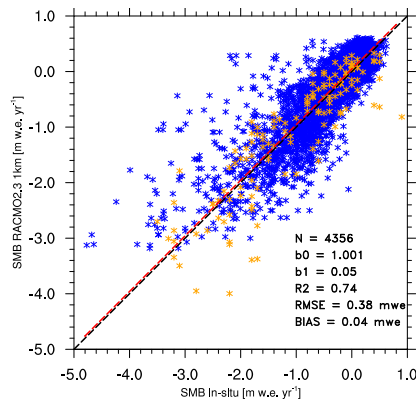
where $\beta^{\text{abl.}}$ and $\beta^{\text{acc.}}$ are the mean binned bias for the ablation and accumulation zones of CAA, $A_{XCAA}^{\text{abl.}}$ is the ablation zones area of NCAA or SCAA, and $A_{XCAA}^{\text{acc.}}$ is the accumulation zones area of NCAA or SCAA. The accumulation bias is assumed to be included in the ablation (SMB) bias, and therefore not spatially integrated over the ablation zone, as in Noël et al. [2017a].



(a) Modelled SMB at 11 km



(b) Downscaled SMB at 1 km version v0.2



(c) Corrected SMB at 1 km version v1.0

Figure 5.5: Comparison of SMB observations collected at 237 sites with a) modelled SMB from RACMO2.3 at 11 km; b) downscaled SMB at 1 km (v0.2) and c) corrected downscaled SMB at 1 km (v1.0). The orange symbols correspond to in situ measurements from Penny ice cap (39 sites, SCAA). The red dashed lines represent the regression including all measurements (NCAA and SCAA) using a perpendicular fit.

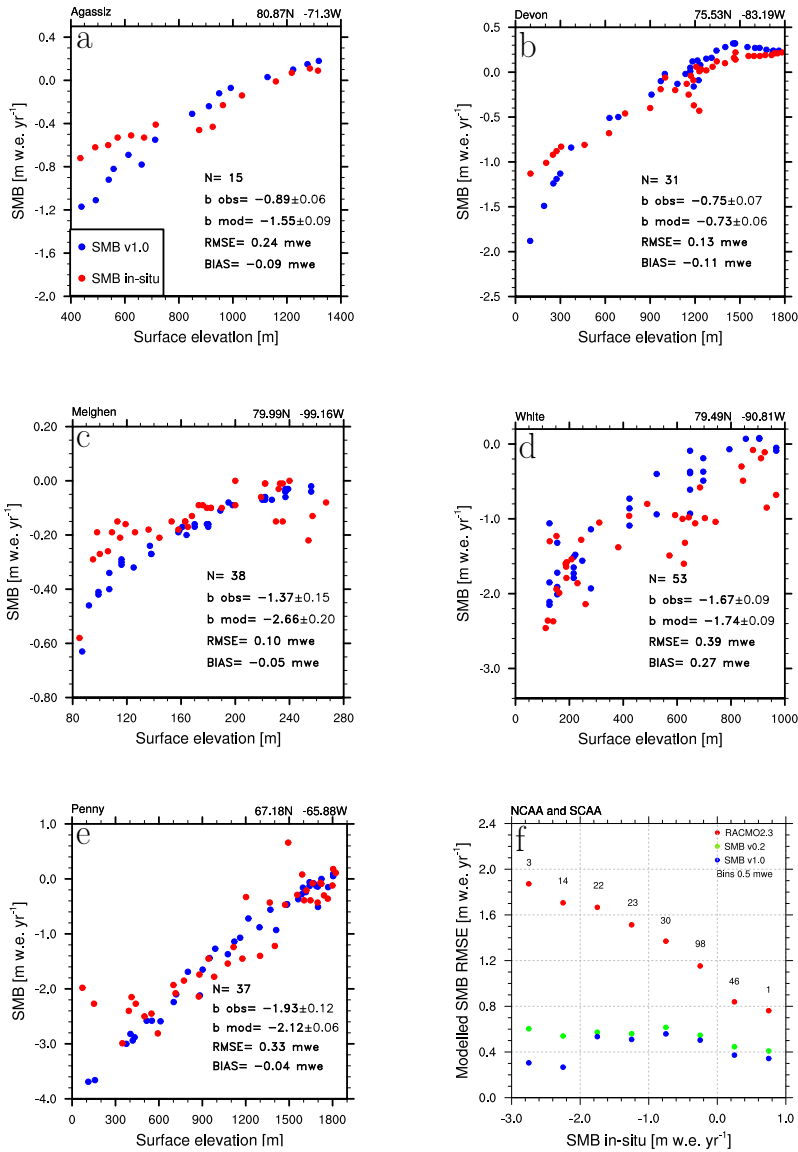


Figure 5.6: Observed (red dots) and downscaled (blue dots, v1.0) SMB for five transects located in NCAA (a-d) and SCAA (e). Name and locations of these transects (a-e in Fig. 1) are listed at the top of each graph. Graphs also list the number of sites used for each transect, linear SMB-to-elevation regression retrieved from observations (b obs) and downscaled (v1.0) data (b mod) in $\text{mm w.e. yr}^{-1} \text{m}^{-1}$, the RMSE and the mean bias. The SMB-to-elevation regressions were calculated by discarding observations below 300 m to exclude floating glacier tongues. Figure 5.6f shows annual mean modelled SMB RMSE (model vs. observations) of the 11 km SMB field in RACMO2.3 (red dots), the downscaled SMB data set v0.2 (green dots) and v1.0 (blue dots) as a function of observed SMB (237 observations). Modelled SMB is grouped in $0.5 \text{ m w.e. yr}^{-1}$ bins except for the first bin, which ranges from -4.0 to $-2.5 \text{ m w.e. yr}^{-1}$. Numbers indicate the number of observations used in each bin.

Remote sensing records

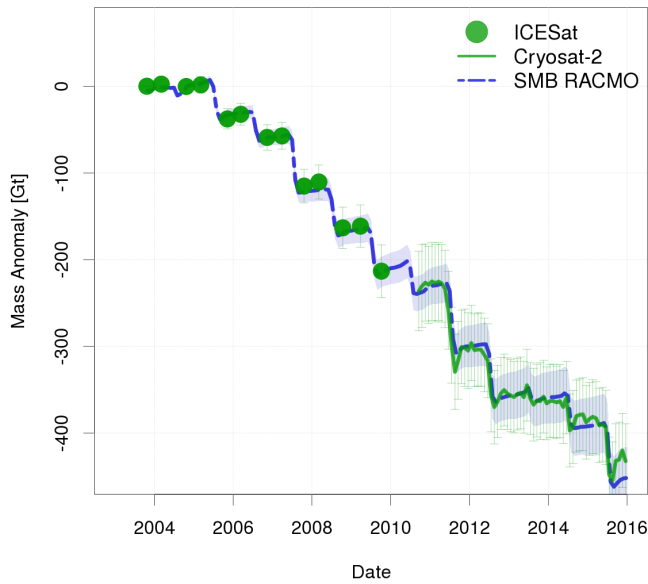
Elevation changes from ICESat (2003-2009) and CryoSat-2 (2010-2015) measurements were derived following Gardner et al. [2013] and Wouters et al. [2015]. For ICESat, observations were grouped every 700 m along repeated ground tracks, whereas for CryoSat-2, neighbouring observations are collected within 1 km of each individual echo location. To these clusters of elevation observations, a model is fitted to estimate the local surface topography and elevation rate at the central point, where outliers are removed in an iterative procedure. Local elevation anomalies at the echo locations are estimated by adding the constant elevation rate of a fitted model to the residuals. These anomalies are used to compute monthly volume anomalies for the NCAA and SCAA, respectively. Elevation anomalies are parameterised as a function of absolute elevation using a third-order polynomial. The resulting fit is used to derive regional volume anomalies within 100 m elevation intervals, by multiplying the polynomial value at each interval's midpoint with the total glaciated area within this elevation bin [Moholdt et al., 2010]. Finally, volume anomalies are converted to mass anomalies by assuming a constant density profile, using the density of ice below the equilibrium line altitude (ELA), and a density of $600 \pm 250 \text{ kg m}^{-3}$ above the ELA.

Figure 5.7 further evaluates the SMB product for NCAA and SCAA (dashed blue line) using independently derived mass changes from ICESat and CryoSat-2 altimetry measurements (green dots and line, respectively). The downscaled data set shows excellent agreement with the altimetry records. Both winter accumulation and summer ablation are accurately resolved. In addition, the SMB product falls well within ICESat/CryoSat-2 measurements uncertainty, although mass loss appears underestimated in summer 2015 for SCAA.

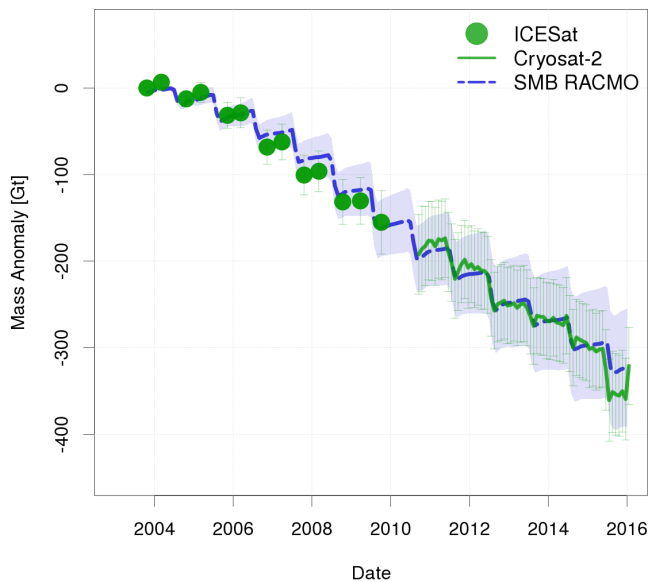
Gardner et al. [2011] estimated 2004-2009 mass loss from GRACE to be $39 \pm 9 \text{ Gt yr}^{-1}$ and $24 \pm 7 \text{ Gt yr}^{-1}$ for NCAA and SCAA, respectively. The downscaled SMB product shows good agreement with mass loss of $33.8 \pm 11.5 \text{ Gt yr}^{-1}$ for the NCAA, i.e. the sum of SMB ($30.3 \pm 11.0 \text{ Gt yr}^{-1}$) and solid ice discharge ($3.5 \pm 0.5 \text{ Gt yr}^{-1}$) [Millan et al., 2017], and $24 \pm 4.5 \text{ Gt yr}^{-1}$ for the SCAA, assuming negligible discharge ($\sim 0.06 \text{ Gt yr}^{-1}$) [Van Wychen et al., 2015]. These results are also in line with Gardner et al. [2011], who obtained a 2004-2009 mass loss of $-34 \pm 13 \text{ Gt yr}^{-1}$ for NCAA, using their PDD SMB model.

5.4 Contemporary climate and recent changes

Figure 5.8 shows time series of SMB components (1958-2015) for a) NCAA, b) SCAA and c) anomalies in annual mean 2-m temperature. Compared to Greenland glaciers and ice caps [Noël et al., 2017a], the climate of CAA ice masses is generally warmer and drier, with mean total precipitation of $\sim 340 \text{ mm w.e. yr}^{-1}$. The ice free tundra surrounding the small CAA glaciers (Fig. 5.1) creates warm summer conditions, resulting in high melt rates. In addition, the prevalent northwesterly winds advect dry air to CAA glaciers, resulting in relatively low precipitation [Lenaerts et al., 2013]. As a result, summer meltwater production systematically exceeds annual precipitation (Figs. 5.8a and b), indicating that refreezing of meltwater plays a key role in sustaining CAA ice masses. While total precipitation shows little temporal variability, meltwater production sharply peaks in warm years (Fig. 5.8c). In the mid-1990s, CAA ice masses experienced a significant near-surface warming ($+ 1.1^\circ\text{C}$), causing enhanced meltwater runoff in both NCAA and SCAA (Figs. 5.8a and b).

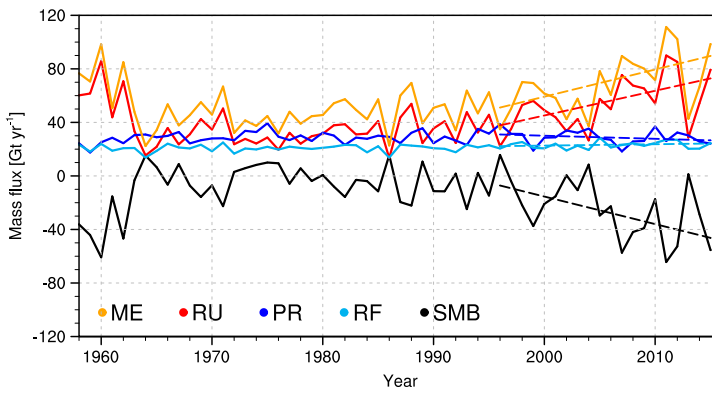


(a) NCAA mass anomaly

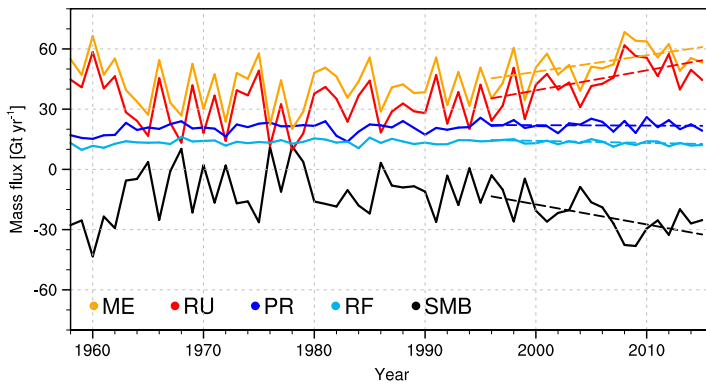


(b) SCAA mass anomaly

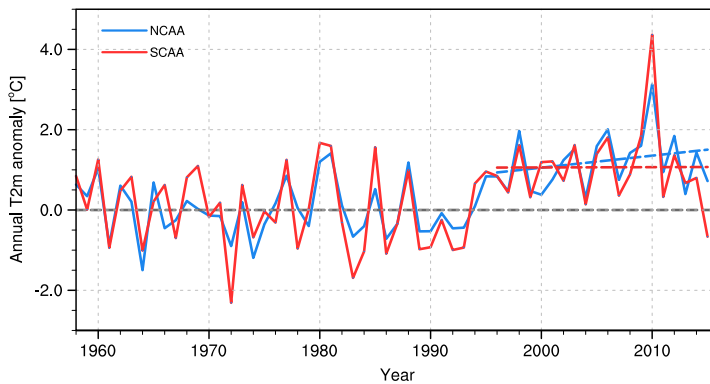
Figure 5.7: Comparison of a) NCAA, b) SCAA-integrated mass anomaly (2004-2015) derived from ICESat (green dots)/CryoSat-2 (green line) altimetry measurements with the downscaled SMB v1.0 (dashed blue line). The light blue envelope represents the estimated uncertainty of the downscaled SMB product. The green bars correspond to estimated uncertainties in ICESat/CryoSat-2 records.



(a) Northern Canadian Arctic Archipelago



(b) Southern Canadian Arctic Archipelago



(c) Near-surface temperature anomaly (1958-1995)

Figure 5.8: Time series of a) NCAA and b) SCAA (1958-2015) SMB components: melt (ME), runoff (RU), total precipitation (PR) and refreezing (RF). Figure 5.8c shows anomalies in annual mean 2-m temperature for NCAA (blue) and SCAA (red). Anomalies are calculated with respect to the period 1958-1995. Dashed lines show trends for the period 1996-2015.

5.4.1 Drivers of the recent warming

Changes in summer (June-July-August) upper atmosphere circulation control the recent CAA warming [Sharp et al., 2011a; Mortimer et al., 2016]. Figure 5.9a shows JJA 700 hPa air temperature from RACMO2 with superimposed wind speed and direction averaged for 1958-1995; changes after year 1996 (1996-2015 minus 1958-1995) are displayed in Fig. 5.9b. For 1958-1995, NCAA and SCAA experience advection of dry and cool polar air in summer (Fig. 5.9a). During the last two decades, anomalously high pressure persisted over Davis Strait along the southwestern coast of Greenland, favouring more frequent northward advection of warmer air by the prevalent westerly winds over the CAA (Fig. 5.9b). This caused successive record high summer temperatures in SCAA and NCAA, up to 1.8°C and 2.5°C warmer than the 1958-1995 mean (Fig. 5.9c). Since 1996, significant warming trends are found in SCAA ($+0.06 \pm 0.03 \text{ }^\circ\text{C yr}^{-1}$) and NCAA ($+0.10 \pm 0.04 \text{ }^\circ\text{C yr}^{-1}$). Sharp et al. [2011a] indicate that the recent increase in summer temperatures leads to early melting of the snow cover in CAA ablation zones, exposing bare ice for longer periods during the melt season and enhancing runoff.

Figure 5.9c reveals a significant anti-correlation between 2-m temperature in NCAA ($R^2 = 0.70$, p-value = $4.4 \cdot 10^{-6}$) and SCAA ($R^2 = 0.63$, p-value = $3.1 \cdot 10^{-5}$) and the North Atlantic Oscillation (NAO) index for the period 1996-2015 (<http://www.cpc.ncep.noaa.gov>). During 1996-2015, a negative NAO index prevailed in summer, i.e. anomalously high pressure over the North Atlantic, which may be linked to the sea ice retreat and the associated increase in sea surface temperature in Davis Strait [Overland and Wang, 2010; Jaiser et al., 2012; Noël et al., 2014]. Comparably negative summertime NAO values occurred in the period 1950-1960 (average NAO index -0.4), peaking in 1957 (-1.1) and in 1958 (-1.6, Fig. 5.9c). These early episodes of negative NAO showed CAA summer 2-m temperature anomalies (Fig. 5.9c) and mass loss (Figs. 5.8a and b) similar to 1996-2015. Early mass loss was also reported by Zdanowicz et al. [2012] who found ice layers formed in the late 1950s in firn cores drilled in the summit region of Penny ice cap.

5.4.2 Before the warming (1958-1995)

Prior to 1996, accumulation from precipitation accounts for 29 Gt yr⁻¹ and 20 Gt yr⁻¹ in NCAA and SCAA (Fig. 5.10c and Tables 1 and 2 for numbers in mm w.e. yr⁻¹). Meltwater production, i.e. 51 Gt yr⁻¹ in NCAA and 42 Gt yr⁻¹ in SCAA, exceeds precipitation by almost a factor of two, highlighting the importance of refreezing to sustain CAA glaciers. For NCAA, high melt rates are restricted to the marginal regions, whereas melt propagates higher up on SCAA glaciers due to their lower elevation and higher near-surface temperature (Figs. 5.10d and e). Unlike NCAA, runoff occurs over all but the very highest sectors of SCAA glaciers (Fig. 5.10b), indicating a longterm deterioration of the firn refreezing capacity (Fig. 5.10f). In SCAA, the firn only retains 32% (13.4 Gt yr⁻¹) of the total melt while the healthier firn area of NCAA ice caps buffers 41% of melt through refreezing (20.8 Gt yr⁻¹). As a result, prior to 1996 NCAA ice caps remained closer to balance ($-11.9 \pm 11.5 \text{ Gt yr}^{-1}$) than SCAA glaciers, which had already suffered significant mass losses ($11.9 \pm 4.5 \text{ Gt yr}^{-1}$) since the early 1980s. Such longterm mass loss in SCAA has previously been reported by Gardner et al. [2012], who estimated the mass loss for 1963-2006 to be $11 \pm 3 \text{ Gt yr}^{-1}$, using altimetry measurements and stereographic images; the downscaled product provides similar results with an average mass loss of $10.9 \pm 4.5 \text{ Gt yr}^{-1}$ for this period.

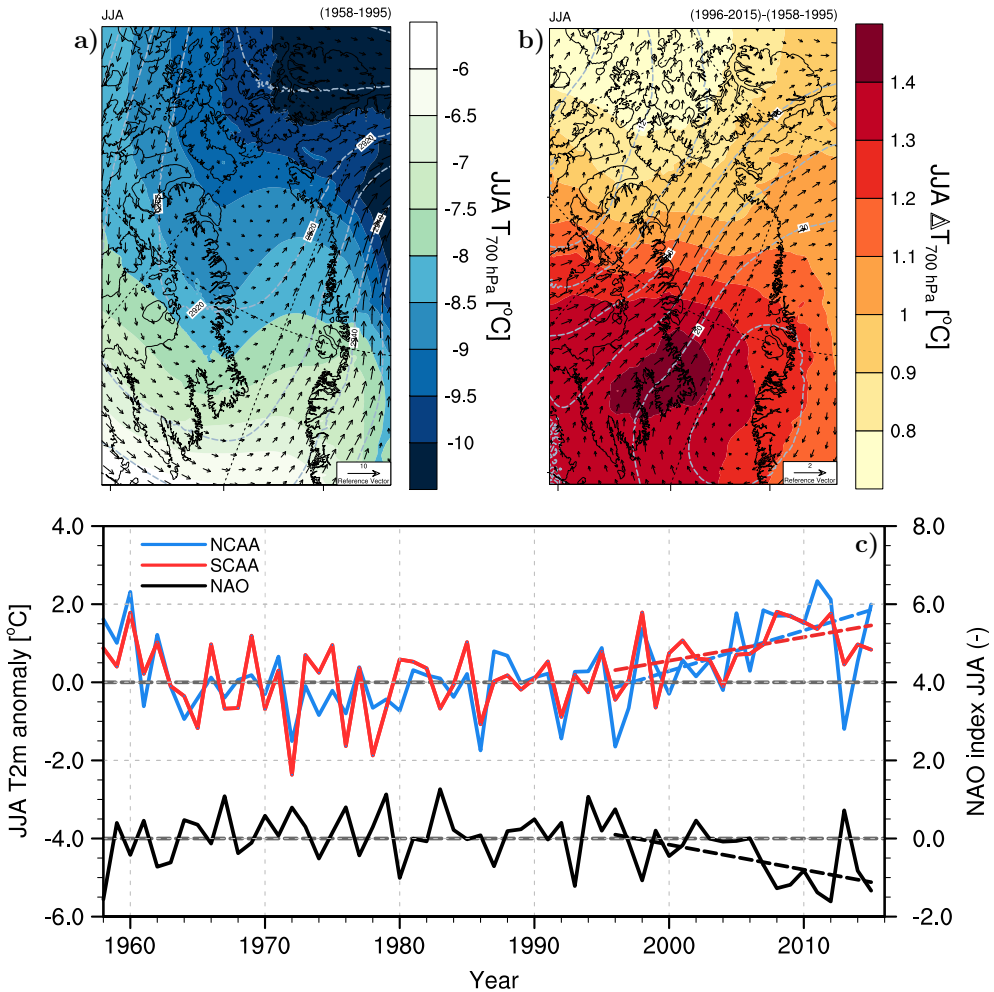


Figure 5.9: a) Average June-July-August (JJA) temperature at 700 hPa for 1958-1995 from RACMO2.3. Mean wind direction is displayed as black arrows with superimposed 700 hPa geopotential heights (m; dashed grey). Wind speed (m s^{-1}) can be estimated using the reference vector shown at the bottom right corner of the map. b) Changes in JJA mean temperature at 700 hPa (1996-2015 minus 1958-1995). Changes in mean wind speed and direction, and 700 hPa geopotential heights are also shown. c) Anomalies in JJA mean 2-m temperature for NCAA (blue) and SCAA (red), and JJA mean NAO index (black; <http://www.cpc.ncep.noaa.gov>). Anomalies are calculated with respect to the period 1958-1995. Dashed lines show trends for the period 1996-2015.

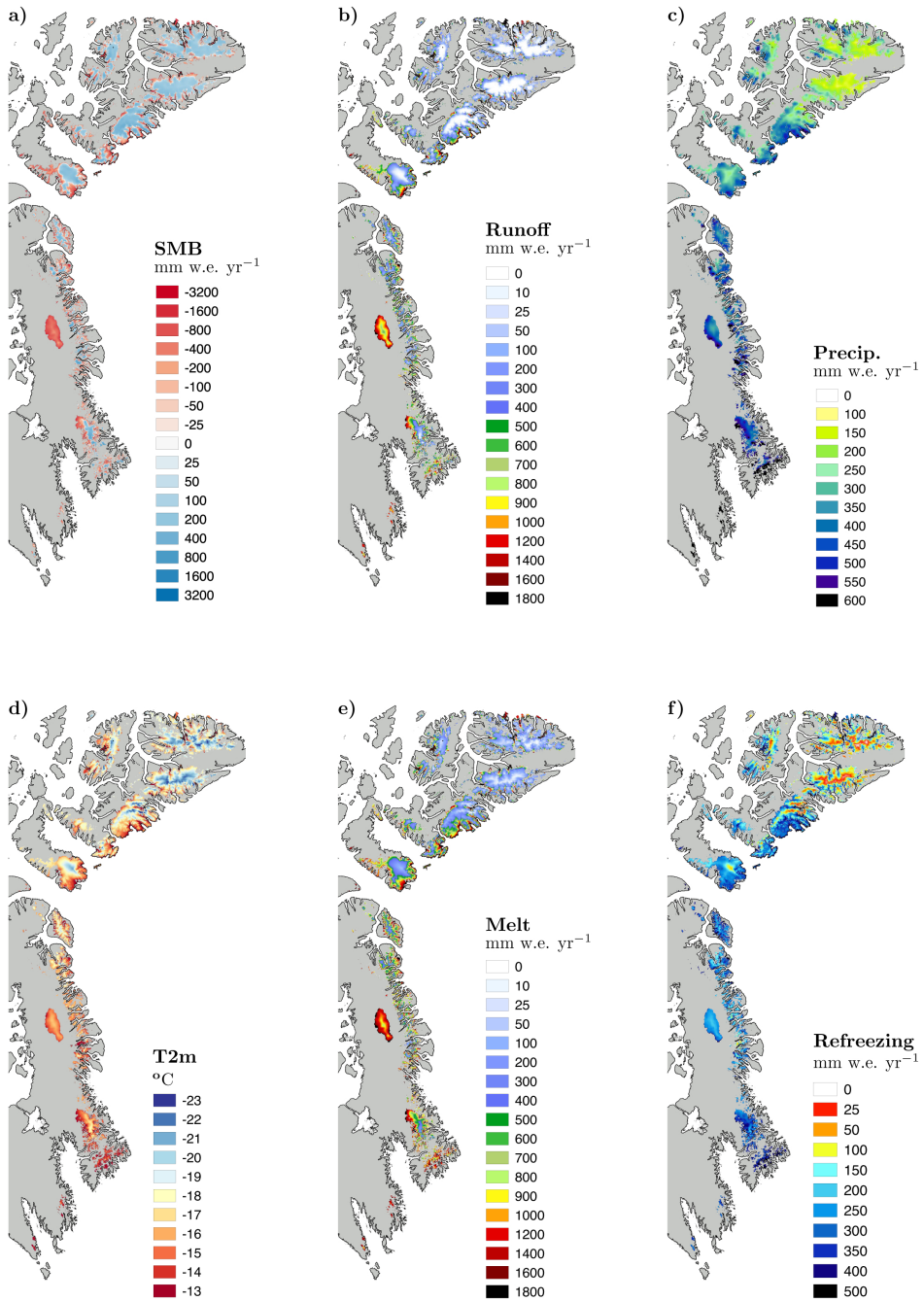


Figure 5.10: SMB components and mean 2-m temperature for 1958-1995. Tundra regions are displayed in light grey.

5.4.3 Mass loss acceleration (1996-2015)

During the last two decades, summer 2-m temperature increased by about 1.1°C (Figs. 5.8c and 5.9c), almost tripling and doubling the pre-1996 mass loss of NCAA ($28.2 \pm 11.5 \text{ Gt yr}^{-1}$) and SCAA ($22.0 \pm 4.5 \text{ Gt yr}^{-1}$) respectively. In NCAA, a combination of increased runoff ($+1.9 \text{ Gt yr}^{-2}$) and reduced precipitation (-0.2 Gt yr^{-2}) contribute to accelerated mass loss (2.1 Gt yr^{-2}) whereas SCAA mass loss acceleration (1.0 Gt yr^{-2}) is exclusively driven by enhanced runoff ($+1.0 \text{ Gt yr}^{-2}$; Tables 1 and 2). To investigate the spatial impact of the recent warming, Fig. 5.11 shows the changes in SMB components (1996-2015 minus 1958-1995). It also reveals a striking contrast: although SCAA experienced a smaller warming (Fig. 5.11d), the increase in melt is larger than in NCAA (Fig. 5.11e). In SCAA, decades of high melt rates have progressively depleted the firn pore space, reducing the ability to buffer the additional meltwater ($+0.8 \text{ Gt yr}^{-2}$) through refreezing (-0.1 Gt yr^{-2}). As a result, all elevations experience enhanced runoff (Fig. 5.11b). In contrast, the elevated firn layers of NCAA experience no additional runoff as enhanced melt (Fig. 5.11e) is partly compensated by increased refreezing (Fig. 5.11f). In SCAA, such mechanism is only found locally in the highest sectors of Bylot and Penny ice caps (Fig. 5.11f).

5.5 Changes in the firn structure

To highlight the latitudinal contrast in meltwater retention regimes, Fig. 5.12 shows scaled vertical profiles of SMB components integrated over elevation bins for individual NCAA and SCAA ice masses before (Figs. 5.12a and e) and after (Figs. 5.12b and f) 1996; the difference between the two periods (1996-2015 minus 1958-1995; Figs. 5.12c and g) and the hypsometry of NCAA and SCAA (Figs. 5.12d and h). Before 1996, NCAA ice caps are almost in balance with extensive accumulation zones above 0.5 of h_{max} , compensating for the mass lost in the ablation areas. In contrast, the ablation zone of SCAA glaciers already extended well above the peak in the hypsometry (0.5 of h_{max}), indicating continued mass loss at all elevations throughout the past six decades.

From 1996 onwards, the equilibrium line of NCAA moved upwards, from ~ 0.35 to ~ 0.5 of h_{max} , beyond the peak in the hypsometry (Fig. 5.12d). This means that only the most elevated firn zones of NCAA do not yet experience sustained mass loss, as increased meltwater is efficiently refrozen in available firn pore space, which mitigates the increase in runoff (Fig. 5.12c). In SCAA, ablation now affects all sectors of the glaciers (Fig. 5.12h). Decades of high meltwater production depleted pore space of the SCAA firn area, which is no longer able to buffer additional liquid water from enhanced melt and rain (Fig. 5.12g). Therefore, runoff increases ($+1.0 \text{ Gt yr}^{-2}$, Table 2) at a greater rate than meltwater production ($+0.8 \text{ Gt yr}^{-2}$, Table 2). As a result, under continuous warming, SCAA glaciers are expected to undergo sustained and irreversible mass loss in the next decades. This mechanism has already been observed on Devon ice cap [Bezeau et al., 2013; Gascon et al., 2013], the southernmost ice body of NCAA, and upon further warming will propagate to higher latitudes.

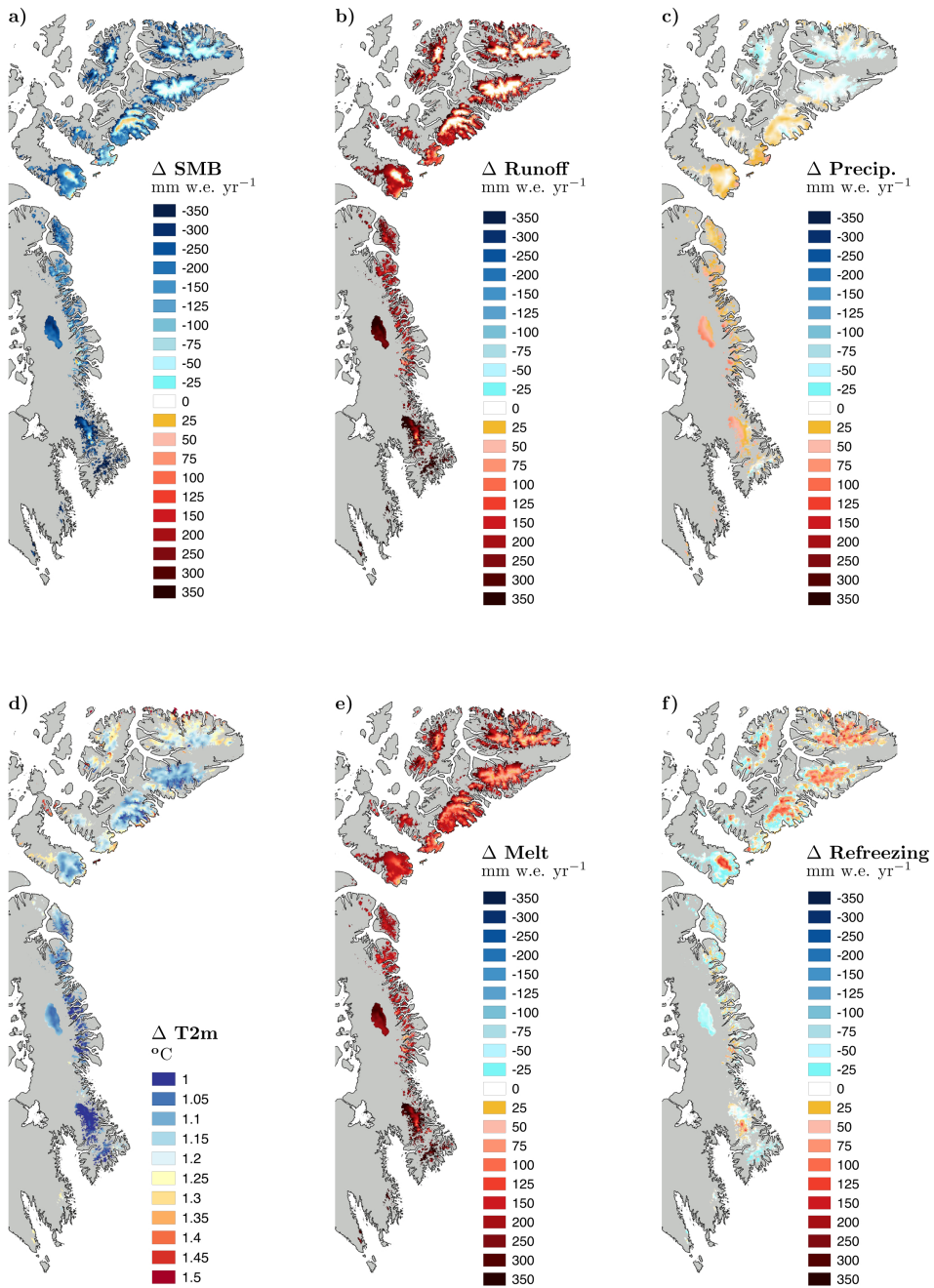


Figure 5.11: Changes in SMB components and mean 2-m temperature (1996-2015 minus 1958-1995). Tundra regions are displayed in light grey.

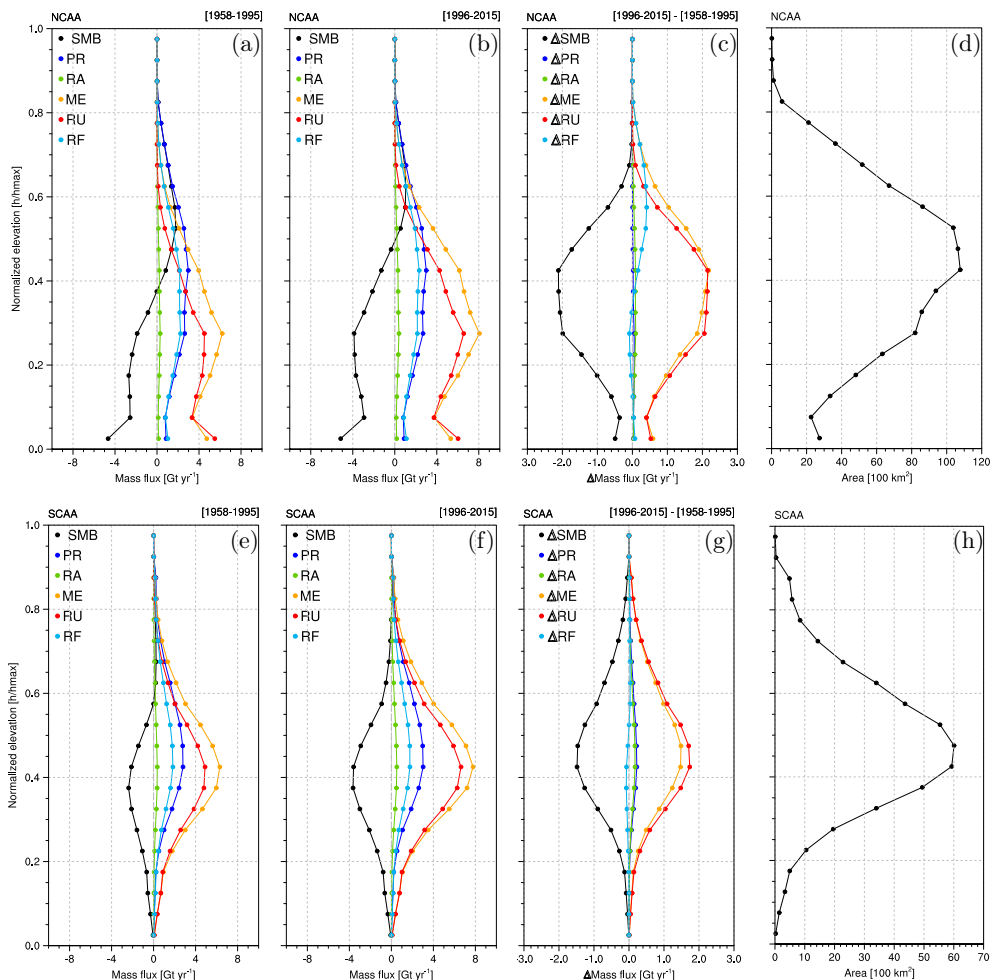


Figure 5.12: Vertical profiles of SMB components integrated over NCAA (upper row) and SCAA (lower row) elevation bins, scaled by the maximum height per region (h_{max}), for the period 1958-1995 (a and e), 1996-2015 (b and f) and the difference between the two periods (1996-2015 minus 1958-1995, c and g). SMB components are spatially integrated within normalised elevation bins (h/h_{max}) of magnitude 0.05. Figures 4 d) and h) show the scaled hypsometries, i.e. total area occupied by each elevation bin, for NCAA and SCAA, respectively. In NCAA and SCAA, h_{max} reaches 2350 m and 2080 m, respectively.

5.6 Six decades of mass loss in the Canadian Arctic Archipelago

Sections 5.6.1 to 5.6.4 focus on Agassiz ice cap (80N, 75W) located in the NCAA and the three major SCAA ice caps, Bylot Island ice cap (73N, 78.5W), Penny ice cap (67N, 66W) and Barnes ice cap (70N, 73.5W), respectively. Figures 5.13 to 5.16 show annual mean SMB for a) 1958-1995, b) 1996-2015; c) time series of annual cumulative SMB components (1958-2015); d) time series of summer (JJA) 2-m temperature; e) integrated SMB, snowfall-to-precipitation and refreezing-to-melt fractions as a function of JJA 2-m temperature anomaly relative to the 1958-1995 mean. In the following sections, we assume mass loss to equal SMB as solid ice discharge remains small for these ice caps [Van Wychen et al., 2015, 2016].

5.6.1 Agassiz ice cap

Agassiz ice cap measures $\sim 21,000 \text{ km}^2$ and is located to the north east of Ellesmere Island in the NCAA. The ice cap shows a longterm equilibrium line altitude at $\sim 1100 \text{ m a.s.l.}$, and its summit reaches $\sim 1980 \text{ m a.s.l.}$ [Gray et al., 2015]. Agassiz is drained by several marine-terminating glaciers covering roughly 40% of the ice cap area [Millan et al., 2017]. Williamson et al. [2008] and Van Wychen et al. [2016] estimated the mean solid ice discharge at $0.41 \pm 0.08 \text{ Gt yr}^{-1}$ for 1999-2002 and 0.12 ± 0.07 for 2000-2015, respectively. This is in line with Millan et al. [2017] who estimated a slowdown of ice discharge by 60% between the periods 1990-2010 ($0.28 \pm 0.05 \text{ Gt yr}^{-1}$) and 2010-2015 ($0.11 \pm 0.05 \text{ Gt yr}^{-1}$), with no significant change after 2000 at four major marine-terminating glaciers.

Owing to an extensive accumulation zone (Fig. 5.13a), Agassiz ice cap remained almost in balance before the recent warming in 1996 (Figs. 5.13c and d) with an average mass loss of $\sim 1.3 \text{ Gt yr}^{-1}$. Mass loss is restricted to narrow ablation zones and marine outlet glaciers, and is primarily driven by meltwater runoff (5.2 Gt yr^{-1}) that exceeds precipitation (4.0 Gt yr^{-1}). In this early period, 41% of surface melt (7.2 Gt yr^{-1}) is retained in the inland firn zone. After 1996, surface melt increased by 46% (10.6 Gt yr^{-1}) affecting not only the marginal ablation zones but also the highest sectors of the ice cap (Fig. 5.11e). In the elevated firn zone, this additional meltwater is efficiently buffered through enhanced refreezing (+18%; 0.5 Gt yr^{-1}). As a result, increased runoff (+57%; 3 Gt yr^{-1}) is restricted to marginal ablation zones which slightly propagated inland, more than tripling the pre-1996 mass loss (4.2 Gt yr^{-1}). Using repeat airborne laser altimetry records from 1995 and 2000, Abdalati et al. [2004] show an ice cap wide thinning of 0.07 m yr^{-1} , dominated by ice loss in marginal ablation zones with little changes in the ice cap interior. As a result, Agassiz ice cap has lost 2.0 Gt yr^{-1} of ice during the 1995-2000 period, similar to the downscaling method suggesting 2.1 Gt yr^{-1} .

Figure 5.13e shows that Agassiz ice cap has lost mass at an average rate of $2.8 \text{ Gt per } ^\circ\text{C}$ for 1958-2015 (black dashed line). To return to balance (SMB = 0), Agassiz would require a summer (JJA) cooling of $\sim 0.5^\circ\text{C}$ compared to pre-1996 mean 2-m temperature (-1.0°C , dashed grey line in Fig. 5.13d). Following a $\sim 3^\circ\text{C}$ summer warming relative to the 1958-1995 mean, a simultaneous snowfall decrease (10%) and higher melt production could reduce the firn refreezing capacity by a factor of 2, i.e. from 40% down to 20%, further decreasing SMB by 9 Gt yr^{-1} .

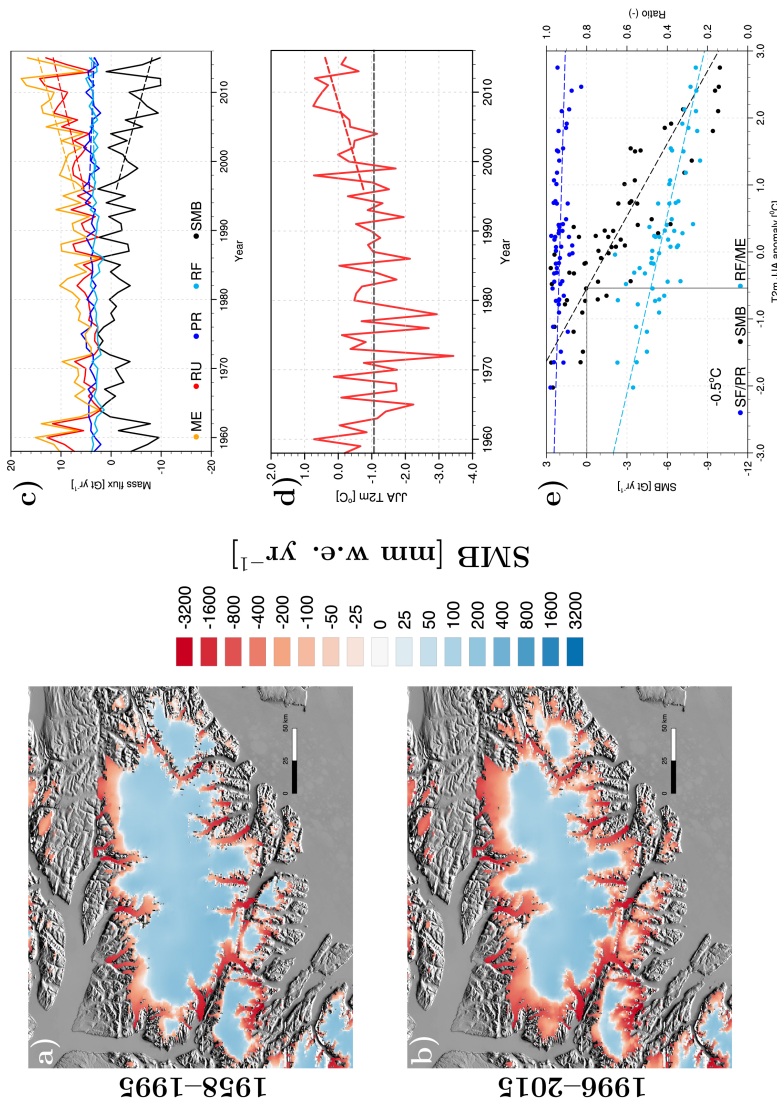


Figure 5.13: Maps of SMB at Agassiz ice cap averaged for periods a) 1958-1995 and b) 1996-2015. Time series of c) SMB components, i.e. melt (ME), runoff (RU), precipitation (PR) and refreezing (RF), and d) JJA 2-m temperature for 1958-2015, averaged over Agassiz ice cap. e) Annual SMB (black), snowfall-to-precipitation ratio (dark blue) and refreezing-to-melt ratio (light blue) as a function of the anomaly in mean JJA 2-m temperature, relative to the 1958-1995 mean (dashed grey line in Fig. 5.13d). The vertical grey line estimates the JJA 2-m temperature anomaly relative to 1958-1995 needed to return Agassiz ice cap to mass balance (SMB = 0).

5.6.2 Bylot Island

Bylot Island is the northernmost ice cap of SCAA, comprising a network of marginal surge-type glaciers [Van Wychen et al., 2015], with an ice thickness of up to 400 m [Van Wychen et al., 2016]. The ice cap covers $\sim 4900 \text{ km}^2$ and its summit elevation is $\sim 1680 \text{ m}$. Despite an extensive inland accumulation zone, Figs. 5.14a and c show that Bylot Island ice cap was already losing mass (1.0 Gt yr^{-1}) before the recent warming (Fig. 5.14d). Significant runoff from marginal glaciers (3.2 Gt yr^{-1}) exceeds the relatively low precipitation (2.2 Gt yr^{-1}). In the early period, Bylot Island showed a similar regime as NCAA ice caps have today, with $\sim 40\%$ of total melt (4.4 Gt yr^{-1}) refrozen in the inland firn. In the last two decades, enhanced melt depleted the available pore space, reducing the refreezing capacity of the firn from 40% to 30%, significantly increasing runoff (+41%; 4.5 Gt yr^{-1}). As a result, the accumulation zone withdrew to higher elevations (Fig. 5.14b) and the mass loss doubled (2.2 Gt yr^{-1}), indicating a recent acceleration. Mass loss measurements from combined stereographic images and satellite altimetry confirm that the average mass loss increased from 1.4 Gt yr^{-1} in 1979-2008 (SPOT) and 1980-2006 (ICESat) to 2.7 Gt yr^{-1} in 2003-2009 (ICESat, Gardner et al. [2012]), in line with 1.1 Gt yr^{-1} and 2.3 Gt yr^{-1} derived from the downscaled SMB product.

Over 1958-2015, Bylot ice cap lost 1.5 Gt of ice per $^{\circ}\text{C}$ warming on average (Fig. 5.14e) and a summer cooling of $\sim 0.7^{\circ}\text{C}$ relative to the average 2-m temperature of the last two decades (-1.2°C , Fig. 5.14d) would be required to bring the ice cap back in balance. Figure 5.14e also highlights an increase in liquid at the expense of solid precipitation, further deteriorating the buffer capacity of the firn layer. Extrapolating the regression in Fig. 5.14e suggests that Bylot Island's refreezing capacity is fully lost for summer temperatures $\sim 3^{\circ}\text{C}$ higher than the 1958-1995 average.

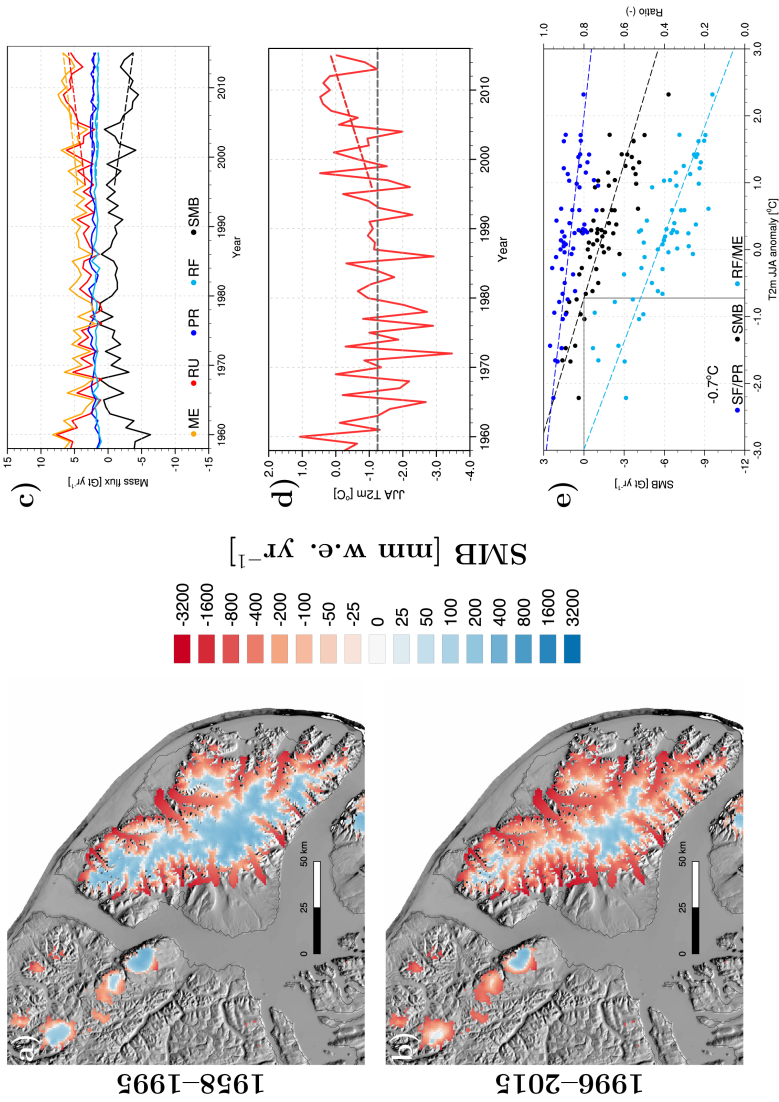


Figure 5.14: As Fig. 5.13 but for Bylot island.

5.6.3 Penny ice cap

Penny ice cap is a remnant of the Laurentide ice sheet, situated at the southern tip of Baffin Island [Zdanowicz et al., 2002]. It is composed of a large central ice mass ($\sim 6500 \text{ km}^2$) feeding several valley glaciers of which two are marine-terminating, i.e. Coronation Glacier in the east and an unnamed glacier in the north. Penny ice cap is the only southern ice body that has a sufficiently elevated interior (up to 1930 m) to enable the formation of a perennial firn zone (Fig. 5.15a) [Zdanowicz et al., 2012]. Satellite observations indicate that Penny ice cap has already been losing mass for several decades [Gardner et al., 2012], i.e. 1.5 Gt yr^{-1} for 1958-2006 (ICESat) and 1.1 Gt yr^{-1} for 1958-2009 (SPOT). This is in line with our results: 1.4 Gt yr^{-1} and 1.6 Gt yr^{-1} , respectively. Prior to the recent warming in 1996 (Fig. 5.15d), mass loss was mostly concentrated on marginal outlet glaciers and in the wide, gently sloping northwestern ablation zone (Fig. 5.15a). Mass loss (1.3 Gt yr^{-1}) resulted from runoff (4.2 Gt yr^{-1}) exceeding precipitation (3.0 Gt yr^{-1}), although 37% of total melt (5.2 Gt yr^{-1}) was refrozen in the snowpack (Fig. 5.15c). After 1996, ablation propagates further inland, restricting the accumulation zone to the highest sectors (Fig. 5.15b). Intensified melt (+33%; 7.8 Gt yr^{-1}) and reduced refreezing capacity (-8%; 28%) enhanced runoff by 50% (6.3 Gt yr^{-1}). As a result, the pre-1996 mass loss increased 2.5 fold (3.1 Gt yr^{-1}), signifying mass loss acceleration. Satellite measurements showing accelerated mass loss from 1.3 Gt yr^{-1} and 2.9 Gt yr^{-1} for 1995-2000 and 2000-2005 (ATM), and 3.3 Gt yr^{-1} in 2003-2009 (ICESat, Gardner et al. [2012]) are in line with our results: 1.6 Gt yr^{-1} , 2.4 Gt yr^{-1} and 3.3 Gt yr^{-1} for the three periods.

Similar to Bylot Island, Penny ice cap lost 1.7 Gt of ice per $^{\circ}\text{C}$ warming (Fig. 5.15e). Here, a summer cooling of $\sim 0.7^{\circ}\text{C}$ with respect to the average 1958-1995 near-surface temperature (-2.0°C) is needed to sustain the ice cap. In addition, Fig. 5.15e highlights the sensitivity of Penny ice cap to increased summer temperature; a summer warming of $\sim 3^{\circ}\text{C}$ leads to $\sim 20\%$ more liquid precipitation at the expense of snowfall, reducing the refreezing capacity of Penny's firn zone to about 10% and hence decreasing SMB by $\sim 6 \text{ Gt yr}^{-1}$. Similar to Bylot Island, Penny ice cap's refreezing capacity will inevitably collapse in a warming climate ($+4^{\circ}\text{C}$ relative to 1958-1995; Fig. 5.15e).

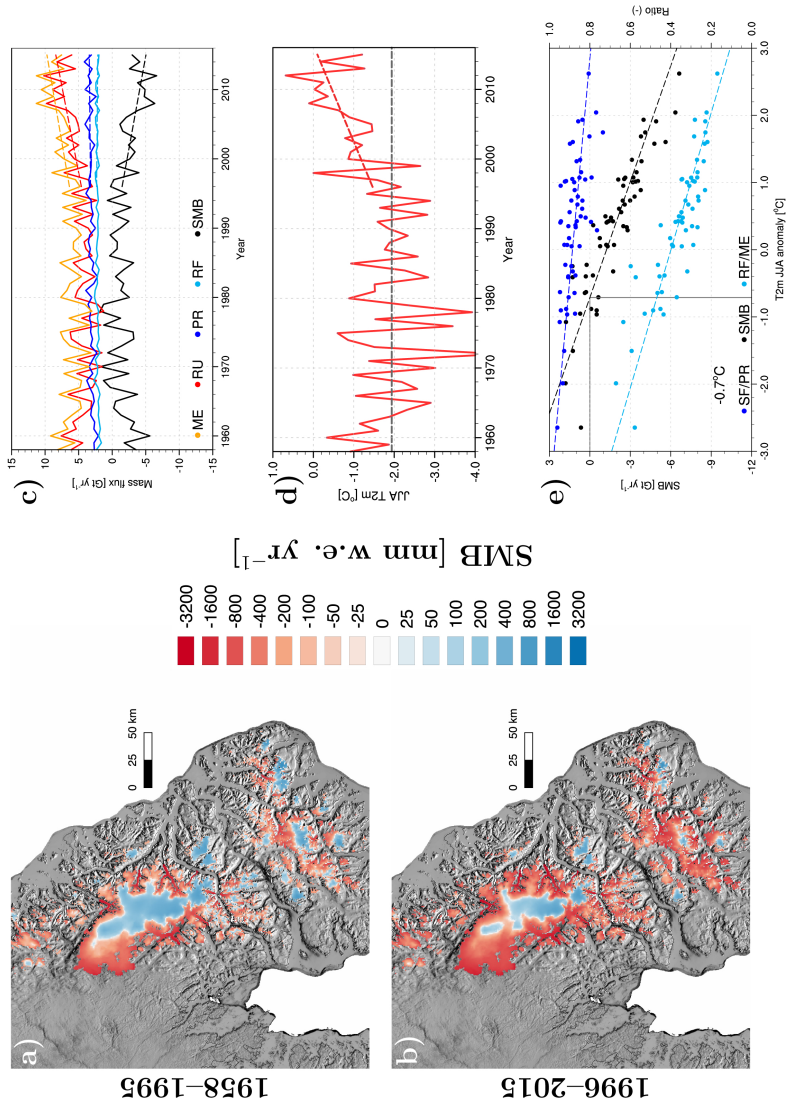


Figure 5.15: As Fig. 5.13 but for Penny ice cap.

5.6.4 Barnes ice cap

Covering an area of $\sim 5900 \text{ km}^2$, Barnes ice cap is another remnant of the Laurentide ice sheet [Gilbert et al., 2017] that is located $\sim 400 \text{ km}$ to the northwest of Penny ice cap. It comprises three main domes, with a maximum ice thickness of 550 m [Clough and Løken, 1968], and is surrounded by outlet glaciers terminating in proglacial lakes. These glaciers contribute to Barnes ice cap mass loss through active calving [Andrews et al., 2002]. Unlike Penny ice cap, Barnes ice cap is too low (summit at 1120 m) to preserve a perennial firn zone. As a result, Barnes only sporadically accumulates mass from superimposed ice [Baird, 1952; Hooke et al., 1987]. At lower elevations, a combination of white, blue, intermediate or debris-covered ice can be found; these regions also show meltwater lakes in depressions, reminiscent of previous surging glacier activity [Holdsworth, 1977].

Figures 5.16a and b show that Barnes ice cap has been undergoing uninterrupted mass loss in the last 58 years (Fig. 5.16c). During the period 1958-1995, precipitation (2.5 Gt yr^{-1}) only forms a shallow snow cover, in which little refreezing (1.5 Gt yr^{-1}) takes place. Therefore, 86% of surface melt (7.7 Gt yr^{-1}) runs off (6.7 Gt yr^{-1}) towards marginal proglacial lakes. This early mass loss is confirmed by Gardner et al. [2012], who estimated the 1960-1995 (ATM) mass loss at 1.9 Gt yr^{-1} . As the downscaling method uses a contemporary (2000-2015), darker MODIS ice albedo product to correct melt, mass loss is generally overestimated prior to the 2000s (4.0 Gt yr^{-1} for 1960-1995). As argued in Noël et al. [2016], too low ice albedo values in MODIS images could result from bright ice pixels being mixed with neighbouring darker wet ice or meltwater lakes. This discrepancy tends to disappear in the more recent period.

After 1996, mass loss from Barnes ice cap started to accelerate as reported by three successive satellite records (ATM, Gardner et al. [2012]): 3.4 Gt yr^{-1} (1995-2000), 4.2 Gt yr^{-1} (2000-2005) and 6.3 Gt yr^{-1} (2005-2011). The downscaled product shows similar results with 4.7 Gt yr^{-1} , 5.3 Gt yr^{-1} and 6.7 Gt yr^{-1} for the three periods. Following the recent warming (Fig. 5.16d), runoff increased by 27% (8.5 Gt yr^{-1}) as a consequence of combined melt increase (+20%, 9.3 Gt yr^{-1}) and reduced refreezing capacity (-4%; 15%). In contrast to Bylot and Penny ice caps, refreezing is almost exclusively driven by winter snowfall accumulation, which decreased by $\sim 5\%$.

Barnes is also $\sim 40\%$ more sensitive to summer warming than Bylot and Penny ice caps, and loses -2.6 Gt of ice per $^\circ\text{C}$ (Fig. 5.16e). Relative to the 1958-1995 average (-0.3°C), Barnes ice cap would require a JJA cooling of 1.6°C to return to balance. Figure 5.16e also suggests that a 2°C summer warming will lead to a $\sim 30\%$ decrease in solid precipitation, and would terminate all liquid water retention at Barnes ice cap. In a recent study, Gilbert et al. [2017] predicted the total disappearance of Barnes ice cap in the next 300 years.

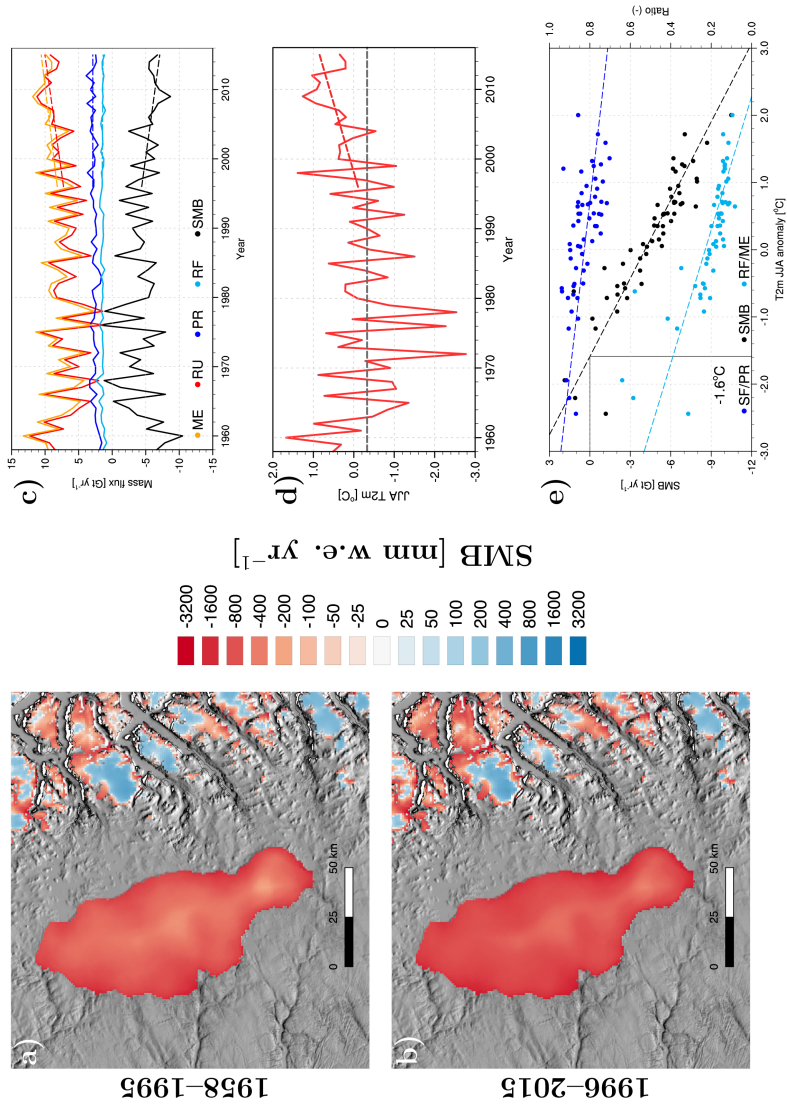


Figure 5.16: As Fig. 5.13 but for Barnes ice cap.

5.6.5 CAA climate sensitivity

Figure 5.17 shows the sensitivity of NCAA (blue) and SCAA (red) SMB to summer warming with respect to the 1958-1995 period. Owing to increased refreezing of meltwater in firn, the healthier NCAA ice caps would only need half the required SCAA summer cooling to return back to balance, with 0.5°C and 0.9°C , respectively. However, NCAA ice caps show a mass loss response to summer warming ($17.8 \text{ Gt per } ^{\circ}\text{C}$) larger than that of the SCAA ($12.6 \text{ Gt per } ^{\circ}\text{C}$), currently losing mass from superimposed ice. This difference reveals a pronounced latitudinal contrast: NCAA ice caps will undergo a larger mass loss acceleration than SCAA ice bodies in the near future as enhanced melt will progressively deplete the remaining firn pore space, drastically increasing meltwater runoff.

Although overly simplistic, i.e. no elevation or glacier retreat feedback is considered, we use a linear regression between SMB and summer 2-m temperature anomaly (black dashed line in Figs. 5.13-5.16e) to study the scales of enhanced mass loss for the four ice caps in a future warming climate. By the end of the 21st Century (2011-2100), for a moderate warming scenario (RCP 4.5), Lenaerts et al. [2013] predict an increase in CAA near-surface temperature of about 6.5°C . As a result, mass loss would increase by 18.2 Gt yr^{-1} (14x), 9.8 Gt yr^{-1} (10x), 11.1 Gt yr^{-1} (9x) and 16.9 Gt yr^{-1} (4x) relative to the 1958-1995 average for Agassiz, Bylot, Penny and Barnes ice caps, respectively.

At the current rate of mass loss (MB in Tables 1 and 2), NCAA ice caps ($22.4 - 37.6 \times 10^3 \text{ Gt}$ of ice; Vaughan et al. [2013]) contribute $0.08 \pm 0.03 \text{ mm yr}^{-1}$ to ongoing sea level rise and could survive for another 800 to 1400 years, whereas the highly sensitive SCAA glaciers ($5.5 - 8.8 \times 10^3 \text{ Gt}$ of ice; Vaughan et al. [2013]) are currently responsible for $0.06 \pm 0.01 \text{ mm yr}^{-1}$ and would totally disappear within 250 to 400 years.

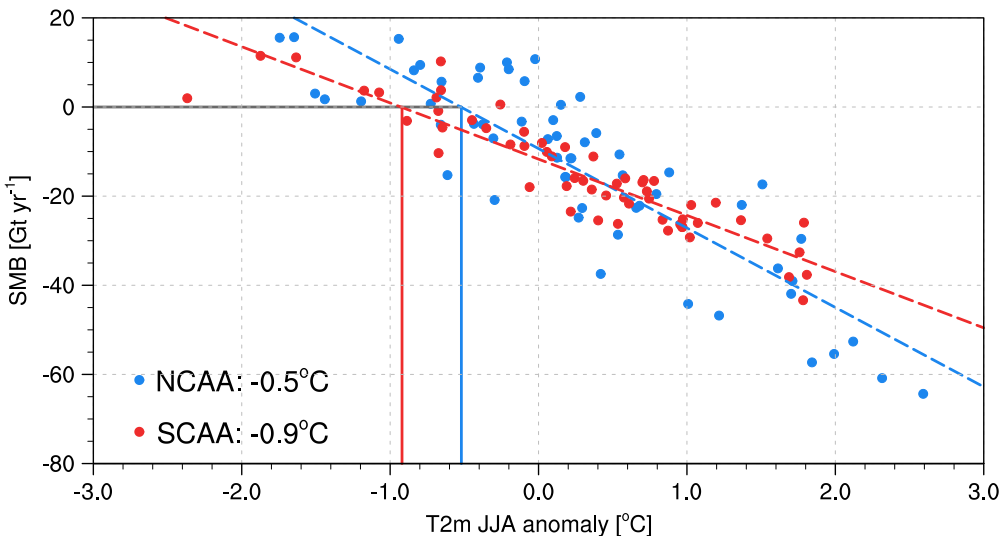


Figure 5.17: SMB as a function of anomaly in JJA 2-m temperature, relative to the 1958-1995 mean, for integrated NCAA (blue) and SCAA (red) ice caps. Dashed lines represent linear SMB-to-temperature regressions; the vertical lines estimate the JJA 2-m temperature anomaly relative to 1958-1995 needed to return NCAA (blue) and SCAA (red) ice caps to mass balance (SMB = 0).

| Mean | Units | MB | SMB | RU | PR | ME | RF |
|-----------|--------------------------|--------------|--------------|--------------|--------------|--------------|-------------|
| 1958-1995 | Gt yr ⁻¹ | -11.9 ± 11.5 | -8.4 ± 11.0 | 36.7 | 28.7 | 50.5 | 20.8 |
| 1996-2015 | Gt yr ⁻¹ | -28.2 ± 11.5 | -24.7 ± 11.0 | 53.5 | 29.0 | 68.3 | 23.0 |
| 1958-1995 | mm w.e. yr ⁻¹ | -114 ± 110 | -80 ± 105 | 352 | 275 | 484 | 199 |
| 1996-2015 | mm w.e. yr ⁻¹ | -270 ± 110 | -237 ± 105 | 513 | 278 | 654 | 220 |
| Trend | Units | MB | SMB | RU | PR | ME | RF |
| 1958-1995 | Gt yr ⁻² | - | 0.44 ± 0.25 | -0.36 ± 0.22 | 0.08 ± 0.06 | -0.28 ± 0.24 | 0.02 ± 0.04 |
| 1996-2015 | Gt yr ⁻² | - | -2.06 ± 0.77 | 1.85 ± 0.64 | -0.23 ± 0.21 | 2.03 ± 0.72 | 0.10 ± 0.11 |

Table 5.1: NCAA-integrated Mass Balance (MB), i.e. the difference between SMB and solid ice discharge ($3.5 \pm 0.5 \text{ Gt yr}^{-1}$) [Millan et al., 2017], and SMB components (top) and trends (bottom) for the periods 1958-1995 and 1996-2015. SMB components include runoff (RU), total precipitation (PR), total melt (ME) and refreezing (RF).

| Mean | Units | MB | SMB | RU | PR | ME | RF |
|-----------|--------------------------|-------------|--------------|--------------|--------------|--------------|--------------|
| 1958-1995 | Gt yr ⁻¹ | -11.9 ± 4.5 | -11.8 ± 4.5 | 32.0 | 20.4 | 41.9 | 13.4 |
| 1996-2015 | Gt yr ⁻¹ | -22.0 ± 4.5 | -21.9 ± 4.5 | 43.9 | 21.9 | 52.3 | 13.3 |
| 1958-1995 | mm w.e. yr ⁻¹ | -275 ± 104 | -273 ± 104 | 740 | 472 | 969 | 310 |
| 1996-2015 | mm w.e. yr ⁻¹ | -509 ± 104 | -506 ± 104 | 1020 | 506 | 1210 | 308 |
| Trend | Units | MB | SMB | RU | PR | ME | RF |
| 1958-1995 | Gt yr ⁻² | - | 0.23 ± 0.19 | -0.16 ± 0.18 | 0.08 ± 0.04 | -0.13 ± 0.17 | 0.04 ± 0.02 |
| 1996-2015 | Gt yr ⁻² | - | -1.00 ± 0.31 | 1.00 ± 0.33 | -0.02 ± 0.09 | 0.82 ± 0.32 | -0.10 ± 0.04 |

Table 5.2: SCAA-integrated Mass Balance (MB), i.e. the difference between SMB and solid ice discharge (0.06 Gt yr^{-1}) [Van Wychen et al., 2015], and SMB components (top) and trends (bottom) for the periods 1958-1995 and 1996-2015. SMB components include runoff (RU), total precipitation (PR), total melt (ME) and refreezing (RF).

5.7 Procedure limitations

Statistical downscaling is an invaluable tool to resolve local SMB patterns over the small CAA ice bodies. However, this technique suffers from several limitations:

a) the performance of the downscaled product strongly depends on the quality of the input data. Here, we use modelled SMB components from RACMO2.3, known to underestimate meltwater runoff in low-lying regions resulting from e.g. too low marginal turbulent heat fluxes [Noël et al., 2015]. In addition, the model uses a relatively coarse topography (GTOPO30) and glacier outlines (GLCC) to estimate the SMB elevation gradients. Inaccuracies in modelled gradients inherently lead to biases in the downscaled product. To address this issue, an updated DEM will be used in forthcoming CAA climate simulations. Nevertheless, Lenaerts et al. [2013] showed that this (outdated) DEM could be used to model realistic SMB over the CAA ice caps, with generally good agreement when compared to in situ measurements.

b) the underestimation of cloud optical thickness in RACMO2.3 leads to SW_d being overestimated, potentially overestimating melt through the ice albedo correction.

c) the downscaled melt and runoff estimates rely on the quality of the MODIS product used for the ice albedo correction. The average 1 km MODIS ice albedo product remains constant in time and is representative for the period 2000–2015. Therefore, bare ice albedo might be underestimated prior to 2000 as the period 2000–2015 includes record high melt years. As discussed in Section 5.3.2, marginal floating glacier tongues generally show underestimated albedo values in MODIS, resulting from a mixed signal from dark meltwater ponds and crevasses, and the surrounding brighter ice captured in a same MODIS cell. In addition, Polashenski et al. [2015] and Casey et al. [2017] showed that the deterioration of MODIS sensor tends to underestimate surface albedo records, hence overestimating melt in the downscaled product.

d) the inability to discriminate between snow-covered and bare ice surfaces at 1 km resolution on a daily basis. Therefore, the downscaling procedure applies the ice albedo correction irrespective of the surface conditions, i.e. even when a shallow snow cover persists few days in the ablation zone in summer.

As a result, additional ice melt (ME_{add}) is overestimated, leading to a relatively low f_{scale} value (0.2). This indicates that only 20% of the additional melt must run off to optimise the agreement of the downscaled product with in situ SMB measurements, while the remainder must be retained through refreezing. This low f_{scale} value stresses the need for further development of the downscaling method and for improved quality of the different forcing data. Solving these limitations, statistical downscaling could be applied to glaciers and ice caps with sparse in situ measurements e.g. Patagonia, assuming $f_{scale} \approx 1$.

5.8 Conclusions

We use a new, 1 km daily SMB product to show that glaciers and ice caps in the Canadian Arctic Archipelago (CAA) have been losing mass for decades. The downscaled product realistically resolves local SMB patterns of small glacierized features, such as narrow outlet glaciers and small ice fields, and has been successfully evaluated using in situ and remote sensing observations.

The SMB of CAA ice masses is primarily controlled by runoff, mitigated by the ability of elevated firn layers to only modestly buffer meltwater through refreezing. While refreezing kept NCAA ice caps near balance until the mid-1990s ($-11.9 \pm 11.5 \text{ Gt yr}^{-1}$), SCAA glaciers already suffered sustained mass loss since the early 1980s ($11.9 \pm 4.5 \text{ Gt yr}^{-1}$). During the last two decades, a shift in the regional circulation towards more frequent occurrence of persistent anticyclonic conditions, favoured warm southwesterly air advection towards CAA glaciers. As a result, successive record warm summers raised the mean near-surface temperature of CAA by 1.1°C , almost tripling ($28.2 \pm 11.5 \text{ Gt yr}^{-1}$) and doubling ($22.0 \pm 4.5 \text{ Gt yr}^{-1}$) the pre-1996 glacial mass loss in NCAA and SCAA, respectively. This recent mass loss acceleration is independently confirmed by satellite altimetry and gravimetry measurements.

For NCAA ice caps, enhanced melt starts to deplete the available pore space of the extensive inland firn, progressively moving the accumulation zones to higher elevations. In SCAA, decades of sustained high melt rates have already deteriorated the firn refreezing capacity to such an extent that runoff accelerates at a faster pace than meltwater production. In a future warming climate, the healthier NCAA ice caps will continue to mitigate mass loss acceleration through increased refreezing until the buffering mechanism collapses. In contrast, the lower-lying SCAA glaciers are expected to undergo irreversible mass loss in the next decades and might totally disappear within 400 years.

Modelling the Greenland ice sheet surface mass balance with RACMO2.3p2

Summary

We evaluate modelled Greenland ice sheet (GrIS) near-surface climate, surface energy balance (SEB) and surface mass balance (SMB) from the updated regional climate model RACMO2 (1958-2016). The new model version, referred to as RACMO2.3p2, incorporates updated glacier outlines, topography and ice albedo fields. Parameters in the cloud scheme governing the conversion of cloud condensate into precipitation have been tuned to correct inland snowfall underestimation; snow properties are modified to reduce drifting snow and melt production in the ice sheet percolation zone. The ice albedo prescribed in the updated model is lower at the ice sheet margins, increasing ice melt locally. RACMO2.3p2 shows good agreement compared to in situ meteorological data and point SEB/SMB measurements, and better resolves SMB patterns than the previous model version, notably in the northeast, southeast, and along the K-transect in southwestern Greenland. This new model version provides updated, high-resolution gridded fields of the GrIS present-day climate and SMB, and will be used for future climate scenario projections in a forthcoming study.

This chapter is based on: B. Noël et al. (2017c), Modelling the climate and surface mass balance of polar ice sheets using RACMO2, Part 1: Greenland (1958-2016), *The Cryosphere Discussions*, 2017c

6.1 Introduction

Predicting future mass changes of the Greenland ice sheet (GrIS) using regional climate models (RCMs) remains challenging [Rae et al., 2012]. The reliability of projections depend on the ability of RCMs to reproduce the contemporary GrIS climate and surface mass balance (SMB), i.e. snowfall accumulation minus ablation from meltwater runoff, sublimation and drifting snow erosion [Van Angelen et al., 2013; Fettweis et al., 2013a]. In addition, model simulations are affected by the quality of the re-analysis used as lateral forcing [Fettweis et al., 2013a, 2017; Bromwich et al., 2015] and by the accuracy of the ice sheet mask and topography prescribed in models [Vernon et al., 2013].

Besides direct RCM simulations, the contemporary SMB of the GrIS has been reconstructed using various other methods, e.g. Positive Degree Day (PDD) models forced by statistically downscaled re-analyses [Hanna et al., 2011; Wilton et al., 2016], mass balance models forced by the climatological output of an RCM (HIRHAM4) [Mernild et al., 2010, 2011], and data assimilation from an RCM combined with temperature and ice core accumulation measurements [Box, 2013]. In addition, Vizcaíno et al. [2013] used the Community Earth System Model (CESM) at 1° resolution (~100 km) to estimate recent and future mass losses of the GrIS.

Polar RCMs have the advantage to explicitly resolve the relevant atmospheric and surface physical processes at high spatial (5 to 20 km) and temporal (sub-daily) resolution. Nonetheless, good RCM performance often results from compensating errors between poorly parameterised processes, e.g. cloud physics [Van Tricht et al., 2016] and turbulent fluxes [Noël et al., 2015; Fausto et al., 2016]. Therefore, considerable efforts have been dedicated to evaluate and improve polar RCM output in Greenland [Ettema et al., 2010b; Van Angelen et al., 2013b; Lucas-Picher et al., 2012; Fettweis et al., 2017; Noël et al., 2015; Langen et al., 2017], using in situ SMB observations [Bales et al., 2001, 2009; Van de Wal et al., 2012; Machguth et al., 2016b], airborne radar measurements of snow accumulation [Koenig et al., 2016; Overly et al., 2016; Lewis et al., 2017] and meteorological records [Ahlstrøm et al., 2008; Kuipers Munneke et al., 2017; Smeets et al., 2017], including radiative fluxes that are required to close the ice sheet surface energy balance (SEB), and hence quantify surface melt energy.

For more than two decades, the polar version of the Regional Atmospheric Climate Model (RACMO2) has been developed to simulate the climate and SMB of the Antarctic and Greenland ice sheets. In previous versions, snowfall accumulation was systematically underestimated in the GrIS interior, while melt was generally overestimated in the percolation zone [Noël et al., 2015]. At the ice sheet margins, meltwater runoff is underestimated over narrow ablation zones and small outlet glaciers that are not accurately resolved in the model's ice mask at 11 km. Locally, this underestimation can exceed several m w.e. yr⁻¹, e.g. at automatic weather station (AWS) QAS_L installed at the southern tip of Greenland [Fausto et al., 2016]. These biases can be significantly reduced by statistically downscaling SMB components to 1 km resolution [Noël et al., 2016]. Computational limitations currently hamper direct near-kilometre simulations of the contemporary GrIS climate, making it essential to further develop RACMO2 model physics at coarser spatial resolution.

Here, we present updated simulations of the contemporary GrIS climate and SMB at 11 km resolution (1958-2016). The updated model incorporates multiple adjustments, notably in the cloud scheme and snow module. Model evaluation is performed using in situ meteorological data and point SEB/SMB measurements collected all over Greenland. We then compare the SMB of the updated model version (RACMO2.3p2) with its predecessor (RACMO2.3p1) for the overlapping period between the two sim-

ulations (1958-2015). Section 6.2 discusses the new model settings and initialisation, together with observational data used for model evaluation. Modelled climate and SEB components are evaluated using in situ measurements in Section 6.3. Changes in SMB patterns between the new and old model versions are discussed in Section 6.4, as well as case studies in northeast, southwest and southeast Greenland. Section 6.5 introduces and evaluates the updated downscaled daily, 1 km SMB product. Section 6.6 discusses the remaining model uncertainties, followed by conclusions in Section 6.7. This manuscript is part of a tandem model evaluation over the Greenland (present study) and Antarctic ice sheets [Van Wessem et al., 2017].

6.2 Model and observational data

6.2.1 The Regional Atmospheric Climate Model RACMO2

The polar ('p') version of the Regional Atmospheric Climate Model (RACMO2) [Van Meijgaard et al., 2008] is specifically adapted to simulate the climate of polar ice sheets. The model incorporates the dynamical core of the High Resolution Limited Area Model (HIRLAM) [Undén et al., 2002] and the physics package cycle CY33r1 of the European Centre for Medium-range Weather Forecasts Integrated Forecast System [ECMWF-IFS, 2008]. It also includes a multi-layer snow module that simulates melt, liquid water percolation and retention, refreezing and runoff [Ettema et al., 2010b], and accounts for dry snow densification following Ligtenberg et al. [2011]. RACMO2 implements an albedo scheme that calculates snow albedo based on prognostic snow grain size, cloud optical thickness, solar zenith angle and impurity concentration in snow [Kuipers Munneke et al., 2011]. In RACMO2, impurity concentration, i.e soot, is prescribed as constant in time and space. The model also simulates drifting snow erosion and sublimation following Lenaerts et al. [2012a]. Previously, RACMO2 has been used to reconstruct the contemporary SMB of the Greenland ice sheet [Van Angelen et al., 2013; Van Angelen et al., 2013b; Noël et al., 2015, 2016] and peripheral ice caps [Noël et al., 2017a], the Canadian Arctic Archipelago [Lenaerts et al., 2013; Noël et al., 2017b], Patagonia [Lenaerts et al., 2014] and Antarctica [Van Wessem et al., 2014a,b].

6.2.2 Surface energy budget and surface mass balance

In RACMO2, the excess energy obtained after closing the surface energy budget (SEB) is used to melt snow and ice (M) at the GrIS surface:

$$\begin{aligned} M &= SW_d + SW_u + LW_d + LW_u + SHF + LHF + G_s \\ &= SW_n + LW_n + SHF + LHF + G_s \end{aligned} \quad (6.1)$$

where SW_d and SW_u are the shortwave down/upward radiation fluxes, LW_d and LW_u are the longwave down/upward radiation fluxes, SHF and LHF are the sensible and latent turbulent heat fluxes, and G_s is the subsurface heat flux. SW_n and LW_n are the net short/longwave radiation at the surface. All fluxes are expressed in $W m^{-2}$ and are defined positive when directed towards the surface.

In the percolation zone of the GrIS, liquid water mass from melt (ME) and rainfall (RA) can percolate through the firn column, and is either retained by capillary forces as irreducible water (RT) or refreezes (RF). Combined with dry snow densification, this progressively depletes firn pore space until the entire column turns into ice (900 kg m^{-3}). The fraction not retained is assumed to immediately run off (RU) to the ocean:

$$RU = ME + RA - RT - RF \quad (6.2)$$

The climatic mass balance [Cogley et al., 2011], hereafter referred to as SMB, is estimated as:

$$SMB = P_{\text{tot}} - RU - SU_{\text{tot}} - ER_{\text{ds}} \quad (6.3)$$

where P_{tot} is the total amount of precipitation, i.e. solid and liquid, RU is meltwater runoff, SU_{tot} is the total sublimation from drifting snow and surface processes, and ER_{ds} is the erosion by the process of drifting snow. All SMB components are expressed in mm w.e. (water equivalent) for point 'specific' SMB values, or in Gt yr^{-1} when integrated over the GrIS.

6.2.3 Model updates

In the cloud scheme, parameters controlling precipitation formation have been modified to reduce the negative snowfall bias in the GrIS interior ($\sim 40 \text{ mm w.e. yr}^{-1}$) [Noël et al., 2015]. To correct for this, the critical cloud content (l_{crit}) governing the onset of effective precipitation formation for liquid-mixed and ice clouds has been increased by a factor 2 (Eqs. 5.35 and 6.39 in ECMWF-IFS [2008]) and 5 (Eq. 6.42 in ECMWF-IFS [2008]), respectively. As a result, moisture transport is prolonged to higher elevations and precipitation is generated further inland.

Furthermore, the previous model version overestimated snow melt in the percolation zone of the GrIS [Noël et al., 2015]. With the aim of minimising this bias, the following parameters have been tuned in the snow module:

- a) The model soot concentration, accounting for dust and black carbon impurities deposited on snow, has been reduced from 0.1 ppmv to 0.05 ppmv, more representative of observed values [Doherty et al., 2010]. A lower soot concentration yields a higher surface albedo, hence decreasing melt [Van Angelen et al., 2012].
- b) The size of refrozen snow grains has been reduced from 2 to 1 mm [Kuipers Munneke et al., 2011]. Consequently, the surface albedo of refrozen snow increases, as smaller particles enhance scattering of solar radiation back to the atmosphere [Kaasalainen et al., 2006].
- c) In previous model versions, the albedo of superimposed ice, i.e. the frozen crust forming at the firn surface, was set equal to the albedo of bare ice (~ 0.55), underestimating surface albedo and hence overestimating melt. The snow albedo scheme now explicitly calculates the albedo of superimposed ice layers (~ 0.75), following Kuipers Munneke et al. [2011].
- d) The saltation coefficient of drifting snow has been approximately halved from 0.385 to 0.190 [Lenaerts et al., 2012a]. Saltation occurs when near surface wind speed is sufficiently high to lift snow grains from

the surface. In RACMO2, this coefficient determines the depth of the saltation layer, i.e. typically extending 0 to 10 cm above the surface, that directly controls the mass of drifting snow transported in the suspension layer aloft (above 10 cm). This revision does not affect the timing and frequency of drifting snow events, which are well modelled [Lenaerts et al., 2012a,b], but only reduces the horizontal drifting snow transport and sublimation, preventing a too early exposure of bare ice during the melt season, especially in the dry and windy northeastern GrIS (Section 6.4.2).

6.2.4 Initialisation and set up

To enable a direct comparison with previous runs, RACMO2.3p2 is run at 11 km horizontal resolution for the period 1958-2016, and is forced at its lateral boundaries by ERA-40 (1958-1978) [Uppala et al., 2005] and ERA-Interim (1979-2016) [Dee et al., 2011] re-analyses on a 6-hourly basis (Fig. 6.1). The forcing consists of temperature, specific humidity, pressure, wind speed and direction being prescribed at each of the 40 vertical atmosphere hybrid model levels. Upper atmosphere relaxation (nudging) is also implemented in this new model version [Van de Berg and Medley, 2016]. As the model does not incorporate a dedicated ocean module, sea surface temperature and sea ice cover are prescribed from the re-analyses [Stark et al., 2007]. The model has about 40 active snow layers that are initialised in September 1957 using the best temperature and density profile estimates derived from the offline IMAU Firn Densification Model (IMAU-FDM) [Ligtenberg et al., 2011]. The data spanning the winter season up to December 1957 serve as an additional spin up for the snowpack and are therefore discarded in the present study.

Relative to previous versions, the integration domain extends further to the west, north and east (Fig. 6.1). This brings the northernmost sectors of the Canadian Arctic Archipelago and Svalbard well inside the domain interior, and further away from the lateral boundary relaxation zone (24 grid cells, black dots in Fig. 6.1). In addition, RACMO2.3p2 utilises the 90 m Greenland Ice Mapping Project (GIMP) Digital Elevation Model (DEM) [Howat et al., 2014] to better represent the glacier outlines and the surface topography of the GrIS. Compared to the previous model version, which used the 5 km DEM presented in Bamber et al. [2001], the GrIS area is reduced by 10,000 km² (Fig. 6.2a). This mainly results from an improved partitioning between the ice sheet and peripheral ice caps, for which the ice-covered area has, in equal amounts, decreased and increased, respectively. The updated topography shows significant differences compared to the previous version, especially over marginal outlet glaciers where surface elevation has considerably decreased (Fig. 6.2b). Bare ice albedo is prescribed from the 500 m MODerate-resolution Imaging Spectroradiometer (MODIS) 16-day Albedo product (MCD43A3), as the 5% lowest surface albedo records for the period 2000-2015 (vs. 2001-2010 in older versions; Fig. 6.2c). In RACMO2, ice albedo is minimised at 0.30 for dark ice in the low-lying ablation zone, and maximised at 0.55 for bright ice under perennial snow cover in the accumulation zone. In previous RACMO2 versions, bare ice albedo of glaciated grid cells without valid MODIS estimate were set to 0.47 [Noël et al., 2015].

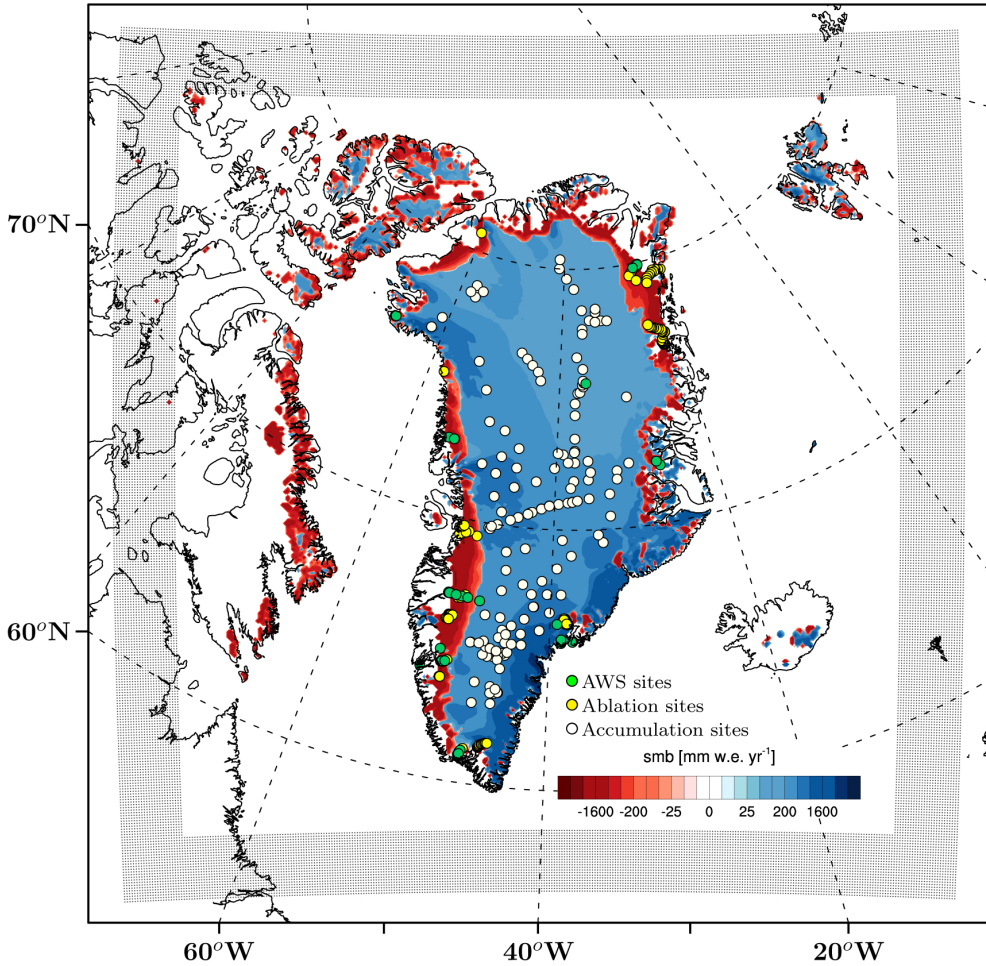


Figure 6.1: SMB (mm w.e. yr^{-1}) modelled by RACMO2.3p2 at 11 km resolution for 2016. Black dots delineate the relaxation zone (24 grid cells) where the model is forced by ERA re-analyses. Ablation sites (213) are displayed as yellow dots, accumulation sites (182) as white dots, and AWS locations (23) are represented in green.

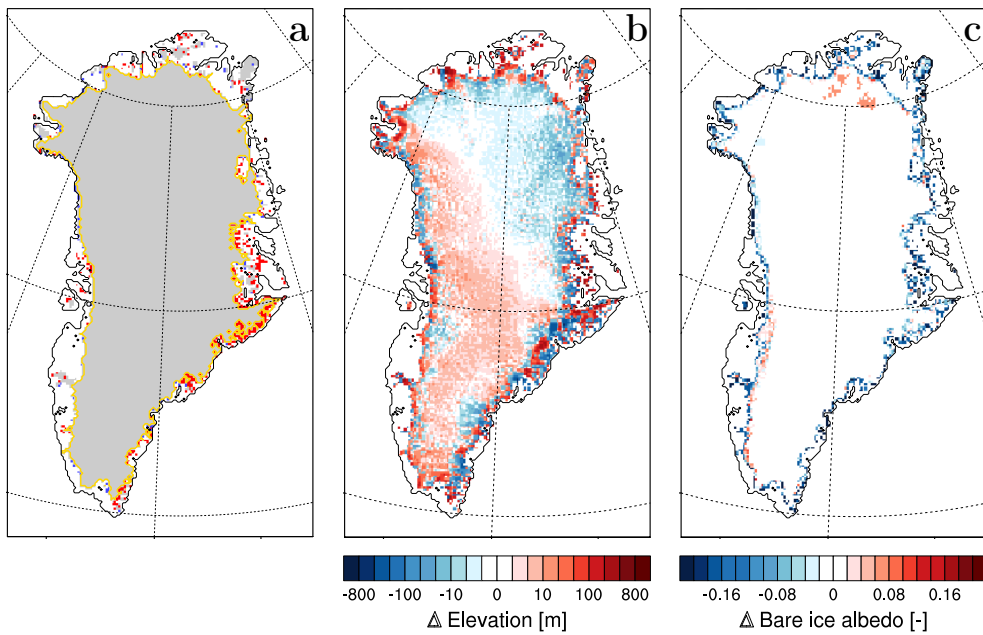


Figure 6.2: Difference in a) ice mask b) surface elevation and c) bare ice albedo between RACMO2.3p2 and RACMO2.3p1. In Fig. 6.2a, the common ice mask for both model versions is displayed in grey, the ice sheet area is outlined in yellow; additional and removed ice-covered cells in RACMO2.3p2 are shown in red and blue, respectively.

6.2.5 Observational data

To evaluate the modelled contemporary climate and SMB of the GrIS, we use daily average meteorological records of near-surface temperature, wind speed, relative humidity, air pressure and down/upward short/longwave radiative fluxes, retrieved from 23 AWS for the period 2004-2016 (green dots in Fig. 6.1). Erroneous radiation measurements, caused e.g. by sensor riming, were discarded by removing daily records showing $SW_{d \text{ bias}} > 6 \sigma_{\text{bias}}$, where $SW_{d \text{ bias}}$ is the difference between daily modelled and observed SW_d and σ_{bias} is the standard deviation of the daily SW_d bias for all measurements. In addition, measurements affected by sensor heating in summer, i.e. showing $LW_u > 318 \text{ W m}^{-2}$, were eliminated as these values represent $T_s > 0^\circ\text{C}$ for $\varepsilon \approx 0.99$, where T_s is the surface temperature and ε the selected emissivity of snow or ice. We only used daily records that were simultaneously available for each of the four radiative components. Eighteen of these AWS sites are operated as part of the Programme for Monitoring of the Greenland Ice Sheet (PROMICE, www.promice.dk) covering the period 2007-2016 [Van As et al., 2011]. Four other AWS sites, namely S5, S6, S9 and S10 (2004-2016), are located along the K-transect in southwest Greenland (67°N , $47\text{-}50^\circ\text{W}$) [Smeets et al., 2017]. Another AWS (2014-2016) is situated in southeast Greenland (66°N ; 33°W) at a firn aquifer site [Forster et al., 2014; Koenig et al., 2014]. The latter five sites are operated by the Institute for Marine and Atmospheric research at Utrecht University (IMAU).

We also use in situ SMB measurements collected at 213 stake sites in the GrIS ablation zone (yellow dots in Fig. 6.1; Machguth et al. [2016b]) and at 182 sites in the accumulation zone (white dots in Fig. 6.1) including snow pits, firn cores [Bales et al., 2001, 2009], and airborne radar measurements [Overly et al., 2016]. We exclusively selected measurements that temporally overlap with the model simulation (1958-2016). To match the observational period, daily modelled SMB is cumulated for the exact number of measuring days at each site.

For model evaluation, we select the grid cell nearest to the observation site in the accumulation zone. In the ablation zone, an additional altitude correction is applied by selecting the model grid cell with the smallest elevation bias among the nearest grid cell and its eight adjacent neighbours. One ablation site and seven PROMICE AWS sites presented an elevation bias in excess of $> 100 \text{ m}$ compared to the model topography and were discarded from the comparison.

6.3 Results: near-surface climate and SEB

We evaluate the modelled present-day near-surface climate of the GrIS in RACMO2.3p2 using data of 23 AWS sites (see Section 6.2.5). Then, we discuss in more detail the model performance at 4 AWS along the K-transect and compare RACMO2.3p2 output to those of RACMO2.3p1.

6.3.1 Near-surface meteorology

Figure 6.3 compares daily mean values of 2-m temperature, 2-m specific humidity, 10-m wind speed, air pressure collected at 23 AWS sites with RACMO2.3p2 output. The modelled 2-m temperature is in good agreement with observations ($R^2 = 0.95$) and with a RMSE of $\sim 2.4^\circ\text{C}$ and a small cold bias of $\sim 0.1^\circ\text{C}$ (Fig. 6.3a). As specific humidity is not directly measured at AWS sites, it is calculated from measured temperature, pressure and relative humidity following Curry and Webster [1999]. The obtained 2-m specific humidity is accurately reproduced in the model ($R^2 = 0.95$) with a RMSE ~ 0.35 g kg^{-1} and a negative bias of 0.13 g kg^{-1} (Fig. 6.3b). The same holds for daily records of 10-m wind speed ($R^2 = 0.68$; Fig. 6.3c), with a small negative bias and RMSE of ~ 2 m s^{-1} . Surface pressure is also well represented ($R^2 = 0.99$) with a small negative bias of 0.8 hPa and RMSE < 6 hPa (Fig. 6.3d). A systematic pressure bias at some stations results from the (uncorrected) elevation difference with respect to the model, which can be as large as 100 m.

6.3.2 Radiative fluxes

Figure 6.4 shows scatter plots of modelled and measured daily mean radiative fluxes, i.e. short/longwave down/upward radiation. Radiative fluxes are also well reproduced by the model with R^2 ranging from 0.83 for LW_d to 0.95 for SW_d (Fig. 6.4), showing relatively small biases of -7.1 W m^{-2} and 3.8 W m^{-2} , and RMSE of 21.2 W m^{-2} and 27.1 W m^{-2} , respectively. The negative bias in LW_d , hence leading to LW_u underestimation of 4.4 W m^{-2} with a small RMSE of 12.1 W m^{-2} , in combination with positive bias in SW_d suggests an underestimation of cloud cover in the ice sheet marginal regions, where most stations are located. The larger bias and RMSE in SW_u of 6.8 W m^{-2} and 32.1 W m^{-2} , respectively, can be ascribed to overestimated surface albedo, especially during summer snowfall episodes, when a bright fresh snow cover is deposited over bare ice. Note that these AWS radiation measurements are also prone to potentially large uncertainties due to preferred location on ice hills, sensor tilt, riming and snow/rain deposition on the instruments, leading to spurious albedo and SW_u data, e.g. the upper left dots in Fig. 6.4b.

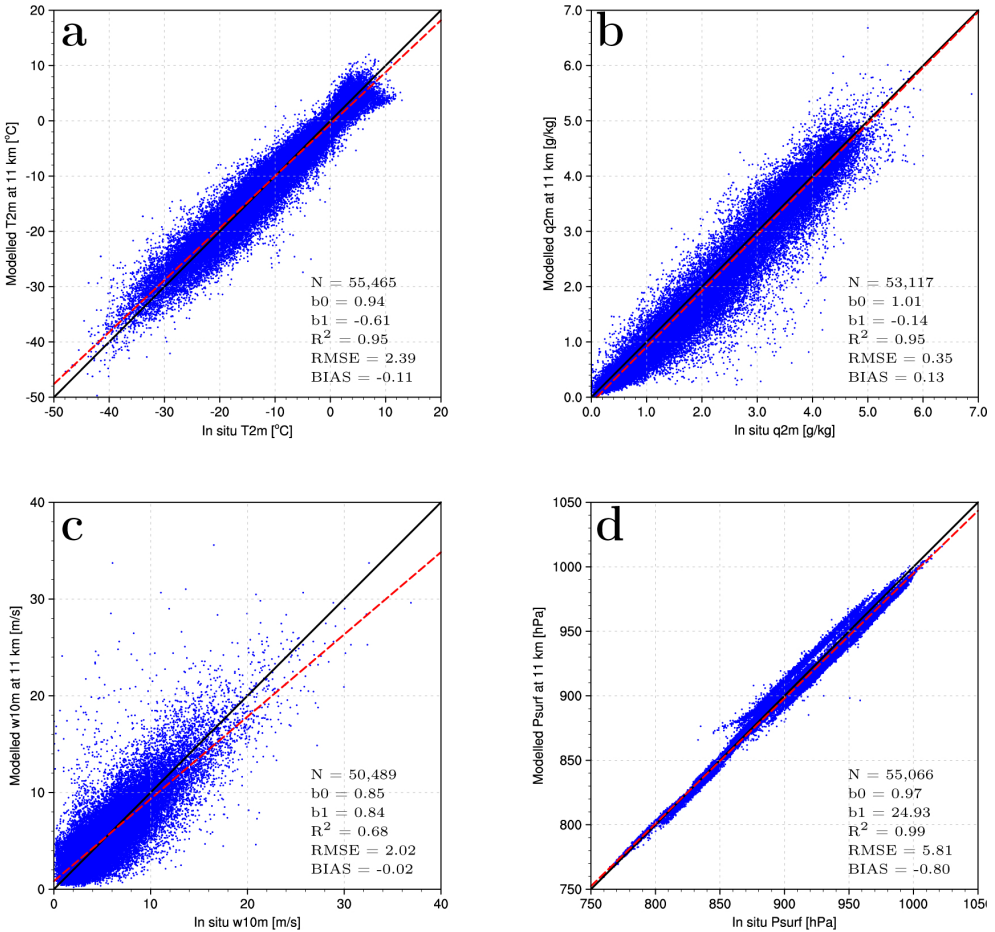


Figure 6.3: Comparison between modelled and observed a) 2-m temperature (T_{2m} , °C), b) 2-m specific humidity (q_{2m} , $g\ kg^{-1}$), c) 10-m wind speed (w_{10m} , $m\ s^{-1}$) and d) surface pressure (P_{surf} , hPa) collected at 23 AWS (green dots in Fig. 6.1). For each variable, the linear regression including all records is displayed as red dashed line. Statistics including number of records (N), regression slope (b_0) and intercept (b_1), determination coefficient (R^2), bias and RMSE are listed for each variable.

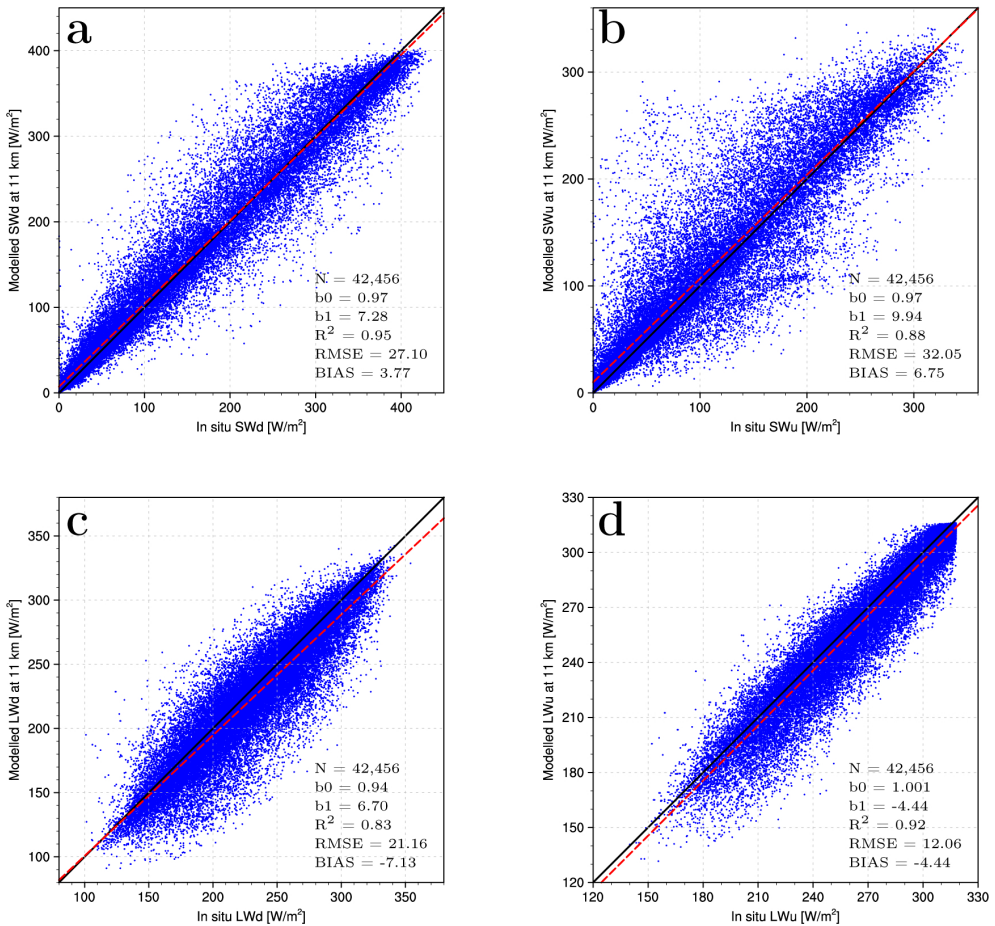


Figure 6.4: Comparison between daily average modelled and observed a) shortwave downward, b) shortwave upward, c) longwave downward and d) longwave upward radiation (W m^{-2}) collected at 23 AWS (green dots in Fig. 6.1). For each variable, regression including all records is displayed as red dashed line. Statistics including number of records (N), the linear regression slope (b_0) and intercept (b_1), determination coefficient (R^2), bias and RMSE are listed for each variable.

6.3.3 Seasonal SEB cycle along the K-transect

The K-transect comprises four AWS sites located in different regions of the GrIS: S5 and S6 are installed in the lower and upper ablation zone, respectively, S9 is situated close to the equilibrium line and S10 in the accumulation zone. Figure 6.5 shows monthly mean modelled (continuous lines, RACMO2.3p2) and observed (dashed lines) SEB components, i.e. net short/longwave radiation (SW_n/LW_n), latent and sensible heat fluxes (LHF/SHF), surface albedo and melt measured at these four AWS sites for the period 2004-2015. Tables 6.1-6.4 list statistics calculated at each individual AWS and for the two model versions.

Low ablation zone

At station S5 (490 m a.s.l.), surface melt is well reproduced in RACMO2.3p2, with a small negative bias of 0.4 W m^{-2} (Table 6.1; Fig. 6.5b). However, this good agreement results from significant error compensation between overestimated SW_n (16.2 W m^{-2}) and underestimated SHF in summer (15.3 W m^{-2} ; Fig. 6.5a). The bias in SW_n is mostly driven by overestimated SW_d (20.7 W m^{-2} ; Table 6.1) and to a lesser extent by SW_u (4.5 W m^{-2}), resulting from too low cloud cover and ice albedo (Fig. 6.5b), respectively. AWS are often installed on snow covered promontories, i.e. hummocks, that maintain higher albedo in summer (~ 0.55) than their surroundings where impurities collect. Mixed reflectance from bright ice cover (~ 0.55) and neighbouring darker tundra, exposed nunataks or meltwater ponds (< 0.30), located within the same MODIS grid cell, likely explains this underestimation. Another explanation stems from the deterioration of MODIS sensors in time, resulting in underestimated surface albedo records [Polashenski et al., 2015; Casey et al., 2017].

LW_n is well reproduced in the model due to similar negative biases in LW_d and LW_u ($\sim 12 \text{ W m}^{-2}$), indicating again too low cloud cover. The large negative bias in SHF is attributed to an inaccurate representation of surface roughness in the lowest sectors of the ablation zone. Smeets and Van den Broeke [2008] show that observed surface roughness for momentum has a high temporal variability at site S5, with a minimum of 0.1 mm in winter, when a smooth snow layer covers the rugged ice sheet topography, and a peak in summer (up to 50 mm), when melting snow exposes hummocky ice at the surface. In RACMO2, surface aerodynamic roughness is prescribed at 1 mm for snow-covered grid cells and at 5 mm for bare ice, hence significantly underestimating values over ice in summer and thus causing too low SHF [Ettema et al., 2010a]. This bias in SHF at S5 is also partly ascribable to too cold conditions (2°C). Although not negligible, LHF contributes little to the energy budget and shows a positive bias of $\sim 3 \text{ W m}^{-2}$, notably in winter.

Upper ablation zone

Station S6 is located at 1010 m a.s.l. in the GrIS upper ablation zone. There, summer melt is overestimated by $\sim 8 \text{ W m}^{-2}$ owing to both too high SW_n and SHF (2.2 W m^{-2} and 7 W m^{-2} , respectively; Fig. 6.5c). As for S5, the bias in SW_n results from overestimated SW_d (6 W m^{-2}) and underestimated SW_u (4 W m^{-2}). At the AWS location, surface albedo progressively declines from 0.60 to ~ 0.40 when bare ice is exposed in late summer, whereas RACMO2.3p2 simulates bare ice at the surface with an albedo of 0.40 throughout summer. As a result, modelled surface albedo is systematically underestimated in summer, especially in July (Fig. 6.5d). Likewise, a small negative bias in LW_n ($\sim 2 \text{ W m}^{-2}$)

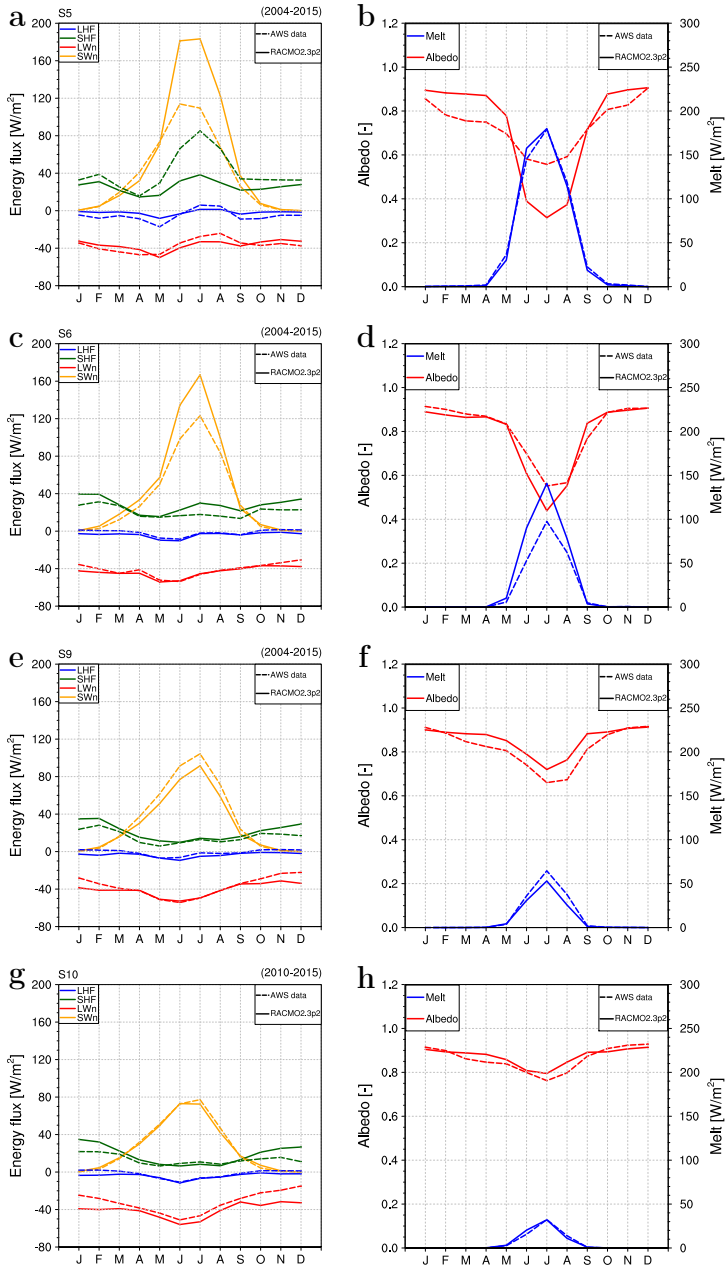


Figure 6.5: Observed and modelled monthly mean a) turbulent and net shortwave/longwave fluxes ($W m^{-2}$) and b) surface albedo and surface melt energy ($W m^{-2}$) at site S5 for 2004-2015. Similar results are shown at S6 for 2004-2015 (c and d), S9 for 2009-2015 (e and f) and S10 for 2010-2015 (g and h).

is obtained as LW_d and LW_u are both slightly underestimated (Table 6.2). Here, 2-m temperature is on average 0.7°C too high, causing a too large SHF (7 W m^{-2}).

Equilibrium line

Close to the equilibrium line, RACMO2.3p2 slightly underestimates summer melt (2.4 W m^{-2} ; Fig. 6.5f and Table 6.3). At station S9 (1520 m a.s.l.), a perennial snow cover maintains a minimum albedo of 0.65 in summer, i.e. when melt wets the snow. A small positive bias in modelled snow albedo (0.03) combined with a slightly underestimated SW_d (1.5 W m^{-2}) lead to an overestimated SW_u (3.5 W m^{-2}), hence underestimating SW_n ($\sim 5 \text{ W m}^{-2}$). Although LW_d and LW_u are overestimated, especially in winter (3.1 W m^{-2} and 0.5 W m^{-2} , respectively), LW_n agrees well with measurements. The 2-m surface temperature shows a 0.5°C positive bias, in turn causing slightly too large SHF ($\sim 5 \text{ W m}^{-2}$; Fig. 6.5e and Table 6.3).

Accumulation zone

All SEB components are well reproduced at site S10 (1850 m a.s.l.). Compensation of minor errors between underestimated SW_d and overestimated SW_u ($\sim 1 \text{ W m}^{-2}$) provides a good agreement with observed SW_n (Fig. 6.5g). Modelled surface albedo also compares well with measurements, with only a small positive bias (0.03; Fig. 6.5h). LW_n is underestimated by $\sim 5 \text{ W m}^{-2}$; this is mainly driven by a too low LW_d and a too large LW_u (Table 6.4). The turbulent fluxes are well captured although a significant bias in SHF persists ($\sim 7 \text{ W m}^{-2}$), especially in winter when LW_d is underestimated. As biases in SHF and LW_d are almost equal, modelled melt matches well with observations despite a small negative bias ($\sim 2 \text{ W m}^{-2}$).

6.3.4 Model comparison along the K-transect

Tables 6.1-6.4 compare statistics of SEB components between RACMO2.3p2 and 2.3p1. Although differences are relatively small, the new model formulation shows general improvements. The increased cloud cover over the GrIS reduced the bias in SW_d and LW_d . Improvements in the representation of turbulent fluxes is partly attributed to the new topography prescribed in RACMO2.3p2 and the better resolved SW_d/LW_d , although significant biases remain at all stations.

At site S5 located in the low ablation zone (Table 6.1), smaller SW_d and lower ice albedo significantly reduce the SW_u bias in RACMO2.3p2, and enhanced LW_d decreases the negative bias in LW_u . As a result, melt increases substantially, reducing the negative bias compared to version 2.3p1. Note that SW_d remains overestimated in RACMO2.3p2. This is compensated by underestimated SHF, i.e. partly caused by underestimated LW_d , providing realistic surface melt. In the upper ablation zone, similar improvements are obtained at site S6 (Table 6.2). Here, all SEB components show smaller biases except for SW_u , as underestimated surface albedo increases the negative SW_u bias.

Above the equilibrium line, enhanced cloud cover also reduces the SW and LW biases at sites S9 and S10 (Tables 6.3 and 6.4). However, surface albedo overestimation in RACMO2.3p2 causes a small increase in melt underestimation.

| AWS Variable | S5 unit | Obs. mean | RACMO2.3p1 | | | RACMO2.3p2 | | |
|-----------------|------------------|--------------|------------|------|-------|------------|------|-------|
| | | | bias | RMSE | R^2 | bias | RMSE | R^2 |
| SW _d | W/m ² | 109.5 | 26.2 | 33.1 | 0.99 | 20.7 | 27.2 | 0.98 |
| SW _u | W/m ² | -70.9 | 15.8 | 25.0 | 0.93 | 4.5 | 34.3 | 0.74 |
| LW _d | W/m ² | 241.4 | -16.7 | 18.5 | 0.97 | -11.8 | 13.4 | 0.97 |
| LW _u | W/m ² | -278.3 | -13.2 | 15.5 | 0.98 | -12.1 | 14.2 | 0.98 |
| SHF | W/m ² | 41.1 | -13.1 | 22.2 | 0.50 | -15.3 | 22.4 | 0.66 |
| LHF | W/m ² | 5.3 | 2.6 | 5.6 | 0.72 | 3.4 | 6.5 | 0.64 |
| ME | W/m ² | 42.6 | -6.8 | 18.0 | 0.96 | -0.4 | 11.9 | 0.97 |
| ALB | (-) | 0.74 | 0.03 | 0.09 | 0.75 | -0.004 | 0.14 | 0.72 |
| T _{2m} | °C | -6.4 | -2.3 | 2.6 | 0.99 | -2.0 | 2.2 | 0.992 |

Table 6.1: Modelled and observed mean SEB components and statistics of the differences (2004-2015) at station S5 in the lower ablation zone (490 m a.s.l.). Statistics include means of measurements collected at S5, model bias (RACMO2.3pX - observations), RMSE of the bias as well as the determination coefficient of monthly mean data. Fluxes are set positive towards the surface.

| AWS Variable | S6 unit | Obs. mean | RACMO2.3p1 | | | RACMO2.3p2 | | |
|-----------------|------------------|--------------|------------|------|-------|------------|------|-------|
| | | | bias | RMSE | R^2 | bias | RMSE | R^2 |
| SW _d | W/m ² | 131.6 | 9.7 | 12.7 | 0.997 | 6.0 | 9.1 | 0.997 |
| SW _u | W/m ² | -95.8 | -2.9 | 16.3 | 0.97 | -3.8 | 16.3 | 0.97 |
| LW _d | W/m ² | 222.3 | -8.8 | 11.4 | 0.96 | -2.7 | 6.5 | 0.97 |
| LW _u | W/m ² | -263.6 | -1.6 | 4.0 | 0.991 | -0.4 | 3.2 | 0.992 |
| SHF | W/m ² | 20.8 | 9.8 | 11.4 | 0.67 | 7.0 | 8.7 | 0.70 |
| LHF | W/m ² | 1.6 | -3.9 | 5.2 | 0.42 | -2.4 | 3.3 | 0.64 |
| ME | W/m ² | 18.7 | 10.6 | 22.0 | 0.96 | 8.3 | 18.1 | 0.97 |
| ALB | (-) | 0.81 | 0.02 | 0.06 | 0.89 | -0.02 | 0.06 | 0.89 |
| T _{2m} | °C | -10.9 | 0.4 | 0.8 | 0.994 | 0.7 | 1.0 | 0.995 |

Table 6.2: Modelled and observed mean SEB components and statistics of the differences (2004-2015) at station S6 in the upper ablation zone (1010 m a.s.l.). Statistics include means of measurements collected at S6, model bias (RACMO2.3pX - observations), RMSE of the bias as well as the determination coefficient of monthly mean data. Fluxes are set positive towards the surface.

| AWS Variable | S9 unit | Obs. mean | RACMO2.3p1 | | | RACMO2.3p2 | | |
|-----------------|------------------|--------------|------------|------|----------------|------------|------|----------------|
| | | | bias | RMSE | R ² | bias | RMSE | R ² |
| SW _d | W/m ² | 141.2 | 2.2 | 6.6 | 0.998 | -1.5 | 7.8 | 0.998 |
| SW _u | W/m ² | -106.5 | 3.5 | 9.4 | 0.991 | 3.5 | 7.6 | 0.994 |
| LW _d | W/m ² | 217.8 | -10.1 | 14.1 | 0.93 | 3.1 | 8.9 | 0.94 |
| LW _u | W/m ² | -255.2 | -1.9 | 5.0 | 0.99 | 0.5 | 3.6 | 0.99 |
| SHF | W/m ² | 15.8 | 7.0 | 9.2 | 0.68 | 5.2 | 7.3 | 0.74 |
| LHF | W/m ² | 0.8 | -3.8 | 5.4 | 0.20 | -2.8 | 4.0 | 0.42 |
| ME | W/m ² | 12.0 | -0.7 | 7.8 | 0.89 | -2.4 | 7.0 | 0.96 |
| ALB | (-) | 0.82 | 0.02 | 0.05 | 0.79 | 0.03 | 0.06 | 0.83 |
| T _{2m} | °C | -13.3 | -0.04 | 0.7 | 0.994 | 0.5 | 0.8 | 0.996 |

Table 6.3: Modelled and observed mean SEB components and statistics of the differences (2009-2015) at station S9 close to the equilibrium line (1520 m a.s.l.). Statistics include means of measurements collected at S9, model bias (RACMO2.3pX - observations), RMSE of the bias as well as the determination coefficient of monthly mean data. Fluxes are set positive towards the surface.

| AWS Variable | S10 unit | Obs. mean | RACMO2.3p1 | | | RACMO2.3p2 | | |
|-----------------|------------------|--------------|------------|------|----------------|------------|------|----------------|
| | | | bias | RMSE | R ² | bias | RMSE | R ² |
| SW _d | W/m ² | 141.5 | 1.7 | 7.0 | 0.998 | -1.1 | 9.2 | 0.996 |
| SW _u | W/m ² | -113.8 | -2.7 | 12.0 | 0.991 | 1.4 | 7.6 | 0.994 |
| LW _d | W/m ² | 220.4 | -14.4 | 17.2 | 0.93 | -6.1 | 10.6 | 0.94 |
| LW _u | W/m ² | -252.5 | -1.0 | 4.8 | 0.99 | 1.2 | 3.5 | 0.992 |
| SHF | W/m ² | 11.9 | 7.6 | 10.8 | 0.57 | 6.6 | 8.2 | 0.79 |
| LHF | W/m ² | -2.7 | -3.5 | 5.6 | 0.22 | -1.3 | 3.1 | 0.71 |
| ME | W/m ² | 8.9 | 2.5 | 6.6 | 0.89 | -2.2 | 4.5 | 0.99 |
| ALB | (-) | 0.86 | -0.01 | 0.04 | 0.69 | 0.03 | 0.04 | 0.76 |
| T _{2m} | °C | -14.6 | 0.5 | 1.0 | 0.991 | 1.0 | 1.4 | 0.994 |

Table 6.4: Modelled and observed mean SEB components and statistics of the differences (2010-2015) at station S10 in the accumulation zone (1850 m a.s.l.). Statistics include means of measurements collected at S10, model bias (RACMO2.3pX - observations), RMSE of the bias as well as the determination coefficient of monthly mean data. Fluxes are set positive towards the surface.

6.4 Results: regional SMB

In Section 6.3, we discussed the overall good ability of RACMO2.3p2 to reproduce the contemporary climate of the GrIS, which is essential to estimate realistic SMB patterns. Here, we first compare SMB of the new and old model over the GrIS. For further evaluation, we zoom in on three regions where large SMB differences exist between the two versions.

6.4.1 Changes in SMB patterns

Figure 6.6a shows SMB from RACMO2.3p2 for the overlapping model period 1958-2015. Differences with the previous version 2.3p1 are shown in Fig. 6.6b and the changes in individual SMB components are depicted in Fig. 6.7. Owing to the modifications in the cloud scheme, clouds are sustained to higher elevations, enhancing precipitation further inland, while it decreases in low-lying regions. Changes are especially large in southeast Greenland where the decrease locally exceeds $300 \text{ mm w.e. yr}^{-1}$. Precipitation in the interior increases by up to $50 \text{ mm w.e. yr}^{-1}$ (Fig. 6.7a). This pattern of change is clearly recognisable in the SMB difference (Fig. 6.6b). In addition, the shallower saltation layer in the revised drifting snow scheme is responsible for reduced sublimation ($\sim 50 \text{ mm w.e. yr}^{-1}$; Fig. 6.7b) that reinforces the overall increase in SMB (Fig. 6.6b). Although drifting snow erosion changes locally, patterns are heterogeneous and the changes remain small when integrated over the GrIS (Fig. 6.7c). This process has only a limited contribution to SMB ($\sim 1 \text{ Gt yr}^{-1}$) resulting from drifting snow being transported away from the ice sheet towards the ice-free tundra and ocean.

In the percolation zone, the decrease in runoff (Fig. 6.7d) is governed by reduced surface melt (Fig. 6.7e), mostly resulting from the smaller grain size of refrozen snow and the lower soot concentration in snow that have increased surface albedo (not shown), further increasing SMB (Fig. 6.6b). In west and north-east Greenland, this decrease in runoff even exceeds that of melt by 50 to $100 \text{ mm w.e. yr}^{-1}$, a result of enhanced precipitation that increased the snow refreezing capacity (Fig. 6.7f). At higher elevations, the decrease in refreezing is exclusively driven by melt reduction (Figs. 6.7e and f), while at the very GrIS margins, the lower ice albedo used in RACMO2.3p2 (Fig. 6.2c) locally increases runoff (Fig. 6.7d), in turn decreasing SMB (Fig. 6.6b).

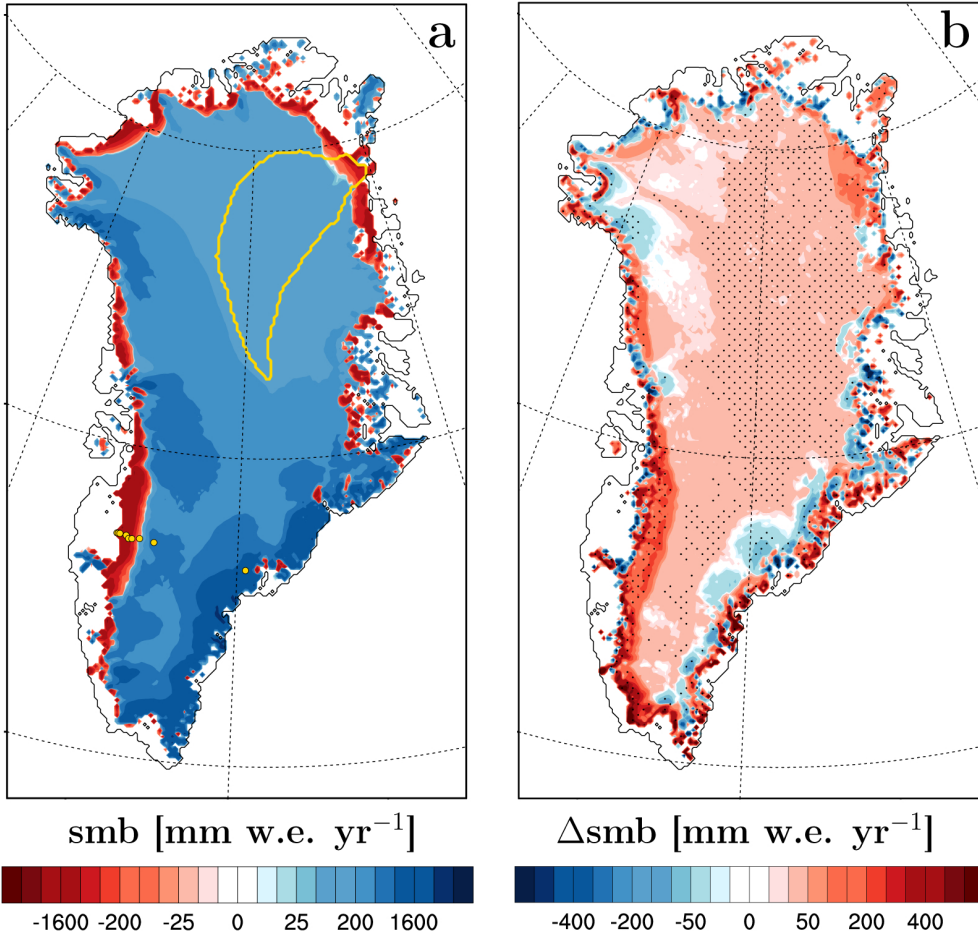


Figure 6.6: a) SMB (mm w.e. yr⁻¹) averaged for the period 1958-2015. The combined Zachariae Isstrøm and Nioghalvfjædsbrae (79N) glacier basins are delineated by the yellow line. Yellow dots locate the K-transect measurement sites in western Greenland and the single AWS operated in southeast Greenland. b) SMB difference (mm w.e. yr⁻¹) between RACMO2.3p2 and RACMO2.3p1 for the period 1958-2015. Areas showing significant difference are stippled in Fig. 6.6b: difference exceeds one unit of standard deviation of the difference between the two model versions.

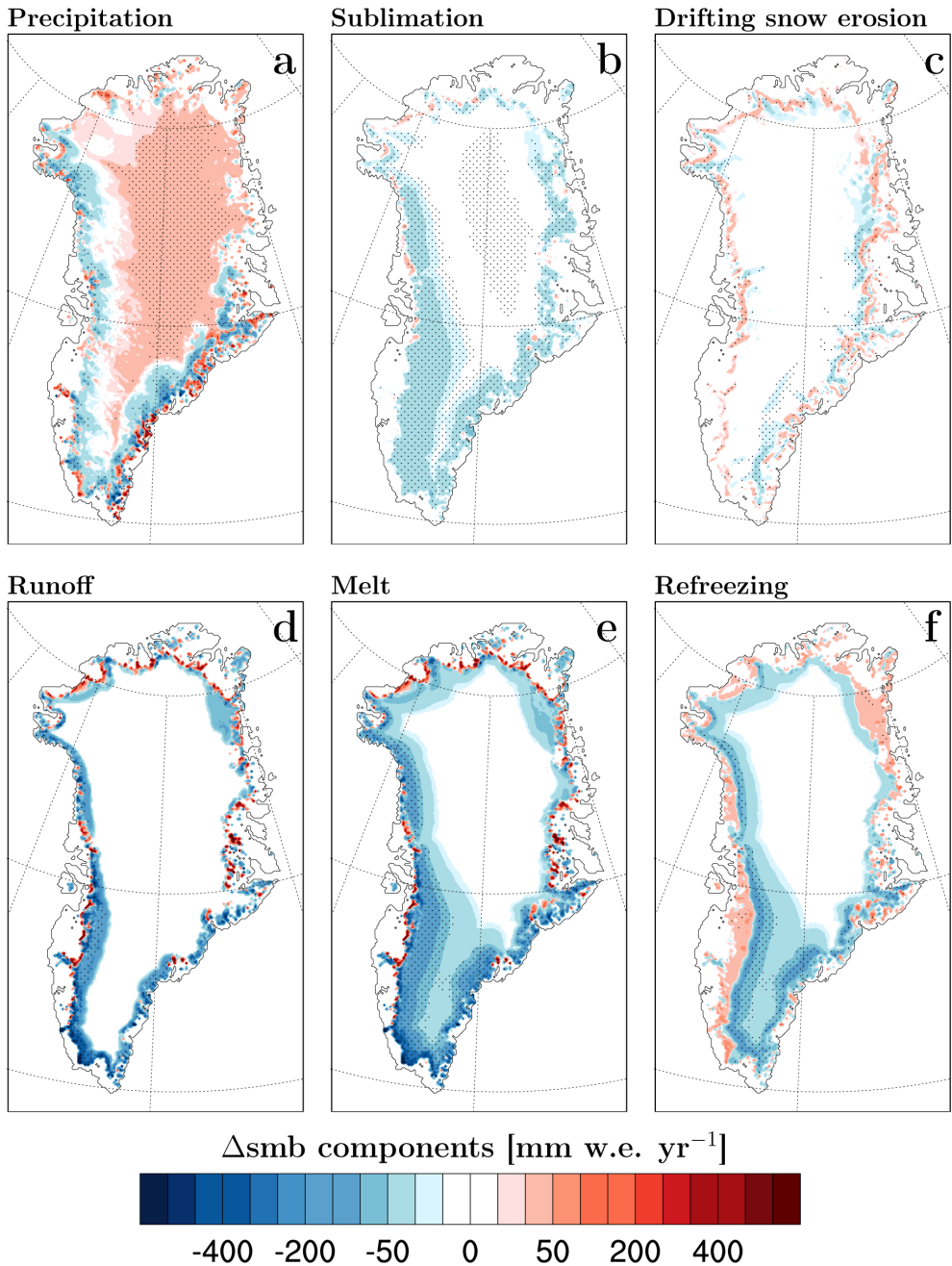


Figure 6.7: Difference in SMB components (mm w.e. yr^{-1}) between RACMO2.3p2 and RACMO2.3p1 averaged for the period 1958-2015. Areas showing significant difference are stippled: difference exceeds one unit of standard deviation of the difference between the two model versions.

6.4.2 Northeast Greenland

For northeast Greenland's two main glaciers, Zachariae Isstrøm and Nioghalvfjærdsbrae (79N glacier; yellow line in Fig. 6.6a), solid ice discharge estimates are available for the period 1975-2015 [Mouginot et al., 2015]. In these two catchments, model updates significantly improve the representation of SMB, that was substantially underestimated in the previous version. Figure 6.8a compares ice discharge (black dots) with modelled SMB (RACMO2.3p2 as blue dots and 2.3p1 in red) integrated over the two glacier basins for 1958-2015. In a balanced system, i.e. before discharge accelerated in 2001, SMB equals ice discharge. Averaged over 1975-2001, modelled SMB in RACMO2.3p2 (20.5 Gt yr^{-1}) is similar to the estimated glacial discharge of 21.2 Gt yr^{-1} , significantly improving upon version 2.3p1 (15.8 Gt yr^{-1}). The negative bias in RACMO2.3p2 (0.7 Gt yr^{-1} ; dashed blue line) is reduced by almost a factor of eight relative to the previous version (5.4 Gt yr^{-1}) and SMB now equals discharge within the uncertainty. Averaged over 2001-2015, basin mass loss accelerated due to enhanced surface runoff, decreasing SMB by 4.2 Gt yr^{-1} , and increased ice discharge (2.8 Gt yr^{-1}).

Figures 6.8b and c show mean SMB for 1958-2015 as modelled by RACMO2.3p2 and 2.3p1, respectively. In the percolation zone, the difference between the two model versions primarily results from the smaller refrozen snow grain size that reduces melt and runoff through increased surface albedo in RACMO2.3p2. To a smaller extent, reduced soot concentration delays the onset of melt in summer. In the ablation zone, snow cover persists longer before bare ice is exposed in late summer, in turn reducing runoff (Fig. 6.7d). Superimposed on this, precipitation has increased over the whole glacier basin (Fig. 6.7a), allowing for enhanced refreezing in snow (Fig. 6.7f) hence increasing SMB by 4.7 Gt yr^{-1} in RACMO2.3p2 (Fig. 6.6b). Note the large interannual variability in modelled SMB showing a maximum and minimum value of approximately 30 Gt yr^{-1} and 8.5 Gt yr^{-1} in RACMO2.3p2 vs. 25 Gt yr^{-1} and 0 Gt yr^{-1} in the previous version, stressing the importance of accurately modelling individual SMB components. In this dry region, underestimation of snowfall accumulation in RACMO2.3p1 initiated a pronounced feedback decreasing SMB: active drifting snow processes erode the shallow snow cover, exposing bare ice prematurely and moving the equilibrium line too far inland (Figs. 6.8b and c).

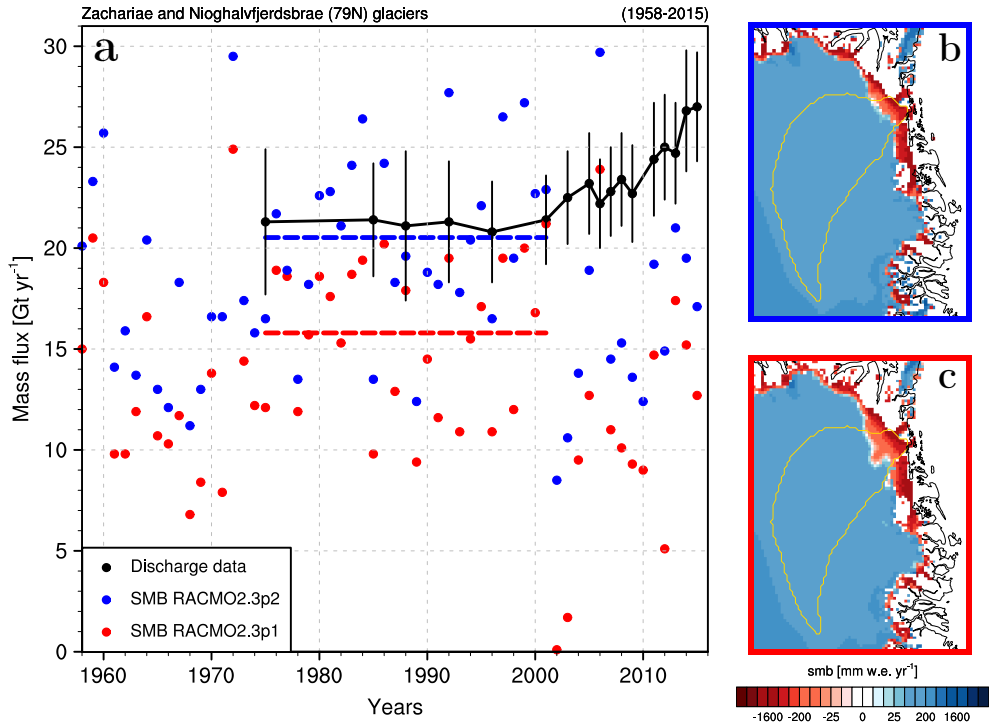


Figure 6.8: *a*) Modelled basin-integrated SMB in RACMO2.3p2 (blue dots) and RACMO2.3p1 (red dots) and ice discharge estimates (black dots, Mouginot et al. [2015]) from the glacier basins of Zachariae Isstrøm and Nioghalvfjærdsbrae (79N) in northeast Greenland (yellow line in Figs. 6.8b and c) for the period 1975-2015. Dashed lines represent average SMB for 1975-2001. Mean SMB as modelled by b) RACMO2.3p2 and c) RACMO2.3p1 in northeast Greenland for the period 1958-2015.

6.4.3 K-transect

The K-transect in southwest Greenland consists of eight stake sites where SMB is measured annually (yellow dots in Fig. 6.6a) [Van de Wal et al., 2012; Machguth et al., 2016b]. Figure 6.9a compares modelled (RACMO2.3p2 as blue dots and RACMO2.3p1 in red), with observed SMB (black dots) along the transect, averaged for the period 1991-2015. Using mean annual SMB at each station, the updated model shows a smaller bias ($-30 \text{ mm w.e. yr}^{-1}$), reduced RMSE ($-205 \text{ mm w.e. yr}^{-1}$), and a larger R^2 (0.97). In the low ablation zone ($< 600 \text{ m a.s.l.}$), the lower ice albedo increases runoff in summer, locally reducing SMB. Decreased runoff in the upper ablation zone, i.e. between 600 and 1500 m a.s.l., increases SMB, improving the agreement at all sites except SHR. A negative bias in SMB remains at site S6 where ice albedo in summer (0.45 in July) is underestimated by up to 0.1 (Fig. 6.5d). Above the equilibrium line ($> 1500 \text{ m a.s.l.}$), in situ stake SMB measurements systematically underestimate climatic SMB, as they do not or only partly account for internal accumulation, i.e. refreezing in the firn. For comparison at S10, we therefore use the difference between modelled total precipitation and melt instead of SMB, decreasing the bias and RMSE in RACMO2.3p2 by $260 \text{ mm w.e. yr}^{-1}$ and $200 \text{ mm w.e. yr}^{-1}$ to $-40 \text{ mm w.e. yr}^{-1}$ and $210 \text{ mm w.e. yr}^{-1}$, respectively. Measured and modelled SMB-to-elevation gradients are estimated using a linear regression: $3.21 \text{ mm w.e. m}^{-1}$ from observations, $2.62 \text{ mm w.e. m}^{-1}$ in RACMO2.3p1, and $3.16 \text{ mm w.e. m}^{-1}$ in RACMO2.3p2, indicating a notable improvement in model performance along the K-transect.

Figures 6.9b and c show time series of measured (dashed lines) and modelled SMB (continuous lines; RACMO2.3p2) at each site along the K-transect for the period 1991-2016. The model realistically captures interannual variability in the SMB signal although substantial biases remain at stations SHR and S6 (Table 6.5).

| Stakes SMB | Obs. mean | RACMO2.3p1 | | | RACMO2.3p2 | | | Coordinates | | |
|---------------|--------------|------------|------|-------|------------|------|-------|----------------------|----------------------|-----------|
| | | bias | RMSE | R^2 | bias | RMSE | R^2 | lon. ($^{\circ}$ W) | lat. ($^{\circ}$ N) | elev. (m) |
| S4 | -4.2 | 0.64 | 0.84 | 0.40 | -0.05 | 0.51 | 0.47 | -50.20 | 67.10 | 383 |
| S5 | -3.7 | 0.64 | 0.79 | 0.45 | -0.08 | 0.46 | 0.50 | -50.09 | 67.10 | 490 |
| SHR | -3.1 | -0.32 | 0.57 | 0.53 | 0.41 | 0.62 | 0.51 | -49.94 | 67.10 | 710 |
| S6 | -1.7 | -0.68 | 0.87 | 0.30 | -0.56 | 0.78 | 0.29 | -49.40 | 67.08 | 1010 |
| S7 | -1.5 | -0.65 | 0.75 | 0.64 | -0.15 | 0.37 | 0.68 | -49.15 | 66.99 | 1110 |
| S8 | -0.8 | -0.31 | 0.49 | 0.62 | -0.03 | 0.28 | 0.76 | -48.88 | 67.01 | 1260 |
| S9 | -0.2 | -0.13 | 0.21 | 0.83 | 0.07 | 0.16 | 0.88 | -48.25 | 67.05 | 1520 |
| S10 | 0.3 | -0.25 | 0.33 | 0.44 | -0.04 | 0.21 | 0.45 | -47.02 | 67.00 | 1850 |

Table 6.5: Modelled and observed mean annual SMB (m w.e. yr^{-1}) and statistics of the differences at S4, S5, SHR, S6, S7, S8 and S9 over 1991-2015; measurements at S10 are compared to modelled total precipitation minus melt for the period 1994-2015. Spatial coordinates of each site are listed.

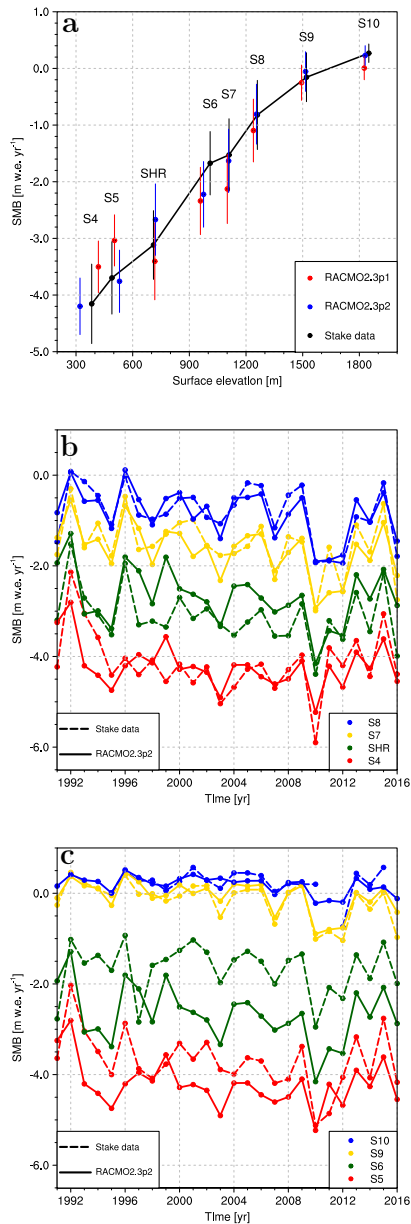


Figure 6.9: a) Observed and simulated SMB ($m \text{ w.e. yr}^{-1}$) along the K-transect in west Greenland (67°N), averaged for the period 1991-2015. The observed SMB (black dots) at S4, S5, SHR, S6, S7, S8, S9 and S10 are based on annual stake measurements; S10 observations cover 1994-2015. The coloured bars represent the standard deviation (1σ) around the 1991-2015 modelled and observed mean value. Modelled SMB at stake sites are displayed for RACMO2.3p2 (blue dots) and RACMO2.3p1 (red dots). Figure 6.9b shows time series of modelled (continuous lines) and observed (dashed lines) annual SMB at stakes S4, SHR, S7 and S8 for the period 1991-2016. Similar time series are shown for the S5, S6, S9 and S10 in Fig. 6.9c.

6.4.4 Southeast Greenland

Southeast Greenland experiences topographically forced precipitation maxima in winter, followed by high melt rates in summer, allowing for the formation of perennial firn aquifers [Forster et al., 2014; Koenig et al., 2014]. In April 2014, an AWS was installed in the aquifer zone of the southeast GrIS (yellow dot in Fig. 6.6a). In August 2015, the AWS was relocated from 1563 m a.s.l (66.18°N and 39.04°W) to 1663 m a.s.l (66.36°N and 39.31°W). Figure 6.10 shows time series of snow albedo and cumulative snow melt energy (expressed in mm w.e.) modelled by RACMO2.3p2 (blue lines) and RACMO2.3p1 (red lines), and calculated from the AWS data (yellow lines) for the summer of 2014. The comparison is limited to 2014 because of a 3 months data gap in summer 2015.

As melt wets the snow in summer, surface albedo gradually decreases from values typical for dry fresh snow (0.85) to wet old snow (~ 0.75) in late summer, before sharply increasing again when a new fresh snow cover is deposited (yellow line in Fig. 6.10a). In the previous model version, surface albedo could drop to values as low as ~ 0.66 in summer (JJA), e.g. days 152 to 243, underestimating albedo by 0.04 on average. The bias is reduced to 0.01 in RACMO2.3p2 as combined lower soot concentration and decreased grain size of refrozen snow increase the surface albedo. The remaining small negative bias is mostly ascribable to a too rapid snow metamorphism from fresh to old snow that leads to a premature drop in surface albedo, e.g. days 140 to 160. Sporadic fresh snow deposition over older snow, characterised by sharp peaks in surface albedo during summer, are well timed by the model. Consequently, the cumulative melt obtained at the end of summer (702 mm w.e.; blue line in Fig. 6.10b) is reduced by ~ 100 mm w.e. relative to RACMO2.3p1 (red line), a significant improvement when compared to observations (639 mm w.e.; yellow line).

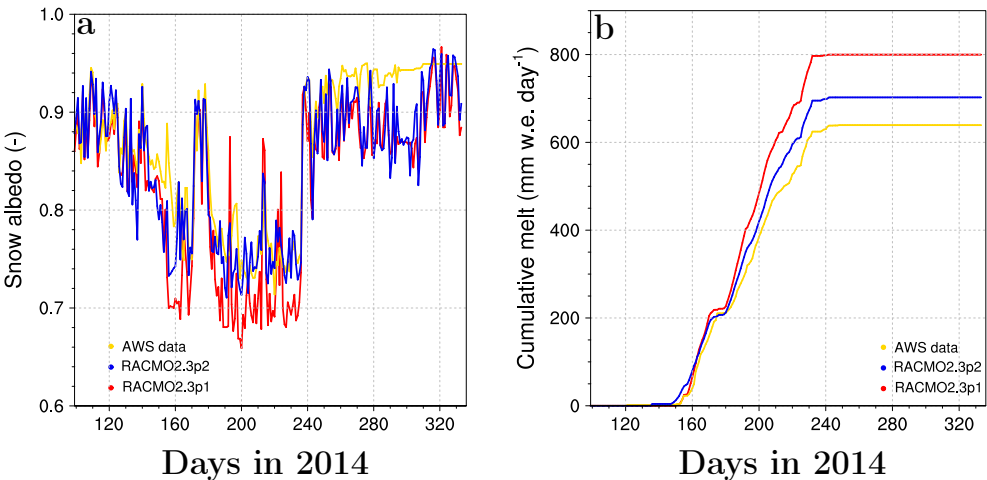


Figure 6.10: Time series of a) daily snow albedo, b) cumulative surface melt (mm w.e. per day) modelled by RACMO2.3p2 (blue lines), RACMO2.3p1 (red lines) and measured (yellow lines) at the southeast AWS (66°N; 33°W; 1563 m a.s.l.) during summer 2014.

6.5 Results: SMB of the contiguous ice sheet

6.5.1 Modelled SMB at 11 km

In Figure 6.11, we evaluate modelled SMB in RACMO2.3p2 using 182 measurements collected in the GrIS accumulation zone (white dots in Fig. 6.1) and 1073 stake observations from 213 sites located in the ablation zone (yellow dots in Fig. 6.1). The increased precipitation in the GrIS interior reduces the negative bias in the 11 km product (blue dots in Fig. 6.11a) compared to the previous model version (red dots in Fig. 6.11a). For the full data set, a significant bias of $-22 \text{ mm w.e. yr}^{-1}$ and RMSE of $72 \text{ mm w.e. yr}^{-1}$ remain in RACMO2.3p2. Sites experiencing the highest precipitation rates on the steep slopes of southeast Greenland ($> 0.5 \text{ m w.e. yr}^{-1}$) primarily contribute to this bias. If only values $< 0.5 \text{ m w.e. yr}^{-1}$ are considered (156 measurements), the bias and RMSE decrease from $-26 \text{ mm w.e. yr}^{-1}$ and $52 \text{ mm w.e. yr}^{-1}$ in RACMO2.3p1 to only $-7 \text{ mm w.e. yr}^{-1}$ and $49 \text{ mm w.e. yr}^{-1}$ in RACMO2.3p2. In the ablation zone (Fig. 6.11b), the updated model performs as well as the previous version [Noël et al., 2016] although SMB remains overestimated in the lower sectors, caused by inaccurately resolved steep slopes, low ice albedo and relatively large turbulent fluxes at the GrIS margins, which require further downscaling (see Section 6.5.2).

Integrated over the GrIS, modelled SMB has increased by 66 Gt yr^{-1} (415 Gt yr^{-1} ; +19%) compared to the previous version. This difference is dominated by a significant increase in SMB in the percolation zone of the GrIS, driven by reduced meltwater runoff (61 Gt yr^{-1} or -22%) and reduced sublimation (10 Gt yr^{-1} or -24%), while precipitation decreased by less than 1% (5 Gt yr^{-1}); the latter can be explained by the smaller GrIS area ($\sim 10,000 \text{ km}^2$ or 0.6%) in the new ice mask. We deem these changes in the 11 km fields to be realistic. For the poorly resolved marginal areas, the SMB product requires further statistical downscaling to reproduce the high melt rates in these rugged regions at the ice sheet margins. At 11 km resolution, runoff is locally underestimated by up to 6 m w.e. yr^{-1} , e.g. station QAS_L in southern Greenland (red stars in Fig. 6.11b).

6.5.2 Downscaled SMB to 1 km

To solve these issues at the margins, we apply the downscaling technique described in Noël et al. [2016], which includes elevation and ice albedo corrections. As a result, modelled runoff increases by 82 Gt yr^{-1} ($\sim 37\%$) to 305 Gt yr^{-1} for the period 1958-2015, compared to the 11 km product, and the SMB bias and RMSE in the GrIS ablation zone are reduced by 480 and 460 mm w.e. yr^{-1} , respectively. The error at QAS_L is reduced to 2 m w.e. yr^{-1} (red stars in Fig. 6.11c). A major improvement upon Noël et al. [2016] is that no additional precipitation correction is required here as the remaining negative bias in the GrIS interior has been almost eliminated in RACMO2.3p2 (Fig. 6.11a). At 1 km resolution, precipitation contributes 693 Gt yr^{-1} to GrIS SMB. Relative to the 11 km product, GrIS-integrated SMB at 1 km decreases by 59 Gt yr^{-1} (-14%) to 356 Gt yr^{-1} , in line with our previous estimate of 338 Gt yr^{-1} (+5%) [Noël et al., 2016]. This confirms once more that 11 km resolution is insufficient to resolve runoff patterns over narrow ablation zones and small outlet glaciers, and that further downscaling is essential to obtain realistic GrIS SMB.

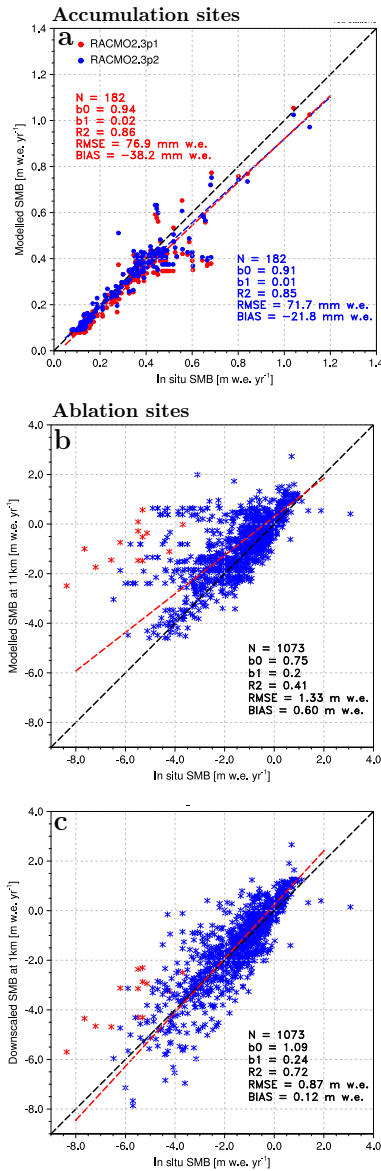


Figure 6.11: Comparison between a) modelled, i.e. RACMO2.3p2 (blue) and RACMO2.3p1 (red) at 11 km, and observed SMB (m w.e. yr^{-1}) collected in the GrIS accumulation zone (white dots in Fig. 6.1). Regressions for RACMO2.3p2 (blue) and version 2.3p1 (red) are displayed as dashed lines. Comparison between SMB measurements from the GrIS ablation zone (yellow dots in Fig. 6.1) and b) original RACMO2.3p2 data at 11 km, c) downscaled product at 1 km. Red stars correspond to measurements collected at station QAS_L at the southern tip of Greenland. Regression including all records is displayed as red dashed line in Figs. 6.11b and c. Main statistics including number of records (N), regression slope (b_0) and intercept (b_1), determination coefficient (R^2), bias and RMSE are listed for each graph.

6.6 Remaining limitations and challenges

6.6.1 Model resolution

Extensive model evaluation confirms that RACMO2.3p2 realistically reproduces the contemporary climate and SMB of Greenland, although significant biases remain. However, while a 11 km grid is sufficient to resolve large-scale inland SMB patterns, it does not well resolve irregular, low-lying regions at the GrIS margins where runoff peaks. There, the main issue remains to accurately resolve total runoff of meltwater from narrow ablation zones and small outlet glaciers. This demonstrates the need for higher resolution (statistically or dynamically) downscaled products, e.g. the 1 km product as presented here, for regional mass balance studies.

An alternative approach is to carry out a dedicated Greenland simulation at higher spatial resolution, e.g. 5.5 km [Langen et al., 2017; Mottram et al., 2017]. This increase in resolution does lead to better resolved SMB gradients over marginal glaciers, without exceeding the physics constraints of a hydrostatic model like RACMO2. Subsequently applying the statistical downscaling technique to this 5.5 km product would likely result in further improvements.

6.6.2 Turbulent fluxes

Another model limitation stems from the turbulent fluxes scheme. While LHF remains generally small and contributes little to the energy budget, accurate SHF is crucial to capture extreme melt events along the GrIS margins [Fausto et al., 2016], such as those that occurred in summer 2012 [Nghiem et al., 2012]. However, SHF shows significant biases in RACMO2.3p2 in low-lying regions at the GrIS margins. Improving the representation of the GrIS surface roughness and surface elevation using higher spatial resolution could reduce these biases.

6.6.3 Surface albedo

Snow melt rate is highly sensitive to soot concentration in snow [Van Angelen et al., 2012]. Although assumed to be constant in time and space in RACMO2, Takeuchi et al. [2014] show a heterogeneous distribution of impurities (soot, dust, microbiological material) over the GrIS, with a gradual increase towards lower elevations due to a) the proximity of dust sources in the tundra region and, b) downslope transport of previously deposited soot by meltwater runoff.

Over bare ice, the accumulation of cryoconites and the growth of algae play a major role in reducing surface albedo [Musilova et al., 2016; Stibal et al., 2017]. Therefore, explicitly modelling impurity concentration on ice, as described in Cook et al. [2017a,b], could substantially improve melt estimates. Future climate projections should include such a bio-darkening feedback [Tedesco et al., 2016b].

6.7 Summary and conclusions

We present a detailed evaluation of the regional climate model RACMO2.3p2 (1958-2016) over the Greenland ice sheet (GrIS). The updated model generates more inland precipitation at the expense of marginal regions, reducing the dry bias in the GrIS interior. Impurity concentration in snow, i.e. soot, has been decreased by a factor of two, minimising the melt rate overestimation in the GrIS percolation zone. We demonstrate that the model successfully reproduces the contemporary climate of the GrIS compared to daily meteorological records and radiative energy flux measurements from 23 AWS sites. Apart from the ultimate margins, the model also proves to accurately capture the seasonal cycle of radiative and turbulent heat fluxes as well as surface albedo along the K-transect in southwest Greenland. Compared to SMB observations, RACMO2.3p2 generally improves on the previous version, especially in the extensive GrIS interior. SMB improvements are also found along the K-transect as well as in northeast and southeast Greenland. This model version will be used for future climate scenario projections at 11 km resolution. Nonetheless, since runoff from narrow glaciers in the GrIS margins remains poorly resolved at this resolution, it is necessary to further statistically downscale present-day and future SMB fields to higher spatial resolutions for use in regional mass balance studies.

Discussion and outlook

7.1 General conclusions

Since the mid-1990s, the GrIS has experienced a significant mass loss acceleration caused by increased meltwater runoff (61%) and elevated solid ice discharge from calving glaciers (39%). To complement scarce in situ measurements and brief remote sensing time series, we show that RCMs are indispensable tools to estimate and understand the SMB of the GrIS, and explain ongoing mass loss. Combining RCM output with in situ and remote sensing measurements, this thesis aims at i) investigating the contemporary climate and mass changes of the GrIS, the Greenland's peripheral GICs and the Canadian Arctic, and ii) identifying and understanding the surface processes that triggered the recent mass loss acceleration. To achieve these goals, we use the state-of-the-art RCM RACMO2 developed and specifically adapted to simulate the climate and SMB of polar ice sheets and ice caps.

First, the present-day (1958-2015) climate and SMB of the GrIS are simulated at 11 km resolution by RACMO2.3. For evaluation, model output is compared to in situ measurements of SMB and SEB, including radiative and turbulent fluxes, collected along the K-transect in southwest Greenland (67°N). Good agreement is found, but significant biases remain. In particular, snowfall accumulation and meltwater runoff are underestimated over the vast interior and along the irregular low-lying margins of the GrIS, respectively.

One of the issues is that a spatial resolution of 11 km is insufficient to resolve the large SMB gradients of the GrIS margins, where narrow ablation zones, small outlet glaciers and marginal ice caps are found. Therefore, we developed a novel statistical downscaling procedure, providing detailed maps of SMB at high spatial (1 km) and temporal resolution (daily) at reasonable computational cost. The downscaled product clearly outperforms the original RACMO2.3 output at 11 km. Due to inherent biases in RACMO2.3, the downscaled product underestimates accumulation in the GrIS interior, and an artificial precipitation correction is required. The new 1 km product should be useful for studies addressing the mass balance of small ice bodies that, although significantly contributing to Greenland mass loss, are not properly resolved at 11 km resolution.

The downscaled product, in combination with remote sensing and in situ SMB measurements, was key to identify and confirm a tipping point in the mass balance of Greenland's GICs in 1997, tripling the mass loss relative to preceding decades (Fig. 7.1). Efficient meltwater refreezing in firn is crucial to sustain the GICs, as summer melt often exceeds precipitation in these dry regions. As a result of Arctic warming, the downscaled product reveals that meltwater retention has drastically decreased for the GICs since 1997, leading to irreversible mass loss. Decades of increasing melt depleted firn pore space, prohibiting active meltwater refreezing in inland accumulation zones and enhancing surface

runoff 65% faster than meltwater production (Fig. 7.2). The much higher GrIS has maintained its refreezing capacity for now, with $\sim 45\%$ of meltwater being retained in the firn layer.

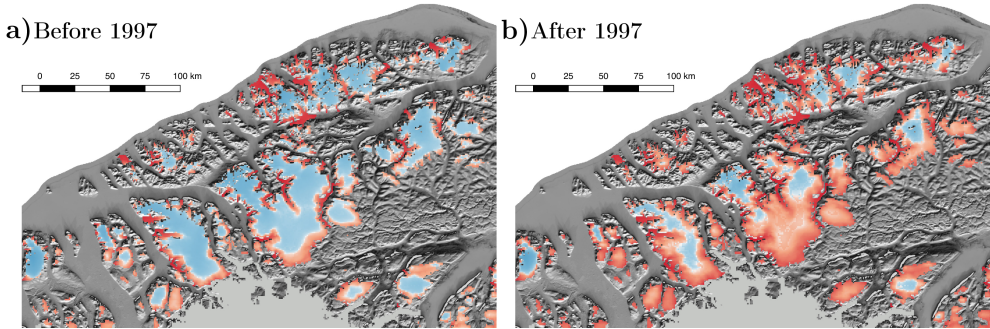


Figure 7.1: *SMB of Hans Tausen ice cap and surrounding small ice bodies in northern Greenland before (a) and after the tipping point in 1997 (b). Since 1997, the accumulation zone (blue) has shrunk and the ablation zone (red) has grown further inland, tripling the pre-1997 mass loss.*

Similar processes are active in the CAA. Frequent southwesterly advection of warm air, driven by sustained negative summer NAO phases, leads to higher near-surface temperatures, enhancing surface melt. While larger and healthier ice caps of the northern CAA compensate increasing melt through more active refreezing in inland firn zones, lower-lying and warmer ice fields of the southern CAA already lost most of their buffering capacity in the early 1980s. Consequently, the southern CAA ice masses have experienced six decades of uninterrupted mass loss and will likely vanish within the next 400 years.

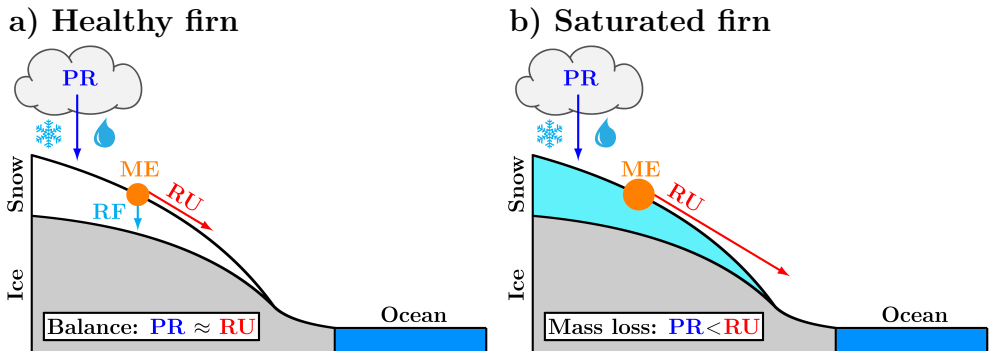


Figure 7.2: *Scheme showing a) active meltwater refreezing in firn for healthy ice caps, b) enhanced runoff over saturated firn of decaying ice caps.*

Based on our comprehensive evaluations of RACMO2.3, we present an updated version of the model, referred to as RACMO2.3p2, that addresses most remaining biases. Updated parameters in the cloud scheme and the snow module eliminate the accumulation bias in the ice sheet interior, and reduce the melt overestimate in the percolation zone. The new 11 km resolution simulation is thoroughly evaluated

against various in situ measurements, and stands out as an improved representation of the contemporary near-surface climate, SEB and SMB of Greenland (1958-2016). Furthermore, the 1 km SMB product no longer requires an additional precipitation correction in the accumulation zone. The new model version will be used to carry out future climate scenario projections for the Arctic region, forced by the state-of-the-art CESM global model. These data will hopefully prove to be useful in many applications, including e.g. mass balance reconstruction, contemporary sea level rise estimate, ice sheet and ice caps dynamics modelling. Especially the 1 km downscaled product is attractive for studies investigating changes in GrIS meltwater retention and addressing the mass balance of small ice bodies or individual glacier catchments.

7.2 Modelling challenges

RACMO2 is constantly evolving and its performance over ice sheets has significantly improved over the years. To further enhance the model accuracy, parameterisation and modelling of specific physical processes still require attention. In the following subsections, we discuss some outstanding modelling challenges in RACMO2.

7.2.1 Clouds and turbulent fluxes

Clouds

Clouds play a pivotal role in the modulation of the GrIS SEB and SMB through surface melt. In spite of this, cloud physics and interactions with the surface remain problematic in RCMs. In particular, cloud properties such as i) the partitioning between liquid, mixed and solid water in clouds, governing the precipitation phase, ii) integrated liquid/ice water content, determining cloud optical thickness and emissivity, and iii) cloud altitude, controlling temperature profiles, strongly affect melt through regulating SW_d and LW_d . In ablation zones, thin and bright clouds mitigate summer melt by reflecting incoming solar radiation, hence reducing SW_d absorption at the dark bare ice surface. In contrast, optically thick clouds are responsible for large LW_d in the highest sectors of the GrIS, warming up the firn and increasing surface melt [Bennartz et al., 2013]. In winter, clouds can directly affect SMB by reducing meltwater refreezing in firn during nighttime, as surface warming by clouds often exceeds surface radiative cooling [Van Tricht et al., 2016]. Compared to Cloud-SAT/Calypso satellite measurements, cloud cover, liquid/ice water content and optical thickness are underestimated in RACMO2.3 [Van Tricht et al., 2016], leading to SW_d being overestimated and LW_d underestimated. Nonetheless, the paucity of available measurements prevents a thorough model evaluation and hampers further cloud physics development.

Sensible heat flux

In the GrIS ablation zone, extreme melt episodes are primarily driven by SHF, e.g. providing up to 60% of melt energy in July 2012 [Fausto et al., 2016]. In these marginal regions, RCMs systematically underestimate SHF [Fettweis et al., 2011; Noël et al., 2015; Fausto et al., 2016], causing significant underestimation of runoff. Improving the representation, in time and space, of the surface aerodynamical roughness could significantly reduce SHF biases.

7.2.2 Surface albedo

Snow

In RACMO2, snow albedo is among other factors parameterised as a function of the impurity concentration in snow, i.e. soot and dust, that significantly affects melt rates [Van Angelen et al., 2012]. In the model, the impurity concentration is assumed constant in time and space, although a maximum concentration is measured in the lower accumulation zone and a minimum in the GrIS interior [Takeuchi et al., 2014]. Prescribing a spatially varying field of impurity concentration, derived from e.g. remote sensing measurements, could improve the modelled snow albedo, and better capture melt distribution and magnitude over the snow-covered GrIS (Lhermitte, personal communication).

Bare ice

In the ablation zone, the growth of algae combined with deposition of cryoconites significantly contribute to bare ice albedo reduction [Musilova et al., 2016; Stibal et al., 2017]. In RACMO2, ice albedo is prescribed from MODIS records of surface albedo, fixed in time but variable in space. Although valuable for the representation of present-day melt, these remote sensing data cannot be used to extrapolate future surface darkening of the ablation zone. To account for the ice albedo decline in time, explicit modelling of the ice albedo variation, based on changes in bio-impurity concentration [Cook et al., 2017a,b], might improve ice melt estimates in future climate projections.

7.2.3 Firn processes

Meltwater retention and refreezing in the firn is key to mitigate GrIS surface runoff. In RACMO2, runoff is produced after saturation of the firn column with refrozen water. Nevertheless, Machguth et al. [2016a] show that the formation of impermeable ice lenses limits the availability of underlying pore space, causing an earlier onset of runoff. In addition, these ice lenses favour lateral water transport in snow and heterogeneous vertical infiltration through preferential ice conduits, i.e. piping [Humphrey et al., 2012]. RACMO2 does not treat lateral water exchange in snow and preferential vertical transport and percolation through semi-impermeable ice lenses. Including these processes in RACMO2 might lead to further improvements.

7.2.4 Spatial resolution and non-hydrostatic models

The 1 km SMB product significantly outperforms the original SMB at 11 km, but the accuracy of the statistical downscaling method remains dependent on the quality of the forcing fields. At 11 km resolution, small ice bodies and narrow ablation zones remain unresolved in RACMO2, introducing uncertainties in the downscaled product. Therefore, erroneous SMB gradients are extrapolated from neighbouring ice sheet grid-cells, and are not necessarily representative of the local climate conditions. This issue highlights the need for a dedicated Greenland simulation at higher spatial resolution, e.g. 5.5 km [Langen et al., 2017; Mottram et al., 2017]. Increasing the horizontal resolution might lead to better resolved glacier outlines and surface topography and enable local estimates of SMB gradients over previously unresolved ice bodies (Fig. 7.3).

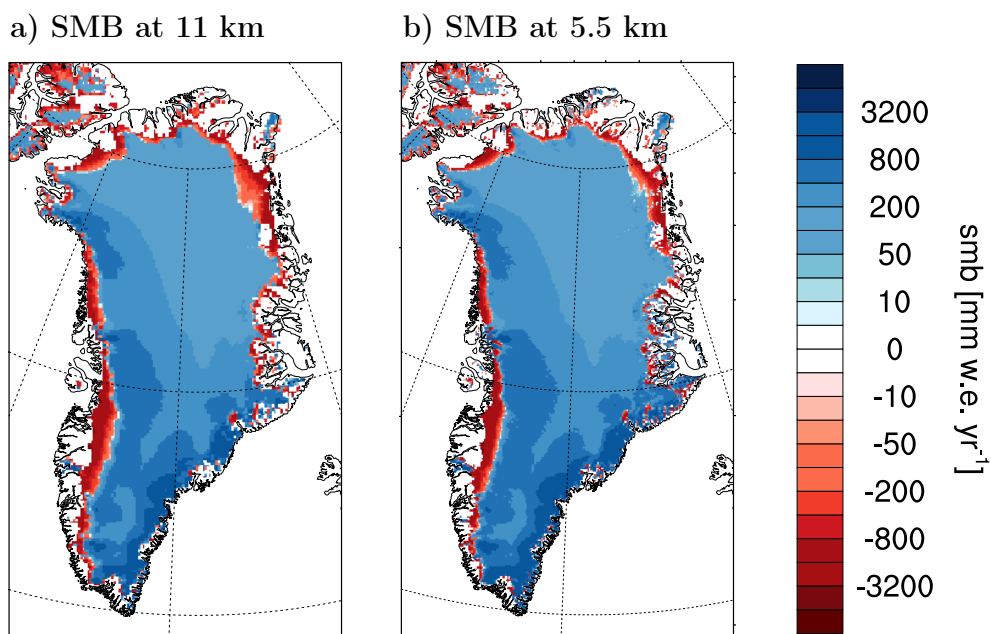


Figure 7.3: Annual SMB as modelled by RACMO2.3p2 at a) 11 km [Noël et al., 2015] and b) 5.5 km for the period 2003-2007 [Van de Berg, personal communication].

However, as RACMO2 is a hydrostatic model, its horizontal resolution cannot be increased indefinitely without violating the physics assumptions of the model. To reach kilometre resolutions, a non-hydrostatic model, capable of explicitly resolving smaller scale turbulence and convection, should be used. For example, the non-hydrostatic model HARMONIE-AROME [Bengtsson et al., 2017] is run operationally to forecast Greenland's weather at 2.5 km resolution since 2016 [Mottram et al., 2016].

7.3 Outlook

This thesis work shows that the representation of the GrIS contemporary climate and SMB is improved in the updated RACMO2.3p2 model and derived statistically downscaled products. The new model version will be used in forthcoming studies, investigating the present-day and future mass loss of Arctic glaciers.

First, a dedicated 5.5 km simulation will be performed over Greenland. To improve the model lateral boundary forcing, recently published ERA5 re-analyses (<https://www.ecmwf.int/>), available at higher horizontal resolution than its predecessor ERA-Interim (31 km vs. 80 km), will be used. To date, ERA5 is restricted to the period 2010-2016, but will soon be extended back to 1979. Further statistically downscaling the 5.5 km product to 1 km or better will hopefully provide a new benchmark of present-day GrIS SMB.

In chapter 5, we show that the downscaling technique can be successfully exported to model other steep and narrow Arctic glaciers. The recent release of the new high-resolution ArcticDEM (0.5 m; <https://www.pgc.umn.edu/data/arcticdem/>) and ice masks from the Randolph Glacier Inventory (RGI) [Pfeffer et al., 2014] offers the opportunity to extend the downscaled product to the small ice caps of Svalbard (Fig. 7.4), Iceland and the Russian Arctic. Combining high-resolution climate modelling and statistical downscaling, we aim at releasing a coherent data set of daily, 1 km (or higher) SMB components covering all Arctic glaciers. In the southern hemisphere, steep local SMB gradients over glaciers in Patagonia [Lenaerts et al., 2013] and the Antarctic Peninsula [Van Wessem et al., 2016] suggest that statistical downscaling could be beneficial to realistically reproduce SMB in these complex terrains.

Finally, we aim at conducting two GrIS climate projections, using RCP2.6 and RCP8.5 scenarios and extending to 2100, forced by the climate output of the Community Earth System Model CESM2.0. Statistically downscaling these future simulations paves the way to better resolve and quantify the future mass loss of Arctic ice bodies, further improving our projections of 21st century sea level rise.

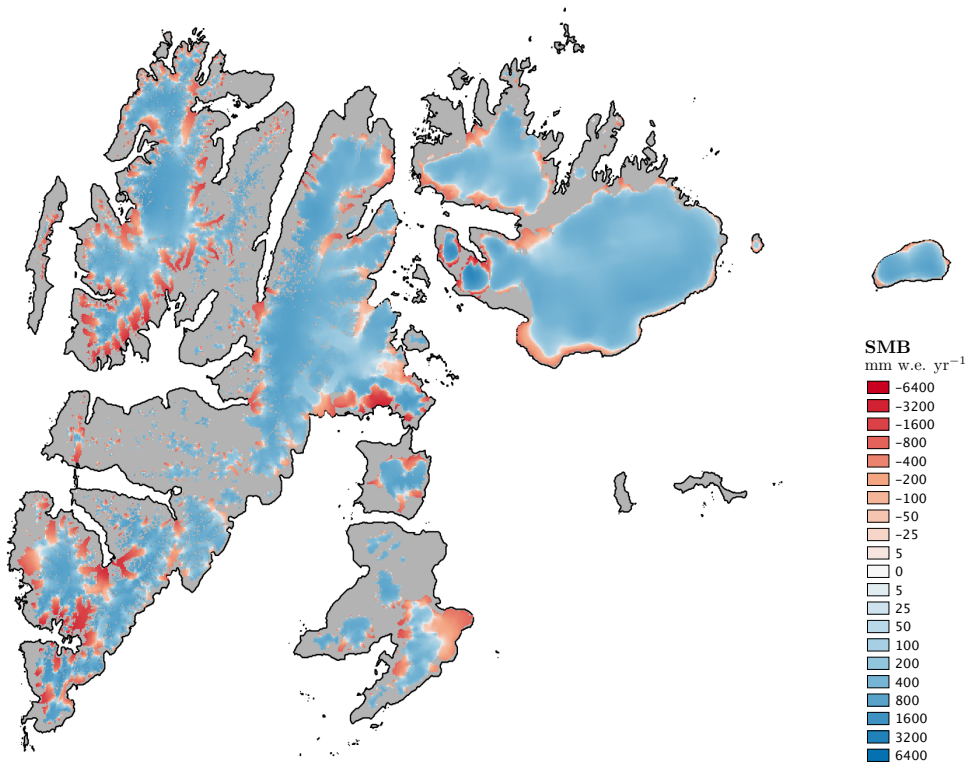


Figure 7.4: First attempt to downscale Svalbard SMB as modelled by RACMO2.3p2 at 11 km to 500 m resolution (1958-2016).

Bibliography

- W. Abdalati, W. Krabill, E. Frederick, S. Manizade, C. Martin, J. Sonntag, R. Swift, R. Thomas, J. Yungel, and R. Koenner. Elevation changes of ice caps in the Canadian Arctic Archipelago. *Journal of Geophysical Research*, 109: F04007, 2004. doi: 10.1029/2003JF000045.
- A. P. Ahlstrøm, P. Gravesen, S. B. Andersen, D. van As, M. Citterio, R. S. Fausto, S. Nielsen, H. F. Jepsen, S. S. Kristensen, E. L. Christensen, L. Stenseng, R. Forsberg, S. Hanson, and D. Petersen. A new Programme for Monitoring the Mass Loss of the Greenland Ice Sheet. *Geologic survey of Denmark and Greenland bulletin*, 15:61 – 64, 2008. doi: www.geus.dk/publications/bull.
- J. T. Andrews, G. Holdsworth, and J. D. Jacobs. Glaciers of the Arctic Islands. Glaciers of Baffin Island. *USGS Professional Paper*, 1386-J-1:J162 – J198, 2002.
- P. D. Baird. Method of nourishment of the Barnes ice cap. *Journal of Glaciology*, 2:2 – 9, 1952.
- R. C. Bales, J. R. McConnell, E. Mosley-Thompson, and B. Csatho. Accumulation over the Greenland ice sheet from historical and recent records. *Journal of Geophysical Research*, 106(D24):33813 – 33825, 2001. doi: 10.1029/2001JD900153.
- R. C. Bales, Q. Guo, D. Shen, J. R. McConnell, G. Du, J. F. Burkhart, V. B. Spikes, E. Hanna, and J. Cappelen. Annual accumulation for Greenland updated using ice core data developed during 2000-2006 and analysis of daily coastal meteorological data. *Journal of Geophysical Research*, 114(D6):D06116, 2009. doi: 10.1029/2008JD011208.
- J. L. Bamber, S. Ekholm, and W. B. Krabill. A new, high-resolution digital elevation model of Greenland fully validated with airborne laser altimeter data. *Journal of Geophysical Research*, 106:6733 – 6745, 2001. doi: 10.1029/2000JB900365.
- H. W. Barker, J. N. S. Cole, J.-J. Morcrette, R. Pincus, P. Räisänen, K. von Salzen, and P. A. Vaillancourt. The Monte Carlo Independent Column Approximation: An assessment using several global atmospheric models. *Quarterly Journal of the Royal Meteorological Society*, 134:1463 – 1478, 2008. doi: 10.1002/qj.303.
- A. C. M. Beljaars, A. R. Brown, and N. Wood. A new parametrization of turbulent orographic form drag. *Quarterly Journal of the Royal Meteorological Society*, 130:1327 – 1347, 2004. doi: 10.1256/qj.03.73.
- L. Bengtsson, U. Andrae, T. Aspelien, Y. Batrak, J. Calvo, W. de Rooy, E. Gleeson, B. Hansen-Sass, M. Homleid, M. Hortal, K. Ivarsson, G. Lenderink, S. Niemelä, K.P. Nielsen, J. Onvlee, L. Rontu, P. Samuelsson, D. S. Muñoz, A. Subias, S. Tijn, V. Toll, X. Yang, , and M. Ø. Költzow. The HARMONIE-AROME Model Configuration in the ALADIN-HIRLAM NWP System. *Mon. Wea. Rev.*, 145:1919 – 1935, 2017. doi: https://doi.org/10.1175/MWR-D-16-0417.1.
- R. Bennartz, M. D. Shupe, D. D. Turner, V. P. Walden, K. Steffen, C. J. Cox, M. S. Kulie, N. B. Miller, and C. Pettersen. July 2012 Greenland melt extent enhanced by low-level liquid clouds. *Nature*, 496(7443):83 – 86, 2013. doi: 10.1038/nature12002.
- P. Bezeau, M. Sharp, D. Burgess, and G. Gascon. Firn profile changes in response to extreme 21st-century melting at Devon Ice Cap, Nunavut, Canada. *Journal of Glaciology*, 59:981 – 991, 2013. doi: http://dx.doi.org/10.3189/2013JG12J208.
- T. Bolch, L. Sandberg Sørensen, S. B. Simonsen, N. Mölg and H. Machguth, P. Rastner, and F. Paul. Mass loss of Greenland's glaciers and ice caps 2003-2008 revealed from ICESat laser altimetry data. *Geophysical Research Letters*, 40(5):875 – 881, 2013. doi: 10.1002/grl.50270.
- M. Bougamont, J. L. Bamber, and W. Greuell. A surface mass balance model for the Greenland Ice Sheet. *Journal of Geophysical Research*, 110:F04018, 2005. doi: 10.1029/2005JF000348.
- J. E. Box. Greenland Ice Sheet Mass Balance Reconstruction. Part II: Surface Mass Balance (1840-2010). *Journal of Climate*, 26:6974 – 6989, 2013. doi: 10.1175/JCLI-D-12-00518.1.
- J. E. Box, X. Fettweis, d M. Tedesco J. C. Stroeve a, D. K. Hall, and K. Steffen. Greenland ice sheet albedo feedback: thermodynamics and atmospheric drivers. *The Cryosphere*, 6:821 – 839, 2012. doi: 10.5194/tc-6-821-2012.
- D. H. Bromwich, A. B. Wilson, L.-S. Bai, G. W. K. Moore, and P. Bauer. A comparison of the regional Arctic System Reanalysis and the global ERA-Interim Reanalysis for the Arctic. *Quarterly Journal of the Royal Meteorological Society*, 142(695):644 – 658, 2015. doi: 10.1002/qj.2527.
- E. W. Burgess, R. R. Forster, J. E. Box, E. Mosley-Thompson, D. H. Bromwich, R. C. Bales, and L. C. Smith. A spatially calibrated model of annual accumulation rate on the Greenland Ice Sheet (1958-2007). *Journal of Geophysical Research*, 115:F02004, 2010. doi: 10.1029/2009JF001293.

- K. A. Casey, C. M. Polashenski, J. Chen, and M. Tedesco. Impact of MODIS sensor calibration updates on Greenland Ice Sheet surface reflectance and albedo trends. *The Cryosphere*, 11:1781 – 1795, 2017. doi: 10.5194/tc-11-1781-2017.
- M. Citterio and A. P. Ahlström. Brief communication "The aerophotogrammetric map of Greenland ice masses". *The Cryosphere*, 7:445 – 449, 2013. doi: 10.5194/tc-7-445-2013.
- J. W. Clough and O. H. Løken. Radio-echo sounding on the Barnes ice cap. In *North-central Baffin Island field report 1967*, Report Series 2, pages 87 – 102. Canada Department of Energy, Mines and Resources, Inland Waters Branch, 1968.
- J. G. Cogley, R. Hock, L. A. Rasmussen, A. A. Arendt, A. Bauder, R. J. Braithwaite, P. Jansson, G. Kaser, M. MÄüller, L. Nicholson, and M. Zemp. Glossary of glacier mass balance and related terms. Technical Report IHP-VII Technical Documents in Hydrology No. 86, IACS Contribution No. 2, UNESCO-IHP, Paris, 2011. Springer New York.
- J. M. Cook, A. J. Hodson, A. S. Gardner, M. Flanner, A. J. Tedstone, C. Williamson, T. D. Irvine-Fynn, R. Bryant J. Nilsson, and M. Tranter. Quantifying bioalbedo: a new physically based model and discussion of empirical methods for characterising biological influence on ice and snow albedo. *The Cryosphere*, 11:2611 – 2632, 2017a. doi: <https://doi.org/10.5194/tc-11-2611-2017>.
- J. M. Cook, A. J. Hodson, A. J. Taggart, S. H. Mernild, and M. Tranter. A predictive model for the spectral "bioalbedo" of snow. *Journal Geophysical Research Earth Surface*, 122:434 – 454, 2017b. doi: 10.1002/2016JF003932.
- J. A. Curry and P. J. Webster. *Thermodynamics of Atmospheres and Oceans*. Academic Press, London, United Kingdom, 1999.
- S. De la Peña, I. M. Howat, P. W. Nienow, M. R. van den Broeke, E. Mosley-Thompson, S. F. Price, D. Mair, B. Noël, and A. J. Sole. Changes in the firm structure of the western Greenland Ice Sheet caused by recent warming. *The Cryosphere*, 9:1203 – 1211, 2015. doi: 10.5194/tc-9-1203-2015.
- D. P. Dee, S. M. Uppala, A. J. Simmons, P. Berrisford, P. Poli, S. Kobayashi, U. Andrae, M. A. Balmaseda, G. Balsamo, P. Bauer, P. Bechtold, A. C. M. Beljaars, L. van de Berg, J. Bidlot, N. Bormann, C. Delsol, R. Dragani, M. Fuentes, A. J. Geer, L. Haimberger, S. B. Healy, H. Hersbach, E. V. Hölm, L. Isaksen, P. Källberg, M. Köhler, M. Matricardi, A. P. McNally, B. M. Monge-Sanz, J.-J. Morcrette, B.-K. Park, C. Peubey, P. de Rosnay, C. Tavolato, J.-N. Thépaut, and F. Vitart. The ERA-Interim reanalysis: configuration and performance of the data assimilation system. *Quarterly Journal of the Royal Meteorological Society*, 137:553 – 597, 2011. doi: 10.1002/qj.828.
- B. Dickson, I. Yashayaev, J. Meincke, B. Turrell, S. Dye, and J. Holfort. Rapid freshening of the deep North Atlantic Ocean over the past four decades. *Nature*, 416:832 – 837, 2002. doi: 10.1038/416832a.
- S. J. Doherty, S. G. Warren, T. C. Grenfell, A. D. Clarke, and R. E. Brandt. Light-absorbing impurities in Arctic snow. *Atmos. Chem. Phys.*, 10:11647 – 11680, 2010. doi: 10.5194/acp-10-11647-2010.
- ECMWF-IFS. Part IV : PHYSICAL PROCESSES (CY33R1). *Technical Report*, 2008.
- E. M. Enderlin and I. M. Howat. Submarine melt rate estimates for floating termini of Greenland outlet glaciers (2000-2010). *Journal of Glaciology*, 59(213):67 – 75(9), 2013. doi: <http://dx.doi.org/10.3189/2013JG12J049>.
- E. M. Enderlin, I. M. Howat, S. Jeong, M.-J. Noh, J. H. van Angelen, and M. R. van den Broeke. An improved mass budget for the Greenland ice sheet. *Geophysical Research Letters*, 43(3):866 – 872, 2014. doi: 10.1002/2013GL059010.
- J. Ettema, M. R. van den Broeke, E. van Meijgaard, and W. J. van de Berg. Climate of the Greenland ice sheet using a high-resolution climate model - Part2: Near-surface climate and energy balance. *The Cryosphere*, 4:529 – 544, 2010a. doi: 10.5194/tc-4-529-2010.
- J. Ettema, M. R. van den Broeke, E. van Meijgaard, W. J. van de Berg, J. E. Box, and K. Steffen. Climate of the Greenland ice sheet using a high-resolution climate model - Part 1: Evaluation. *The Cryosphere*, 4:511 – 527, 2010b. doi: 10.5194/tc-4-511-2010.
- R. S. Fausto, D. van As, J. E. Box, W. Colgan, P. L. Langen, and R. H. Mottram. The implication of nonradiative energy fluxes dominating Greenland ice sheet exceptional ablation area surface melt in 2012. *Geophysical Research Letters*, 43:1944 – 8007, 2016. doi: 10.1002/2016GL067720.
- X. Fettweis. Reconstruction of the 1979-2006 Greenland ice sheet surface mass balance using the regional climate model MAR. *The Cryosphere*, 1:21 – 40, 2007. doi: 10.5194/tc-1-21-2007.
- X. Fettweis, H. Gallée, F. Lefebvre, and J.-P. van Ypersele. Greenland surface mass balance simulated by a regional climate model and comparison with satellite-derived data in 1990-1991. *Climate Dynamics*, 24:623 – 640, 2005. doi: 10.1007/s00382-005-0010-y.
- X. Fettweis, M. Tedesco, M. van den Broeke, and J. Ettema. Melting trends over the Greenland ice sheet (1958-2009) from spaceborne microwave data and regional climate models. *The Cryosphere*, 5:359 – 375, 2011. doi: 10.5194/tc-5-359-2011.
- X. Fettweis, B. Franco, M. Tedesco, J. H. van Angelen, J. T. M. Lenaerts, M. R. van den Broeke, and H. Gallée. Estimating the Greenland ice sheet surface mass balance contribution to future sea level rise using the regional atmospheric climate model MAR. *The Cryosphere*, 7:469 – 489, 2013a. doi: 10.5194/tc-7-469-2013.

- X. Fettweis, E. Hanna, C. Lang, A. Belleflamme, M. Erpicum, and H. Gallée. Brief communication: Important role of the mid-tropospheric atmospheric circulation in the recent surface melt increase over the Greenland ice sheet. *The Cryosphere*, 7:241 – 248, 2013b. doi: 10.5194/tc-7-241-2013.
- X. Fettweis, J. E. Box, C. Agosta, C. Amory, C. Kittel, C. Lang, D. van As, H. Machguth, and H. Gallée. Reconstructions of the 1900–2015 Greenland ice sheet surface mass balance using the regional climate MAR model. *The Cryosphere*, 11:1015 – 1033, 2017. doi: 10.5194/tc-11-1015-2017.
- P. W. Fitzgerald, J. L. Bamber, J. K. Ridley, and J. C. Rougier. Exploration of parametric uncertainty in a Surface Mass Balance Model applied to the Greenland Ice Sheet. *Journal of Geophysical Research*, 117:F01021, 2012. doi: 10.1029/2011JF002067.
- L. Foresta, N. Gourmelen, F. Pálsson, P. Nienow, H. Björnsson, and A. Shepherd. Surface elevation change and mass balance of Icelandic ice caps derived from swath mode CryoSat-2 altimetry. *Geophysical Research Letters*, 43(23): 138 – 145, 2016. doi: 10.1002/2016GL071485.
- R. R. Forster, J. E. Box, M. R. van den Broeke, C. Miège, E. W. Burgess, J. H. van Angelen, J. T. M. Lenaerts, L. S. Koenig, J. Paden, C. Lewis, S. P. Gogineni, C. Leuschen, and J. R. McConnell. Extensive liquid meltwater storage in firn within the Greenland ice sheet. *Nature Geoscience*, 7(2):95 – 98, 2014. doi: 10.1038/ngeo2043.
- B. Franco, X. Fettweis, C. Lang, and M. Erpicum. Impact of spatial resolution on the modelling of the Greenland ice sheet surface mass balance between 1990–2010, using the regional climate model MAR. *The Cryosphere*, 6:695 – 711, 2012. doi: 10.5194/tc-6-695-2012.
- J. G. Fyke, M. Vizcaino, W. Lipscomb, and S. Price. Future climate warming increases Greenland ice sheetsurface mass balance variability. *Geophysical Research Letters*, 41(2):470 – 475, 2014. doi: 10.1002/2013GL058172.
- A. Gardner and M. Sharp. Sensitivity of net mass-balance estimates to near-surface temperature lapse rates when employing the degree-day method to estimate glacier melt. *Annals of Glaciology*, 50(50):80 – 86, 2009. ISSN 7. doi: <https://doi.org/10.3189/172756409787769663>.
- A. Gardner, G. Moholdt, A. Arendt, and B. Wouters. Accelerated contributions of Canada's Baffin and Bylot Island glaciers to sea level rise over the past half century. *The Cryosphere*, 6(5):1103 – 1125, 2012. doi: 10.5194/tc-6-1103-2012.
- A. S. Gardner, G. Moholdt, B. Wouters, G. J. Wolken, D. O. Burgess, M. J. Sharp, J. G. Cogley, C. Braun, and C. Labine. Sharply increased mass loss from glaciers and ice caps in the Canadian Arctic Archipelago. *Nature*, 473:357 – 360, 2011. doi: 10.1038/nature10089.
- A. S. Gardner, G. Moholdt, J. G. Cogley, B. Wouters, A. A. Arendt, J. Wahr, E. Berthier, R. Hock, W. T. Pfeffer, G. Kaser, S. R. M. Ligtenberg, T. Bolch, M. J. Sharp, J. O. Hagen, M. R. van den Broeke, and F. Paul. A reconciled estimate of glacier contributions to sea level rise: 2003 to 2009. *Science*, 340(6134):852 – 857, 2013. doi: 10.1126/science.1234532.
- G. Gascon, M. J. Sharp, D. O. Burgess, P. Bezeau, and A. Bush. Changes in accumulation area firn stratigraphy and meltwater flow during a period of climate warming, Devon Ice Cap, Nunavut, Canada. *Journal of Geophysical Research*, 118:2380 – 2391, 2013. doi: 10.1002/2013JF002838.
- D. B. Gesch and K. S. Larson. Techniques for development of global 1-kilometer digital elevation models. In *In Proc. Pecora Thirteenth Symposium*, CD-ROM, Bethesda, Md., 1998. Am. Soc. Photogrammetry Remote Sens.
- A. Gilbert, G. E. Flowers, G. H. Miller, K. Refsnider, N. E. Young, and V. Radić. The projected demise of Barnes Ice Cap: evidence of an unusually warm 21st century Arctic. *Geophysical Research Letters*, 2017. doi: 10.1002/2016GL072394. Accepted article.
- H. Goelzer, P. Huybrechts, S. C. B. Raper, M.-F. Loutre, H. Goosse, and T. Fichefet. Millennial total sea-level commitments projected with the earth system model of intermediate complexity loveclim. *Environmental Research Letters*, 7(045401):9 pp., 2012. doi: 10.1088/1748-9326/7/4/045401.
- H. Goelzer, P. Huybrechts, J. J. Fürst, F. M. Nick, M. L. Andersen, T. L. Edwards, X. Fettweis, A. J. Payne, and S. Shannon. Sensitivity of Greenland ice sheet projections to model formulations. *Journal of Glaciology*, 59(216): 733 – 749, 2013. doi: 10.3189/2013JoG12J182.
- Government of Canada Natural Resources Canada Map Information Branch. *Canadian Digital Elevation Model Product Specifications Edition 1.1*. GeoGratis Client Services, 2144 King Street West, Suite 010 Sherbrooke, Quebec, Canada, 2016.
- L. Gray, D. Burgess, L. Copland, M. N. Demuth, T. Dunse, K. Langley, and T. V. Schuler. CryoSat-2 delivers monthly and inter-annual surface elevation change for Arctic ice caps. *The Cryosphere*, 9:1895 – 1913, 2015. doi: 10.5194/tc-9-1895-2015.
- W. Greuell and J. Oerlemans. Sensitivity studies with a mass balance model including temperature profile calculations inside the glacier. *Zeitschrift für Gletscherkunde und Glazialgeologie*, 22:101 – 124, 1986. ISSN 0044-2836.
- E. Hanna, P. Huybrechts, I. Janssens, J. Cappelen, K. Steffen, and A. Stephens. Runoff and mass balance of the Greenland ice sheet: 1958–2003. *Journal of Geophysical Research*, 110:D13108, 2005. doi: 10.1029/2004JD005641.

- E. Hanna, P. Huybrechts, K. Steffen, J. Cappelen, R. Huff, C. Shuman, T. Irvine-Fynn, S. Wise, and M. Griffiths. Increased Runoff from Melt from the Greenland Ice Sheet: A Response to Global Warming. *Journal of Climate*, 21: 331 – 341, 2008. doi: 10.1175/2007JCLI1964.1.
- E. Hanna, J. Cappelen, X. Fettweis, P. Huybrechts, A. Luckman, and M. H. Ribergaard. Hydrologic response of the Greenland ice sheet: the role of oceanographic warming. *Hydrological Processes*, 23:7 – 30, 2009. doi: 10.1002/hyp.7090.
- E. Hanna, P. Huybrechts, J. Cappelen, K. Steffen, R. C. Bales, E. Burgess, J. R. McConnell, J. P. Steffensen, M. Van den Broeke, L. Wake, G. Bigg, M. Griffiths, and D. Savas. Greenland Ice Sheet surface mass balance 1870 to 2010 based on Twentieth Century Reanalysis, and links with global climate forcing. *Journal of Geophysical Research*, 116: D24121, 2011. doi: 10.1029/2011JD016387.
- E. Hanna, J. M. Jones, J. Cappelen, S. H. Mernild, L. Wood, K. Steffen, and P. Huybrechts. The influence of North Atlantic atmospheric and oceanic forcing effects on 1900-2010 Greenland summer climate and ice melt/runoff. *International Journal of Climatology*, 33:862 – 880, 2013. doi: 10.1002/joc.3475.
- E. Hanna, X. Fettweis, S. H. Mernild, J. Cappelen, M. H. Ribergaard, C. Shuman, K. Steffen, L. Wood, and T. L. Mote. Atmospheric and oceanic climate forcing of the exceptional Greenland Ice Sheet surface melt in summer 2012. *Journal of Climatology*, 34(4):1022 – 1037, 2014. doi: 10.1002/joc.3743.
- E. Hanna, T. E. Cropper, R. J. Hall, and J. Cappelen. Greenland Blocking Index 1851-2015: a regional climate change signal. *International Journal of Climatology*, 36(15):4847 – 4861, 2016. doi: 10.1002/joc.4673.
- J. Harper, N. Humphrey, W. T. Pfeffer, J. Brown, and X. Fettweis. Greenland ice-sheet contribution to sea-level rise buffered by meltwater storage in firn. *Nature*, 491:240 – 243, 2012. doi: 10.1038/nature11566.
- R. L. Hawley, Z. R. Courville, L. M. Kehrl, E. R. Lutz, E. C. Osterberg, T. B. Overly, and G. J. Wong. Recent accumulation variability in northwest Greenland from ground-penetrating radar and shallow cores along the Greenland Inland Traverse. *Journal of Glaciology*, 60(220):375 – 382, 2014. doi: 10.3189/2014JoG13J141.
- V. Helm, A. Humbert, and H. Miller. Elevation and elevation change of Greenland and Antarctica derived from CryoSat-2. *The Cryosphere*, 8:1539 – 1559, 2014. doi: 10.5194/tc-8-1539-2014.
- G. Holdsworth. Surge activity on the Barnes Ice Cap. *Nature*, 269(5629):588 – 590, 1977.
- R. LeB. Hooke, G. W. Johnson, K. A. Brugger, B. Hanson, and G. Holdsworth. Changes in mass balance, velocity, and surface profile along a flow line on Barnes Ice Cap, 1970-1984. *Can. J. Earth Sci.*, 24:1550 – 1561, 1987. URL www.nrcresearchpress.com.
- I. M. Howat and A. Eddy. Multi-decadal retreat of greenland’s marine-terminating glaciers. *Journal of Glaciology*, 57 (203):389 – 396, 2011. doi: 10.3189/002214311796905631.
- I. M. Howat, A. Negrete, and B. E. Smith. The Greenland Ice Mapping Project (GIMP) land classification and surface elevation data sets. *The Cryosphere*, 8:1509 – 1518, 2014. doi: 10.5194/tc-8-1509-2014.
- N. F. Humphrey, J. T. Harper, and W. T. Pfeffer. Thermal tracking of meltwater retention in greenland’s accumulation area. *Journal of Geophysical Research*, 117, 2012. doi: 10.1029/2011JF002083.
- R. Jaiser, K. Dethloff, D. Handorf, A. Rinke, and J. Cohen. Impact of sea ice cover changes on the Northern Hemisphere atmospheric winter circulation. *Tellus*, 64:11 p., 2012. doi: 10.3402/tellusa.v64i0.11595.
- I. Janssens and P. Huybrechts. The treatment of meltwater retention in mass-balance parameterizations of the Greenland ice sheet. *Annals of Glaciology*, 31:133 – 140, 2000.
- I. Joughin, W. Abdalati, and M. Fahnestock. Large fluctuations in speed on greenland’s jakobshavn isbræ glacier. *Nature*, 432:608 – 610, 2004. doi: 10.1038/nature03130.
- I. Joughin, B. E. Smith, D. E. Shean, and D. Floricioiu. Brief Communication: Further summer speedup of Jakobshavn Isbræ. *The Cryosphere*, 8:209 – 214, 2014. doi: 10.5194/tc-8-209-2014.
- S. Kaasalainen, M. Kaasalainen, T. Mielonen, J. Suomalainen, J. I. Peltoniemi, and J. Näränen. Optical properties of snow in backscatter. *Journal of Glaciology*, 52(179):574 – 584, 2006.
- S. A. Khan, K. H. Kjær, M. Bevis, J. L. Bamber, J. Wahr, K. K. Kjeldsen, A. A. Bjørk, N. J. Korsgaard, L. A. Stearns, M. R. van den Broeke, L. Liu, N. K. Larsen, and I. S. Muresan. Sustained mass loss of the northeast Greenland ice sheet triggered by regional warming. *Nature Climate Change*, 4:292 – 298, 2014. doi: 10.1038/NCLIMATE2161.
- M. A. King, Z. Altamimi, J. Boehm, M. Bos, R. Dach, P. Elosegui, F. Fund, M. Hernández-Pajares, D. Lavallee, P. Jorge, M. Cerveira, N. Penna, R., E. M. Riva, P. Steigenberger, T. van Dam, L. Vittuari, S. Williams, and P. Willis. Improved Constraints on Models of Glacial Isostatic Adjustment: A Review of the Contribution of Ground-Based Geodetic Observations. *Surveys in Geophysics*, 31(5):465 – 507, 2010. doi: 10.1007/s10712-010-9100-4.
- L. S. Koenig, C. Miège, R. R. Forster, and L. Brucker. Initial in situ measurements of perennial meltwater storage in the Greenland firn aquifer. *Geophysical Research Letters*, 41:81 – 85, 2014. doi: 10.1002/2013GL058083.
- L. S. Koenig, A. Ivanoff, P. M. Alexander, J. A. MacGregor, X. Fettweis, B. Panzer, J. D. Paden, R. R. Forster, I. Das, J. R. McConnell, M. Tedesco, C. Leuschen, and P. Gogineni. Annual Greenland accumulation rates (2009-2012) from airborne snow radar. *The Cryosphere*, 10:1739 – 1752, 2016. doi: 10.5194/tc-10-1739-2016.

- M. Krapp, A. Robinson, and A. Ganopolski. Semic: an efficient surface energy and mass balance model applied to the Greenland ice sheet. *The Cryosphere*, 11:1519 – 1535, 2017. doi: <https://doi.org/10.5194/tc-11-1519-2017>.
- P. Kuipers Munneke, M. R. van den Broeke, J. T. M. Lenaerts, M. G. Flanner, A. S. Gardner, and W. J. van de Berg. A new albedo parameterization for use in climate models over the Antarctic ice sheet. *Journal of Geophysical Research*, 116:D05114, 2011. doi: 10.1029/2010JD015113.
- P. Kuipers Munneke, S. R. M. Ligtenberg, M. R. van den Broeke, J. H. van Angelen, and R. R. Forster. Explaining the presence of perennial liquid water bodies in the firn of the Greenland Ice Sheet. *Geophysical Research Letters*, 41(2): 476 – 483, 2014. doi: 10.1002/2013GL058389.
- P. Kuipers Munneke, S. R. M. Ligtenberg, B. P. Y. Noël, I. M. Howat, J. E. Box, E. Mosley-Thompson, J. R. McConnell, K. Steffen, J. T. Harper, S. B. Das, and M. R. van den Broeke. Elevation change of the Greenland Ice Sheet due to surface mass balance and firn processes, 1960-2014. *The Cryosphere*, 9:2009 – 2025, 2015. doi: 10.5194/tc-9-2009-2015.
- P. Kuipers Munneke, C. J. P. P. Smeets, C. H. Reijmer, J. Oerlemans, R. S. W. van de Wal, and M. R. van den Broeke. The K-transect in West-Greenland: long-term (2003-2016) surface energy balance observations. *Arctic, Antarctic and Alpine Research*, 2017. submitted.
- P. L. Langen, R. S. Fausto, B. R. M. Vandecrux, R. H. Mottram, and J. E. Box. Liquid Water Flow and Retention on the Greenland Ice Sheet in the Regional Climate Model HIRHAM5: Local and Large-Scale Impacts. *Frontiers in Earth Science*, 4(110):18 pp., 2017. doi: 10.3389/feart.2016.00110.
- J. T. M. Lenaerts, M. R. van den Broeke, J. H. Angelen, E. van Meijgaard, and S. J. Déry. Drifting snow climate of the Greenland ice sheet: a study with a regional climate model. *The Cryosphere*, 6:891 – 899, 2012a. doi: 10.5194/tc-6-891-2012.
- J. T. M. Lenaerts, M. R. van den Broeke, S. J. Déry, E. van Meijgaard, W. J. van de Berg, Stephen P. Palm, and J. Sanz Rodrigo. Modeling drifting snow in Antarctica with a regional climate model: 1. methods and model evaluation. *Journal of Geophysical Research - Atmospheres*, 117(D5):D05108, 2012b. doi: 10.1029/2011JD016145.
- J. T. M. Lenaerts, J. H. van Angelen, M. R. van den Broeke, A. S. Gardner, B. Wouters, and E. van Meijgaard. Irreversible mass loss of Canadian Arctic Archipelago glaciers. *Geophysical Research Letters*, 40(5):1 – 5, 2013. doi: 10.1002/grl.50214.
- J. T. M. Lenaerts, M. R. van den Broeke, J. M. van Wessem, and W. J. van de Berg. Extreme Precipitation and Climate Gradients in Patagonia Revealed by High-Resolution Regional Atmospheric Climate Modeling. *American Meteorological Society*, 27:4607 – 4621, 2014. doi: 10.1175/JCLI-D-13-00579.1.
- G. Lewis, E. Osterberg, R. Hawley, B. Whitmore, H. P. Marshall, and J. Box. Regional Greenland accumulation variability from Operation IceBridge airborne accumulation radar. *The Cryosphere*, 11:773 – 788, 2017. doi: 10.5194/tc-11-773-2017.
- S. R. M. Ligtenberg, M. M. Helsen, and M. R. van den Broeke. An improved semi-empirical model for the densification of Antarctic firn. *The Cryosphere*, 5:809 – 819, 2011. doi: 10.5194/tc-5-809-2011.
- S. R. M. Ligtenberg, P. Kuipers Munneke, and M. R. van den Broeke. Present and future variations in antarctic firn air content. *The Cryosphere*, 8:1711 – 1723, 2014. doi: <https://doi.org/10.5194/tc-8-1711-2014>.
- Y.-L. Lin, R. D. Farley, and H. D. Orville. Bulk Parameterization of the Snow Field in a Cloud Model. *Journal of Applied Meteorology*, 22:1065 – 1092, 1983. doi: 10.1175/1520-0450(1983)022<1065:BPOTSF>2.0.CO;2.
- P. Lucas-Picher, M. Wulff-Nielsen, J. H. Christensen, Gudfinna Adalgeirsdóttir, and Ruth M. and S. B. Simonsen. Very high resolution regional climate model simulations over Greenland: Identifying added value. *Journal of Geophysical Research*, 117:D02108, 2012. doi: 10.1029/2011JD016267.
- H. Machguth, P. Rastner, T. Bolch, N. Mölg, L. Sandberg Sørensen, G. Adalgeirsdottir, J. H. van Angelen, M. R. van den Broeke, and X. Fettweis. The future sea-level rise contribution of Greenland's glaciers and ice caps. *Environmental Research Letters*, 8(2):025005, 2013. doi: 10.1088/1748-9326/8/2/025005.
- H. Machguth, M. MacFerrin, D. van As, J. E. Box, C. Charalampidis, W. Colgan, R. S. Fausto, H. A. J. Meijer, E. Mosley-Thompson, and R. S. W. van de Wal. Greenland meltwater storage in firn limited by near-surface ice formation. *Nature Climate Change*, 6:390 – 393, 2016a. doi: 10.1038/nclimate2899.
- H. Machguth, H. Thomsen, A. Weidick, A. P. Ahlstrøm, J. Abermann, M. L. Andersen, S. Andersen, A. A. Bjørk, J. E. Box, R. J. Braithwaite, C. E. Bøggild, M. Citterio, P. Clement, W. Colgan, R. S. Fausto, K. G. S. Gubler, B. Hasholt, B. Hynek, N. Knudsen, S. Larsen, S. Mernild, J. Oerlemans, H. Oerter, O. Olesen, C. Smeets, K. Steffen, M. Stober, S. Sugiyama, D. van As, M. van den Broeke, and R. S. van de Wal. Greenland surface mass balance observations from the ice sheet ablation area and local glaciers. *Journal of Glaciology*, pages 1 – 27, 2016b. doi: 10.1017/jog.2016.75.
- B. A. Marzeion, A. H. Jarosch, and M. Hofer. Past and future sea-level change from the surface mass balance of glaciers. *The Cryosphere*, 6:1295 – 1322, 2012. doi: 10.5194/tc-6-1295-2012.
- D. McGrath, W. Colgan, N. Bayou, A. Muto, and K. Steffen. Recent warming at Summit, Greenland: Global context and implications. *Geophysical Research Letters*, 40(10):2091 – 2096, 2013. doi: 10.1002/grl.50456.

- M. McMillan, A. Shepherd, N. Gourmelen, A. Dehecq, A. Leeson, A. Ridout, T. Flament, A. Hogg, L. Gilbert, T. Benham, M. van den Broeke, J. A. Dowdeswell, X. Fettweis, B. Noël, and T. Strozzì. Rapid dynamic activation of a marine-based Arctic ice cap. *Geophysical Research Letters*, 41(24):8902 – 8909, 2014. doi: 10.1002/2014GL062255.
- M. McMillan, A. Leeson, A. Shepherd, K. Briggs, T. W. K. Armitage, A. Hogg, P. Kuipers Munneke, M. van den Broeke, B. Noël, W. J. van de Berg, S. Ligtenberg, M. Horwath, A. Groh, A. Muir, and L. Gilbert. A high-resolution record of Greenland mass balance. *Geophysical Research Letters*, 43(13):7002 – 7010, 2016. doi: 10.1002/2016GL069666.
- S. H. Mernild, G. E. Liston, C. A. Hiemstra, and J. H. Christensen. Greenland Ice Sheet Surface Mass-Balance Modeling in a 131-Yr Perspective, 1950-2080. *American Meteorological Society*, 11:3 – 22, 2010. doi: 10.1175/2009JHM1140.1.
- S. H. Mernild, G. E. Liston, C. A. Hiemstra, J. H. Christensen, M. Stendel, and B. Hasholt. Surface Mass Balance and Runoff Modeling Using HIRHAM4 RCM at Kangerlussuaq (Søndre Strømfjord), West Greenland, 1950-2080. *American Meteorological Society*, 24:609 – 623, 2011. doi: 10.1175/2010JCLI3560.1.
- C. Miège, R. R. Forster, L. Brucker, L. S. Koenig, D. Kip Solomon, J. D. Paden, J. E. Box, E. W. Burgess, J. Z. Miller, L. McNerney, N. Brautigam, R. S. Fausto, and S. Gogineni. Spatial extent and temporal variability of Greenland firn aquifers detected by ground and airborne radars. *Geophysical Research Letters*, 121(12):2381 – 2398, 2016. doi: 10.1002/2016JF003869.
- R. Millan, J. Mougnot, and E. Rignot. Mass budget of the glaciers and ice caps of the Queen Elizabeth Islands, Canada, from 1991 to 2015. *Environmental Research Letters*, 12(2):024016, 2017. doi: <https://doi.org/10.1088/1748-9326/aa5b04>.
- G. Moholdt, C. Nuth, J. Ove Hagen, and J. Kohler. Recent elevation changes of Svalbard glaciers derived from ICESat laser altimetry. *Remote Sensing of Environment*, RSE-07713(:):12 p., 2010. doi: 10.1016/j.rse.2010.06.008.
- T. Moon, I. Joughin, B. Smith, and I. Howat. 21st-Century Evolution of Greenland Outlet Glacier Velocities. *Science*, 336(6081):576 – 578, 2012. doi: 10.1126/science.1219985.
- J.-J. Morcrette, H. W. Barker, J. N. S. Cole, M. J. Iacono, and R. Pincus. Impact of a new radiation package, McRad, in the ECMWF integrated forecast system. *Monthly Weather Review*, 136:4773 – 4798, 2008. doi: 10.1175/2008MWR2363.1.
- M. Morlighem, C. N. Williams, E. Rignot, L. An, J. E. Arndt, J. L. Bamber, G. Catania, N. Chauchè, J. A. Dowdeswell, B. Dorschel, I. Fenty, K. Hogan, I. Howat, A. Hubbard, M. Jakobsson, T. M. Jordan, K. K. Kjeldsen, R. Millan and L. Mayer, J. Mougnot, B. P. Y. Noël and C. Ó Cofaigh, S. Palmer, S. Rysgaard, H. Seroussi, M. J. Siegert, P. Slabon, F. Straneo, M. R. van den Broeke, W. Weinrebe, M. Wood, and K. B. Zinglensen. BedMachine v3: Complete bed topography and ocean bathymetry mapping of Greenland from multi-beam echo sounding combined with mass conservation. *Geophysical Research Letters*, 2017. doi: 10.1002/2017GL074954.
- C. A. Mortimer, M. Sharp, and B. Wouters. Glacier surface temperatures in the Canadian High Arctic, 2000-15. *Journal of Glaciology*, 62(235):963 – 975, 2016. doi: 10.1017/jog.2016.80.
- R. Mottram, E. Gleeson, and K. P. Nielsen. The Glaciers of HARMONIE. *Geophysical Research Abstracts*, 18:1 p., 2016. doi: EGU2016-14229. poster.
- R. Mottram, F. Boberg, P. Langen, S. Yang, C. Rodehacke, J. H. Christensen, and M. S. Madsen. Surface Mass balance of the Greenland ice Sheet in the Regional Climate Model HIRHAM5: Present State and Future Prospects. *Low Temperature Science*, 75(105):105 – 115, 2017. doi: 10.14943/lowtemsci.75.105.
- J. Mougnot, E. Rignot, B. Scheuchl, I. Fenty, A. Khazendar, M. Morlighem, A. Buzzi, and J. Paden. Fast retreat of Zachariae Isstrøm, northeast Greenland. *Science*, 350(6266):1357 – 1361, 2015. doi: 10.1126/science.aac7111.
- V. M. R. Muggeo. Estimating regression models with unknown break-points. *Statistics in Medicine*, 22(:):3055 – 3071, 2003. doi: 10.1002/sim.1545.
- M. Musilova, M. Tranter, J. L. Bamber, N. Takeuchi, and A. M. Anesio. Experimental evidence that microbial activity lowers the albedo of glaciers. *Geochemical Perspectives Letters*, 2:106 – 116, 2016. doi: 10.7185/geochemlet.1611.
- S. V. Nghiem, D. K. Hall, T. L. Mote, M. Tedesco, M. R. Albert, K. Keegan, C. A. Shuman, N. E. DiGirolamo, and G. Neumann. The extreme melt across the Greenland ice sheet in 2012. *Geophysical Research Letters*, 39(20):L20502, 2012. doi: 10.1029/2012GL053611.
- F. M. Nick, A. Vieli, I. M. Howat, and I. Joughin. Large-scale changes in Greenland outlet glacier dynamics triggered at the terminus. *Nature Geoscience*, 2:110 – 114, 2009. doi: 10.1038/ngeo394.
- F. M. Nick, A. Vieli, M. Langer Andersen, I. Joughin, A. Payne, T. L. Edwards, F. Pattyn, and R. S. W. van de Wal. Future sea-level rise from Greenland's main outlet glaciers in a warming climate. *Nature*, 497(7448):235 – 238, 2013. doi: 10.1038/nature12068.
- B. Noël, X. Fettweis, W. J. van de Berg, M. R. van den Broeke, and M. Erpicum. Sensitivity of Greenland Ice Sheet surface mass balance to perturbations in sea surface temperature and sea ice cover: a study with the regional climate model MAR. *The Cryosphere*, 8:1871 – 1883, 2014. doi: 10.5194/tc-8-1871-2014.

- B. Noël, W. J. van de Berg, E. van Meijgaard, P. Kuipers Munneke, R. S. W. van de Wal, and M.R. van den Broeke. Evaluation of the updated regional climate model RACMO2.3: summer snowfall impact on the Greenland Ice Sheet. *The Cryosphere*, 9:1831 – 1844, 2015. doi: 10.5194/tc-9-1831-2015.
- B. Noël, W. J. van de Berg, H. Machguth, S. Lhermitte, I. Howat, X. Fettweis, and M. R. van den Broeke. A daily, 1 km resolution data set of downscaled Greenland ice sheet surface mass balance (1958-2015). *The Cryosphere*, 10(5): 2361 – 2377, 2016. doi: 10.5194/tc-10-2361-2016.
- B. Noël, W. J. van de Berg, S. Lhermitte, B. Wouters, H. Machguth, I. Howat, M. Citterio, G. Moholdt, J. T. M. Lenaerts, and M. R. van den Broeke. A tipping point in refreezing accelerates mass loss of Greenland’s glaciers and ice caps. *Nature Communications*, 8:14730, 2017a. doi: 10.1038/ncomms14730.
- B. Noël, W. J. van de Berg, S. Lhermitte, B. Wouters, N. Schaffer, and M. R. van den Broeke. Six decades of glacial mass loss in the Canadian Arctic Archipelago. *Journal of Geophysical Research Earth Surface*, 2017b. in review.
- B. Noël, W. J. van de Berg, J. M. van Wessem, E. van Meijgaard, D. van As, J. T. M. Lenaerts, S. Lhermitte, P. Kuipers Munneke, C. J. P. P. Smeets, L. H. van Ulf, R. S. W. van de Wal, and M. R. van den Broeke. Modelling the climate and surface mass balance of polar ice sheets using RACMO2, Part 1: Greenland (1958-2016). *The Cryosphere Discussion*, 2017c.
- J. E. Overland and M. Wang. Large-scale atmospheric circulation changes are associated with the recent loss of Arctic sea ice. *Tellus*, 62:1 – 9, 2010. doi: 10.1111/j.1600-0870.2009.00421.x.
- T. B. Overly, R. L. Hawley, V. Helm, E. M. Morris, and R. N. Chaudhary. Greenland annual accumulation along the egi line, 1959-2004, from asiras airborne radar and detailed neutron-probedensity measurements. *The Cryosphere Discussion*, 9:6791 – 6828, 2015. doi: 10.5194/tcd-9-6791-2015,2015.
- T. B. Overly, R. L. Hawley, V. Helm, E. M. Morris, and R. N. Chaudhary. Greenland annual accumulation along the EGIG line, 1959-2004, from ASIRAS airborne radar and neutron-probe density measurements. *The Cryosphere*, 10: 1679 – 1694, 2016. doi: 10.5194/tc-10-1679-2016.
- G. Nina Petersen, J. E. Kristjánsson, and H. Olafsson. Numerical simulations of Greenland’s impact on the Northern Hemisphere winter circulation. *Tellus A*, 56(2):102 – 111, 2004. doi: 10.1111/j.1600-0870.2004.00047.x.
- W. T. Pfeffer, A. A. Arendt, A. Bliss, T. Bolch, J. G. Cogley, A. S. Gardner, J.-O. Hagen, R. Hock, G. Kaser, C. Kienholz, E. S. Miles, G. Moholdt, N. Mölg, F. Paul, V. Radić, P. Rastner, B. H. Raup, J. Rich, M. J. Sharp, and The Randolph Consortium. The Randolph Glacier Inventory: a globally complete inventory of glaciers. *Journal of Glaciology*, 60 (221):537 – 552, 2014. doi: 10.3189/2014JG13J176.
- C. M. Polashenski, J. E. Dibb, M. G. Flanner, J. Y. Chen, Z. R. Courville, A. M. Lai, J. J. Schauer, M. M. Shafer, and M. Bergin. Neither dust nor black carbon causing apparent albedo decline in Greenland’s dry snow zone: Implications for MODIS C5 surface reflectance. *Geophysical Research Letters*, 42(21):9319 – 9327, 2015. doi: 10.1002/2015GL065912.
- S. F. Price, A. J. Payne, I. M. Howat, and B. E. Smith. Committed sea-level rise for the next century from Greenland ice sheet dynamics during the past decade. *Proc Natl Acad Sci U S A*, 108(22):8978 – 8983, 2011. doi: 10.1073/pnas.1017313108.
- J. G. L. Rae, G. Aðalgeirsdóttir, T. L. Edwards, X. Fettweis, J. M. Gregory, H. T. Hewitt, J. A. Lowe, P. Lucas-Picher, R. H. Mottram, A. J. Payne, J. K. Ridley, S. R. Shannon, W. J. van de Berg, R. S. W. van de Wal, and M. R. van den Broeke. Greenland ice sheet surface mass balance: evaluating simulations and making projections with regional climate models. *The Cryosphere*, 6:1275 – 1294, 2012. doi: 10.5194/tc-6-1275-2012.
- S. Rahmstorf, J. E. Box, G. Feulner, M. E. Mann, A. Robinson, S. Rutherford, and E. J. Schaffernicht. Exceptional twentieth-century slowdown in Atlantic Ocean overturning circulation. *Nature Climate Change*, 5:475 – 480, 2015. doi: 10.1038/nclimate2554.
- P. Rastner, T. Bolch, N. Mölg, H. Machguth, R. Le Bris, and F. Paul. The first complete inventory of the local glaciers and ice caps on Greenland. *The Cryosphere*, 6:1483 – 1495, 2012. doi: 10.5194/tc-6-1483-2012.
- E. Rignot, J. E. Box, E. Burgess, and E. Hanna. Mass balance of the Greenland ice sheet from 1958 to 2007. *The Cryosphere*, 35:L20502, 2008. doi: 10.1029/2008GL035417.
- E. Rignot, I. Velicogna, M. R. van den Broeke, A. Monaghan, and J. Lenaerts. Acceleration of the contribution of the Greenland and Antarctic ice. *Geophysical Research Letters*, 38:L05503/1 – L05503/5, 2011. doi: 10.1029/2011GL046583.
- I. Sasgen, M. R. van den Broeke, J. L. Bamber, E. Rignot, L. Sandberg Sørensen, B. Wouters, Z. Martinec, I. Velicogna, and S. B. Simonsen. Timing and origin of recent regional ice-mass loss in Greenland. *Earth and Planetary Science Letters*, 333 – 334:293 – 303, 2012. doi: 10.1016/j.epsl.2012.03.033.
- M. Sharp, D. O. Burgess, J. G. Cogley, M. Ecclestone, C. Labine, and G. J. Wolken. Extreme melt on Canada’s Arctic ice caps in the 21st century. *Geophysical Research Letters*, 38(11):L11501, 2011a. doi: 10.1029/2011GL047381.
- M. Sharp, D. O. Burgess, J. G. Cogley, M. Ecclestone, C. Labine, and G. J. Wolken. Extreme melt on Canada’s Arctic ice caps in the 21st century. *Geophysical Research Letters*, 38(11):L11501, 2011b. doi: 10.1029/2011GL047381.

- A. Shepherd, E. R. Ivins, G. A. V. R. Barletta, M. J. Bentley, S. Bettadpur, K. H. Briggs, D. H. Bromwich, R. Forsberg, N. Galin, M. Horwath, S. Jacobs, I. Joughin, M. A. King, J. T. M. Lenaerts, J. Li, S. R. M. Ligtenberg, A. Luckman, S. B. Luthcke, M. McMillan, R. Meister, G. Milne, J. Mouginot, A. Muir, J. P. Nicolas, J. Paden, A. J. Payne, H. Pritchard, E. Rignot, H. Rott, L. Sandberg Sørensen, T. A. Scambos, B. Scheuchl, E. J. O. Schrama, B. Smith, A. V. Sundal, J. H. van Angelen, W. J. van de Berg, M. R. van den Broeke, D. G. Vaughan, I. Velicogna, J. Wahr, P. L. Whitehouse, D. J. Wingham, D. Yi, D. Young, and H. J. Zwally. A Reconciled Estimate of Ice-Sheet Mass Balance. *Science*, 338(6111):1183 – 1189, 2012. doi: 10.1126/science.1228102.
- A. P. Siebesma, P. M. M. Soares, and J. Teixeira. A Combined Eddy-Diffusivity Mass-Flux Approach for the Convective Boundary Layer. *Journal of the Atmospheric Sciences*, 64:1230 – 1248, 2007. doi: <http://dx.doi.org/10.1175/JAS3888.1>.
- C. J. P. P. Smeets and M. R. Van den Broeke. Temporal and Spatial Variations of the Aerodynamic Roughness Length in the Ablation Zone of the Greenland Ice Sheet. *Boundary Layer Meteorology*, 128:315 – 338, 2008. doi: 10.1007/s10546-008-9291-0.
- C. J. P. P. Smeets, P. Kuipers Munneke, D. van As, M. R. van den Broeke, W. Boot, J. Oerlemans, H. Snellen, C. H. Reijmer, and R. S. W. van de Wal. The K-transect in west Greenland: twenty-three years of weather station data. *Arctic, Antarctic and Alpine Research*, 2017. in press.
- L. S. Sørensen, S. B. Simonsen, K. Nielsen, P. Lucas-Picher, G. Spada, G. Adalgeirsdottir, R. Forsberg, . and C. S. Hvidberg. Mass balance of the Greenland ice sheet (2003-2008) from ICESat data - the impact of interpolation, sampling and firn density. *The Cryosphere*, 5:173 – 186, 2011. doi: 10.5194/tc-5-173-2011.
- J. D. Stark, Exeter Met Office, C. J. Donlon, M. J. Martin, and M. E. McCulloch. OSTIA: An operational, high resolution, real time, global sea surface temperature analysis system. *OCEANS 2007 - Europe*, pages 1 – 4, 2007. doi: 10.1109/OCEANSE.2007.4302251. Conference Publications.
- C. R. Steger, C. H. Reijmer, M. R. van den Broeke, N. Wever, R. R. Forster, L. S. Koenig, P. Kuipers Munneke, M. Lehning, S. Lhermitte, S. R. M. Ligtenberg, C. Miège, and B. P. Y. Noël. Firn Meltwater Retention on the Greenland Ice Sheet: A Model Comparison. *Frontiers in Earth Science*, 5(3):16 pp., 2017. doi: 10.3389/feart.2017.00003.
- M. Stibal, J. E. Box, K. A. Cameron, P. L. Langen, M. L. Yallop, R. H. Mottram, A. L. Khan, N. P. Molotch, N. A. M. Christmas, F. C. Quaglia, D. Remias, C. J. P. P. Smeets, M. R. van den Broeke, J. C. Ryan, A. Hubbard, M. Tranter, D. van As, and A. P. Ahlstrøm. Algae Drive Enhanced Darkening of Bare Ice on the Greenland Ice Sheet. *Geophysical Research Letters*, 44:9 pp., 2017. doi: 10.1002/2017GL075958.
- J. Stroeve, J. E. Box, F. Gao, S. L. Liang, A. Nolin, and C. Schaaf. Accuracy assessment of the MODIS 16-day albedo product for snow: comparisons with Greenland in situ measurements. *Remote Sensing of Environment*, 94:46 – 60, 2005. doi: 10.1016/j.rse.2004.09.011.
- J. Stroeve, J. E. Box, Z. Wang, C. Schaaf, and A. Barletta. Re-evaluation of MODIS MCD43 Greenland albedo accuracy and trends. *Remote Sensing of Environment*, 138:199 – 214, 2013. doi: 10.1016/j.rse.2013.07.023.
- J. C. Stroeve. Assessment of Greenland albedo variability from the advanced very high resolution radiometer Polar Pathfinder data set. *Journal of Geophysical Research*, 106:360 – 374, 2001. doi: 10.1016/S0034-4257(00)00179-6.
- H. Sundqvist. A parameterization scheme for non-convective condensation including prediction of cloud water content. *Quarterly Journal of the Royal Meteorological Society*, 104:677 – 690, 1978. doi: 10.1002/qj.49710444110.
- N. Takeuchi, N. Nagatsuka, J. Uetake, and R. Shimada. Spatial variations in impurities (cryoconite) on glaciers in northwest Greenland. *Bulletin of Glaciological Research*, 32:85 – 94, 2014. doi: 10.5331/bgr.32.85.
- M. Tedesco, M. Serreze, and X. Fettweis. Diagnosing the extreme surface melt event over southwestern Greenland in 2007. *The Cryosphere*, 2:159 – 166, 2008. doi: 10.5194/tc-2-159-2008.
- M. Tedesco, X. Fettweis, M. R. van den Broeke, R. S. W. van de Wal, C. J. P. P. Smeets, W. J. van de Berg, M. C. Serreze, and J. E. Box. The role of albedo and accumulation in the 2010 melting record in Greenland. *Environmental Research Letters*, 6:014005, 2011. doi: 10.1088/1748-9326/6/1/014005.
- M. Tedesco, M. Lütjhe, K. Steffen, N. Steiner, X. Fettweis, I. Willis, N. Bayou, and A. Banwell. Measurement and modeling of ablation of the bottom of supraglacial lakes in western Greenland. *Geophysical Research Letters*, 39(2): L02502, 2012. doi: 10.1029/2011GL049882.
- M. Tedesco, X. Fettweis, T. Mote, J. Wahr, P. Alexander, J. E. Box, and B. Wouters. Evidence and analysis of 2012 Greenland records from spaceborne observations, a regional climate model and reanalysis data. *The Cryosphere*, 7: 615 – 630, 2013. ISSN 1994 - 0416. doi: 10.5194/tc-7-615-2013.
- M. Tedesco, J. E. Box, J. Cappelen, R. S. Fausto, X. Fettweis, T. Mote, C. J. P. P. Smeets, D. van As, I. Velicogna, R. S. W. van de Wal, and J. Wahr. Greenland Ice Sheet, [in "State of the Climate in 2015"]. *Bull. Amer. Meteor. Soc.*, 97:S173 – S226, 2016a.
- M. Tedesco, S. Doherty, X. Fettweis, P. Alexander, J. Jeyaratnam, and J. Stroeve. The darkening of the Greenland ice sheet: trends, drivers, and projections (1981-2100). *The Cryosphere*, 10:477 – 496, 2016b. doi: 10.5194/tc-10-477-2016.

- M. Tedesco, T. Mote, X. Fettweis, E. Hanna, J. Jeyaratnam, J. F. Booth, R. Datta, and K. Briggs. Arctic cut-off high drives the poleward shift of a new Greenland melting record. *Nature Communications*, 7:11723, 2016c. doi: 10.1038/ncomms11723.
- A. M. Tompkins, K. Gierens, and G. Rädel. Ice supersaturation in the ECMWF integrated forecast system. *Quarterly Journal of the Royal Meteorological Society*, 133:53 – 63, 2007. doi: 10.1002/qj.14.
- P. Undèn, L. Rontu, H. Järvinen, P. Lynch, J. Calvo, G. Cats, J. Cuxart, K. Eerola, C. Fortelius, J. A. Garcia-Moya, C. Jones, G. Lenderlink, A. McDonald, R. Mcgrath, B. Navascues, N. W. Nielsen, V. Degaard, E. Rodriguez, M. Rummukainen, K. Sattler, B. H. Sass, H. Savijarvi, B. W. Schreur, R. Sigg, and H. The. HIRLAM-5. *Scientific Documentation*, 2002. Technical Report.
- S. M. Uppala, P. W. Kållberg, A. J. Simmons, U. Andrae, V. Da Costa Bechtold, M. Fiorino, J. K. Gibson, J. Haseler, A. Hernandez, G. A. Kelly, X. Li, K. Onogi, S. Saarinen, N. Sokka, R. P. Allan, E. Andersson, K. Arpe, M. A. Balmaseda, A. C. M. Beljaars, L. Van De Berg, J. Bidlot, N. Bormann, S. Caires, F. Chevallier, A. Dethof, M. Dragosavac, M. Fisher, M. Fuentes, S. Hagemann, E. Hölm, B. J. Hoskins, L. Isaksen, P. A. E. M. Janssen, R. Jenne, A. P. McNally, J-F. Mahfouf, J-J. Morcrette, N. A. Rayner, R. W. Saunders, P. Simon, A. Ster, K. E. Trenberth, A. Untch, D. Vasiljevic, P. Viterbo, and J. Woollen. The ERA-40 re-analysis. *Quarterly Journal of the Royal Meteorological Society*, 131:2961 – 3012, 2005.
- J. H. Van Angelen, J. T. M. Lenaerts, S. Lhermitte, X. Fettweis, P. Kuipers Munneke, M. R. van den Broeke, E. van Meijgaard, and C. J. P. P. Smeets. Sensitivity of Greenland Ice Sheet surface mass balance to surface albedo parameterization: a study with a regional climate model. *The Cryosphere*, 6:1175 – 1186, 2012. doi: 10.5194/tc-6-1175-2012.
- J. H. Van Angelen, J. T. M. Lenaerts, M. R. van den Broeke, X. Fettweis, and E. van Meijgaard. Rapid loss of firn pore space accelerates 21st century greenland mass loss. *Geophysical Research Letters*, 40:2109 – 2113, 2013. doi: 10.1002/grl.50490.
- J. H. Van Angelen, M. R. van den Broeke, B. Wouters, and J. T. M. Lenaerts. Contemporary (1969-2012) evolution of the climate and surface mass balance of the Greenland ice sheet. *Surveys in Geophysics*, 2013a. doi: 10.1007/s10712-013-9261-z.
- J. H. Van Angelen, M. R. van den Broeke, B. Wouters, and J. T. M. Lenaerts. Contemporary (1969-2012) evolution of the climate and surface mass balance of the Greenland ice sheet. *Surveys in Geophysics*, 35(5):1155 – 1174, 2013b. doi: 10.1007/s10712-013-9261-z.
- D. Van As, R. S. Fausto, A. P. Ahlström, S. B. Andersen, M. L. Andersen, M. Citterio, K. Edelvang, P. Gravesen, H. Machguth, F. M. Nick, S. Nielsen, and A. Weidick. Temperature and ablation records from the Programme for Monitoring of the Greenland Ice Sheet (PROMICE). *Geological Survey of Denmark and Greenland Bulletin*, 23:73 – 76, 2011. URL www.geus.dk/publications/bull1.
- W. J. Van de Berg and B. Medley. Brief Communication: Upper-air relaxation in RACMO2 significantly improves modelled interannual surface mass balance variability in Antarctica. *The Cryosphere*, 10:459 – 463, 2016. doi: <https://doi.org/10.5194/tc-10-459-2016>.
- W. J. Van de Berg, M.R. van den Broeke, C.H. Reijmer, and E. van Meijgaard. Reassessment of the Antarctic surface mass balance using calibrated output of a regional atmospheric climate model. *Journal of Geophysical Research*, 111: D11104, 2006. doi: 10.1029/2005JD006495.
- R. S. W. Van de Wal, W. Greuell, M. R. van den Broeke, C. H. Reijmer, and J. Oerlemans. Surface mass-balance observations and automatic weather station data along a transect near Kangerlussuaq, West Greenland. *Annals of Glaciology*, 42:311 – 316, 2005. doi: 10.3189/172756405781812529.
- R. S. W. Van de Wal, W. Boot, C. J. P. P. Smeets, H. Snellen, M. R. van den Broeke, and J. Oerlemans. Twenty-one years of mass balance observations along the K-transect, West Greenland. *Earth System Science Data*, 4:31 – 35, 2012. doi: 10.5194/essdd-5-351-2012.
- M. R. Van den Broeke, P. Smeets, J. Ettema, and P. Kuipers Munneke. Surface radiation balance in the ablation zone of the west Greenland ice sheet. *Journal of Geophysical Research: Atmospheres*, 113:D13105, 2008. doi: 10.1029/2007JD009283.
- M. R. Van den Broeke, P. Smeets, and J. Ettema. Surface layer climate and turbulent exchange in the ablation zone of the west Greenland ice sheet. *International Journal of Climatology*, 29:2309 – 2323, 2009. doi: 10.1002/joc.1815.
- M. R. Van den Broeke, P. Smeets, and R. S. W. van de Wal. The seasonal cycle and interannual variability of surface energy balance and melt in the ablation zone of the west Greenland ice sheet. *The Cryosphere*, 5:377 – 390, 2011. doi: 10.5194/tc-5-377-2011.
- M. R. Van den Broeke, E. Enderlin, I. Howat, P. Kuipers Munneke, B. Noël, W. J. van de Berg, E. van Meijgaard, and B. Wouters. On the recent contribution of the Greenland ice sheet to sea level change. *The Cryosphere*, 10:1933 – 1946, 2016. doi: 10.5194/tc-10-1933-2016.
- M. R. Van den Broeke, J. Box, X. Fettweis, E. Hanna, B. Noël, M. Tedesco, D. van As, W. J. van de Berg, and L. van Kampenhout. Greenland Ice Sheet Surface Mass Loss: Recent Developments in Observation and Modeling. *Current Climate Change Reports*, 3(4):345 – 356, 2017. doi: 10.1007/s40641-017-0084-8.

- E. Van Meijgaard, L. H. van Ulft, W. J. van de Berg, F. C. Bosveld, B. van den Hurk, G. Lenderink, and A. P. Siebesma. *Technical Report 302: The KNMI regional atmospheric climate model RACMO version 2.1*. Royal Netherlands Meteorological Institute, De Bilt, 2008.
- E. Van Meijgaard, L.H. van Ulft, G. Lenderink, S.R. de Roode, L. Wipfler, R. Boers, and R. M. A. Timmermans. Refinement and application of a regional atmospheric model for climate scenario calculations of Western Europe. *Climate Change Spatial Planning Publication*, KVR 054/12, 2012.
- K. Van Tricht, S. Lhermitte, J. T. M. Lenaerts, I. V. Gorodetskaya, T. S. L'Ecuyer, B. Noël, M. R. van den Broeke, D. D. Turner, and N. P. M. van Lipzig. Clouds enhance Greenland ice sheet meltwater runoff. *Nature communications*, 7 (10266), 2016. doi: 10.1038/ncomms10266.
- J. M. Van Wessem, C. H. Reijmer, J. T. M. Lenaerts, W. J. van de Berg, M. R. van den Broeke, and E. van Meijgaard. Updated cloud physics in a regional atmospheric climate model improves the modelled surface energy balance of Antarctica. *The Cryosphere*, 8:125 – 135, 2014a. doi: 10.5194/tc-8-125-2014.
- J. M. Van Wessem, C. H. Reijmer, M. Morlighem, J. Mouginot, E. Rignot, B. Medley, I. Joughin, B. Wouters, M. A. Depoorter, J. L. Bamber, J. T. M. Lenaerts, W. J. van de Berg, M. R. van den Broeke, and E. van Meijgaard. Improved representation of East Antarctic surface mass balance in a regional atmospheric climate model. *Journal of Glaciology*, 60(222):761 – 770, 2014b. doi: 10.3189/2014JogG14J051.
- J. M. Van Wessem, S. R. M. Ligtenberg, C. H. Reijmer, W. J. van de Berg, M. R. van den Broeke, N. E. Barrand, E. R. Thomas, J. Turner, J. Wuite, T. A. Scambos, and E. van Meijgaard. The modelled surface mass balance of the Antarctic Peninsula at 5.5km horizontal resolution. *The Cryosphere*, 10:271 – 285, 2016. doi: 10.5194/tc-10-271-2016.
- J. M. Van Wessem, W. J. van de Berg, B. P. Y. Noël, E. van Meijgaard, G. Birnbaum, C. L. Jakobs, K. Krüger, J. T. M. Lenaerts, S. Lhermitte, S. R. M. Ligtenberg, B. Medley, C. H. Reijmer, K. van Tricht, L. D. Trusel, L. H. van Ulft, B. Wouters, J. Wuite, and M. R. van den Broeke. Modelling the climate and surface mass balance of polar ice sheets using RACMO2, Part 2: Antarctica (1979-2016). *The Cryosphere Discussions*, 2017. doi: <https://doi.org/10.5194/tc-2017-202>. in review.
- W. Van Wychen, L. Copland, D. O. Burgess, L. Gray, and N. Schaffer. Glacier velocities and dynamic discharge from the ice masses of Baffin Island and Bylot Island, Nunavut, Canada. *Can. J. Earth Sci.*, 52:980 – 989, 2015. doi: [dx.doi.org/10.1139/cjes-2015-0087](https://doi.org/10.1139/cjes-2015-0087).
- W. Van Wychen, J. Davis, D. O. Burgess, L. Copland, L. Gray, M. Sharp, and C. Mortimer. Characterizing interannual variability of glacier dynamics and dynamic discharge (1999-2015) for the ice masses of Ellesmere and Axel Heiberg Islands, Nunavut, Canada. *Journal of Geophysical Research: Earth Surface*, 121:39 – 63, 2016. doi: 10.1002/2015JF003708.
- D. G. Vaughan, J. C. Comiso, I. Allison, J. Carrasco, G. Kaser, R. Kwok, P. Mote, T. Murray, F. Paul, J. Ren, E. Rignot, O. Solomina, K. Steffen, and T. Zhang. *Observations: Cryosphere. In: Climate Change 2013: The Physical Science Basis. Contribution of Working Group I to the Fifth Assessment Report of the Intergovernmental Panel on Climate Change [Stocker, T.F., D. Qin, G.-K. Plattner, M. Tignor, S.K. Allen, J. Boschung, A. Nauels, Y. Xia, V. Bex and P.M. Midgley (eds.)]*. Cambridge University Press, Cambridge, United Kingdom and New York, NY, USA, 2013.
- I. Velicogna. Increasing rates of ice mass loss from the Greenland and Antarctic ice sheets revealed by GRACE. *Geophysical Research Letters*, 36:L19503, 2009. doi: 10.1029/2009GL040222.
- I. Velicogna and J. Wahr. Acceleration of greenland ice mass loss in spring 2004. *Nature*, 443:329 – 331, 2006. doi: 10.1038/nature05168.
- C. L. Vernon, J. L. Bamber, J. E. Box, M. R. van den Broeke, X. Fettweis, E. Hanna, and P. Huybrechts. Surface mass balance model intercomparison for the Greenland ice sheet. *The Cryosphere*, 7:599 – 614, 2013. doi: 10.5194/tc-7-599-2013.
- M. Vizcaíno, W. H. Lipscomb, W. J. Sacks, J. H. van Angelen, B. Wouters, and M. R. van den Broeke. Greenland Surface Mass Balance as Simulated by the Community Earth System Model. Part I: Model Evaluation and 1850-2005 Results. *Journal of Climate*, 26:7793 – 7812, 2013. doi: 10.1175/JCLI-D-12-00615.1.
- U. Weiser, M. Olefs, W. Schöner, G. Weyss, and B. Hynek. Correction of broadband snow albedo measurements affected by unknown slope and sensor tilts. *The Cryosphere*, 10:775 – 790, 2016. doi: 10.5194/tc-10-775-2016.
- P. W. White. Part IV : PHYSICAL PROCESSES (CY23R4). *Technical Report*, 2001.
- S. Williamson, M. Sharp, J. Dowdeswell, and T. Benham. Iceberg calving rates from northern Ellesmere Island ice caps, Canadian Arctic, 1999-2003. *Journal of Glaciology*, 54(186):391 – 400, 2008. doi: 10.3189/002214308785837048.
- D. J. Wilton, A. Jowett, E. Hanna, G. R. Bigg, M. R. van den Broeke, X. Fettweis, and P. Huybrechts. High resolution (1 km) positive degree-day modelling of Greenland ice sheet surface mass balance, 1870-2012 using reanalysis data. *Journal of Glaciology*, 63(237):176 – 193, 2016. doi: 10.1017/jog.2016.133.
- B. Wouters, J. L. Bamber, M. R. van den Broeke, J. T. M. Lenaerts, and I. Sasgen. Limits in detecting acceleration of ice sheet mass loss due to climate variability. *Nature Geoscience*, 6:613 – 616, 2013. doi: 10.1038/ngeo1874.

- B. Wouters, A. Martín-Español, V. Helm, T. Flament, J. M. van Wessem, S. R. M. Ligtenberg, M. R. van den Broeke, and J. L. Bamber. Dynamic thinning of glaciers on the Southern Antarctic Peninsula. *Science*, 348(6237.):899 – 903, 2015. doi: 10.1126/science.aaa5727.
- C. Zdanowicz, A. Smetny-Sowa, D. Fisher, N. Schaffer, L. Copland, J. Eley, and F. Dupont. Summer melt rates on Penny Ice Cap, Baffin Island: Past and recent trends and implications for regional climate. *Journal of Geophysical Research*, 117(F2):F02006, 2012. doi: 10.1029/2011JF002248.
- C. M. Zdanowicz, D. A. Fischer, I. Clark, and D. Lacelle. An ice-marginal $\delta^{18}\text{O}$ record from Barnes Ice Cap, Baffin Island, Canada. *Annals of Glaciology*, 35(1):145 – 149, 2002. doi: <https://doi.org/10.3189/172756402781817031>.
- H. Zekollari, P. Huybrechts, B. Noël, W. J. van de Berg, and M. R. van den Broeke. Sensitivity, stability and future evolution of the world's northernmost ice cap, Hans Tausen Iskappe (Greenland). *The Cryosphere*, 11:805 – 825, 2017. doi: 10.5194/tc-11-805-2017.

Abbreviations

| | |
|------------------------|---|
| AWS | Automatic Weather Station |
| BIA | Bare Ice Albedo |
| CAA | Canadian Arctic Archipelago |
| CDEM | Canadian Digital Elevation Model |
| CESM | Community Earth System Model |
| D | Solid ice Discharge |
| DEM | Digital Elevation Model |
| ECMWF | European Centre for Medium-range Weather Forecasts |
| ELA | Equilibrium Line Altitude |
| ER or ER _{ds} | Erosion from drifting snow |
| ESM | Earth System Model |
| FDM | Firn Densification Model |
| G _s | Ground heat flux (subsurface) |
| GICs | Glaciers and Ice Caps (Greenland) |
| GIMP | Greenland Ice Mapping Project |
| GLCC | Global Land Cover Characteristics |
| GrIS | Greenland Ice Sheet |
| GRACE | Gravity Recovery and Climate Experiment |
| Gt | Gigaton |
| HIRLAM | High Resolution Limited Area Model |
| ICESat | Ice, Cloud and land Elevation Satellite |
| IFS | Integrated Forecasts System |
| IMAU | Institute for Marine and Atmospheric research at Utrecht University |
| JJA | June-July-August |
| KNMI | Royal Netherlands Meteorological Institute |
| K-transect | Kangerlussuaq transect |
| LHF | Latent Heat Flux |
| LW _d | Longwave downward radiation |
| LW _n | Longwave net radiation |
| LW _u | Longwave upward radiation |
| M | Melt energy |
| MAR | Modèle Atmosphérique Régional |
| ME | Melt from snow and/or ice |
| MB | Mass Balance |
| MBM | Mass Balance Method |
| MODIS | MODerate-resolution Imaging Spectroradiometer |
| NAO | North Atlantic Oscillation |

| | |
|-------------------------|---|
| NASA | National Aeronautics and Space Administration |
| NCAA | North Canadian Arctic Archipelago |
| NCAR | National Centre for Atmospheric Research |
| NCEP | National Centre for Environmental Prediction |
| P_{tot} | Precipitation (total) |
| PDD | Positive Degree Day |
| PROMICE | PROgramme for Monitoring of the Greenland Ice Sheet |
| RA | Rainfall |
| RACMO | Regional Atmospheric Climate MOdel |
| RCM | Regional Climate Model |
| RCP | Representative Concentration Pathways |
| RF | Refreezing |
| RGI | Randolph Glacier Inventory |
| RMSD | Root Mean Square Difference |
| RMSE | Root Mean Square Error |
| RT | Retention |
| RU | Runoff of meltwater |
| SAR | SATellite Radar interferometer |
| SCAA | South Canadian Arctic Archipelago |
| SEB | Surface Energy Budget or Surface Energy Balance |
| SF | Snowfall |
| SHF | Sensible Heat Flux |
| SLR | Sea Level Rise equivalent |
| SMB | Surface Mass Balance |
| SU or SU_{tot} | Sublimation (total) from surface and snow drift processes |
| SW_{d} | Shortwave downward radiation |
| SW_{n} | Shortwave net radiation |
| SW_{u} | Shortwave upward radiation |
| WE or w.e. | Water equivalent |

Acknowledgements

To begin with, I would like to thank my promotor and co-promotor, Michiel and Willem Jan. Thank you for your trust during these last four years. Despite your tight schedule, you were always available to supervise my research. I can not believe how much we achieved together and how much I learned from your experience and advice. Working with the both of you at IMAU was a privilege.

Michiel, thank you for your enthusiastic supervision of my research project, your constant encouragements and support (in harder times). Discussing with you has always been very inspiring, as you easily share your experience and knowledge. I really appreciated every piece of advice and edits you provided on my presentations and paper drafts. These have notably improved my scientific writing but also the overall quality and impact of our publications. Thank you for giving me the opportunity to travel worldwide, promoting my research in international conferences.

Willem Jan, thank you for your availability, your daily supervision, especially at the beginning of my PhD, and for sharing your knowledge on RACMO2. Your expertise on coding, statistics, and model physics have always impressed me, and encouraged me to improve myself. I really enjoyed sitting with you to discuss about modelling, solving programming issues or improving the quality of our publications.

I spent an amazing and entertaining time at IMAU. Melchior, Lennert, Christian, Leo and Jan, thank you for introducing me to the Netherlands and for making my integration at IMAU so smooth. Besides being great colleagues, you also became dear friends. I will never forget our informal HOEMBA pizza beer parties, the Friday afternoon drinks, the conference nights out, ... On top of that, you taught me french words I had never heard before, e.g. "bateau de plaisir" or "ordinateur extraordinaire". Over the last four years, I have been very lucky to share my office with Jan (the famous), Leo (the expert), and more recently Melchior (the landlord). I really enjoyed discussing and working with you and hope we will keep in touch and collaborate in the future!

I would also like to thank our more recent HOEMBA recruits (Marta, Stan, Tijn, Christiaan and Larissa) and the new head (Sharon). With you, HOEMBA meetings slowly evolved from pizza-beer anarchy to an actual PhD (mental) support group (Tijn et al., 2017), a great step towards PhD wellness! I also spent numerous memorable lunch breaks and had a lot of fun with each member of our lunch group (Bas, Hans, Werner, Antonija, Sarah, and Heiko). Thank you for sharing random and sometimes absurd low-level discussions! I am really indebted to my colleagues from the Ice and Climate group (Bert, Stefan, Peter, Roderik and Carleen) for the help provided at different stages of my research. Special thank goes to Marcel for the time spent on fixing my recalcitrant computer.

Finally, I am really grateful to each of my committee member for reviewing and evaluating my research work. I hope you enjoyed reading this thesis as much as I valued my time at IMAU.

Je voudrais également remercier mes chers amis belges, Sylvain (le poil-de-culteur) et Raphaël (monsieur Frissen), avec qui je forme le clan des "trois mousquetaires" de la climatologie liégeoise promotion 2013 ; mon aîné et mentor climatologique Julien (le bouky), et mes chers amis Henri-Paul (le riton), Sébastien (le shaman) et Nicolas (l'Américain). Je vous remercie pour votre amitié fidèle, l'aide procurée lors de mon déménagement aux Pays-Bas, nos virées épiques au Dikke Dries, nos longues soirées en conférence ou dans d'autres estaminets de Liège ou d'Utrecht. En particulier, merci Sylvain pour ton soutien, ta confiance et ton amitié indéfectible !

Pendant toute la durée de ma thèse, j'ai bénéficié de l'aide et du soutien inconditionnel de ma famille. Je remercie tout particulièrement ma maman qui m'a épaulé tout au long de mon parcours scientifique dans les bons et les moins bons moments. Je remercie également mes deux soeurs, Laure et Lise, mes modèles de réussite. Votre intelligence et votre bienveillance m'ont toujours poussé à m'améliorer. Merci pour votre affection, pour m'avoir accompagné dans de nombreux voyages à travers la Hollande ou encore pour votre aide précieuse au cours de mes nombreux déménagements. Je remercie tout spécialement Lise pour ses conseils avisés lors de la relecture et de la réalisation de la couverture de cette thèse. Finalement, je voudrais remercier ma grand-mère et marraine pour son enthousiasme envers ma recherche, sa confiance en mes compétences, et son incroyable soutien tout au long de ma thèse. Encore une fois, merci à vous tous !

Publications

First author

B. Noël, X. Fettweis, W. J. van de Berg, M. R. van den Broeke, and M. Erpicum. Sensitivity of Greenland Ice Sheet surface mass balance to perturbations in sea surface temperature and sea ice cover: a study with the regional climate model MAR. *The Cryosphere*, 8: 1871 - 1883, 2014. doi: 10.5194/tc-8-1871-2014.

B. Noël, W. J. van de Berg, E. van Meijgaard, P. Kuipers Munneke, R. S. W. van de Wal, and M.R. van den Broeke. Evaluation of the updated regional climate model RACMO2.3: summer snowfall impact on the Greenland Ice Sheet. *The Cryosphere*, 9: 1831 - 1844, 2015. doi: 10.5194/tc-9-1831-2015.

B. Noël, W. J. van de Berg, H. Machguth, S. Lhermitte, I. Howat, X. Fettweis, and M. R. van den Broeke. A daily, 1 km resolution data set of downscaled Greenland ice sheet surface mass balance (1958-2015). *The Cryosphere*, 10(5): 2361 - 2377, 2016. doi: 10.5194/tc-10-2361-2016.

B. Noël, W. J. van de Berg, S. Lhermitte, B. Wouters, H. Machguth, I. Howat, M. Citterio, G. Moholdt, J. T. M. Lenaerts, and M. R. van den Broeke. A tipping point in refreezing accelerates mass loss of Greenland's glaciers and ice caps. *Nature Communications*, 8: 14730, 2017a. doi: 10.1038/ncomms14730.

B. Noël, W. J. van de Berg, S. Lhermitte, B. Wouters, N. Schaffer, and M. R. van den Broeke. Six decades of glacial mass loss in the Canadian Arctic Archipelago. *Journal of Geophysical Research Earth Surface*, 2017b. in review.

B. Noël, W. J. van de Berg, J. M. van Wessem, E. van Meijgaard, D. van As, J. T. M. Lenaerts, S. Lhermitte, P. Kuipers Munneke, C. J. P. P. Smeets, L. H. van Ulf, R. S. W. van de Wal, and M. R. van den Broeke. Modelling the climate and surface mass balance of polar ice sheets using RACMO2, Part 1: Greenland (1958-2016). *The Cryosphere Discussions*, 2017c. <https://doi.org/10.5194/tc-2017-201>.

Co-author

T. Moon, I. Joughin, B. Smith, M. R. van den Broeke, W. J. van de Berg, B. Noël, and M. Usher. Distinct patterns of seasonal Greenland glacier velocity, *Geophysical Research Letters*, 41:7209 - 7216, 2014 .doi:10.1002/2014GL061836.

M. McMillan, A. Shepherd, N. Gourmelen, A. Dehecq, A. Leeson, A. Ridout, T. Flament, A. Hogg, L. Gilbert, T. Benham, M. van den Broeke, J. Dowdeswell, X. Fettweis, B. Noël, T. Strozzi. Rapid dynamic activation of a marine-based Arctic ice cap, *Geophysical Research Letters*, 41: 8902 - 8909, 2014. doi:10.1002/2014GL062255.

S. de la Peña, I. M. Howat, P. W. Nienow, M. R. van den Broeke, E. Mosley-Thompson, S. F. Price, D. Mair, B. Noël, and A. J. Sole. Changes in the firn structure of the western Greenland Ice Sheet caused by recent warming, *The Cryosphere*, 9: 1203 - 1211, 2015. doi:10.5194/tc-9-1203-2015.

P. Kuipers Munneke, S. R. M. Ligtenberg, B. P. Y. Noël, I. M. Howat, J. E. Box, E. Mosley-Thompson, J. R. McConnell, K. Steffen, J. T. Harper, S. B. Das and M. R. van den Broeke. Elevation change of the Greenland Ice Sheet due to surface mass balance and firn processes, 1960-2014, *The Cryosphere*, 9: 2009 - 2025, 2015. doi:10.5194/tc-9-2009-2015.

K. Van Tricht, S. Lhermitte, J. T. M. Lenaerts, I. V. Gorodetskaya, T. S. L'Ecuyer, B. Noël, M. R. van den Broeke, D. D. Turner and N. P. M. van Lipzig. Clouds enhance Greenland ice sheet meltwater runoff. *Nature Communications* 7: 10266, 2016. doi: 10.1038/ncomms10266.

T. Bartholomäus, L. Stearns, D. Sutherland, E. Shroyer, J. Nash, R. Walker, G. Catania, D. Felikson, D. Carroll, M. J. Fried, B. P. Y. Noël and M. Van Den Broeke. Contrasts in the response of adjacent fjords and glaciers to ice-sheet surface melt in West Greenland, *Annals of Glaciology*, 57(73): 25 - 38, 2016. doi:10.1017/aog.2016.19.

M. McMillan, A. Leeson, A. Shepherd, K. Briggs, T. W. K. Armitage, A. Hogg, P. Kuipers Munneke, M. van den Broeke, B. Noël, W. J. van de Berg, S. Ligtenberg, M. Horwarth, A. Groh, A. Muir, L. Gilbert. A high-resolution record of Greenland mass balance, *Geophysical Research Letters*, 43: 7002 - 7010, 2016. doi:10.1002/2016GL069666.

D. Carroll, D. A. Sutherland, B. Hudson, T. Moon, G. A. Catania, E. L. Shroyer, J. D. Nash, T. C. Bartholomäus, D. Felikson, L. A. Stearns, B. P. Y. Noël and M. Van Den Broeke. The impact of glacier geometry on meltwater plume structure and submarine melt in Greenland fjords, *Geophysical Research Letters*, 43: 9739 - 9748, 2016. doi:10.1002/2016GL070170.

M. R. van den Broeke, E. M. Enderlin, I. M. Howat, P. Kuipers Munneke, B. P. Y. Noël, W. J. van de Berg, E. van Meijgaard, B. and Wouters. On the recent contribution of the Greenland ice sheet to sea level change, *The Cryosphere*, 10: 1933 - 1946, 2016. doi:10.5194/tc-10-1933-2016.

L. A. Stevens, M. D. Behn, S. B. Das, I. Joughin, B. P. Y. Noël, M. R. van den Broeke, and T. Herring. Greenland Ice Sheet flow response to runoff variability, *Geophysical Research Letters*, 43(11): 295-11,303, 2016. doi:10.1002/2016GL070414.

L. N. Boisvert, J. N. Lee, J. T. M. Lenaerts, B. Noël, M. R. van den Broeke, and A. W. Nolin. Using remotely sensed data from AIRS to estimate the vapor flux on the Greenland ice sheet: Comparisons with observations and a regional climate model, *Journal Geophysical Research Atmosphere*, 122: 202 - 229, 2017. doi:10.1002/2016JD025674.

C. R. Steger, C. H. Reijmer, M. R. van den Broeke, N. Wever, R. R. Forster, L. S. Koenig, P. Kuipers Munneke, M. Lehning, S. Lhermitte, S. R. M. Ligtenberg, C. Miège and B. P. Y. Noël. Firn Meltwater Retention on the Greenland Ice Sheet: A Model Comparison, *Frontiers Earth Science*, 5:3, 2017. doi: 10.3389/feart.2017.00003.

H. Zekollari, P. Huybrechts, B. Noël, W. J. van de Berg and M. R. van den Broeke. Sensitivity, stability and future evolution of the world's northernmost ice cap, Hans Tausen Iskappe (Greenland), *The Cryosphere*, 11: 805-825, 2017. doi:10.5194/tc-11-805-2017.

D. Felikson, T. C. Bartholomäus, G. A. Catania, N. J. Korsgaard, K. H. Kjær, M. Morlighem, B. Noël, M. van den Broeke, L. A. Stearns, E. L. Shroyer, D. A. Sutherland and J. D. Nash. Inland thinning on the Greenland ice sheet controlled by outlet glacier geometry, *Nature Geoscience*, 10: 366 - 369, 2017. doi:10.1038/ngeo2934.

M. Morlighem, C. N. Williams, E. Rignot, L. An, J. E. Arndt, J. L. Bamber, G. Catania, N. Chauché, J. A. Dowdeswell, B. Dorschel, I. Fenty, K. Hogan, I. Howat, A. Hubbard, M. Jakobsson, T. M. Jordan, K. K. Kjeldsen, R. Millan, L. Mayer, J. Mouginot, B. P. Y. Noël, C. Ó Cofaigh, S. Palmer, S. Rysgaard, H. Seroussi, M. J. Siegert, P. Slabon, F. Straneo, M. R. van den Broeke, W. Weinrebe, M. Wood and K. B. Zinglensen. BedMachine v3: Complete bed topography and ocean bathymetry mapping of Greenland from multi-beam echo sounding combined with mass conservation, *Geophysical Research Letters*, 34 pp., 2017. doi: 10.1002/2017gl074954.

J. M. van Wessem, B. P. Y. Noël, W. J. van de Berg, C. L. Jakobs, C. H. Reijmer, M. R. van den Broeke, K. Krüger, G. Birnbaum, L. D. Trusel, S. Lhermitte, B. Medley, J. Wuite, and E. van Meijgaard. Modelling the climate and surface mass balance of polar ice sheets using RACMO2, Part 1: Antarctica (1979-2016), *The Cryosphere Discussions*, 2017. <https://doi.org/10.5194/tc-2017-202>.

I. Overeem, B. D. Hudson, J. P. M. Syvitski, A. B. Mikkelsen, B. Hasholt, M. R. van den Broeke, B. P. Y. Noël and M. Morlighem. Substantial export of suspended sediment to the global oceans from glacial erosion in Greenland, *Nature Geoscience*, 8 pp., 2017. doi: 10.1038/ngeo3046.

M. R. van den Broeke, J. Box, X. Fettweis, E. Hanna, B. Noël, M. Tedesco, D. van As, W. J. van de Berg and L. van Kampenhout. Greenland Ice Sheet Surface Mass Loss: Recent Developments in Observation and Modeling, *Current Climate Change Reports*, 3(4): 345-356, 2017. doi: 10.1007/s40641-017-0084-8.

L. C. Smith, K. Yang, L. H. Pitcher, B. T. Overstreet, V. W. Chu, A. K. Rennermalm, J. C. Ryan, M. G. Cooper, C. J. Gleason, M. Tedesco, J. Jeyaratnam, D. van As, M. R. van den Broeke, W. J. van de Berg, B. Noël, P. L. Langen, R. I. Cullather, B. Zhao, M. J. Willis, A. Hubbard, J. E. Box, B. A. Jenner, A. E. Behar. Direct measurements of meltwater runoff on the Greenland ice sheet surface, *PNAS*, 114(50): E10622?E10631, 2017. doi: 10.1073/pnas.1707743114.

Submitted

D. Van As, B. Hasholt, A. P. Ahlstrøm, J. E. Box, J. Cappelen, W. Colgan, R. S. Fausto, S. H. Mernild, A. B. Mikkelsen, B. P. Y. Noël, D. Petersen and M. R. Van den Broeke. The longest observationally-constrained record of Greenland ice sheet meltwater discharge (1949-2016). *Arctic, Antarctic, and Alpine Research*, 2017.

Curriculum vitae

Brice Noël



- 22-05-1991 Born in Oupeye (Belgium)
- 1996 – 2002 Primary school, Ecole communale, Haccourt
2002 – 2008 Secondary school, Collège S^t Hadelin, Visé
- 2008 – 2011 BSc Geography, Université de Liège
Bachelor thesis title: *Analyse des interactions entre l'ENSO et les inondations du Queensland.*
- 2011 – 2013 MSc Climatology, Université de Liège
Master thesis title: *Assessing the oceanic forcings influence on the Greenland Ice Sheet surface mass balance with the regional climate model MAR.*
- 2013 – 2017 PhD at IMAU, Utrecht University
Thesis title: *Modelling the surface mass balance of the Greenland ice sheet and neighbouring ice caps: a dynamical and statistical downscaling approach.*
Promotor: prof. dr. M.R. van den Broeke
Co-promotor: dr. W.J. van de Berg
- 2017 – Postdoctoral research at IMAU, Utrecht University

Awards

- 2013 Best Master Thesis in Climatology, Université de Liège
2015 Outstanding Student Paper Awards (OSPA), AGU Fall Meeting
2017 Best Poster Presentation, Physics Department Day, Utrecht University